THÈSE

En vue de l'obtention du

DOCTORAT DE L'UNIVERSITÉ DE TOULOUSE

Délivré par :

Université Toulouse 3 Paul Sabatier (UT3 Paul Sabatier)

Présentée et soutenue par :
Marie Hoarau
le Jeudi 03 Novembre 2016

Titre :

Towards new bioinorganic hybrid catalysts based on amyloid fibres

---

École doctorale et discipline ou spécialité :
ED SDM : Chimie, Biologie, Santé - CO 042

Unité de recherche :
LCC (UPR CNRS 8241) - LISBP (UMR CNRS/INSA 5504)

Directeur/trice(s) de Thèse :

Dr Emmanuel Gras
Pr Magali Remaud-Siméon

Jury :

Pr Christophe Cullin	Rapporteur	CBMN, Bordeaux
Dr Vincent Forge	Rapporteur	LCBM, Grenoble
Dr Jean-Marc Escudier	Examinateur	SPCMIB, Toulouse
Dr Stéphane Ménage	Examinateur	LCBM, Grenoble
Pr Thomas Ward	Examinateur	University of Basel
Dr Isabelle André	Membre invité	LISBP, Toulouse
Dr Christelle Hureau	Membre invité	LCC, Toulouse
Dr Emmanuel Gras	Directeur de thèse	LCC, Toulouse
Pr Magali Remaud-Siméon	Directrice de thèse	LISBP, Toulouse

Remerciements

Tout d’abord, je souhaite remercier les membres de mon jury, pour avoir accepté d’évaluer mes travaux, mais aussi pour avoir fait de ma soutenance de thèse une discussion très enrichissante. Je remercie en particulier Prof Christophe Cullin et Dr Vincent Forge pour le soin que vous avez mis à la lecture de mon manuscrit. Je remercie également Prof Thomas Ward de m’avoir fait l’honneur de présider mon jury, et d’avoir « arbitré » la discussion (parfois houleuse) avec une grande gentillesse.

Mes remerciements vont ensuite à mes directeurs de thèse, tout d’abord pour m’avoir choisie pour mener à bien ce projet. Aussi difficile fut-il, je pense qu’aucun sujet ne m’aurait mieux convenu.

Magali, un immense merci pour m’avoir introduite dans le monde merveilleux de la biologie, dans lequel je me sens à présent (presque) comme chez moi ! Merci pour ta gentillesse, ta patience et ta disponibilité. J’espère avoir l’opportunité de poursuivre dans ce domaine passionant qu’est l’ingénierie enzymatique.

Emmanuel, je te remercie pour ta gentillesse et ta bonne humeur, et pour tes conseils sur la partie synthèse. Merci également de t’être aventuré dans le monde de la biologie avec moi ! J’espère t’avoir prouvé que Paris Centre est (aussi) une bonne fac ! ;)

Christelle, un grand merci pour ton aide et ton implication sur la partie bio-inorganique, et pour l’écriture des publications. Merci aussi pour m’avoir introduit dans le cercle du FrenchBIC! Je souhaite le meilleur à la nouvelle équipe Alzoid.

Isabelle, je te remercie pour ta gentillesse et ta patience lors de ma découverte du docking ! Je reste convaincue que nos calculs ont été un vrai plus pour ce projet, et j’espère avoir l’occasion de réutiliser cet outil à l’avenir.

Enfin, Peter, je te remercie pour les nombreuses connaissances que tu m’as apportées sur le peptide, et pour les discussions toujours enrichissantes. J’aurais aimé travailler avec toi plus longtemps.

Parmi les services techniques du LCC, je souhaite également remercier Sonia Mallet-Ladeira, pour les structures aux rayons X, Christian Bijani, pour la RMN des peptides, et Lionel Rechignat pour les mesures RPE.

Cette thèse n’aurait pas pu aboutir sans l’aide de tous les membres de l’EAD1 (au LISBP) et de l’équipe F (au LCC). Chacun d’entre vous, à un moment ou à un autre, m’a apporté le soutien, les encouragements, et la motivation nécessaires pour mener à bien ce projet.

En particulier, je souhaite remercier Romain pour m’avoir transmis ses connaissances en biologie moléculaire, et Yannick pour son aide pour la purification des peptides. Je n’aurais jamais pu y arriver sans votre patience et vos encouragements.

Toujours au LISBP, un gros merci à Lisa, Louise, Barbara et Virginie, pour les séances de papotage/raleries, les soirées jeux et les supers cadeaux de thèse! Vous avez été d’un très grand soutien au cours de ces trois ans et je vous en remercie.

Je n’oublierais pas non plus Nathalie, Alexandra, Pauline, Marina, les deux Manon, Etienne, Marie G, les deux Julien, Sayani… Vous avez tous contribué à faire de mon séjour au LISBP une expérience fantastique!

Pour le LCC, je voudrais remercier Alexandre et Carine, pour avoir partagé avec moi le statut « mi-bio, mi-chimie », et pour les nombreuses pauses-café / brainstorming, et les discussions sans queue ni tête. Vous m’avez apporté bien plus que vous ne l’imaginez!

Un grand merci aussi à Viviane, pour ta joie de vivre tellement essentielle à l’équipe.

Amandine, Clémence, Valentina, merci de faire de l’équipe F une petite famille, où l’on ne s’ennuie jamais! Je n’oublie pas non plus Elena, Sara, Olivia, Melisa, Mireia, Omar, Daniel … Merci à tous!

Pour finir sur une touche plus personnelle, je tiens à remercier mes parents et mes deux sœurs, dont le soutien a été essentiel tout au long de ces trois ans. Une thèse est un chemin semé d’embuches qu’on ne peut pas parcourir seul, et grace à vous je ne l’ai jamais été. Cécile, un grand merci d’avoir été là, depuis si longtemps. Marion, on l’a fait ! Qui l’aurait cru il y a huit ans… Et bien sur, Olivier, mon amour, tu es ma force et mon courage, et rien n’aurait été possible sans toi.

List of abbreviations

Values are expressed following the International System Units. Amino acids are referred in the text using their IUPAC three-letter codes. Nucleic acids are referred using their one-letter IUPAC codes. Atoms are referred in the text using their element symbols.

Aβ: Amyloid-β

ACN: acetonitrile

AD: Alzheimer’s Disease

AFM: Atomic Force Microscopy

Bpy: 2,2’-bipyridine

CV: Cyclic Voltammetry

DNA: Deoxyribonucleic acid

DOSY: Diffusion Spectroscopy

Ee : enantiomeric excess

Er : enantiomeric ratio

EPR: Electron Paramagnetic Resonance

ESI-MS: Electrospray Ionization Mass Spectrometry

IAPP: Islet Amyloid Polypeptide

IB: Inclusion bodies

LC-MS: Liquid Chromatography-Mass Spectrometry

MLCT: Metal to ligand charge transfer

NMR: Nuclear Magnetic Resonance

PB: Phosphate Buffer

PDB: Protein Data Bank

Phen: 1,10-phenanthroline

Salophen: N,N'-bis(3,5-di-tert-butylsalicylidene)-1,2-diaminobenzene

SDS-PAGE: Sodium Dodecyl Sulfate Polyacrylamide Gel Electrophoresis

STD: Saturation Transfer Difference

TEM: Transmission Electron Microscopy

Th-S: Thioflavin-S

Th-T: Thioflavin-T

TON: turnover number

Tpy: 2,2’:6’,2’’-terpyridine

UV-Vis: UV-Visible spectrophotometry

WT: wild-type

Table of content

General introduction

It is announced, XXIst century will be that of ecology. For Chemistry, this is reflected by the Green Chemistry Principles, aiming at developing environmentally friendly alternatives to existing chemical processes. This comes with the use of catalysts, which can be used in small amounts to convert efficiently high amounts of substrates. But even employed in small amounts, catalysts can represent important source of pollution, especially when using heavy metals or ligands requiring multi-step syntheses. Research efforts thus tend to promote the development of new generations of catalysts.

Among the different possible approaches, one consists in seeking inspiration from enzymes. This gave rise to various elaboration strategies including the development of biomimetic coordination complexes, directed evolution of enzymes, or the development of artificial metalloenzymes. These systems aim at combining the efficiency of natural enzymes with the wide scope of reactivities and substrates of coordination catalysts, the overall system being fully biocompatible. Presence of a biomolecule (either nucleic acids or proteins) is also expected to confer rate enhancement, selectivity, and specificity, as observed in naturally occurring enzymes.

In this context, decided to focus on Amyloid fibres as a support biomolecule for our hybrid catalysts. These protein aggregates have unique properties, including robustness, stiffness, heat and solvent resistance that make them good candidates for catalytic applications. Because they are insoluble, they could also be easily recycled.

This thesis focuses on the elaboration of bioinorganic hybrid catalysts made of incorporation of coordination complexes into Amyloid fibres. To this view, a new expression and purification procedure was developed for Amyloid-β in *Escherichia coli*, enabling the rapid production of reliable peptide samples (see Chapter II).

A series of organic ligands was designed, inspired by reported amyloid-incorporating molecules. Corresponding Cu(II), Fe(II) and Ru(II) coordination complexes were synthesized and fully characterized, using various spectroscopic techniques, including NMR, EPR, cyclic voltammetry, UV-Visible and fluorescence spectrophotometry (see Chapter III).

These complexes were subsequently tested for their interaction with Amyloid fibres. UV-Visible and fluorescence measurements allowed to highlight candidates displaying good intercalation into fibres. Further investigations using UV-Visible and NMR afforded insights on the nature of binding sites and the interaction pattern of coordination complexes. These results were supported by docking studies (see Chapter IV).

Finally, the catalytic activity of our systems was assessed on styrene epoxidation reaction. All these results prompted us to draw outlooks for the evolution of our hybrid systems, both in terms of interaction with fibres and in terms of catalytic efficiency (see Chapter V).

Chapter I. Context of the project

Introduction

This project lies in the context of the development of artificial metalloenzymes, aiming at combining the strengths of chemistry and biology to develop innovative hybrid catalysts. Among the different existing methodologies, we got interested in the non-covalent incorporation of coordination complexes into biomolecules, which constitutes a straightforward and versatile alternative to bioconjugation strategies.

We propose to apply this strategy to amyloid fibres. These highly ordered protein assemblies have numerous occurrences in Nature, and share a characteristic cross β-sheet structure which might suits non-covalent intercalation. They are also very stable and resistant, which has prompted their use for various nanotechnology applications.

In the frame of this thesis, we chose to focus on Amyloid-β peptide. Because of its implication in Alzheimer’s Disease, this peptide has been extensively studied for its interaction with a wide set of molecules.

In a first part, this chapter portrays the field of artificial metalloenzymes, focusing on the approach consisting in incorporation of a metal complex into biomolecules, taking advantage of this sophisticated surrounding.

In a second part, an overview of amyloid proteins is proposed, going from their natural occurrences to their applications in nanotechnology.

Finally, focus is made on amyloid-β peptide, which was selected for this project. A precise description of its features is given, laying the foundations for the rest of the study.

I. Context of the study: artificial metalloenzymes

This chapter is adapted from: Hoarau, M., Hureau, C., Gras, E., and Faller, P. (2016). Coordination complexes and biomolecules: A wise wedding for catalysis upgrade. Coordination Chemistry Reviews 308, 445–459. Original article is in Annex III.

I.1. Role and importance of artificial metalloenzymes in catalysis

"*Chemistry without catalysis would be a sword without a handle, a light without brilliance, a bell without sound*." As nicely stated by Alwin Mittasch, catalysis plays an essential role in modern chemistry. Over the last 15 years, three Nobel Prizes were awarded for works on metal-based catalysis, reinforcing the importance of coordination complexes in organic synthesis.

From a general view, coordination catalysis utilises a large selection of metal ions, ligands and substrates to achieve a large set of reactivities. The reactivity of a coordination complex is mainly based on the tuning of its redox properties, substrate accessibility and/or Lewis acidity of its metallic centre. This is achieved by modulating the donor/acceptor character of the ligands and by controlling their geometry, arrangement and bulkiness around the metallic centre. For instance, steric hindrance can be used to induce substrate selectivity. Chemists excel at developing very sophisticated ligands that confer to complexes the desired properties. However, this has several limitations, among which the multi-step synthesis of the ligands and the use of rare metal ions, which represent significant economical and ecological concerns. An alternative would be to go towards "greener" processes inspired from Nature.

In Nature, enzymes are in charge of catalytic reactions, displaying extremely high rates, selectivity and specificity, optimised by evolution. By observing metalloenzymes, it appears that the first, second and outer coordination spheres play a crucial role in tuning the reactivity of the metallic centre. Indeed within enzymes the reactivity is not only driven by steric control of the metal site by the ligands but also *via* remote interactions (H bonding, electrostatic, stacking etc.) that guide the substrate into the active site, position it to ease the reaction, and help the release of the products. In other words, the strength of enzymes resides in the combination of inner and outer sphere effects, which confers rate enhancement, specificity and selectivity. Moreover the mobility, dynamics and/or conformational changes of the protein chain can help to adopt the most suitable geometry for the active site. All of this makes enzymes very powerful catalysts, but only considering a single reactivity and a limited series of substrates.

Chemists thus developed synthetic analogues of enzyme active sites, to better understand the structure-properties relationships. The ultimate goal would be to identify and select the crucial parameters for powerful catalysis, getting rid of the less pertinent ones. Among others, such mimics (structural, functional or both) were proposed for hydrogenases [1–4], superoxide dismutases [5–8], photosynthetic system [9,10] or oxygenases [11]. These systems go from the simplest, using very usual metallic ions and ligands [12] to the most sophisticated ones [13–15]. Even though models of metalloenzymes are very helpful for investigation purposes, they are often poor catalysts.

Different alternatives emerged to develop bioinorganic hybrid systems whose catalytic activity could compete with enzymes, often termed as “Artificial Metalloenzymes” [16–25]. Some of them proposed to modify natural enzymes or proteins to confer them non-native reactivity, while some other proposed to create new metalloproteins with fully controlled topology (Section I.2). In the context of this thesis, this chapter will focus on the approach consisting in incorporating coordination complexes into various biomolecules to form hybrid catalysts (Section I.3).

I.2. Different approaches for artificial metalloenzymes elaboration

I.2.a. Replacing the native metal ion of an enzyme

The replacement of the native metallic ion of an enzyme represents a first strategy, relatively easy to develop. It consists in replacing the native metallic ion of an enzyme by another, modifying its reactivity. Kaiser and co-workers first exemplified this approach in 1976. By changing Zn(II) with Cu(II) in carboxypeptidase A, they showed that the native activity was completely inhibited, and substituted by oxidizing properties [26].

Subsequent studies from Soumillion and colleagues showed that substituting Zn(II) by Mn(II) in carbonic anhydrase gave rise to an epoxidase activity [27]. In parallel, Kazlauskas *et al.* showed that the same Mn(II) carbonic anhydrase also displays peroxidase activity [28]. Figure 1 shows the X-ray structure of the active site of a Mn(II)-substituted human carbonic anhydrase II. It appears that the same amino acids are involved in the coordination of Zn(II) and of Mn(II) (*i.e.* His 94, His 96, and His 119), showing that the overall organization of the active site is not distorted by the substitution of the metallic ion. Some mutagenesis studies showed that several other amino acids within the catalytic pocket influence catalysis, further confirming the crucial importance of the whole environment.

Another step forward was the replacement of Zn(II) with a metallic ion of low natural abundance. This was achieved by incorporating Rh(I) into human carbonic anhydrase II. This system catalysed olefin hydrogenation and styrene hydroformylation with moderate to good yields and selectivities [29,30].

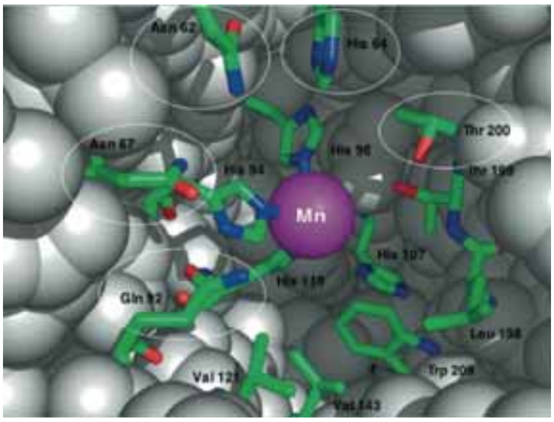

Figure 1: X-ray crystal structure of Mn(II) replacing Zn(II) in human carbonic anhydrase II. *Residues affecting catalysis efficiency and selectivity are circled in white.*

Carbonic anhydrase constitutes a typical illustration of how a simple swap of metallic ion in an enzyme can dramatically modify its reactivity. Unfortunately, this strategy can only be applied to a few, rather exceptional, enzymes, and in most cases more significant modifications are required.

I.2.b. Operating mutations in enzyme active site

Metalloenzymes are very sophisticated systems, in which both the inner and outer coordination spheres have strong impact on enzymatic activity. In the active site, the nature and geometry of coordinating amino acids allow the fine-tuning of the redox potential and Lewis acidity of metal ions, which dictates enzyme specificity. Apart from the active site, residues can play a role in substrate selectivity, facilitating their conveyance to the catalytic pocket. Another strategy for the development of new enzyme-like systems thus consists in mutating amino acids of metalloenzymes. This can be achieved by random mutagenesis, screening a wide library of mutants for a specific activity, or by site-directed mutagenesis with support of molecular modelling.

A representative example is the engineering of cytochrome P450, an iron hemoprotein which catalyses mono-oxygenation of substrates by molecular dioxygen. By performing some mutations on its active site, either site-directed or random, it is possible to enlarge the set of substrates of cytochrome P450 while keeping its good oxidizing properties [31]. The Cys apical ligand of the heme centre of cytochrome P450 was replaced by Ser, removing the “thiolate push”, and thus preventing the native monooxygenase activity (*i.e.* C-O bond formation). Combination with other mutations was also needed to reach specific reactivities, such as intramolecular amination (C-N bond formation) [32,33] and carbene transfer to olefins [34,35] with good yields and selectivities.

Another interesting example was proposed by Lu and co-workers, who gave WT-myoglobin (Figure 2A) a nitric oxide reductase activity, by mutating three residues of the natural active site and thus inducing the coordination of a second Fe ion (Figure 2B) [36]. Similarly, WT-myoglobin was implemented to coordinate Cu ion, thus displaying a 4-electrons dioxygen reductase activity [37,38].

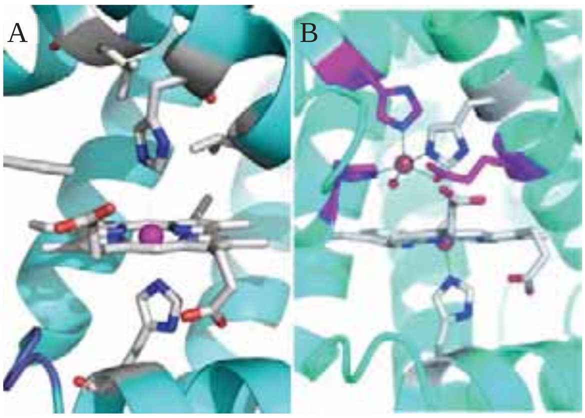

Figure 2: Myoglobin-based artificial metalloenzyme. A: *Native active site of myoglobin (PDB1JP6),* ***B:*** *Engineered active site of myoglobin. Native residues appear in grey, mutated residues appear in pink, Fe centres appear in red.*

I.2.c. De novo design of artificial metalloenzymes

De novo protein design constitutes an original alternative for artificial metalloenzymes elaboration. It consists in the rational design of new proteins, which fold into well-controlled 3D structures. A typical example is the triple helix bundle developed by the Pecoraro's group, formed by hydrophobic interactions between amphiphilic helices (Figure 3). These systems, first developed to study the binding of toxic heavy metals [37], have required huge effort to control the geometry of the binding site [39]. These systems were then transposed for Cu [40,41] and Zn coordination [42,43] showing promising catalytic activities [44–46] such as nitrite reductase [41], hydrolase [43] and hydratase [42].

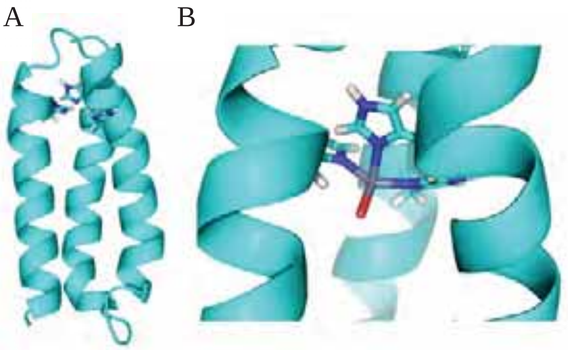

Figure 3: The three stranded coiled coils developed by Pecoraro group. A: *General view of the protein scaffold.* ***B:*** *Detail of Zn(II) coordination sphere.*

I.3. An original approach: incorporation of metal complexes into biomolecules

I.3.a. Concept

In parallel to these strategies, an alternative approach was proposed, at the frontier of biology and inorganic chemistry. It consists in incorporating a coordination complex displaying catalytic activity inside a biomolecule. The complex, which only possesses first coordination sphere effects from its ligands, could thus also benefit from second and outer sphere effects due to the biomolecule. In other words, biomolecules are proposed to bring what coordination complexes are missing compared with enzymes: outer sphere effects.

One of the strength of this approach is the huge variety of biomolecules, complexes and catalytic reactions that can be considered. It is also strongly supported by directed evolution together with chemical optimization, enabling to fully optimise the system.

Different strategies were proposed in literature to bind a coordination complex to a biomolecule. Three main possibilities have been investigated:

- Non-covalent anchoring, taking advantage of weak additive interactions between the biomolecule and the coordination complex (electrostatic, hydrophobic, H-bonding…). This method is very convenient, but the localisation of the complex can lack specificity.
- Covalent attachment of the coordination complex to a biomolecule. This strategy is more time demanding and consists in the bioconjugation of the complex either with an amino acid (natural or not) or with a nucleotide. This strategy enables a more precise positioning of the complex.
- Functionalization of a native guest of a protein with a coordination complex, taking advantage of natural interactions. The bioconjugation step is thus facilitated by the limited size of the cofactor. In the case of proteins, this approach ensures the burying of the complex inside the protein pocket.

These strategies were successfully applied to various biomolecules, including DNA, proteins, enzymes or peptides. Representative examples are depicted in the next sections.

I.3.b. Incorporation of metal complexes into DNA

With their structure in double helix, nucleic acids are one of the most elegant natural examples of chirality. The DNA double helix constitutes a rare example of switch from central molecular chirality to helical supramolecular chirality. Nature uses RNA for metal-driven catalysis in ribozymes, but its low stability so far prevented its use for catalytic applications. DNA was thus logically a privileged scaffold for asymmetric catalysis.

- Intercalation of coordination complexes into natural double-strand DNA

In their seminal paper, Roelfes and Feringa presented the first example of a direct transfer of chirality from natural DNA to a Cu(II) complex involved in Diels–Alder reaction [47]. It was promoted by stacking interactions between DNA and a Cu(II) complexes linked to a DNA-intercalating moiety. When tested for catalytic Diels-Alder reaction, these systems showed a strong predominance for the expected *endo* product. The enantiomeric composition was dependent on linker length and when the linker becomes too long, ee’s dropped dramatically. Subsequently, the same authors showed that direct interaction of Cu(II) complexes within DNA *via* stacking with aromatic ligands displayed better activity in cyclopropanation reaction [48]. This anchoring approach was thus used in subsequent studies, where these Cu(II) complexes afforded ee’s up to 99% when involved in Diels–Alder reaction, Friedel–Crafts, *syn*-Hydratation of enones or Michael additions [49–51]. Interestingly, they showed that in the Friedel–Crafts and Diels–Alder reactions, the replacement of a bipyridine by a terpyridine causes a swap of enantiopreference [51]. The Cu(II) to ligand ratio was also investigated with respect to the cyclopropanation reaction and increasing the Cu(II):L ratio from 1:2 to 1:1 leads to an improvement in the ee values. In the meantime, Wang *et al.* showed the crucial role of the helix chirality by studying *L*- and *D*-DNA interacting with a Cu(II) bipyridine complex [52]. The *L*- and *D*-hybrid systems, tested on Friedel–Crafts and Michael addition, showed “mirror” selectivities, the switch from one to the other inducing a switch of chiral induction. This highlights the fundamental importance of both the biomolecule and the metal complex, both of them influencing selectivity.

Lastly, Park and colleagues demonstrated the dramatic influence of the oligonucleotide sequence: the ee values strongly depend on the nucleotide GC or TA content and whether the A, T or G, C bases are alternated. The oligonucleotide length is also significant [53]. They also propose a model for the binding of the catalyst in the DNA helix (Figure 4) [54,55].

- Covalently-functionalized oligonucleotides

A very different strategy proposed by Roelfes’ group consists in covalently functionalizing an oligonucleotide with a ligand. Upon hybridization with a DNA template and coordination with Cu(II), a DNA helix is formed with the coordination complex in its vicinity. This approach is convenient in terms of screening, allowing variations in nucleotides, linkers and ligands. It also ensures a better preservation of the whole structure. When tested for Diels-Alder cycloaddition, the different systems displayed ee’s up to 93%. Expectedly, this effect is substantially dependent on the nucleotides surrounding the anchoring position [56]. Similar studies were conducted on synthetic DNA functionalized with a diene–Ir(I) complex. The resulting catalysts yielded 28% ee in kinetic resolution of phenyl allyl acetate [57]. Finally, Sugiyama and colleagues proposed to graft DNA strands on two points of a bipyridine. Upon metallation and hybridization, the resulting catalyst showed 86% ee for

Friedel–Crafts alkylation [53]. Despite the variable efficiency of these catalysts, they constitute the first examples of covalently functionalized DNA operating catalysis. The wholeness of this kind of hybrid systems should be more easily preserved than those where the coordination catalyst is bound to DNA by non-covalent interactions.

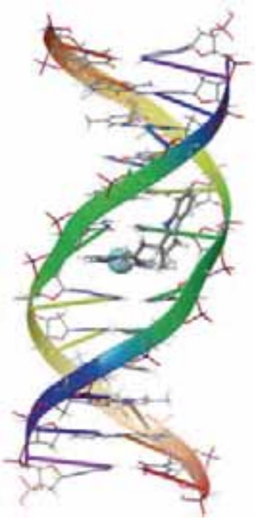

Figure 4: A binding model for intercalation of a coordination complex into double-helix DNA.

I.3.c. Incorporation of metal complexes into proteins

Virtually any of the 35,000 known proteins might exhibit some level of interaction with a coordination complex, thus becoming a potential catalyst. Nevertheless, to obtain a significant impact of the protein environment on catalysis, the coordination complex and the protein chain have to be in close proximity. Because of this requirement, a first criterion for selection of an appropriate host candidate is the presence of a large enough vacant space buried inside the protein. In this way, the coordination complex would be surrounded by protein and take fully advantage of this interaction. This reaction pocket could also contribute to confer selectivity and even specificity to substrates.

(a) Incorporation of a coordination complex into an apo-protein

A straightforward strategy for the elaboration of hybrid catalysts is the insertion of a synthetic catalyst into a protein from which the native metallic cofactor has been removed, thus taking advantage of the cavity left vacant.

- Case of planar coordination complexes

The first example is the incorporation of coordination complexes into apo-myoglobin, which naturally hosts an iron porphyrin. Because of their planar structure and their high catalytic efficiency, Schiff base complexes were considered as good candidates to replace the hemic group. The first approach was envisaged by Carey *et al.* consisting in the covalent dual anchoring of functionalized Mn(III) or Cr(III) salen complexes into the hydrophobic pocket of apo-myoglobin. To do so, a covalent link was made by the creation of two disulfide bridges using methane thiosulfonate salen derivatives and Cys mutations, the positions of which were determined by molecular modelling. The corresponding Cys mutants were expressed, produced and purified, then bioconjugated to the Schiff base complex. Modelling studies showed that the complex was positioned in the active site exactly at the same place as the hemic group in the wild type myoglobin, as depicted in Figure 5.

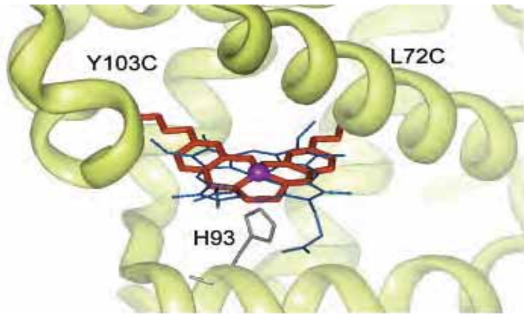

Figure 5: Myoglobin active centre modified with Mn(salen)-type complex. *Complex is covalently attached on the two L72C and Y103C mutated positions. The position of the hemic group in wild-type myoglobin is shown in blue showing the correct positioning of the coordination complex.*

The interest of the double anchoring of the coordination catalyst has been established by comparison with a single-point attached counterpart in the sulfoxidation of thioanisole: both the ee values and the rate were improved. This is fully consistent with a better immobilisation of the complex inside the cavity, taking thus full advantage of a better-defined environment [58]. These systems could now be further improved by directed evolution, or applied to a wider set of reactivities, but the overall process might represent a rather time-consuming approach.

Another possibility, potentially easier but also probably less topologically defined, consists in direct incorporation of Schiff base complexes into apo-myoglobin mutants [59]. The crystal structures obtained showed that the complexes were positioned in pertinent mutants at the exact same place as the hemic group in the wild-type myoglobin. Even if the rate was improved by optimising the ligand, the ee obtained for thioanisole sulfoxidation did not exceed 33%.

Comparison with the previous example leads to three general remarks: (i) Imposing a fixed position using covalent anchorage may preclude the most suitable location of the catalysts for catalytic enhancement, whereas more freedom is given to the system in non-covalent anchoring, (ii) in contrast, regarding the ee values, a much more dynamic interaction leads to a loss of influence of the proteic environment and thus to a lower chiral induction, (iii) combining the two approaches, *i.e.* mutations to covalently anchor the catalyst and to optimize the binding pocket could be more appropriate.

In this context, Lewis and co-workers found a good compromise: allowing the complex to choose its best position, and then covalently grafting it *in situ* [60]. To do so, they functionalized their Mn-terpyridine complex with a maleimide group. The resulting coordination complex was incubated with Cys mutants of nitrobindin. Once the complex is set at its most suitable place inside the protein, the formation of a carbon-sulfur covalent bond allows the immobilization of the complex. The mutants displaying the most efficient bioconjugation were considered as the most appropriate, and were tested for several catalytic oxidation reactions. In the best case, the product was obtained with 99% yield. Yet the ee's obtained remain low (7%) indicating that the most suitable positioning of the metallic complex in the protein may not efficiently transfer the chiral information from the environment to the reaction product. The topology of the edifice still needs to be improved for example allowing the metallic cofactor to choose its most favourable position inside the protein. The reactivity of the maleimide allows its permanent binding at the right position, limiting dynamic exchanges; but the precise positioning into a chiral pocket might require a thorough screening to allow a significant chiral induction to be achieved.

- Case of non-planar coordination complexes

Non-planar coordination complexes were inserted into proteins involved in the transport of metallic complexes. They have the advantage to exist natively in the apo-form and are able to bind coordination complexes easily. Thus, Fe(II) complexes of the diamino-pyridine BPMEN and BPMCN ligands were incorporated into the apo-form of the periplasmic nickel-binding protein NikA (where NikA binds Ni(II) in form of a coordination complex). The resulting hybrid displays sulfoxidation activity with good to moderate yields. In that case, suitable substrates were determined by docking studies [61]. To illustrate this, Figure 6 shows the crystal structure obtained for the incorporation of an analogous Fe(II) complex into NikA, which was involved in arene dihydroxylation of the ligand itself [62].

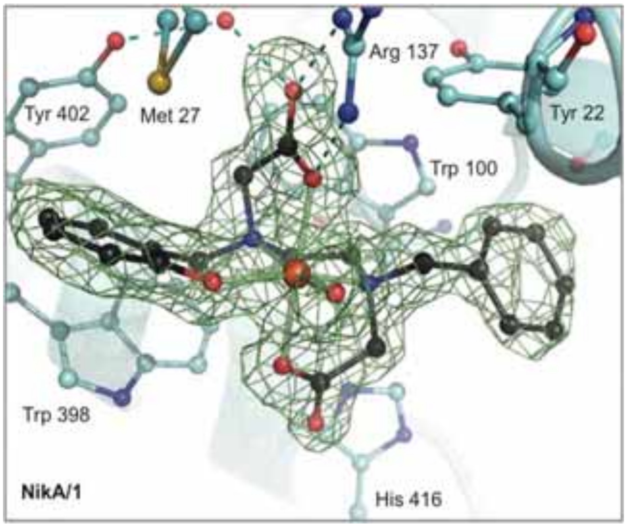

Figure 6: Crystal structure of the Fe coordination complex incorporated into periplasmic nickel-binding protein (NikA) and electron density map of FeL.

The other example is FhuA that incorporates the Hoveyda–Grubbs catalyst. This system showed efficient polymerization with a preference for the *cis* form [63]. This was assigned to the cavity effect of FhuA, which has a β-barrel structure and hence a confined space. Similar results were also reported for another hybrid system namely the β-barrel protein aponitrobindin functionalized with CpRh(I). These examples nicely illustrate the fundamental effect of the confinement to force the reaction even to its less favoured stereochemical outcome.

- A specific case: Ferritin

An even more pronounced confinement can be obtained with apo-ferritin, a hollow protein with several relatively small access-channels. A Rh(I)-norbornadiene complex was inserted in the cavity of apo-ferritin, where it reacted to form a covalent bond with a cysteine. The Rh complex catalyses the polymerization of phenyl acetylene with restricted molecular weight and a narrow molecular weight distribution due to the cavity effect [64].

(b) Incorporation of a coordination complex into an hollow protein

A more chancy strategy is to consider proteins which do not natively host metallic complex but possess cavities, for instance for the transport of organic molecules. Even though these cavities are not naturally used for catalysis, they remain an asymmetric environment, allowing stereoselectivity to be expected. When the cavity is sufficiently small, using of non-covalent anchoring approach was preferred.

- The host cavity is made by a monomeric protein

A very simple strategy to form hybrid catalyst was introduced by Ward and co-workers, who incorporated vanadium oxide [65] or osmium oxide [66] into streptavidin. The resulting systems displayed selectivities up to 95% ee for olefins dihydroxylation. Subsequently, an elegant biomimetic oxidation system was developed by incorporating a corrole metallic complex into albumins. The complex was buried inside the protein *via* interaction with the sulfonato and pentafluorophenyl groups that decorated the corrole central group. This system was tested for thioanisole sulfoxidation using hydrogen peroxide, showing efficient reactivity and promising ee’s [67]. Another example, using the same strategy, was the incorporation of Mn(III) complexes into xylanase, a protein displaying affinity for synthetic Fe(II) porphyrins. When tested for styrene oxidation, the system displayed moderate yields, but good selectivities (up to 80%) [68].

- The host cavity is made by supramolecular interaction of proteins

In a recent study, Roelfes and co-workers showed that the hydrophobic interface formed upon dimerization of proteins could also be used as an active site. Copper complexes grafted onto dimerized Lactococcal multidrug resistance regulator were used to catalyse Diels–Alder cycloaddition with excellent efficiency and selectivity [69]. Similarly, Hilvert developed a system based on a small heat shock protein, able to form spherical capsids, functionalized with Grubbs–Hoveyda catalyst. This system demonstrated good properties for olefin metathesis [70].

- Grafting of coordination complex outside a cavity

An hybrid system was developed by Inaba *et al.*, in which Sc(III) bipyridine complex is covalently grafted onto the surface of proteins. The hybrid exhibits moderate results both in terms of conversion and ee values for ring-opening reaction [71].

I.3.d. Functionalization of a natural cofactor of a protein

- Biotin/(Strept)avidin system

In an effort to simplify the elaboration of hybrid catalysts, some groups proposed to attach the coordination complex onto natural cofactors of proteins, taking advantage of the strong host–guest interaction to incorporate the complex at a precise place in the protein. The most common example is the biotin-(strept)avidin couple, in which the interaction is very strong ($K_D \approx 10^{-15}$ M) and fast (binding rate constant of biotin-streptavidin is in a range of 3.0×10^6 - 4.5×10^7 M^{-1} s^{-1}) [72]. Conjugation of catalysts onto biotin, followed by interaction with avidin or streptavidin, affords highly reliable systems [73]. This also permits one to get rid of the complicated step of bioconjugation with a protein.

In 2003, Ward and co-workers developed a phosphine functionalized biotin which upon metallation with Rh(I) and incorporation into avidin and streptavidin was able to catalyse asymmetric hydrogenation with 96% ee after 15 h. Interestingly, avidin and streptavidin offered opposite enantiopreference [74]. Much effort was made in subsequent studies to improve this system, considering different optimization parameters. Different anchoring positions, metallic ions and ligands were tested, as well as different mutants of the host protein. Finally, a library of substrates was tested. This “chemogenetic” optimization allowed determination of a system with high selectivity. After the chemogenetic selection, a careful study of crystal structures allowed to point out other mutations of interest, further improving the catalysts [75]. This constitutes a very elegant example of combined chemical and genetic optimization, showing the full potential of this yet simple system.

In subsequent studies, Ward and colleagues showed that a unique mutated position (112 or 121) into His allowed a dual anchoring, both by biotin/streptavidin interaction and by Rh coordination by His, as shown in Figure 7. This appeared highly beneficial to the system: conversion increased from 60 to 100%, and ee values from 0 to 79% for transfer hydrogenation of a prochiral imine compared with the wild type protein [76]. This study only considered the transfer hydrogenation, but other reactivities were also demonstrated. As such, biotinylated Rh(III) complexes were efficient for C-H activation [77] and imine reduction [78,79]. In a very comprehensive study, the same group investigated several parameters with respect to the hydrogen transfer reaction, including the nature of the coordination complex and the influence of the mutants at position 112. Interestingly, the nature of the complex impacted strongly the transfer of chirality, with the two enantiomers being detected depending on the catalysts used. Also, with a given catalyst, the two enantiomers can be obtained depending on the nature of the mutants at position 112 [80]. More recently, Cp-Ir(III) complexes were also successfully used for NAD^+ reduction [81].

Mn salen complexes were also tested for asymmetric sulfoxidation, displaying somewhat low yields and selectivities, therefore illustrating that this strategy cannot be systematically generalized, and requires cautious optimization [82].

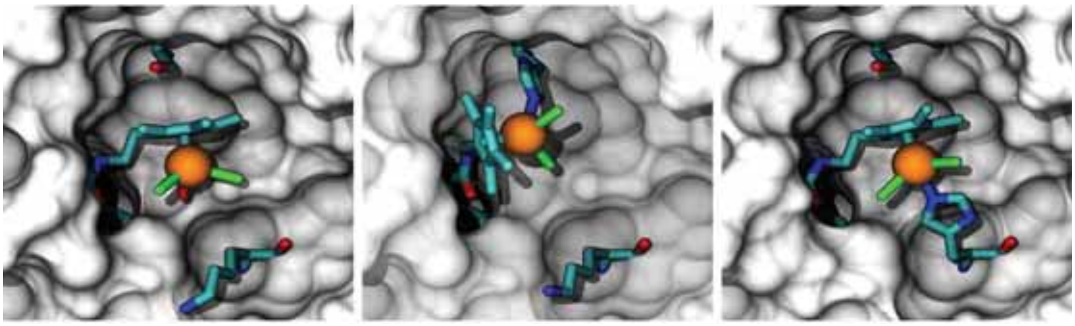

Figure 7: Docking studies of Rh-functionalized biotin into WT-streptavidin (left), S112H (middle) and K121H streptavidin (right). The double anchoring of the coordination complex improves the catalytic properties of the system.

- Other host-guest systems

Still within this context, an original example is the use of a natural protein inhibitor to constitute hybrid catalysts proposed by Matsuo and co-workers. They functionalized an inhibitor of chymotrypsin with a linker and a catalytic entity. The inhibitor goes into the active site of the enzyme and the coordination complex is thus positioned inside the hydrophobic pocket, and can intercept the incoming substrates. In the present case, the functionalized Grubbs–Hoveyda complex was able to catalyze ring-closing metathesis with good rates [83]. Finally, Mahy and co-workers used neocarzinostatin, a cytotoxic protein known to recognize specifically enediyne derivatives. Since these compounds are of limited stability, the authors used a formerly established mutant that binds tightly testosterone. An iron–porphyrin complex was then decorated with a testosterone moiety and inserted into the cavity. The resulting system was subsequently tested for thioanisole sulfoxidation, but showed only low enantioselectivity [84].

I.4. Incorporation of metal complexes into antibodies

An original strategy is the use of the antibody–antigen recognition. The presence of exogeneous species in a body leads to the production of antibodies directed against it, forming a very stable duplex. In the case of an exogeneous metallic complex, the association with an antibody would modify the environment of the metallic centre in an asymmetric manner, and could display interesting catalytic properties.

As such, Mahy's group aimed at developing cytochrome P450 mimics by raising antibodies against natural or synthetic porphyrins [85]. In this case, the protein environment also serves as a protection against heme oxidative degradation. The resulting Fe(III)-porphyrin-antibody complex showed good peroxidase activity with a large scope of peroxide sources and substrates [86]. Looking for a system bearing an apical ligand on the metallic centre, antibodies were then directed against Microperoxidase 8. The resulting scaffold was tested for peroxidase activity [87], nitration of phenol [88] and thioanisole sulfoxidation [89]. Even though the catalytic performance of these systems is yet limited, this study constitutes a proof of concept for the use of antibody–metal complex system as hydrid catalysts. Subsequently, an attempt was made using the so-called "Trojan horse strategy". The porphyrin group was attached to an estradiol molecule, which allowed binding to an anti-estradiol antibody. The catalytic rates were thus improved, but the ee's remained low, witnessing the low influence of the protein environment [90]. This strategy could find applications with diverse metal complexes.

I.5. Incorporation of metal complexes into peptides

With their shorter length and their possible chemical synthesis, peptides were proposed as an interesting alternative for proteins. Their handling is also less sensitive, and their functionalization is easier. However, their high flexibility also makes the rationalization of their quaternary structure more difficult.

In a first trial to design a catalyst-peptide hybrid, Lewis *et al.* developed tetrapeptides bearing Pd or Ir metallacycle on their N-terminal end (Figure 8). These constructions conserved the reactivity of the free complexes, but unfortunately no selectivity was observed. The authors proposed that in its favoured conformation, the peptide scaffold is too far from the metallic centre to influence its reactivity [91].

To get a stronger influence, the coordination complex was grafted along the peptide chain, using a non-natural amino acid as the anchor. Christensen and colleagues proposed to incorporate phosphine-modified amino acids either in one or two points of the peptide backbone (Figure 8). In this way, peptidic environment surrounds the coordination complexes. This first attempt displayed high yields but mild selectivities [92]. Importantly, the doubly coordinated complex showed better yields and selectivity than its single-point attachment analogue. This is consistent with an increasing burying of the catalytic centre in the peptidic scaffold. In a subsequent work, a second generation of ligands enabled the remarkable improvement of selectivity. They also demonstrated that inverting the stereochemistry of the amino acids induces an inversion of the stereochemistry of the products [93].

The use of three-dimensionally ordered peptides was also proposed, in order to reduce the dynamic of the system. As such, Gilbertson group developed a library of β-turn peptides decorated with phosphine ligands. The resulting hybrid catalysts are efficient for Michael addition, with ee's up to 85% [94].

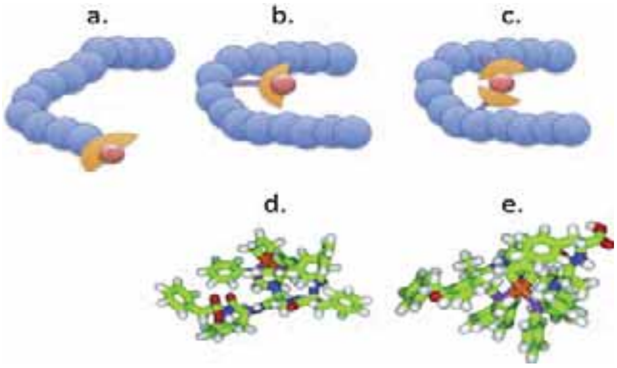

Figure 8: Schematic representations and molecular models of peptide-based systems. *Coordination complexes can be attached on the N-terminal end (a), in the middle (b,d), or on two points of the peptides (c,e).*

These different examples establish peptides as promising hosts for metal complexes. Compared with proteins, the issues are opposite: here, there is no risk of steric hindrance, contrariwise it seems that the peptide backbone should surround the catalytic moiety as much as possible. The somewhat easy development of peptide libraries should strongly help to solve this problem.

I.6. Outlooks

All these examples highlight the wide diversity of applications that can arise from this area of hybrid catalysts prepared from coordination complexes host in biomolecules: chiral scaffolds can be constituted from a large scope of biomolecules and used to target a wide range of reactivities. At this point, none of these systems can compete with naturally occurring enzymes in terms of speed rates (all the processes presented above being complete in a few hours to a few days). However, they clearly establish that the catalytic properties of a coordination complex can be highly enriched by the stereochemical induction brought by biomolecules. Compared with standard coordination catalysts they offer interesting alternative as they can induce enantioselectivity without requiring time-consuming production of sophisticated ligands, which is also expensive and generates waste.

Finally, it appears that many biomolecules are still to be explored. Some promising examples involving auto-assembling proteins, including fibres, needles, disc and rod structures obtained with amphiphilic proteins and peptides recently appeared in literature, showing interesting extension of this research field to heterogeneous catalysis [95,96]. Within this context, this thesis proposes the use of amyloid fibres as a support for the elaboration of hybrid catalysts.

II. Amyloid fibres: a bio-nanomaterial as a support for catalysis

II.1. Definition of amyloids

The definition of amyloids is foremost structural. It concerns polypeptides that, additionally to their native folding can adopt a second, very stable and ordered structuration.

Under their amyloid form, these polypeptides display a common cross β-sheet structure that consists of ordered arrays of β-sheets, whose side-chains interdigitate to form a hydrophobic interface (Scheme 1.A). β-sheets are composed of β-strands that bind together by H bonds between backbone amides (Scheme 1.B). When under amyloid forms, proteins form insoluble aggregates with unique physical properties (see II.2.d).

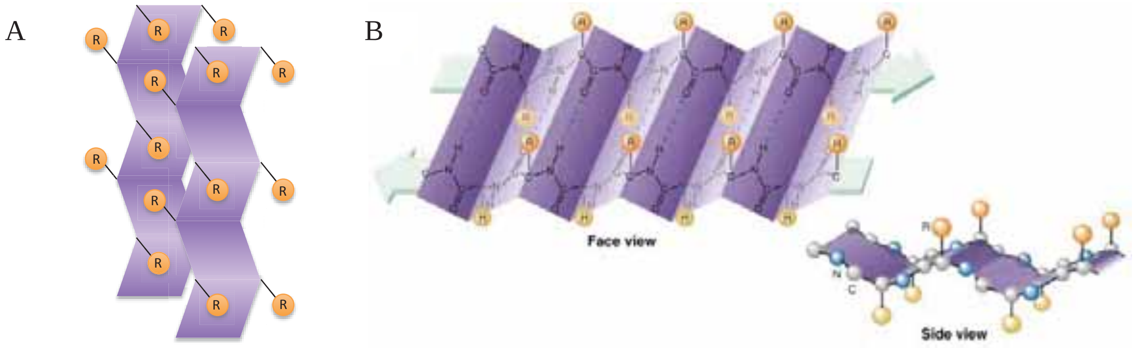

Scheme 1: Representation of amyloid structuration. A: *Cross β-sheet structure. β-sheets appear in purple, side-chains appear in yellow.* ***B:*** *Face and side views of a β-sheet (purple) composed of two β-strands (green arrows) interacting through H bonds between amides.*

II.2. Natural occurrences of amyloids

II.2.a. Role in disease

Amyloid aggregates were first discovered in the context of human diseases in the 1850s. Today, 23 amyloidogenic proteins are related to human diseases, targeting various organs including brain, nervous system, kidney, or heart. Some amyloid diseases are global health issues whereas other only concern a limited number of patients. Their causes can be genetic, sporadic or even infectious. The formation pathway of amyloid aggregates is often part of a very complex process and thus scarcely understood.

Here are three typical examples of amyloid diseases, aiming at showing the diversity in terms of mechanisms and toxicity.

- Alzheimer's disease (AD) is perhaps the most famous "amyloid disease". It is characterized by the presence of amyloid plaques in the brain (Figure 9A) that adsorb onto neuronal and glial cells and interfere with neurotransmission [97]. According to the so-called amyloid cascade hypothesis, monomeric amyloid-β peptide (Aβ) first assembles into oligomers, which are then reorganized to form fibres, the three species being in dynamic equilibrium [98]. Although the overall mechanism of the disease is poorly understood, it is widely acknowledged that the major toxicity arises from amyloid-β oligomers, which mediate inflammation and harm neurons [99]. However fibres are also toxic, causing membrane deformation, and promoting the formation of aggregation-prone species [100]. Different therapeutic approaches are proposed, either decreasing Aβ production, inhibiting its aggregation, or improving its clearance [101].

- Amyloid deposits are also found on pancreas of patients suffering from Type II diabetes. They result from the dysregulated production of Islet Amyloid Polypeptide (IAPP), which forms deposits on the surface of pancreas (Figure 9B). They have a dual toxicity, accelerating cellular apoptosis of pancreatic cells and decreasing insulin secretion. As for Aβ, studies showed that only the aggregated forms of IAPP were toxic, probably due to their interaction with cell membranes [102]. Therapeutic approaches consist in limiting production and aggregation of IAPP [103].
- A mediatised example of amyloid-related disease is spongiform encephalopathies, also known as Prion diseases. These rare neurodegenerative pathologies are due to Prion proteins, naturally present in the brain and the spine under a safe conformation. But Prion can adopt an alternative folding, becoming insoluble and hydrophobic, and thus toxic for the brain. A misfolded protein can catalyse the conversion of normally folded ones, promoting the accumulation of amyloid deposits in cells (Figure 9C). Prion proteins are infectious agents, and can be spread between individuals (animals and/or humans) by inoculation of infected tissues or fluids. Yet, most cases remain sporadic or familial [104].

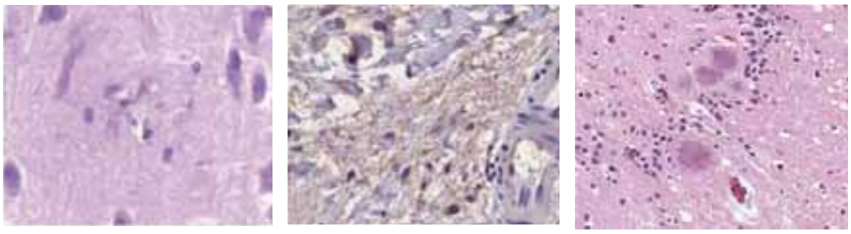

Figure 9: Micrographs of amyloid deposits. A: *Amyloid-β plaques in the brain of Alzheimer's disease patient.* ***B:*** *Islet Amyloid Polypeptide in the pancreas of type II diabetes patient.* ***C:*** *Prion protein in the brain of variant Creutzfeldt-Jakob patient.*

II.2.b. Functional amyloids

First discovered in the context of diseases, it took about one century to find out that amyloid fibres also play salutary role in organisms. Examples of so-called “functional amyloids” imply all types of organisms, from bacteria to mammals.

High content of amyloids is found in bacterial biofilms. In *E. coli* and *Salmonella*, amyloid fibres are formed by Curli proteins. They self-assemble into β-sheet rich fibres on the surface of bacteria, ensuring their adherence on any type of surface, and promoting their interaction. Their role is thus crucial for biofilm formation. They also protect bacteria against external attacks [105].

In fungi, hydrophobins were found to display amyloid character. Once secreted, hydrophobins self-assemble into amphiphilic monolayers at the air/growth medium interface. This results in a decrease of the surface tension, enabling the growth of fungi in aerial conditions. Hydrophobin coating also contribute to maintain water and gaz exchanges between fungi and its environment. Finally, hydrophobins also coat fungi spores, preventing immune response in hosts and helping spores dispersion in environment. At the molecular scale, hydrophobins display rodlets structure, stabilized by four disulphide bridges [106].

In insects and fish, amyloid fibres are present in high amounts in eggs envelope as chorion proteins. Their role is to protect embryo against environmental aggressions, such as temperature or pressure variations, or microorganisms. Chorion proteins contain a central domain with repeating glycine residues, which was shown to aggregate into characteristic β-sheet structure *in vitro* [107].

In mammals, amyloid fibres are implied in the biosynthesis of melanin. Upon proteolytic cleavage, 80-kDa fragments of glycoprotein Pmel17 are released and auto-assemble in melanosomes to form fibres. Those fibres play a dual role, both promoting synthesis of melanin by template effect, and preventing the release of toxic synthetic precursors. A careful control of the secretion pathway together with fast aggregation kinetics prevent the propagation of toxic amyloid species in the organism [108]. A partial repeat sequence rich in Pro, Ser and Thr was shown to be crucial for auto-assembly [109].

These examples illustrate the diversity of functional amyloids, both in nature (size, origin, AA content…) and role (protective, functional, structural, catalytic…). This diversity is likely to further extend with discovery of new amyloids.

II.2.c. A characteristic quaternary structure or a highly stable energetic state?

Under physiological conditions, amyloid is considered as a quaternary structure that only concerns a limited number of proteins, even though this number tends to increase over the years. However, some examples show that proteins displaying no apparent amyloidogenic character could acquire it upon denaturation. This was reported when bringing proteins into organic solvents [110] or at non-physiological pH [111] or upon heating [112]. Similar effect was reported with overexpression of insoluble proteins in *E. coli*, leading to formation of inclusion bodies with amyloid character. This prompted people to hypothesize amyloid as a particular energetic state, which can be reached by any protein provided high concentration and sufficient denaturation. When looking closely to all proposed structures of amyloid fibres, we see that the intermolecular interactions at the root of amyloids consist in H-bonding between the amide groups of the main chains. From a strictly conformational point of view, almost any protein or peptide could actually adopt an amyloid state. Thus, the question is not anymore « what makes a protein form amyloid? » but rather « what makes some proteins stable in their amyloid state in physiological conditions? ».

II.2.d. Common characteristics of amyloids

The amyloid-forming proteins are very diverse, both in size, shape and function, and finding sequence homologies between them is often deceptive. Yet, the propensity to form fibres can often be attributed to a short core sequence (<10 AA). Although amyloids are broadly hydrophobic, a high content in hydrophobic residues in this central core is not the key to for forming amyloids. Contrariwise, it seems that the presence of specific molecular interactions among the side chains is required, which can involve various types of amino acids. As such, a high content of Gln, Asn, and Val was reported in the core of various disease-related proteins [113]. But aromatic amino acids are also frequent, probably driving the formation of fibres.

Whatever their length, origin or sequence, amyloid proteins share in common to auto-assemble along a major axis to form fibres of 6-12 nm diameter and few μm long, with a characteristic cross-β structure. Amyloid fibres thus display very characteristic X-rays diffraction patterns. The formation conditions of fibres are highly variable, going from physiologically relevant to extreme conditions. Interestingly, it appears that structural amyloid fibres display isomorphic structure, whereas disease related amyloids have polymorphic structures.

In fibres, two types of interactions are observed. In the one hand, β-sheet formation is promoted by H-bonds involving peptide backbones. These intermolecular H-bonds run parallel to the fibre axis. In the other hand, specific interactions between peptide side-chains are observed (hydrophobic interactions, π-stacking, saline bridges…). These interactions run perpendicularly to the fibre axis, and can either be intramolecular or intermolecular (in the case of "staggering", or of interaction between filaments, see III.2.d). They result in stabilization of the cross-β folding [114].

Mechanical studies demonstrated that their tensile strength was comparable to steel and their stiffness to silk [115]. They are also highly insoluble, and resistant to heat, organic solvents and proteases. The classification of a protein as an amyloid often arises from its specific binding to amyloid-specific dyes, including Congo Red (displaying apple green birefringence upon binding amyloids) or Thioflavin-T (displaying a shift of its emission wavelength upon binding amyloids) [116] (see Section III.2.a).

II.3. Amyloid fibres as nanomaterials

Amyloid fibres have exceptional physical properties: they are very strong and stable, they are resistant to heat, organic solvents, denaturing agents and proteolysis. This contrasts with the image of proteins as delicate and sensitive and paves the way to new biotechnological applications.

II.3.a. Amyloid fibres as a template for nanostructure formation

In 2003, Lindquist and colleagues proposed to use amyloid fibres as template for the formation of gold and silver nanotubes [117]. To this goal, a mutant of yeast Prion was prepared, displaying cysteine residues on the surface of fibres. By an electrodeposition procedure, gold and silver were deposited onto the fibre surface. The resulting nanotubes were found to display good conductivity and low resistance, with dimensions suitable for microelectronic applications. The same year, Gazit *et al.* demonstrated that peptides fibres could be used as molds for nanowires synthesis [118]. They showed that the Aβ derived Phe-Phe dipeptide was forming hollow fibres with a central pore, filled with aqueous medium. When heating in the presence of silver ions together with citric acid, metallic nanowires are formed within the fibres. A final proteolytic digestion of the peptide scaffold allows the release of nanowires. Finally, Lynn’s group showed that sophisticated superstructures could be obtained from the KLVFFAE segment peptides of Aβ [119]. Fibres can switch from disorganized flexible nanotubes to highly ordered laminar superstructure by simple addition of sulfate ions. All these nanomaterials could find applications in nanodevices.

II.3.b. Amyloid fibres as a grafting support

Several studies showed that it is possible to operate some amino acid substitutions in amyloidogenic proteins without altering their aggregative properties. Starting from there, several groups proposed to graft functional entities on amyloid fibres, as it is already widely done with other nanomaterials. As such, Wickner’s group proposed to fuse different enzymes or fluorescent proteins with a yeast prion protein [120]. They showed that fibre formation was not impacted by the presence of fusion proteins, and that their native folding and activity was maintained upon aggregation. This constitutes the first example of enzymes supported on amyloid fibres, and could be of interest for enzyme immobilization. Subsequently, Baldwin et al. fused a cytochrome *b* to the SH3 aggregation-prone domain [121]. Upon auto-assembly, cytochrome *b* is able to stoichimetrically bind metalloporphyrins, and the resulting scaffold displays a high surface density of porphyrins. It thus constitutes a good model system for long-distance electron transfers.

II.3.c. Amyloid-based hydrogels

Another use of amyloid peptides is the formation of hydrogels. Xu's group showed that Fmoc-protected dipeptides were able to form two-dimensional gels when heated in acidic conditions [122]. Dipeptides are then able to switch from hydrogel state to solution state upon interaction with a specific biological ligand. Hydrogels display physical properties similar to amyloid fibres, and could find applications for drug delivery or tissue repair.

II.3.d. …catalysis?

Until now, only a few preliminary examples of amyloid fibres as a support for catalysis were reported. Yet, some natural amyloids display intrinsic catalytic properties, mostly when coordinating metal ions. As such, Alzheimer's related amyloid-β peptide is able to coordinate copper ions [123], thus catalysing production of reactive oxygen species from molecular dioxygen [124]. Similar results were achieved with De Novo designed peptides. Korendovych and colleagues designed heptapeptides that self-assemble into fibres in presence of zinc ions [125]. The resulting scaffolds display esterase activity on *p*-nitrophenylacecate, zinc playing the role of metal cofactor in catalysis. Subsequently, Friedman *et al.* developed a library-based approach to screen for catalytic amyloids [126]. They demonstrated that at acidic pH, some of these short peptides do not require metal ions to perform catalysis. Some are even catalytically active in extreme conditions. These results led them to consider amyloids as a catalytic precursor of modern enzymes.

Another approach consists in decorating fibres with catalytic species. Very recently, Bolisetty *et al.* proposed to use β-lactoglobulin membranes decorated with gold or palladium nanoparticles for continuous flow catalysis [127]. Nanoparticles are synthesized in presence of fibres and bind them by strong electrostatic interactions. When passing through the membrane, an aqueous solution of 4-nitrophenol undergoes reduction into 4-aminophenol with total conversions. This system displays faster kinetics than free nanoparticles, showing the benefit of support immobilization.

III. Molecular description of amyloid-β peptides

III.1. Amyloid-β peptides

III.1.a. General features

Alzheimer's disease related amyloid-β peptide exist in two major forms in the brain, of respectively 40 (A$\beta_{1\text{-}40}$) and 42 (A$\beta_{1\text{-}42}$) amino acids. Their sequences differ one from another by the presence of two extra residues at the C-terminal end of A$\beta_{1\text{-}42}$.Their molecular masses are of 4329.845 g/mol (A$\beta_{1\text{-}40}$) and 4514.082 g/mol (A$\beta_{1\text{-}42}$). Their pI is estimated to be 5.59, and their total charge is of -3 at physiological pH.

III.1.b. Sequence

When looking closely to their sequence, they are constituted of two distinct domains. In the N-terminal part, residues 1 to 16 form a highly dynamic and poorly structured domain. It is mainly constituted of polar residues and is able to coordinate metal ions, such as Cu, Zn or Fe [123]. In the other hand, the C-terminal part of the peptide (residues 17 to the end) is mainly composed of hydrophobic residues. This domain is responsible for the hydrophobic interactions at the origin of the cross-β structure. More specifically, this domain is constituted of two β-strands, separated by a β-turn, which ensure the characteristic β-sheet conformation. The so-called central hydrophobic core, involving residues 17 to 21, is described as being an essential motif for aggregation (Figure 10).

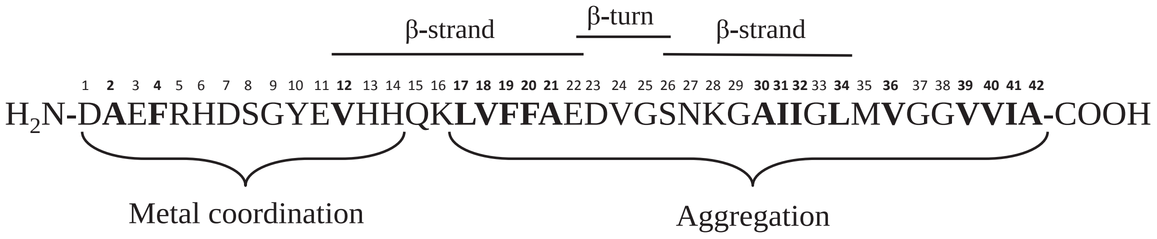

Figure 10: Numbered sequence of A$\beta_{1\text{-}42}$ and the corresponding secondary structure. *Hydrophobic residues appear in bold.*

III.1.c. Solubility and storage

Because of their high content in hydrophobic residues, amyloid-β peptides are poorly soluble in water, and have tendency to auto-assemble rapidly. Though, solubility is improved when solubilizing peptides at extreme pH (<2 or >11), maximizing the total charge. This also contributes to maintain peptides in a somewhat monomeric state, taking advantage of repulsive interactions. For this reason, stock solutions of peptides are often constituted at extreme pH, and pH is reset to physiological range right before experiments.

III.1.d. Spectrophotometry

Aβ peptides contain a single tyrosine residue, which is used for their quantification by UV-Vis spectrophotometry. When pH is above pK_a (>12), tyrosine is deprotonated and displays a characteristic absorption band at 293 nm, with a molar absorption coefficient of 2400 $L.mol^{-1}.cm^{-1}$. This band completely disappears for pH below pK_a (<10), when tyrosine residue gets protonated. Measuring absorbance at high and low pH thus allows a precise quantification of tyrosine content of a sample, which is directly correlated to the amount of peptide [128].

Because they contain no tryptophan residue, Aβ peptides have very low intrinsic fluorescence, attributed to the single tyrosine residue (λ_{exc} = 274 nm, λ_{em} = 303 nm, ϕ = 0.14 in water at 23 °C).

III.1.e. Metal binding properties

With its coordinating amino acids and its important flexibility, the N-terminal domain of Aβ peptides is able to coordinate metal ions. In particular, coordination of Fe(II), Zn(II), Cu(I) and Cu(II) with peptides was extensively studied, and coordination models were proposed [123,129,130].

III.2. Amyloid-β fibres

III.2.a. Thioflavin-T: a reporter of amyloid-β aggregation

Aβ aggregation is often studied using fluorescent reporters, for which at least one of the features is modified upon interaction with amyloid fibres. Among the existing reporters for aggregation (Congo Red, Nile Red, ANS, Bis-ANS…), the most widely used is Thioflavin-T (Th-T). Upon binding amyloid fibres, this benzothiazole derivative exhibits a red shift in excitation (λ_{exc} = 385 nm to λ_{exc} = 450 nm) and in emission (λ_{exc} = 445 nm to λ_{exc} = 482 nm). More importantly, its fluorescence intensity is exalted by several orders of magnitude upon interaction (Scheme 2.B). It is thus possible to follow Aβ aggregation by monitoring fluorescence at 482 nm with time, obtaining a typical sigmoidal curve [131] (see III.2.b).

At the molecular scale, the recognition of amyloid fibres by Th-T is not fully understood. Yet, it is widely accepted that the exaltation of fluorescence upon binding is due to an immobilization of the rotatable bond of Th-T, which would stabilize the excited state responsible for fluorescence (Scheme 2.A). Both experimental and computational studies also converge to say that Th-T intercalates in side chain channels of fibres, and is thus aligned to the fibre axis [132] (Scheme 2.C.). Although some sequence preferences were observed, no interaction between Th-T and specific amino acids have yet been reported.

Yet, several biases were reported on the use of Th-T in fibrillization assays. First, Th-T was shown to bind hydrophobic pockets of globular proteins, as exemplified by the crystal structure of Th-T binding acetylcholinesterase (PDB 2J3Q). This lack of specificity represents an issue for studies in physiological medium. Moreover, Th-T fluorescence was shown to strongly depend on pH, ionic strength or presence of organic molecules/solvents, which prevent quantitative measurements [133,134]. Finally, a recent study demonstrated that Th-T promotes aggregation at high concentration by playing a role of template [135]. Despite that, Th-T remains the most convenient reporter for aggregation studies.

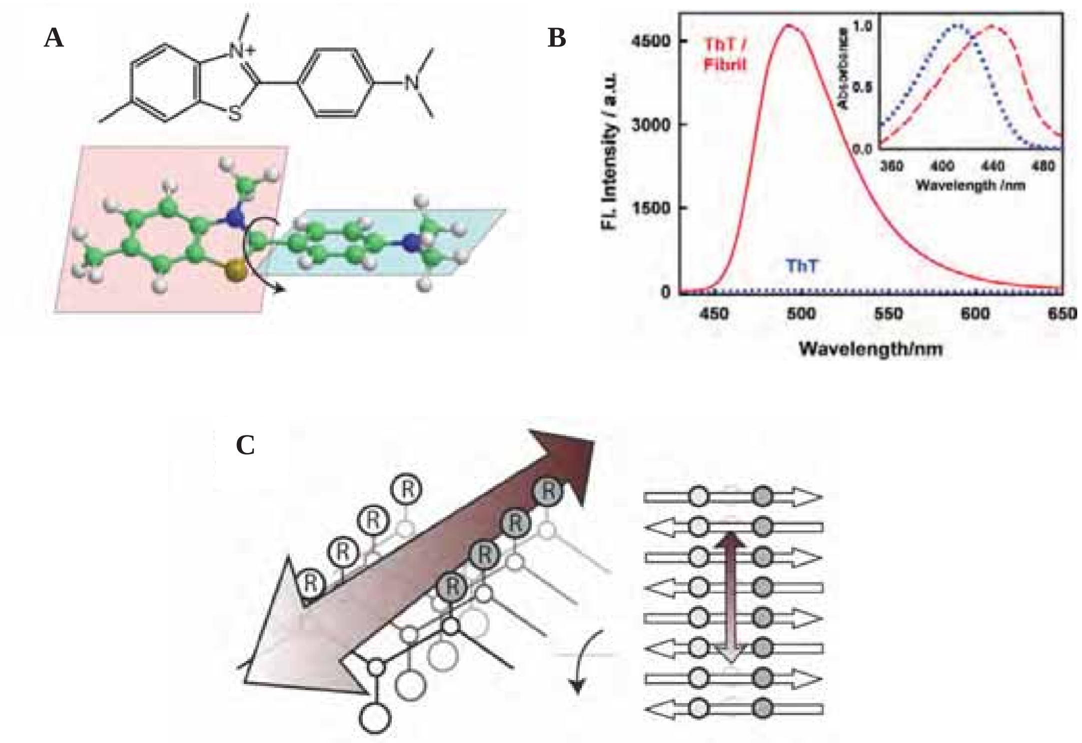

Scheme 2: Th-T binding to amyloid fibres. A. *Structure of Th-T and schematic illustration of its rotative bond.* ***B.*** *UV-Vis and fluorescence spectra in presence and absence of Aβ fibres.* ***C.*** *Schematic illustration of Th-T binding site in side-chains channels on the surface of amyloid fibres.*

III.2.b. Aggregation process of amyloid-β fibres

As stated before, Aβ aggregation can be monitored *in vitro* using Th-T as fluorescent probe. This aggregation assay displays a typical sigmoidal profile, which consists of three phases. First, a lag phase, resulting from monomers self-assembly into soluble oligomers. Follows a rapid growth phase, corresponding to the elongation of fibres, and finally a plateau, corresponding to a final stable fibrillar state. Several studies were conducted to investigate kinetics and thermodynamics of the aggregation process [136]. This profile is modified in the case of seeding, *i.e.* introduction of low amounts of pre-aggregated forms at the beginning of aggregation. This results in a disappearance of the lag phase, aggregated forms playing the role of template and triggering aggregation (Scheme 3).

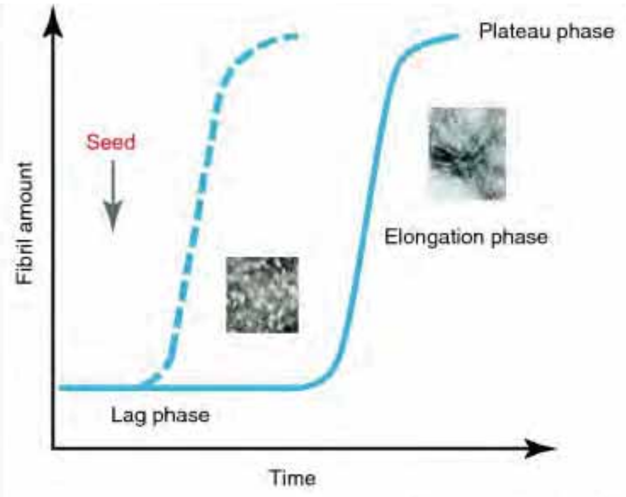

Scheme 3: Typical aggregation curves with time in the presence and absence of seeding.

Despite numerous studies aiming at elucidating Aβ aggregation mechanism, the precise nature of steps and intermediates remains unclear [136–138]. Among many other proposed mechanisms, Smith group suggested the existence of two distinct aggregation pathways for Aβ_{1-42} depending on initial monomer concentration [139]. At low concentration (< 20 μM), aggregation starts with a nucleation step, followed by an elongation of fibres by monomers addition (Scheme 4, Mechanism 1). This process is characterized by a high content of monomers and the absence of oligomers. NMR experiments showed that the shift from monomers to nucleated forms was reversible in the first hours of aggregation.

At high monomer concentration (> 20-30 μM), the mechanism involves the formation of low molecular weight oligomers that stack together into higher molecular weight oligomers. This process is irreversible, and results in a rapid increase of fluorescence during the first hour of aggregation experiments. Follows a lag phase, corresponding to the lateral assembly of high molecular weight oligomers into protofibrils. This state displays a typical β-hairpin structure, with intramolecular H bonds. The formation of fibres is completed by a conformational change of protofibrils that shift from antiparallel β-hairpin to β-sheet conformation, stabilized by intermolecular H bonds between peptides (Scheme 4, Mechanism 2). This results in an important increase of Th-T fluorescence.

These processes were shown to strongly depend on temperature: below 15°C, a high monomer content could be detected by NMR, whatever the initial Aβ_{1-42} concentration. At higher temperature, the monomer content depends on initial concentration.

More generally, most studies agree that the aggregation process also strongly depends on other growth parameters, including agitation, pH or ionic strength. Many reports also indicate that Aβ_{1-42} is more aggregation-prone than Aβ_{1-40}; an explanation may have been found by resolving fibre structures (see Section III.2.d.).

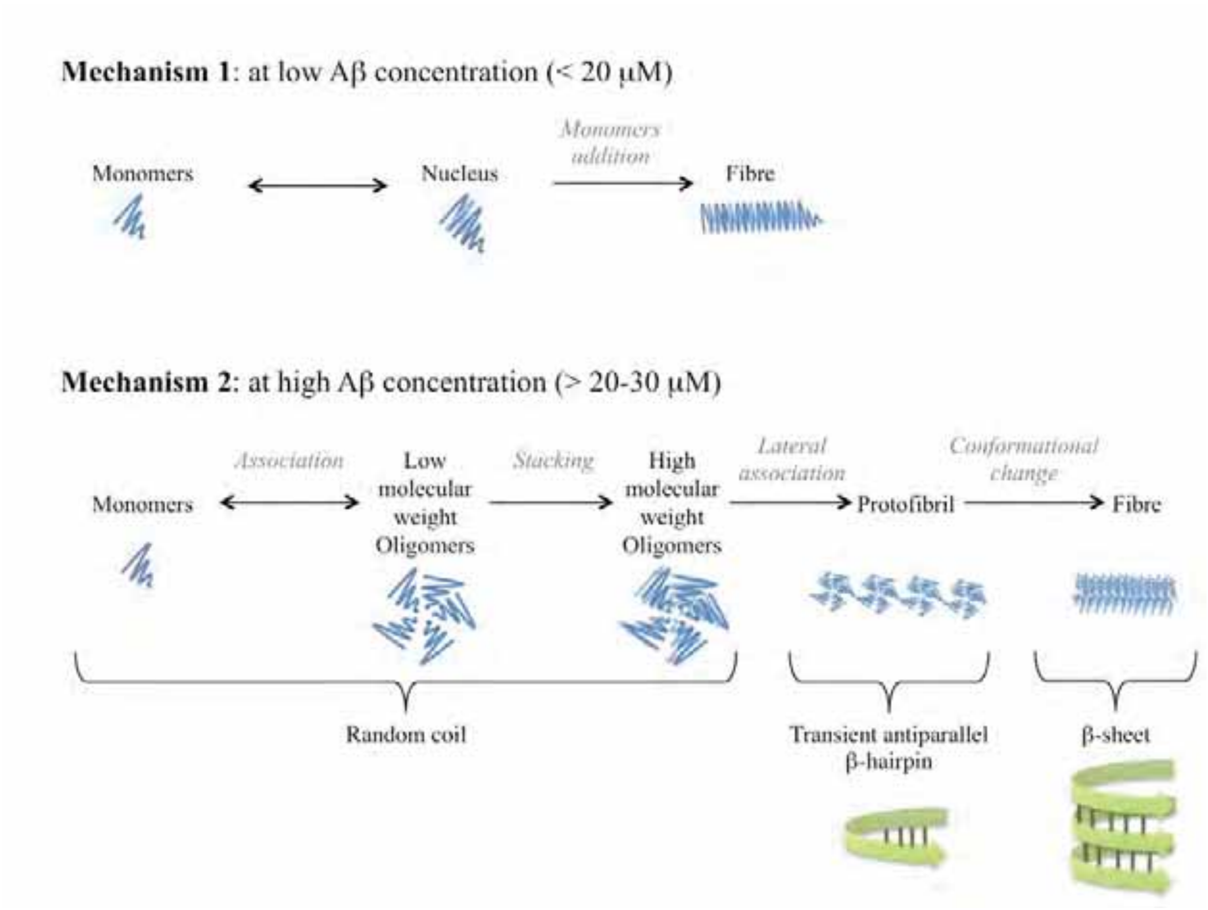

Scheme 4: Aggregation mechanisms for low and high peptide concentrations as described by Smith group.

Depending on the aggregation process, the morphology of the fibres obtained is different. A study from Petkova *et al.* showed that the presence or not of agitation during aggregation has a strong influence on $A\beta_{1-40}$ fibre morphology [140]. One could relate these effects to differences in stabilization of oligomeric species. Interestingly, the resulting fibres displayed differences in neurotoxicity *in vitro*. They also showed that morphologies were maintained upon seeding for several generations. This was used for preparation of highly structurally homogeneous samples for fibre structure elucidation (Section III.2.c).

III.2.c. Fibre characterisation

The formation of insoluble well-ordered protein aggregates is unusual in biology, and few characterization tools can be applied to them. Because of their one-dimensional structure, crystals of amyloid fibres cannot be isolated. Their insoluble nature also precludes the use of some conventional techniques such as circular dichroism or solution NMR. Microscopy techniques, such as AFM or TEM, enable the visualization of fibres, and can allow concluding on their morphological features when using high-resolution machines (Figure 11). The most suitable technique to obtain a structure of fibres at the atomic level is solid-state NMR, but it requires important amounts of highly homogeneous material and isotopic labelling. Indeed, differences in fibril growth conditions induce important polymorphism, preventing structure resolution. Yet, model structures were proposed for A$\beta_{1\text{-}40}$ and A$\beta_{1\text{-}42}$ fibres.

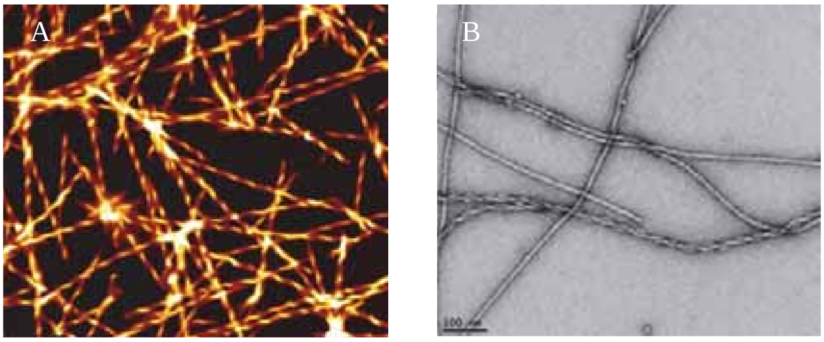

Figure 11: AFM (A) and TEM (B) images of Aβ fibres.

III.2.d. Structures of amyloid-β peptides

- A$\beta_{1\text{-}40}$

Different structures of A$\beta_{1\text{-}40}$ are proposed in literature, all based on solid-state NMR studies. Figure 12 shows three models of A$\beta_{1\text{-}40}$ fibres found on the Protein Data Base. Each of them shows fibres as the stacking of two or three protofilaments, the variations being attributable to differences in fibre growth conditions. Each structure displays a β-turn-β structural motif, in which the hydrophobic cluster is tightly packed, with side-chain contacts experimentally observed between Phe19 and Leu34, Val 36, Ile32. A salt bridge between Lys28 and Asp23 is also observed, stabilising the β-turn-β structure. Finally, a displacement along the fibre axis, called “staggering” is observed: one β-strand of a peptide “N” is facing the other β-strand of the peptide “N+1” [141–143].

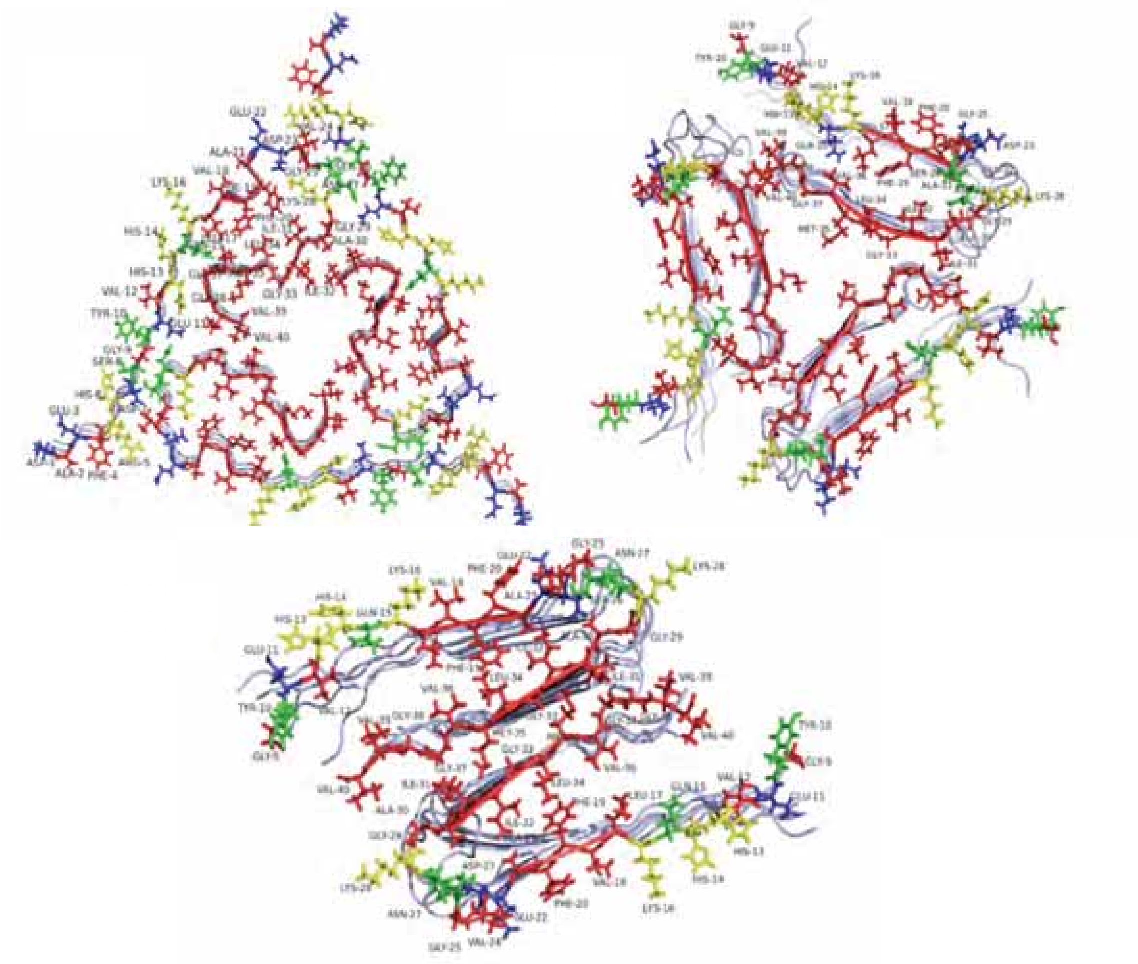

Figure 12: Different model structures of Aβ$_{1-40}$ fibres (PDB: (A) 2M4J, (B) 2LMP, (C) 2LMN). *Red: non-polar residues, Green: polar residues, yellow: basic residues, blue: acidic residues.*

- Aβ$_{1-42}$

Two structures are proposed in literature for Aβ$_{1-42}$ fibres, with respective PDB codes 2BEG [144] and 2MXU [145] (Figure 13). 2BEG was obtained in 2005 from quenched hydrogen/deuterium

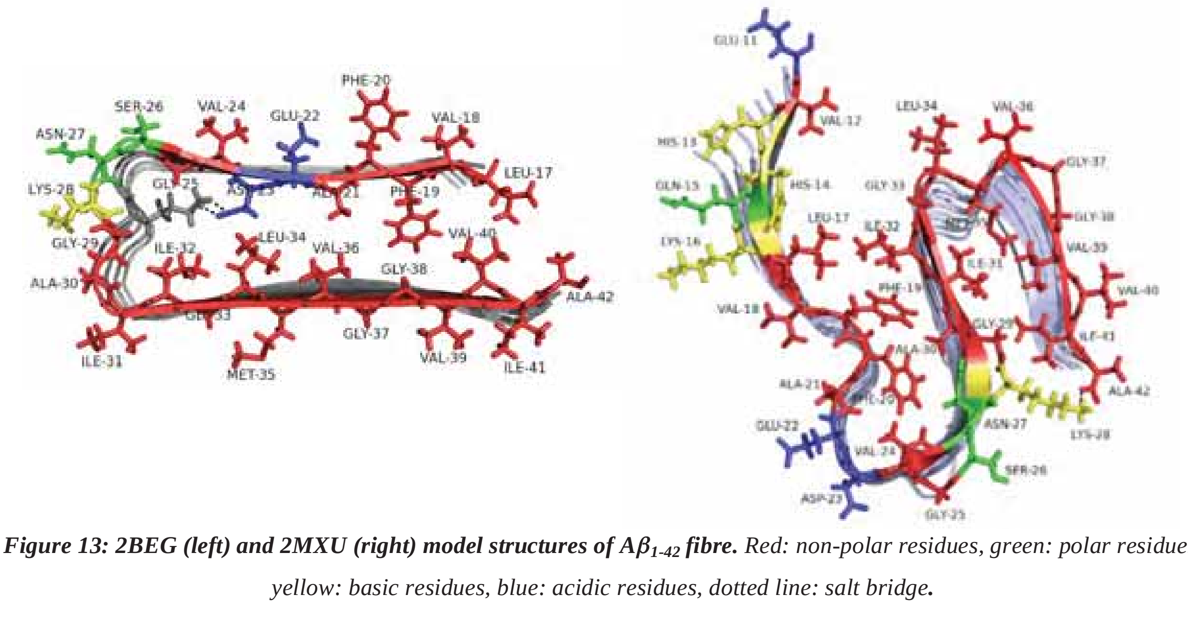

Figure 13: 2BEG (left) and 2MXU (right) model structures of Aβ$_{1-42}$ fibre. *Red: non-polar residues, green: polar residues, yellow: basic residues, blue: acidic residues, dotted line: salt bridge.*

exchange NMR. It presents a U-shaped fibre in which contacts are formed between Phe19-Gly38 and Ala21-Val36. A salt bridge is formed between Asp23 and Lys28. Staggering is also observed, residues from peptide “N” facing residues of peptide “N+1”.

The 2MXU structure was proposed in 2015 by solid-state NMR analyses [145]. It was obtained from highly structurally homogeneous samples, produced by multiple seeding cycles. This structure reveals a triple β-sheet motif, with three β-strands regions. The residues forming the “hydrophobic cluster” (Leu17-Ala21) are tightly packed with Ala30 and Ile32. In the other β-sheet, Ile32, Met35 and Val39 are in close contact. A salt bridge between Lys28 and Ala42 further stabilizes this structure. $A\beta_{1-42}$ fibre is thus very rigid. Unlike $A\beta_{1-40}$, no stacking between filaments or staggering has been observed. Distance between peptides is of 5 Å and diameter of fibril is of 4 nm.

IV. Objectives of the study

The aim of this thesis consisted in developing new hybrid catalysts made by interaction between catalytically active metal complexes and amyloid fibres.

As stated before, amyloid fibres were successfully used as bionanomaterials for several applications (Section II.3). Their unique quaternary structure combined with their high stability and resistance to heat and organic solvents make them promising candidates for applications in catalysis. Because of their insoluble character, catalysts made of amyloid fibres would also be recyclable. Among amyloidogenic proteins, Aβ peptides are probably the most studied. Even though studying their aggregation remains complicated since very conditions-dependent, it is also well documented.

Among the different existing approaches for artificial metalloenzyme elaboration, we chose to focus on the one relying on the non-covalent incorporation of coordination complexes into biomolecules (Section I.3). Firstly, because it encompasses the skills of the two research groups involved in this thesis, *i.e.* bioinorganic chemistry and protein engineering. Secondly, because amyloid fibres are known to interact with various types of molecules, providing a background for interaction studies. Finally, this approach enables the rapid screening of coordination complexes, to select the best hybrid candidate.

Here, we propose an original use of amyloid fibres as a support for catalysis.

This manuscript describes the elaboration of new hybrid catalysts by incorporating metal complexes into amyloid fibres made of Aβ peptides.

- **Chapter II** describes the optimized expression of MAβ peptides in *Escherichia coli*, and their purification following a novel approach. Their aggregation properties were assessed, establishing recombinant MAβ peptides as suitable models for aggregation studies *in vitro*.
- **Chapter III** describes the synthesis of a series of phenyl-terpyridine ligands and of the corresponding Cu(II), Fe(II) and Ru(II) complexes. The different compounds were characterized using various physicochemical techniques, and their catalytic activity on oxidation reactions was assessed.
- **Chapter IV** describes the study of the interaction between metal complexes and Aβ fibres. Different techniques, such as fluorimetry, UV-Visible spectrophotometry, and NMR were used to assess the interaction. Interestingly, differences were observed depending on the nature of the complex.
- Finally, preliminary catalytic assays were conducted on the hybrid scaffolds made of metal complexes inserted into Aβ fibres, as described in **Chapter V**. This constitutes a first proof of concept for hybrid catalyst elaboration based on amyloid fibres.

Chapter II. Recombinant production of Amyloid-β peptides

This chapter is adapted from: Hoarau, M., Malbert, Y., Irague, R., Hureau, C., Faller, P., Gras, E., André, I., and Remaud-Siméon, M. (2016). A Robust and Efficient Production and Purification Procedure of Recombinant Alzheimers Disease Methionine-Modified Amyloid-β Peptides. PLOS ONE 11, e0161209. Original article appears in Annex III.

Introduction

Whereas Alzheimer's Disease constitute a major health issue of the XXIst century, the causes and mechanisms of disease are still poorly understood. In particular, the implication of amyloid-β peptide, which aggregates to form insoluble plaques in the brain, is the focus of many investigations, both *in vitro* and *in vivo [146,147]*.

In this context, there is an increased need for reliable source of Amyloid-β peptides.

This chapter describes **a new production and purification protocol for Amyloid-β 1-40 and 1-42 in *Escherichia coli***.

In a first part, an overview of existing procedures for Amyloid-β production is given, including chemical and recombinant methods.

In a second part, expression and purification of a His-tagged Amyloid-β 1-42 is proposed, taking advantage of affinity chromatography for purification.

In a third part, an alternative strategy is proposed for Met-Amyloid-β production, taking advantage of inclusion body formation in bacteria.

Finally, Met-Amyloid-β 1-40 and 1-42 were fully characterized using LC-MS, NMR, and Thioflavin-T aggregation assay. These results appear in **the last part** of this chapter.

I. Production routes of Amyloid-β peptides

I.1. Context: need for amyloid-β peptides

Alzheimer’s disease constitutes a major health issue, and much research effort is currently being devoted to better understand the causes and mechanisms of the disease. In particular, understanding the behaviour of amyloid-β (Aβ) peptides is a key issue, their implication in the disease remaining unclear.

For *in vitro* experimentation, disposing of reliable Aβ samples displaying reproducible behaviours is crucial. Indeed, aggregation was shown to be highly sensitive to many factors, such as temperature, concentration, agitation, but also storage or sample preparation [139,148]. But most importantly, both the presence of contaminants and the presence of pre-aggregated forms of the peptide were shown to strongly alter the course of aggregation, either inhibiting it or yielding no fibrillary material. In this regard, the easy access to pure and homogeneous Aβ samples is still challenging and essential for *in vitro* experimentation.

I.2. Different routes for amyloid-β peptides production

I.2.a. Solid phase peptide synthesis

Most investigations on Aβ are usually performed with chemically synthesized peptides. Solid-phase peptide synthesis consists of successive couplings of *N-ter* protected amino acids on a solid support. The desired peptide is obtained upon deprotection and cleavage. Although convenient and easily accessible, solid phase peptide synthesis can be complex in term of purification. Indeed, the presence of peptides with altered sequences caused by non-quantitative synthetic steps or of racemized peptides is observed, which can hardly be removed, even by up-to-date purification methods. Traces of salts or metal ions were also reported [149]. Finally, the presence of pre-formed aggregates due to storage conditions is frequent. All of this results in significant variations of aggregation properties from batch to batch. This has been recently exemplified in a study, which showed that the recombinant peptide is more aggregation-prone and more neurotoxic than its synthetic analogue, demonstrating a deleterious effect of synthetic procedures on peptide properties [150]. This has encouraged the exploration of various biological routes to access recombinant Aβ peptides and get rid of such issues.

I.2.b. Recombinant production

Recombinant DNA expression, also referred as molecular cloning, is of huge importance in biochemistry and biotechnology. It consists in inserting a foreign DNA segment into a self-replicating DNA vector. When cloned in a suitable organism, the DNA fragment will replicate together with the vector. If the fragment is positioned downstream a promoter, this leads to the production of a messenger RNA and the protein corresponding to its coding sequence [151].

Recombinant peptide production can provide high yields of polypeptides with perfect sequence fidelity. It also enables the rapid generation of large mutant libraries by random mutagenesis. Finally, it represents a clean production process, all the materials used being issued from biological sources.

Different recombinant production protocols are proposed in the literature for Aβ peptides. Some attempts were made in yeast [152] or by combining recombinant and synthetic procedures [153] but, to date, the most common expression system remains *Escherichia coli*. Most often, peptides are appended with a fusion protein that may enhance their solubility and facilitate their isolation and purification using affinity chromatography. However, such strategies raise several issues. First of all, despite the usually increased solubility of the fusion proteins, a non-negligible amount of the peptide frequently remains in the insoluble fraction, thus requiring an extra denaturation step for complete recovery [154,155]. Moreover, a cleavage site has to be intended, which position is critical. If not carefully chosen, cleavage will introduce amino-acids at the terminal end of the peptide, potentially modifying its aggregation and metal-binding properties [156,157]. The same drawback exists with smaller affinity tags [158,159]. This problem was solved with the use of proteolytic enzymes such as the Factor Xa or the enterokinase, whose cleavage sites was introduced in the construction to enable the formation of native Aβ [160,161]. Still, such methods are time-consuming and require many purification steps, including long affinity chromatography purification procedures that inevitably result in a loss of peptide. To overcome this drawback, it was proposed to express native Aβ in *E. coli* [162,163]. Notably, Aβ forms insoluble inclusion bodies (IBs) when expressed in *E. coli* in their native form. This was exploited by Walsh and co-workers to isolate pure recombinant MA$\beta_{1\text{-}40}$ and MA$\beta_{1\text{-}42}$ by anion-exchange purification [162] and by Cullin and co-workers, applying a dialysis-based purification protocol [164].

I.2.c. Our strategy

In order to obtain clean Aβ peptide samples, we envisioned two parallel strategies for producing the recombinant peptides. In the one hand, we proposed to fuse the genes encoding the peptides with a gene coding for a cleavable 6xHis purification tag to promote the easy purification of the peptides (Scheme 5, construction 1). In the other hand, we also explored the recombinant production of the two Aβ peptides devoid of any tag in *E. coli* and investigate the development of a purification protocol taking advantage of inclusion body formation for purification (Scheme 5, constructions 2 and 3). These peptides will be referred as MAβ in the following, due to the presence of a codon start methionine on their *N*-ter end. Both strategies were conducted in parallel.

Construction 1: His-tagged Aβ$_{1-42}$

MGSS**HHHHHH**SSG**LVPR**^{T}**GS**HM**DAEFRHDSGYEVHHQKLVFFAEDVGSNKGAIIGLMVGGVVIA**

Construction 2: MAβ$_{1-42}$

M**DAEFRHDSGYEVHHQKLVFFAEDVGSNKGAIIGLMVGGVVIA**

Construction 3: MAβ$_{1-40}$

M**DAEFRHDSGYEVHHQKLVFFAEDVGSNKGAIIGLMVGGVV**

Scheme 5: Targeted peptide sequences. *Native Aβ sequence appears in black (Aβ$_{1-42}$ in constructions 1 and 2, Aβ$_{1-40}$ in construction 3). 6xHis tag appears in blue, thrombin recognition sequence appears in green, other amino acids appear in grey. ^{T} indicates thrombin cleavage site.*

II. His-tagged Aβ$_{1\text{-}42}$

II.1. Vector construction

Because we had no pre-existing plasmid containing sequence coding for Aβ peptides, a first plasmid, named pET28_His_Thromb_Ab42 was ordered (Scheme 6). It consists in a pET28a plasmid comprising a gene coding for His tag, thrombin cleavage site, and Aβ$_{1\text{-}42}$ downstream a T7 promoter. It also possesses a kanamycin resistance gene. A second 6xHis tag is present, but will not be expressed in this construction. This plasmid was used as template for the formation of further constructions (see 0.).

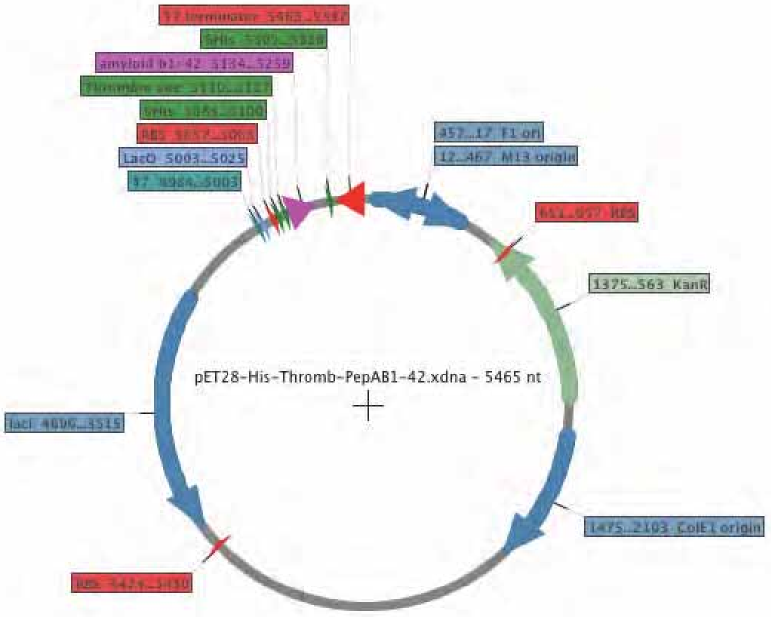

Scheme 6: Representation of pET28_His_Thromb_Ab42 plasmid.

II.2. Expression and purification

E. coli BL21 cells were transformed with pET28_His-Thromb_Ab42 and expression experiments were performed. Expression was induced for 4 h at 37 °C, and cells were harvested and lysed. Interestingly, the SDS-PAGE analyses showed that the overexpressed His-Thromb-Aβ$_{1\text{-}42}$ peptide was contained in the insoluble fraction. After the centrifugation of the cell lysate, the pellet was solubilized in 8 M urea, and applied on TALON resin. Elution with increasing concentrations of imidazole afforded peptides with acceptable purity (Figure 14). The nature of the peptide obtained was validated by anti-His Western-Blot analysis. A first attempt of thrombin cleavage was made, showing partial cleavage (Figure 15).

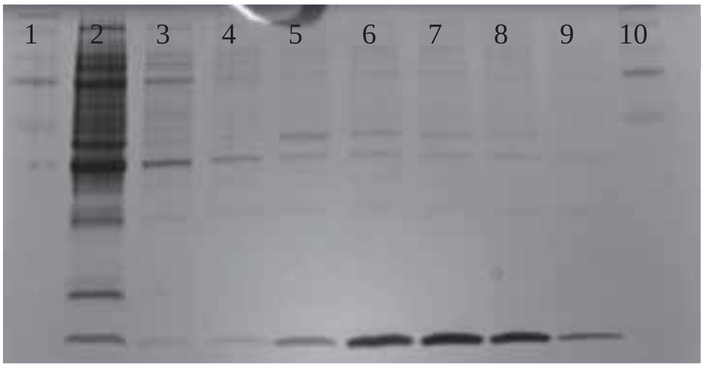

Figure 14: Purification of His-Thromb-Aβ_{1-42} peptide. *Insoluble fraction from bacterial lysis was applied on TALON resin and incubated. Supernatant was discarded (lane 2) and resin was washed twice with lysis buffer (lanes 3 and 4). Peptide was then eluted using Imidazole 25, 50, 100, 200, 300 and 400 mM (lanes 5-9). Samples were compared with 10-250 kDa protein ladder (lanes 1 and 10).*

At this stage, we chose to stop efforts on this strategy to focus on the formation of native Aβ peptides. First of all, because we had no guarantee that once cleaved, the GSHMAβ_{1-42} peptide obtained would be able to aggregate into fibres, whereas MAβ_{1-42} aggregation was reported in literature. Secondly, the presence of the 6xHis tag implied at least one chromatographic purification step and preferably two steps to ensure a good level of purity. In addition, although a cleavage site had been introduced in our construct to remove the 6xHis tag, the cleaved peptide would contain 4 additional residues at its *N* terminal end, which could also affect aggregation. All of this prompted us to focus on MAβ production.

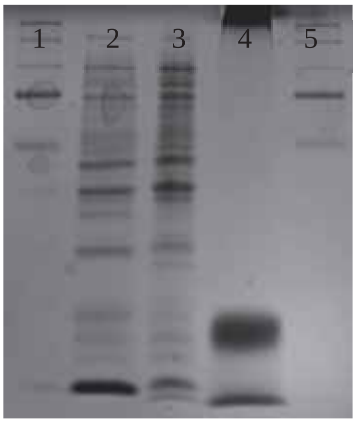

Figure 15: Preliminary result of Thrombin cleavage of His-Thromb-Aβ_{1-42}. *His-Thromb-Aβ_{1-42} (lane 2) was incubated for 4h with thrombin at room temperature, leading to partial cleavage (lane 3). The resulting peptide presents a band similar to commercial Aβ_{1-42} (lane 4). Samples were compared with 10-250 kDa protein ladder (lanes 1 and 5).*

III. MA$\beta_{1\text{-}42}$ and MA$\beta_{1\text{-}40}$

A second strategy consisted in expressing amyloid peptides in absence of tags, the presence of a *N-ter* methionine due to the start codon being the only difference with Alzheimer's disease related peptides.

III.1. Vector construction

- pET28_MAb42

The gene encoding MA$\beta_{1\text{-}42}$ was obtained by PCR from pET28_His_Thromb_Ab42, using primers with floating tails comprising the restriction sites NcoI and XhoI. The amplicon and the pET28 vector were digested with the same restriction enzymes. The two parts were ligated to yield the expected pET28_MAb42 (Scheme 7), which was transformed into competent *E. coli* cells. Sequencing of the insert confirmed the quality of the construction.

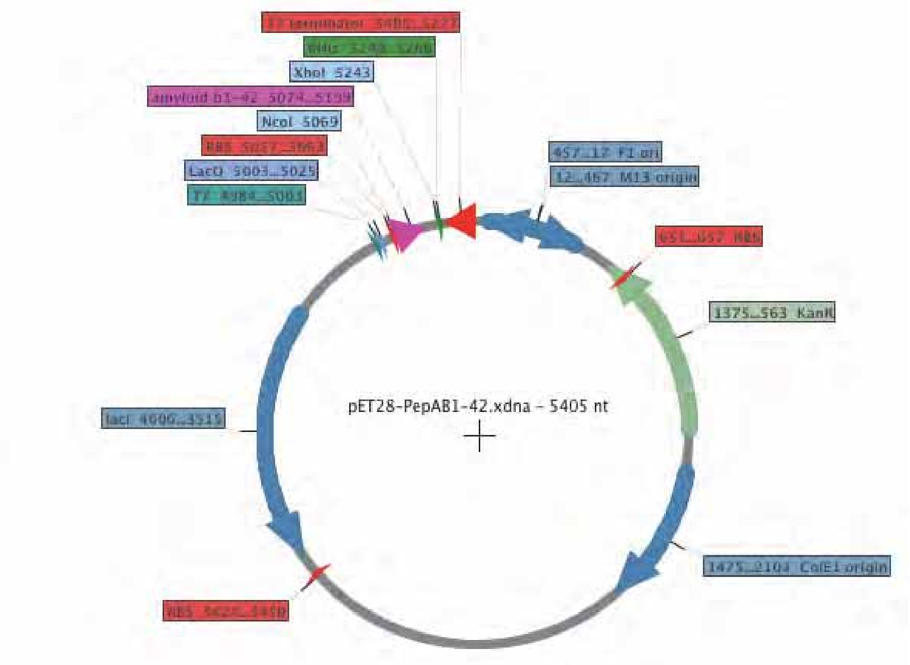

Scheme 7: Representation of pET28_MAb42 plasmid.

- pET28_MAb40

pET28_MAb40 was obtained from pET28_MAb42 using the same strategy. The sequence coding for MA$\beta_{1\text{-}40}$ was amplified by PCR. The forward primer used was complementary to pET28_MAb42, whereas the reverse primer possessed a floating tail with a BamHI restriction site. Both pET28_MAb42 and the insert were digested by NcoI and BamHI and ligated, to form pET28_MAb40, as shown in Scheme 8.

These two plasmids were used to transform *E. coli* BL21(DE3) cells, and produce MAβ_{1-40} and MAβ_{1-42} peptides.

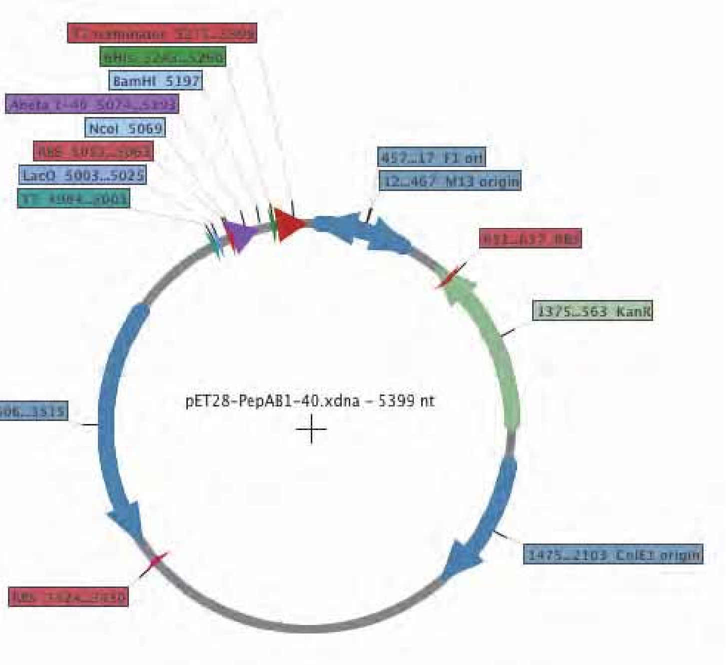

Scheme 8: Representation of pET28_MAb40 plasmid.

III.2. Expression of MAβ peptides

III.2.a. Formation of bacterial inclusion bodies

MAβ peptide production analysis revealed that most of the peptides were recovered in the insoluble fraction after cell lysate, possibly corresponding to the formation of inclusion bodies (IB). Indeed, when insoluble proteins are overexpressed in *E. coli*, this may sometimes result in the formation of IB at the poles of the cell. First considered as amorphous aggregates, IB were found to display amyloid structural features [165]. In particular, they are positive to amyloid specific dyes.

As such Thioflavin-S (Th-S), which is usually used for staining amyloid plaques, was recently shown to stain bacterial IBs of MAβ peptides, both *in vivo* and *in vitro*. This property was used to detect protein aggregation in bacteria [163], or to screen *in vivo* for aggregation inhibitors [166].

In our case, microscopy of *E. coli* cells treated with Th-S confirmed the presence of inclusion bodies, located at the poles of cells (Figure 16). This property was used to assess the production of MAβ and optimise the expression conditions.

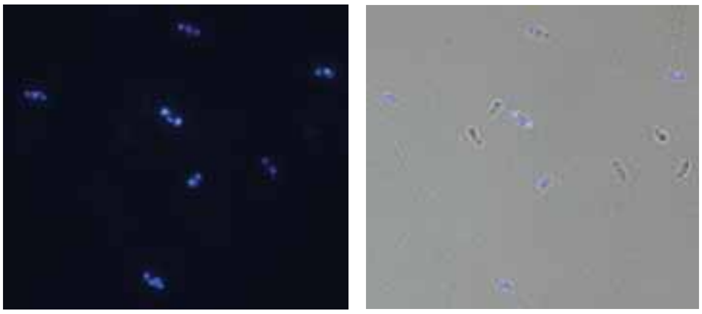

Figure 16: Visualisation of bacterial IB of MA$\beta_{1\text{-}42}$. A. *E. coli cells expressing MA$\beta_{1\text{-}42}$ incubated in Th-S observed by fluorescence microscopy.* ***B.*** *Overlay of fluorescence and visible microscopy images.* ***Experimental conditions:*** *λ_{exc} = 340-380 nm, dichroic = 400, λ_{em} = 425 nm, 63x magnification.*

III.2.b. Optimisation of expression conditions

To determine optimal conditions for peptide expression, we envisioned a procedure based on Th-S monitoring. Cells from different cultures were sampled, incubated with Th-S and their fluorescence spectra were recorded with a fluorimeter. This allowed us to study the effect of induction time, temperature, and inducer concentration on MA$\beta_{1\text{-}42}$ expression in *E. coli*.

- Time of induction

In order to use Th-S staining as a tool for the optimization of peptide expression, the correlation between IB content and the Th-S fluorescence level had to be established. To do so, cultures expressing MA$\beta_{1\text{-}42}$ were stopped at different induction times. The cells were sampled, incubated with Th-S, and their emission spectra were recorded. As shown in Figure 17.A, the fluorescence level increased during the first 4 hours of induction and then reached a plateau. The corresponding cultures were lysed and peptide was purified and analysed by SDS-PAGE. A good accordance was observed between the amount of purified peptide and the fluorescence level (Figure 17.B). Based on these results, a 4 h induction was considered as adequate and applied throughout the rest of the study.

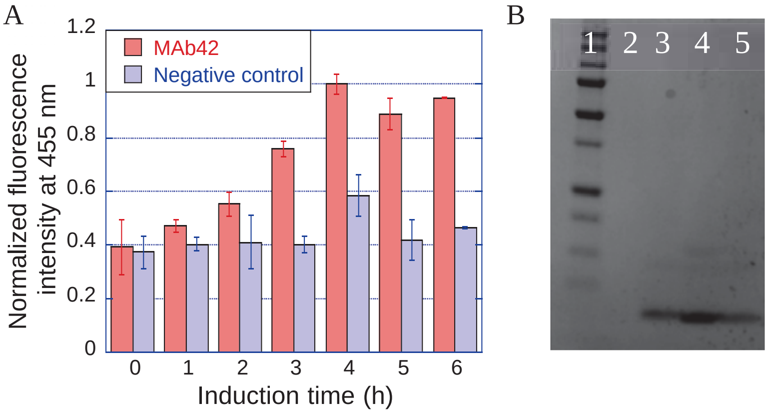

Figure 17: MA$\beta_{1\text{-}42}$ expression monitoring with time using Thioflavin-S. A. *Variations of normalized fluorescence of Th-S-treated E. coli cells expressing MA$\beta_{1\text{-}42}$ with induction time.* ***B.*** *SDS-PAGE of purified inclusion bodies from E. coli cultures expressing MA$\beta_{1\text{-}42}$; lane 1: 10-250 kDa protein ladder, lane 2 to 5: samples taken at 0, 2, 4, and 6 hours of growth, respectively.*

- Inducer concentration

Th-S monitoring was used to screen for the optimal concentration of IPTG inducer. No significant variations of IB production was observed with IPTG concentration comprised between 0.5 and 1.5 mM (Figure 18). Contrariwise, increased levels of protein contaminants were observed when using 1 or 1.5 mM IPTG, which could be due to the overexpression of *E. coli* chaperones [167]. Induction at 0.5 mM IPTG was thus preferred for the rest of the study.

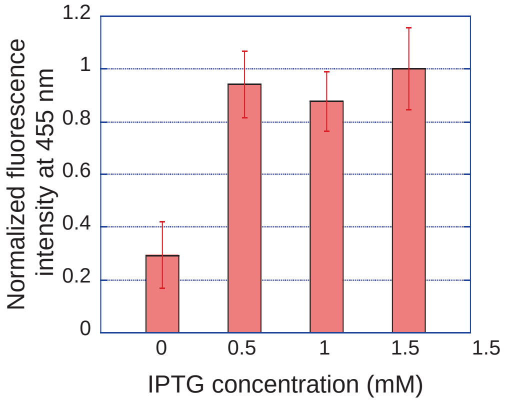

Figure 18: Th-S fluorescence of E.coli cells expressing MA$\beta_{1\text{-}42}$ induced with different IPTG concentrations. *Cells were induced at 37°C for 4 h.*

- Temperature

The optimal temperature of cell growth was investigated using the same strategy. *E. coli* cells expressing MA$\beta_{1\text{-}42}$ were grown at 23, 30 and 37 °C. As shown in Figure 19, the temperature allowing the formation of a maximal amount of IBs was 37 °C.

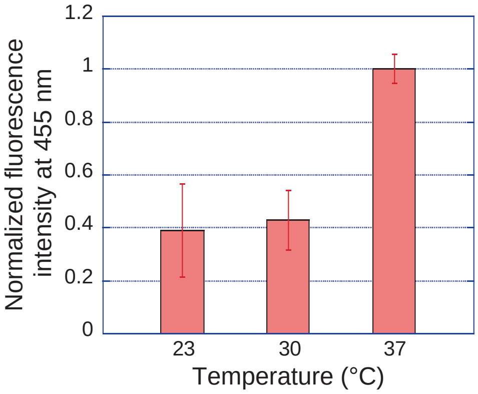

Figure 19: Th-S fluorescence of E. coli cells expressing MA$\beta_{1\text{-}42}$ at various temperatures. *Cells were induced with 0.5 mM IPTG for 4 h.*

III.3. Purification of MAβ peptides

III.3.a. Inclusion body isolation

As Aβ peptides were produced as IBs, the first step of the purification procedure consisted in isolating and purifying IBs. The main challenge of this approach was to succeed in removing proteins and nucleic acids that could be trapped in the IBs or stacked on their surface.

First, the previously reported “soni-removal” method, which consists of multiple sonication and centrifugation cycles, was performed to roughly eliminate nucleic acids and proteins stacked at the IB surface [168]. At this stage, Th-S fluorescence visualization of isolated IBs confirmed that their average size remained unchanged, showing no deterioration due to sonication (Figure 20).

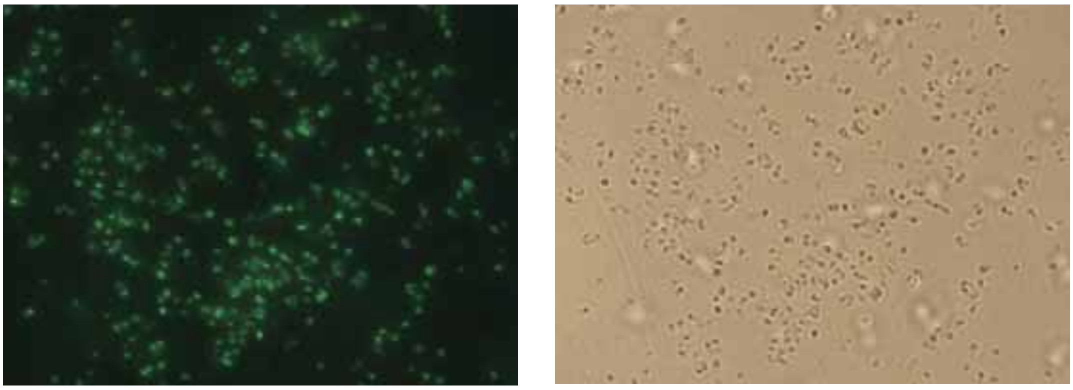

Figure 20: Visualization of IB after bacterial lysis. A. *MAβ$_{1-42}$ IB incubated in Th-S observed by fluorescence microscopy.* ***B.*** *Corresponding visible microscopy image.* ***Experimental conditions****: λ_{exc} = 450-490 nm, dichroic = 500, λ_{em} = 500-550 nm, 63x magnification.*

III.3.b. Purification of monomeric MAβ peptides

In a first trial to purify MAβ$_{1-42}$, IBs were solubilized using 8 M urea and then passed through a DEAE Sepharose, following the described procedure. As seen in Figure 21, this protocol enables the removal of most protein contaminants. Unfortunately, it did not allow the elimination of a 13-kDa *E. coli* protein contaminant, regardless of IPTG concentration used for induction. This protein could not be eliminated by ultrafiltration, indicating that the urea treatment did not allow breaking the interaction probably existing between the 13-kDa protein and the peptide (Figure 21 lanes 4 and 5). Because the peptide and the protein are close in size, purification of the mixture seems complicated. We thus decided to turn to another denaturation method.

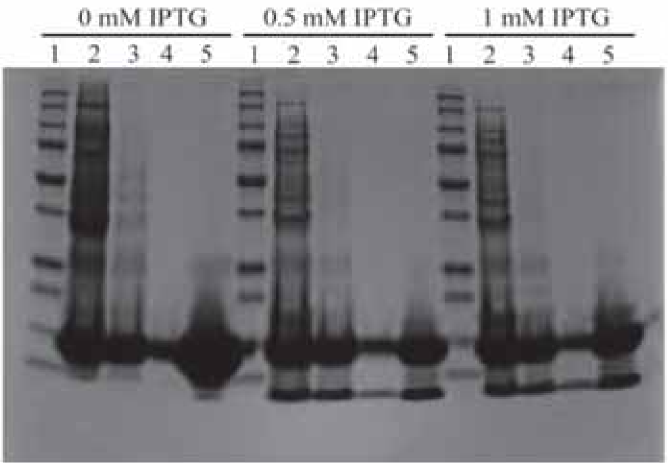

Figure 21: Purification protocol of MA$\beta_{1\text{-}42}$ IBs dissolved in 8M urea*. Lane 1: 10-250 kDa protein marker, lane 2: IBs after urea denaturation, lane 3: after passing through DEAE resin, lane 4: after 30-kDa ultrafiltration, lane 5: after 3-kDa concentration.*

Aβ peptides have an isoelectric point of about 5-6, and are soluble at high pH. IBs were thus first incubated with 50 mM sodium hydroxide, to solubilize MAβ. Solution was then neutralized, leading to the precipitation of a large amount of proteins, while MAβ peptides remain in the supernatant (Figure 22.B, lanes S1 and P2). The high pH denaturation/neutralization cycle was applied twice to maximize MAβ recovery (Figure 22.B, lane S2). Further completion of contaminant elimination was carried out by ultrafiltration of the solubilized peptides followed by concentration, respectively on 30-kDa and 3-kDa molecular weight cut-off membranes. As shown on the electrophoresis gel (Figure 22.B, lane F), the ultrafiltration step allowed getting one single band around 5 kDa, the presence of any protein contaminant being excluded. The schematic representation of this protocol is shown in Figure 22.A.

Contrariwise to urea denaturation, it seems that high pH treatment do break the interaction between peptide and contaminating protein, which is then easily removed by ultrafiltration.

III.4. Monitoring of MAβ peptides purity

At this step, one important issue was the monitoring of sample purity at the various stages of the purification procedure. The Bradford protein assay was eliminated because it does not give any information on sample purity and only allows the determination of a global protein content. Combination of UV-Vis spectrophotometry with gel electrophoresis was clearly preferred. Indeed, SDS-PAGE permits to visualize the presence of protein contaminants while UV-Vis analyses inform on the predominant presence of either nucleic acids (λ = 260 nm) or specific amino acids, namely tryptophan (λ = 280 nm), tyrosine/tyrosinate (λ = 274 nm/λ = 293 nm) and phenylalanine (λ = 257 nm) [169]. Both methods were thus combined to assess the purity level of the peptide samples depending on the purification steps as shown in Figure 22.C. After denaturation (Figure 22.C, spectrum D), a lot of species are present. The supernatant harvested after neutralization (Figure 22.C, spectrum S1+S2) still contain proteins but is already devoid of nucleic acids. After ultrafiltration, the sample was too diluted to give an informative UV spectrum (Figure 22.C, spectrum F). Finally, the concentration step yielded a pure sample showing a UV signature with the typical UV band at λ = 293 nm corresponding to the tyrosinate form (Figure 22.C, spectrum C). This typical profile is conserved after size exclusion chromatography, which was performed to isolate only monomeric peptide before aggregation assays (Figure 22.C, spectrum SEC). Overall, these analyses confirmed the high level of purity of the peptide preparation.

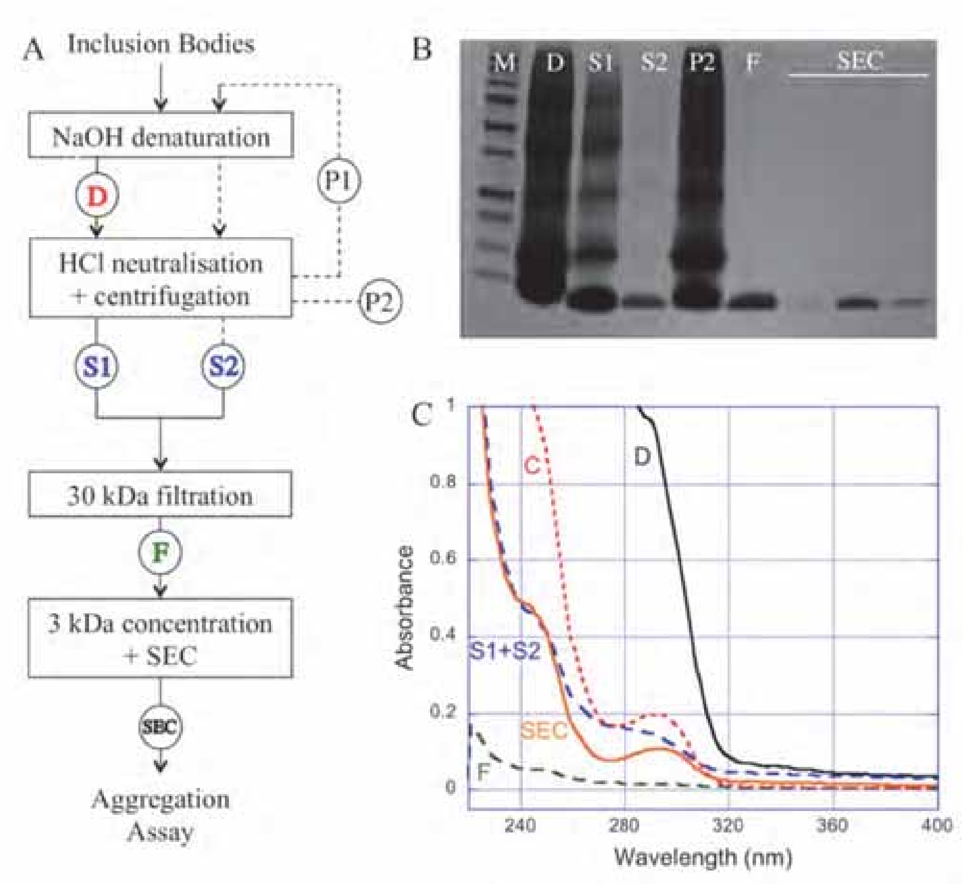

Figure 22: Purification monitoring of MAβ. A. *Simplified scheme of the purification procedure. Circled letters correspond to samples collected for either UV/Vis measurements or gel analysis. Supernatant S1 and S2, and pellet P1 and P2 correspond to the supernatant and the precipitate obtained for the two cycles of denaturation/neutralisation.* ***B.*** *SDS-PAGE at different steps of purification, compared with 10-250 kDa protein marker (lane M).* ***C****. UV-Vis spectra at pH 12 after IBs denaturation (D), after denaturation/neutralisation cycles (S1+S2), after 30-kDa ultrafiltration (F), after concentration (C), and after size exclusion chromatography (SEC).*

As the sample was devoid of any protein contaminants, the pH-dependent absorption of Tyr was used to estimate the peptide yield. Absorption spectra of the peptides were thus recorded at pH 12 (showing the absorption band of tyrosinate at 293 nm) and at pH 2 (displaying no tyrosinate band). Subtracting spectra allowed the precise quantification of the tyrosine content of the sample, which enabled the estimation of the peptide yield as being around 4 mg/L of culture, which is in the same range as those previously reported, comprised between 3 and 7 mg/L [154,155,160,170,171] (see Table 1).

IV. Peptide characterization

IV.1. LC-MS analyses

To characterize the peptides, LC-MS analyses were conducted right after the concentration step on both peptides. Because they are hydrophobic and aggregation-prone, chromatography of amyloid peptides is often complicated. Peptide samples were acidified and analysed on a C4 column.

MA$\beta_{1\text{-}40}$ affords a clean chromatographic trace with a major peak at 10.8 min. The mass spectrum associated to this peak displays peaks corresponding to peptides protonated 3, 4 and 5 times (Figure 23.A and Figure 23.C). MA$\beta_{1\text{-}42}$ chromatogram is less resolved, with a shoulder arising in front of the main peak (Figure 23.B and Figure 23.D). The masses detected for both the shoulder and the peak are consistent with the calculated masses of MA$\beta_{1\text{-}42}$, indicating that oligomeric forms of MA$\beta_{1\text{-}42}$ could be present. This is consistent with the high propensity of A$\beta_{1\text{-}42}$ to aggregate.

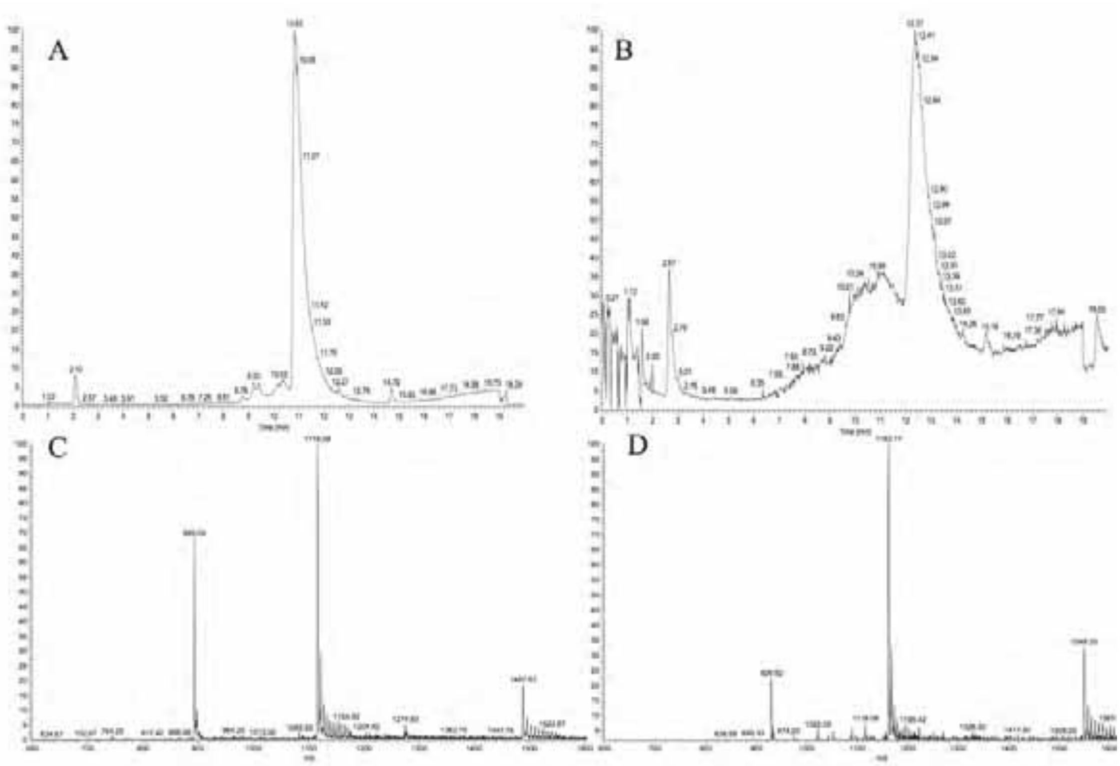

***Figure 23: LC-MS analysis of MA$\beta_{1\text{-}40}$ and M$\beta_{1\text{-}42}$*. A.** *LC trace of MA$\beta_{1\text{-}40}$ monitored by mass detection.* **B.** *LC trace of MA$\beta_{1\text{-}42}$ monitored by mass detection.* **C.** *MS of MA$\beta_{1\text{-}40}$ displaying $[M+5H]^{5+}$, $[M+4H]^{4+}$, and $[M+3H]^{3+}$ peaks (expected values: 892.65, 1115.56, 1487.07).* **D.** *MS of MA$\beta_{1\text{-}42}$ displaying $[M+5H]^{5+}$, $[M+4H]^{4+}$, and $[M+3H]^{3+}$ peaks (expected values: 929.47, 1162.17, 1548.44).*

IV.2. ^{1}H NMR analyses

^{1}H NMR spectra of both peptides were then recorded, and compared with commercially available synthetic $A\beta_{1-40}$ (Figure 24). They display the typical signals usually observed for $A\beta_{1-40}$ peptide. In the aromatic region, signals corresponding to the Hδ and Hε of aromatic residues are well defined. As such, Phe 19 and 20 (*ca.* 7.2 ppm and *ca.* 7.3 ppm) and Tyr 10 (*ca.* 7.95 ppm and *ca.* 6.8 ppm) can be distinguished. Slight shifts are observed for His 6, 13 and 14 (*ca.* 7.8 ppm and *ca.* 7.1 ppm), which can be attributed to pH variations. The absence of signal *ca.* 7.5 ppm confirms the absence of Trp residue in the peptides. Expectedly, signals corresponding to Hα (4.5-3.8 ppm) and Hβ (3.2-2.6 ppm and 2.3-1.5 ppm) are more difficult to attribute in details. In the aliphatic region, signals corresponding to Lys 16 and 28 (1.4 ppm) and to Val and Leu (1.0-0.7 ppm) are observed. Finally, the signal at 3.9 ppm reveals the presence of a methionine residue for the recombinant peptides as expected.

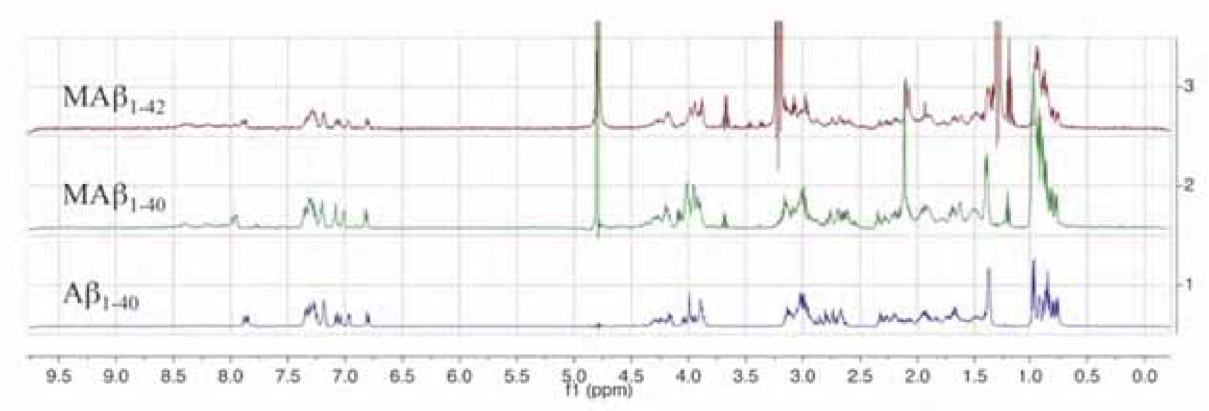

Figure 24: ^{1}H NMR of $MA\beta_{1-40}$ and $MA\beta_{1-42}$ compared with $A\beta_{1-40}$. *Samples of MAβ in water are diluted to 100 μM in 100 mM phosphate buffer pH 7 in D_2O. Synthetic $A\beta_{1-40}$ is dissolved in NaOD and diluted to 100 μM in the same conditions. Signals at 4.75 ppm correspond to H_2O, and signals at 3.25 ppm and 1.25 ppm correspond to traces of ethanol.*

IV.3. Thioflavin-T aggregation assay

Because most *in vitro* studies on Aβ peptides consist in studying their aggregative properties in various conditions, it was essential to ensure that the auto-assembling properties of the peptides are conserved upon this purification process. Prior to this, it was important to remove traces of oligomeric species, to ensure a homogeneous aggregation process. The monomeric forms of the two peptides were thus isolated by SEC, and were then submitted to Th-T aggregation assay.

In 26 h, both peptides afford a characteristic sigmoidal aggregation curve with aggregation half-times around 15 h (Figure 25). The MAβ peptides obtained through our purification procedure thus conserved their auto-assembling properties. The same results were obtained with peptide batches from different cultures, showing the high robustness of the purification procedure in terms of reproducibility. This purification protocol could thus be applied for routine lab-scale MAβ production.

This also confirms that the presence of a *N*-ter Met residue does not affect the aggregation properties of MAβ peptides as previously reported [157]. Removing Met residue could be beneficial for specific studies such as metal coordination, but does not seem mandatory for classical aggregation assays.

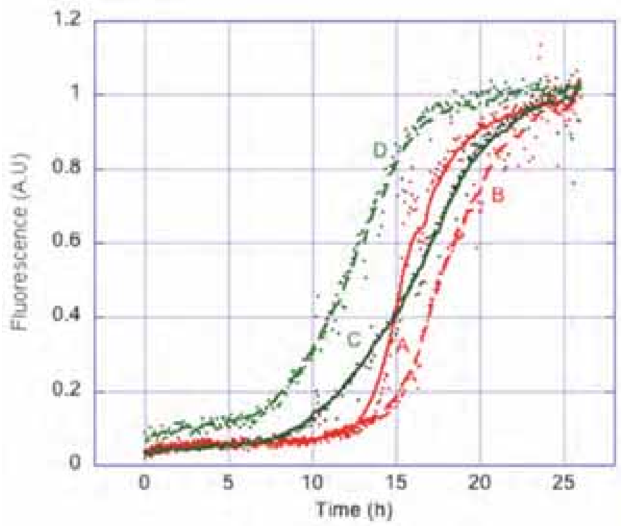

Figure 25: Normalized aggregation curves of MA$\beta_{1\text{-}40}$ and MA$\beta_{1\text{-}42}$. *Two different batches of MA$\beta_{1\text{-}40}$ (A and B) and MA$\beta_{1\text{-}42}$ (C and D) (20 μM) aggregate in the presence of Th-T (10 μM) in phosphate buffer (50 mM, pH 7). Assay was run at 37°C with gentle shaking. Each experiment was run in triplicates.*

Long-term peptide storage was attempted by flash-freezing peptide samples in NaOH 15 mM, and storing it at -20°C. Peptide was then slowly defrozen at 4°C a few weeks later. However, this process completely inhibited peptide's aggregation properties, and other strategies will be to envisage.

Conclusion

We proposed two strategies to produce Aβ peptides in *E. coli*. The first one consists in appending a cleavable 6xHis tag on the *N*-ter part of Aβ. This allows peptide purification on metal affinity resin, affording samples clean enough to be submitted to protease cleavage. The second strategy consists in expressing Aβ without any tag except the start codon associated Met. In that case, peptide is forming IBs, which are positive to Th-S fluorescent dye. This property was used to determine optimal conditions for IBs formation in *E. coli*. Following expression, IBs were isolated from bacterial lysate. At this stage, we chose to solubilize IBs using NaOH; upon neutralization, most of contaminant proteins precipitate, whereas MAβ remains in solution. This contrasts with usual urea denaturation, which does not allow to get rid of contaminants. Last purification steps consist in two successive ultrafiltrations, affording clean samples of peptides.

Peptide characterization was achieved by LC-MS and ^{1}H analyses, and Th-T aggregation assay was run with both peptides, confirming their good auto-assembling properties.

Table 1 presents a comparison between our work and the previously reported procedures for Aβ production in *E. coli*. Many of them are using fusion proteins or tags, which implies long affinity chromatography procedures. Interestingly, these procedures do not necessarily allow complete purification, and further steps can be required. Finally, they often imply the presence of extra amino acids on the peptide upon cleavage. A strategy using MAβ was previously proposed, but here again the purification was completed using chromatography (Table 1, line 2). In contrast with all of this, our method is chromatography-free, purification being achieved by simple centrifugation and ultrafiltration steps. The whole production and purification process can thus be completed within two days.

In terms of purity monitoring, we have proposed a combination of UV and gel electrophoresis, which had never been reported before. Yet, UV-Vis constitutes a convenient way to determine the presence of contaminating Trp-containing proteins (Aβ peptides being devoid of Trp). A final aggregation assay has also been conducted, appearing as crucial to ensure of the auto-assembling properties of the peptides obtained.

Thanks to this method, we dispose of a rapid and convenient source of MAβ peptides. Further work would now consist in improving its properties to serve as support for coordination catalysts. As such, Th-S staining could be used to develop high-throughput screening for peptide mutants, seeking for sequence with increased aggregative properties. Interaction with metal complexes could also be improved with the help of directed evolution together with molecular modelling (see Chap. IV).

Table 1: Previously reported results for Aβ recombinant production.

E. coli strain	**Plasmid**	**Peptide**	**Fusion protein**	**Strategy**	**Purification**	**Yield**	**UV**	**Sequencing**	**MS**	**Aggregation**	**Ref**
MG1655	pQE-80L	^{15}N isotope-labelled $A\beta_{1-42}$	IFABP	IB + affinity	2 x Ni-NTA column + HPLC	6 mg/L	✗	✗	✓	✗	[160]
BL21 DE3 PLysS Star	PetSac	$MA\beta_{1-42}$ $MA\beta_{1-42}$	/	IB	DEAE-cellulose + SEC	n.d.	✗	✓	✓	✓	[162]
BL21 (DE3)	pSK+	$XA\beta_{1-42}$	GST	affinity	Ni-NTA + affinity column	15 mg/L	✗	✗	✗	✗	[161]
BL21 star (DE3)	pET14b	$A\beta_{1-40}$	/	affinity	2xNi-NTA + HPLC	n.d.	✗	✗	✓	✓	[158]
BL21-Codon Plus (DE3)	pGEX-2T	$A\beta_{1-40}$ and $GSIEGRA\beta_{1-42}$	GST	affinity	affinity column + HPLC	7 mg/L	✗	✗	✓	✗	[170]
MG1665	pQE-80L	$A\beta_{1-40}$ $A\beta_{1-42}$	IFABP	IB + affinity	Ni-NTA column + SEC + HPLC	3mg/L	✗	✗	✓	✗	[155]
BL21 (DE3)	pGEX-4T-1	$GSA\beta_{1-42}$	GST	affinity	affinity resin + dessalting column + affinity column	0.54 mg/L	✗	✗	✗	✗	[172]
BL21 DE3 PLysS	pCOLD-TF	$XXXA\beta_{1-42}$	Ubiquitin	soluble fusion protein + affinity	Ni-NTA column	3mg/L	✗	✗	✗	✗	[171]
BL21 (DE3)	pET28a	$GGA\beta_{1-42}$	Ubiquitin	IB + affinity	Ni-NTA column + affinity column + HPLC	4 mg/L	✗	✓	✗	✗	[154]
BL21 star (DE3)	pET15b	$GSHMA\beta_{1-42}$	/	affinity	Ni-NTA column + HPLC	n.d.	✗	✗	✗	✓	[159]
BL21 (DE3)	?	$A\beta_{1-42}$	Poly peptide	IB + affinity	Ni-NTA column + HPLC	19 mg/L	✗	✗	✓	✓	[150]
BL21 (DE3) PLysS	PetSac	$MA\beta_{1-42}$	/	IB	2xDialysis	n.d.	✗	✓	✗	✓	[164]

Chapter III. Elaboration of coordination catalysts

Introduction

Towards the development of new hybrid bioinorganic catalysts, a key element is the elaboration of metal complexes displaying interaction with amyloid fibres.

Inspired by existing amyloid probes, we chose to focus on flat aromatic ligands, expecting an interaction with β-sheet structures. In particular, poly pyridine ligands are of interest, as being widely used in coordination chemistry and catalysis. Several functionalizations were proposed, seeking to increase the non-covalent interactions between complexes and fibres and enabling coupling.

This chapter describes the synthesis of a series of terpyridine ligands and of corresponding Cu(II), Fe(II) and Ru(II) complexes.

In a first part, synthesis of five functionalized terpyridine ligands is described. The different synthetic routes available are introduced, including Kröhnke condensation, which was used in this project.

In a second part, corresponding Cu(II), Fe(II) and Ru(II) complexes were synthesized, and fully characterized by different techniques, including X-rays crystallography, NMR, EPR, MS, UV-Visible and fluorescence spectrophotometry, and cyclic voltammetry.

Resulting metal complexes were subsequently tested for their interaction with amyloid fibres, and for their catalytic properties.

I. Design of ligands

I.1. Requirements for hybrid catalysts elaboration

In the context of this thesis, our aim was to develop coordination catalysts that would incorporate into fibres of amyloid-β peptides. Toward this goal, in addition to good coordination and catalytic properties, designed metal complexes had to display non-covalent interaction with fibres. These three parameters were thus considered for ligand elaboration.

I.1.a. Interaction with fibres

One of the searched property for our ligands was their ability to bind to amyloid fibres. In this view, we sought inspiration among the huge set of probes developed to visualize amyloid fibres [173]. These scaffolds go from very simple to more sophisticated structures. Some examples appear on Scheme 9, showing important structural diversity.

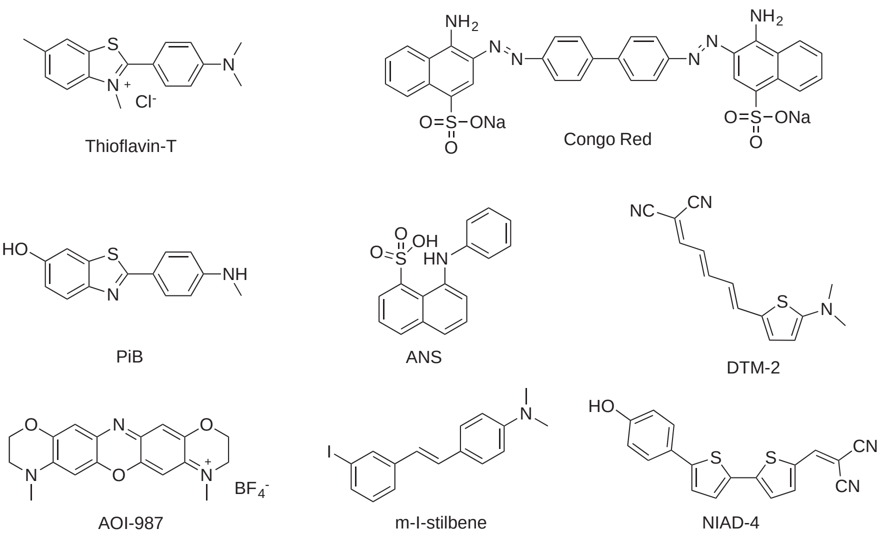

Scheme 9: Variety of probes for amyloid-β fibres.

Considering these structures, it is likely that the non-covalent interaction with fibres consist of π-stacking (due to the numerous aromatic cycles) and H-bonding (due to the presence of H-bonds accepting atoms). These two parameters will thus be considered for our structures.

I.1.b. Metal complex formation

A second desired characteristic of our target was to be able to coordinate different metal ions. Indeed, one of the interests of the proposed hybrid systems is their versatility in terms of potential catalytic reactions. It would be of great interest to incorporate various metal ions within the same ligand, in order to extend the scope of reactivity of the system.

It is well established that monomeric Aβ peptides display good affinity for biologically relevant metal ions [123,129,156]. As an example, apparent association constants of Aβ are *ca.* 10^6 M^{-1} for Zn(II), *ca.* 10^{10} M^{-1} for Cu(II) [137]. To ensure that there will be no competition between designed ligands and peptides to chelate metal ions, we sought for ligands with high metal affinity constants.

I.1.c. Catalysis

Several parameters are important to consider for a catalyst:

- Stability

A first important parameter is complex stability: the complex must be able to operate an important number of catalytic cycles without ligand decoordination or metal precipitation. Also, as the fibres are produced at μM scale, and could limit substrate accessibility, high turnover numbers (TON) are required to develop systems with measurable catalytic activity.

- Catalytic cycle

An important parameter for our scaffolds is that the interaction between fibres and complexes remains constant during the catalytic process. Though, during the catalytic cycle, metal ion is exposed to redox-cycle, and to substrate coordination/decoordination. It would thus be preferable to consider fibre-complex interaction would be promoted by ligands, whose geometry is unchanged along the catalytic cycle and remote of the metal centre.

- Substrate accessibility

When incorporating complexes into fibres, it is important to ensure that the catalytic site remains available to substrates. We thus chose hemilabile ligands, in order to allow substrate coordination.

- Water compatibility

In the context of development of green catalysts, we are interested in running catalytic reactions in aqueous environment. Metal complexes should thus be stable in presence of water. Because fibres constitute a hydrophobic environment, complexes and substrates should not necessarily be hydrosoluble. Yet, reaction intermediate should not be air or moisture sensitive.

I.2. Targeted structures

Considering all these requirements, three types of ligands were selected: terpyridine, bipyridine, and its constrained analogue phenanthroline, and salophen (Scheme 10). All of them have been extensively described, for diverse applications including supramolecular chemistry [174], material sciences [175,176], sensor development [177,178], or catalysis [179–181]. Their strength resides in their perfectly defined coordination geometry, and in their extended π-conjugation which confers unique electronic and photophysical properties [180,182,183].

Metal complexes of these ligands display very different geometries: M(**tpy**)$_2$ is forming two perpendicular planes, whereas M(**bpy**)$_3$ and M(**phen**)$_3$ are rather spherical, and M(**salophen**) is planar. These differences might result in different interaction with amyloid fibres.

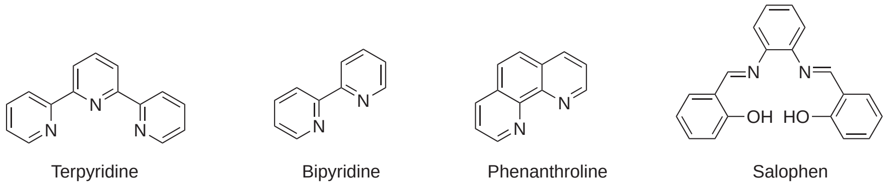

Scheme 10: Ligands selected for this study.

Bipyridine, phenanthroline and salophen are commercially available, and were used to form the corresponding metal complexes. In addition to commercial terpyridine, we decided to design functionalized terpyridines to increase the available aromatic region and enable the study of the effect of functional groups variations on fibre-complex interaction to be studied.

I.3. State of art on terpyridine ligands

I.3.a. Advantages of terpyridine

Based on these requirements, we considered the synthesis of terpyridine ligands. Firstly, to take advantage of their relatively straigthforward synthesis and functionalization (see I.3.b). They can also form complexes with several metal ions, including Fe, Ru, Os, Cu, Mn, Co, Ni [184,185] with binding constant above 10^8 M^{-1} in ACN [186] and are very stable, as examplified by the reported dissociation rate of 10^{-7} s^{-1} for Fe(**tpy**)$_2$ in water [187]. For these reasons, they have been reported for numerous catalytic applications [188,180,189]. Different examples of artificial metalloenzymes using terpyridine metal complexes have even been reported in literature [51,60,190] (see Chapter I).

I.3.b. Synthetic routes for terpyridine

- Kröhnke condensation

Kröhnke synthesis of terpyridine occurs between α-pyridinium methyl ketone and pyridinyl prop-2-enone in the presence of ammonium acetate [191]. The reaction starts with an enolization, followed by a Michael addition. Addition of ammonium acetate on the ketone followed by cyclisation affords the terpyridine. Scheme 12 depicts the reaction mechanism as proposed in literature [192]. This reaction presents a good atom economy, the only by-products of this reaction being pyridine and acetic acid. The resulting terpyridine can be substituted on the lateral pyridine and in *para* position of the central one [193,194].

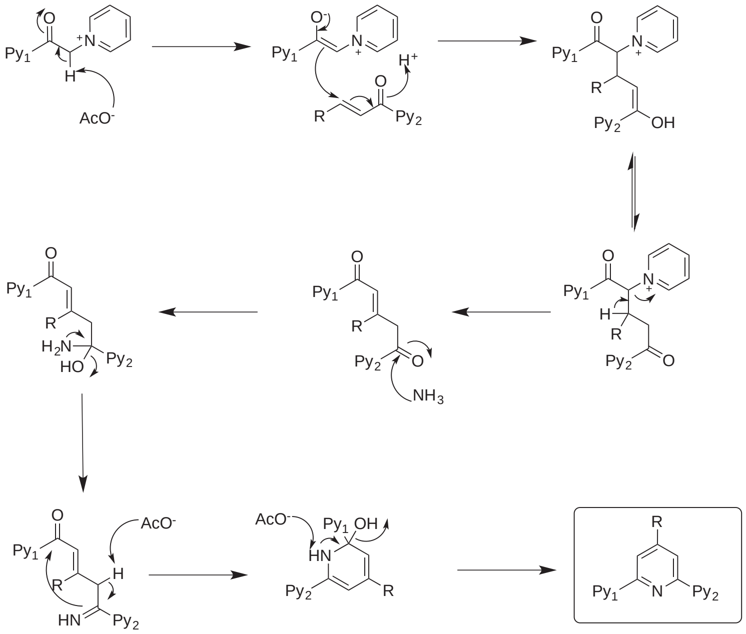

***Scheme 12: Reaction mechanism of Kröhnke terpyridine synthesis.** Reaction occurs in methanol in presence of NH_4OAc in excess, heating to reflux for 6h. Py stands for pyridine.*

A reaction based on a similar mechanism consists in starting with 2,6-diacetylpyridine. Upon reaction with I_2 and pyridine, a bis(pyridinium) iodide is formed, which undergoes condensation with α,β-unsaturated aldehyde (Scheme 11). This yields terpyridine substitutable in positions 4,4’’ and 5,5’’ [195].

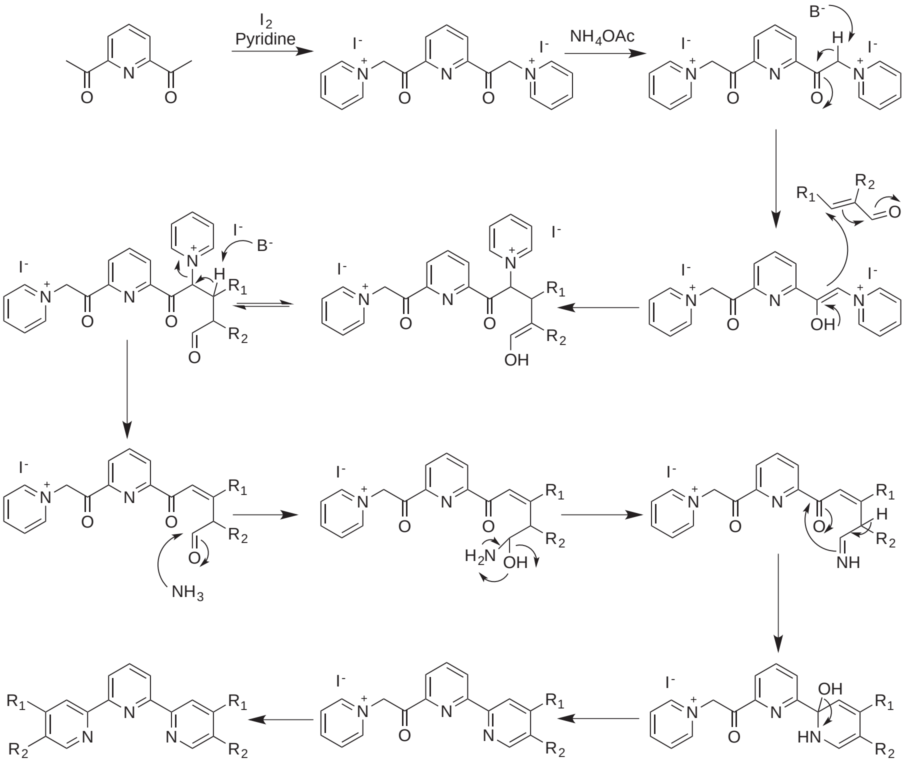

***Scheme 11: Proposed mechanism for terpyridine synthesis starting from 2,6-diacetylpyridine.** B stands for base, which can be either ammonia or acetate.*

- Condensation of 1,5-diketones

A different strategy consists in the condensation of 1,5-diketones with ammonium acetate, cyclizing the central pyridine ring. The resulting terpyridine can be substituted in 4’ position (Scheme 13) [196].

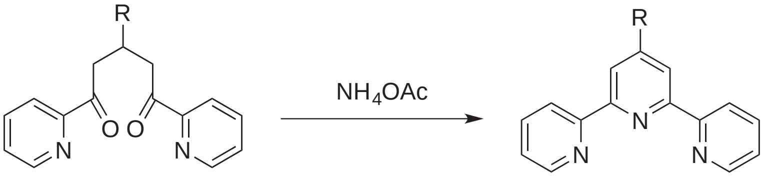

Scheme 13: Terpyridine synthesis by 1,5-diketone condensation.

- α-oxoketene dithioacetal method

An alternative procedure relies on the condensation of 2-acetylpyridine enolate with α-oxoketene dithioacetal in presence of ammonium acetate (Scheme 14). Further reaction on the thiomethyl group enables the functionalization in position 4’. Terpyridines can also be substituted in an asymmetric manner, by starting with the suitably substituted enolate [197].

The mechanism of this reaction involves a Michael addition, followed by the release of a thiomethyl group. Nucleophilic attack by ammonia followed by cyclization afford the 4’ thiomethyl terpyridine (Scheme 14). Thiomethyl group can subsequently react to give a variety of derivatives.

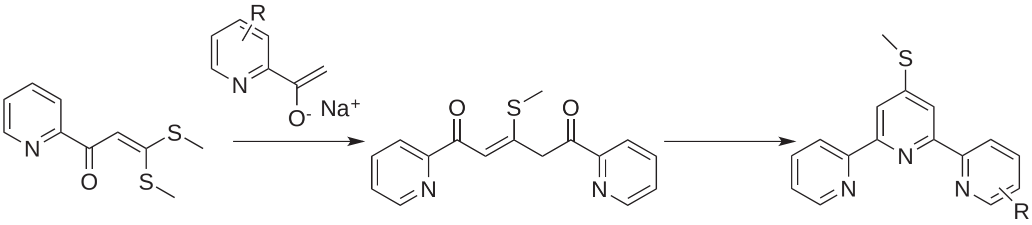

Scheme 14: Terpyridine synthesis by α-oxoketene dithioacetal method. R, R’ = H, alkyl, vinyl.

- Jameson method

A very similar strategy consists in starting with (dimethylamino)enone instead of dithioacetal. Here again, ammonium acetate plays both the role of base and nucleophile. The mechanism involved is also similar, the most significant difference being the difference between the leaving groups (Scheme 15).

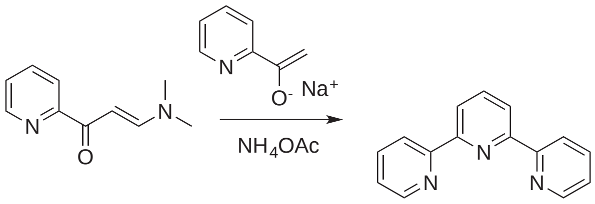

Scheme 15: Jameson method for terpyridine synthesis.

- Cross-coupling strategies

A more modern strategy consists in performing cross-coupling reactions to obtain symmetric terpyridines. As such, Stille coupling was often used, either using dihalogenated central pyridine with tin-substituted lateral pyridine [198], or in the other way round [199] (Scheme 16.1). Suzuki-Miyaura cross-coupling was also proposed, here again the halogen atom and the borate group can be held by one partner or the other [193] (Scheme 16.2).

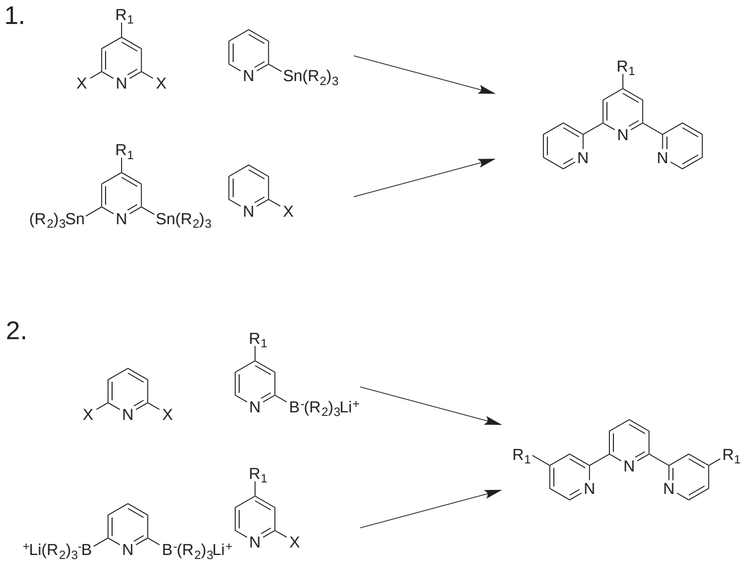

Scheme 16: Synthetic routes for terpyridines by cross-coupling strategy. 1: *Stille coupling.* **2:** *Suzuki-Miyaura coupling.*

Cross-couplings present the advantage of being very specific while allowing various substitutions of the two partners. However, terpyridines being very chelating ligands, formation of metal complexes is difficult to avoid, and purification can become tricky.

Cross-couplings are catalysed by Pd(0), which is often formed *in situ* from Pd(II) precursor. A first step consists in the oxidative addition of the aryl halide on Pd(0), forming a Pd(II) adduct. Transmetallation with an organometallic compound provides the bi-aryl adduct, that is released through a reductive elimination step, while Pd(0) is regenerated (Scheme 17).

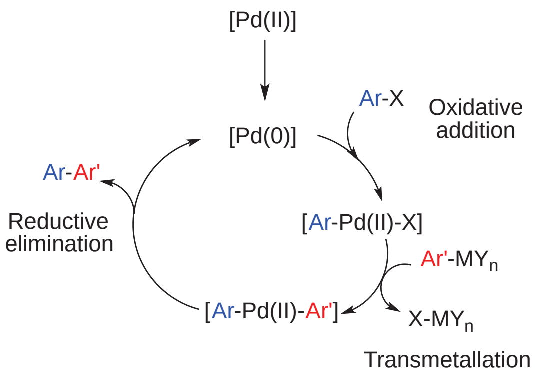

Scheme 17: Schematic catalytic cycle of cross-coupling reactions. *Ar stands for Aryl, X is a halogen, M is a metal, and Y is a ligand.*

I.3.c. Targeted structures

In the frame of this project, we chose to functionalize terpyridine with a phenyl ring in position 4’, further increasing the aromatic surface available for interaction (Scheme 18). The phenyl ring was functionalized in position 10 with different groups. First of all, this enables a preliminary screen for interacting moieties. This also allows the conjugation of various functional groups, such as interacalating moieties or probes. A covalent grafting to peptides could also be envisaged in future studies.

Our synthetic efforts thus focused on developing a series of *p*-functionalized 4-phenyl-2,2’ :6’,2’’-terpyridine ligands (Scheme 18).

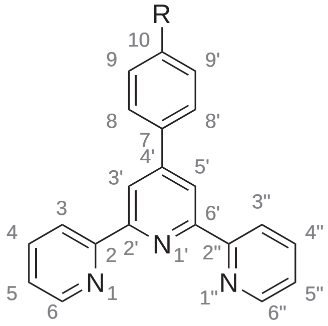

Scheme 18: Targeted ligands with corresponding numbering scheme.

I.4. Results

I.4.a. Experimental procedure

A one-pot procedure for the Kröhnke condensation was performed between an aldehyde bearing the desired substituent with two molecules of acetylpyridine in presence of potassium hydroxide in a mixture of ethanol and ammonia [194]. The solution was refluxed overnight, leading to a white precipitate, which was collected by filtration. When observed, residual impurities were removed by simple recrystallization in ethanol.

Interestingly, the substituent seems to have an effect on the reaction yield. As such, nitrophenyl and phenol did not lead to the desired product, whereas other aryl groups did react, according to our expectations.

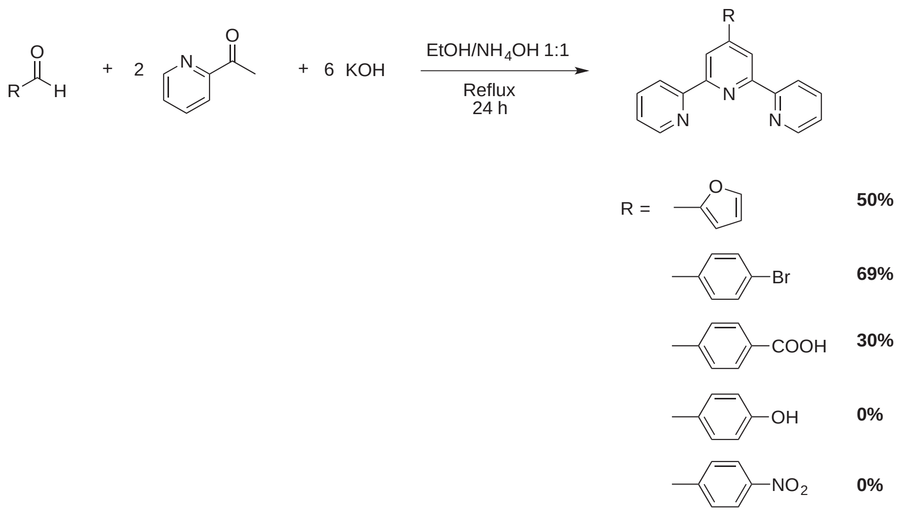

Scheme 19: Direct synthesis of p-substituted phenyl terpyridine derivatives.

In the case of nitrophenyl, this was solved by synthesizing separately the enone and the pyridinium salt [200]. The condensation was then achieved in pyridine in presence of ammonium acetate, heating overnight to reflux (Scheme 20).

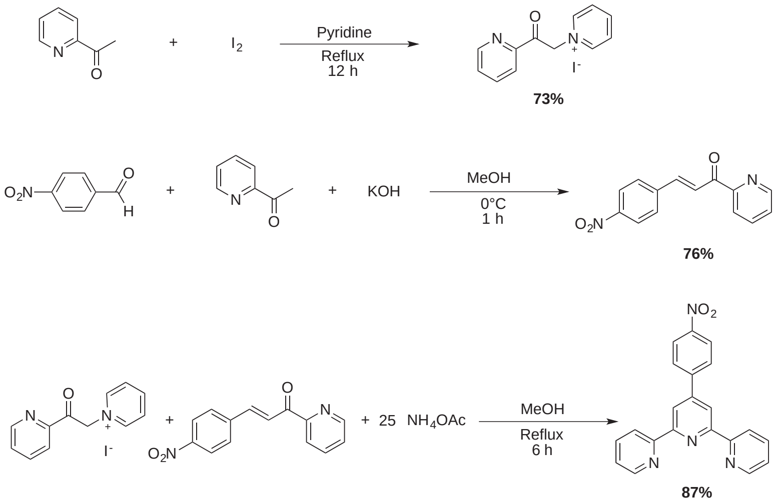

Scheme 20: Stepwise synthesis of p-nitrophenyl terpyridine.

p-nitrophenyl terpyridine can then be reduced to form *p*-aminophenyl terpyridine. A first possibility is the reduction of the nitro group with hydrazine in the presence of Pd/C. The desired amino ligand is obtained upon 3 h reflux in ethanol [198] (Scheme 21.A).

Another approach is a reduction by tin chloride under acidic conditions (Scheme 21.B). Both strategies are similar, affording *p*-aminophenyl terpyridine in good yields within a few hours, and in both cases, metal salts are removed by filtration on Celite.

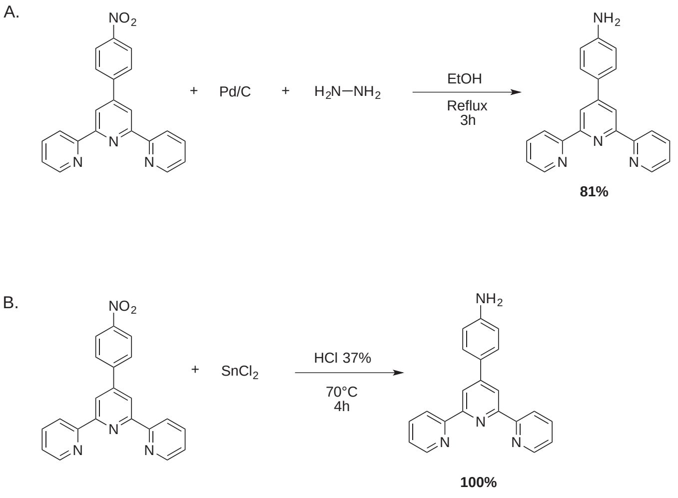

Scheme 21: Two possible synthetic routes for p-aminophenyl terpyridine.

Finally, 4’-furyl terpyridine can be oxidized by potassium permanganate under basic conditions, forming 4’-carboxylic acid terpyridine (Scheme 22) [201]. Here again, the product is recovered by simple filtration.

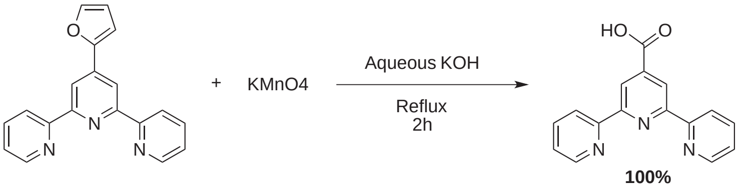

Scheme 22: Synthesis of 4’-carboxylic acid terpyridine.

I.4.b. Products obtained

A series of six terpyridine ligands was obtained from this strategy (Scheme 23). All these compounds were fully characterized by NMR, IR, and MS, to ensure of their nature and purity (see Experimental procedures). The different functional groups could induce variable interaction with fibres. In particular, $\mathbf{L}^2$ and $\mathbf{L}^6$ have pKa around 4, and will be under carboxylate form at physiological pH. $\mathbf{L}^1$ might form H-bonds with peptides, whereas $\mathbf{L}^3$ could interact *via* polar interaction. Different binding behaviour can thus be expected from these ligands.

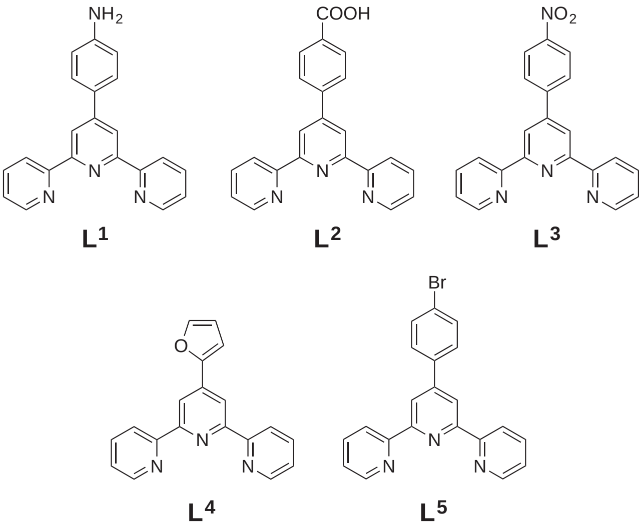

Scheme 23: Summary of available terpyridine ligands.

I.4.c. ^{1}H NMR preliminary assessment of electronic properties

A first determination of the electronic effect of the different substituents was achieved by comparing the chemical shifts of terpyridine protons. Variability in chemical shifts would attest of an important inductive or mesomeric effect.

To determine the extent of the electronic effect of the functional group three sets of protons were chosen: H9,9’, which are the closest from the substituting group, H3’,5’, to see the effect on the central pyridine, and H6,6’’ which are directly linked to the coordinating N. The chemical shifts appear in Figure 26.A. It appears that the influence of the functional group is limited to the phenyl ring. Indeed, protons 9,9’ display important variations, but chemical shifts of protons 3’,5’ and 6,6’’ remain unchanged. Expectedly, the variations of chemical shift can be directly correlated to the electro-withdrawing character of the substituents (Figure 26.C). As such, among the ligands holding a phenyl group, nitro group induces the most important deshielding, followed by the carboxylate and the bromide.

A

Ligand	H3'+5'	H9+9'	H6+6’’
L^1	8.62	8.5	8.75
L^2	8.74	8.04	8.78
L^{3*}	8.76	8.37	8.74
L^4	8.71	/	8.78
L^5	8.71	8.50	8.73
L^6	8.79	/	8.72
tpy*	8.62	/	8.71
Average	8.71 ± 0.08	8.35 ± 0.31	8.74 ± 0.03

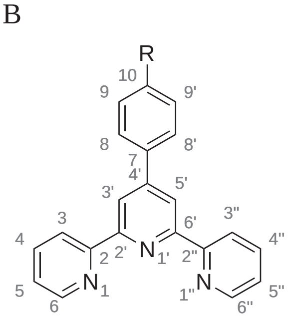

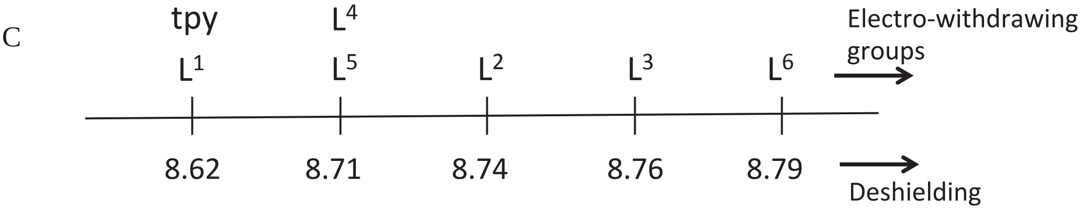

Figure 26: Variations of ^{1}H NMR chemical shifts of phenyl-substituted terpyridines. A: *Chemical shifts obtained for the ligands. All spectra were recorded in DMSO-d_6, except those noted * which were recorded in CDCl$_3$.* ***B:*** *Numbering scheme for phenyl-substituted terpyridine.* ***C:*** *Classification of ligands as a function of the deshielding due to their functional groups.*

II. Synthesis of metal complexes

II.1. Copper (II) complexes

II.1.a. Synthesis

The synthesis of CuL_2 complexes is straightforward, consisting in a reaction between Cu(II) nitrate and two equivalents of terpyridine. Dropwise addition of a Cu(II) solution to a ligand solution causes an immediate change in colour. The metal complex is then isolated by precipitation, thanks to an ion exchange between nitrate and hexafluorophosphate (Scheme 24).

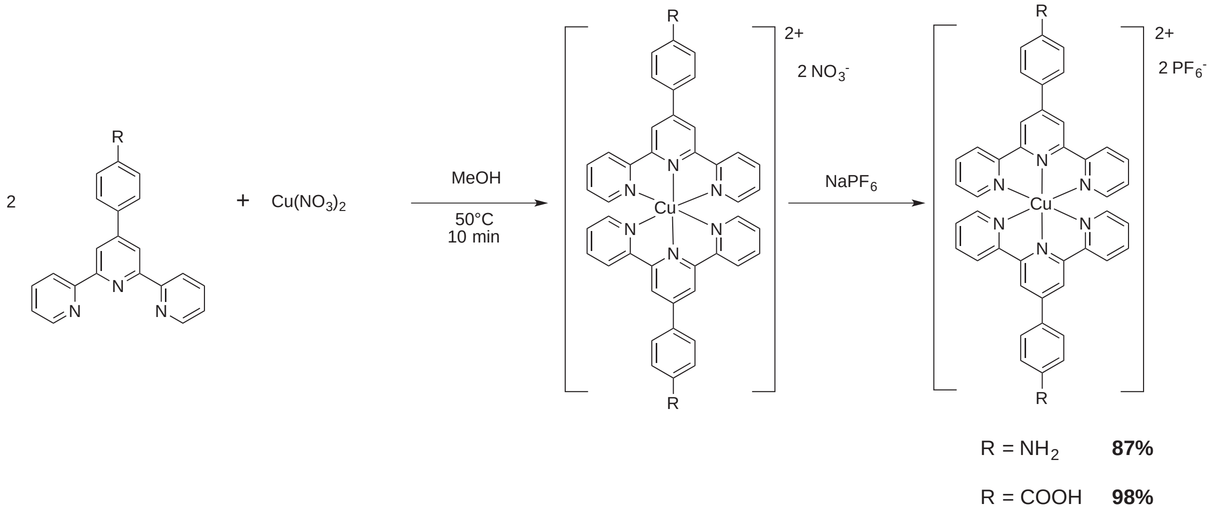

Scheme 24: Synthesis of $CuL_2(PF_6)_2$ complexes.

Cu(**bpy**)$_3$ and Cu(**salophen**) were synthesized following the same protocol with 47% and 88% yields, respectively. Cu(**salophen**) being neutral, the anion exchange step was not required to induce complex precipitation.

II.1.b. X-ray structures

- $Cu(L^1)_2(PF_6)_2$

Crystals were obtained for Cu($\mathbf{L^1}$)$_2$(PF_6)$_2$ by slow diffusion of diethyl ether in ACN. The structure shows the two terpyridine in nearly perpendicular planes centred on the Cu(II) (angle N1-Cu-N4 *ca.* 91.6 degrees). Cu-N distances are shorter for central pyridines (*ca* 1.97 Å) than for the lateral ones (2.17 Å). The phenyl rings show a torsion angle with central pyridine rings, respectively of 17.98 and 35.77 degrees.

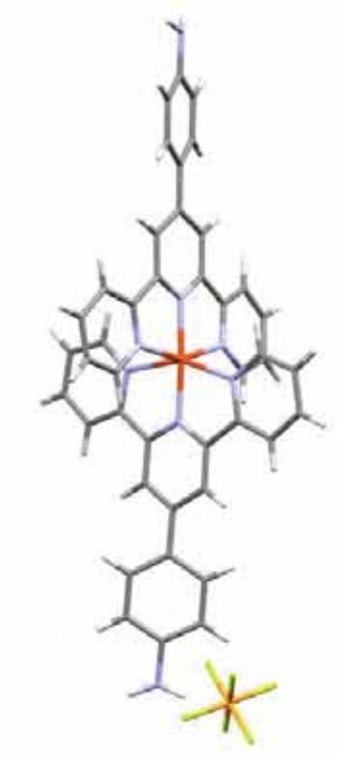

Figure 27: Crystal structure obtained for Cu(L^1)$_2$(PF_6)$_2$.

- Cu(salophen)

Crystals of Cu(**salophen**) were obtained by slow evaporation of ACN. The X-ray structure shows a primitive motif constituted of two parallel complexes. Complex is almost planar (angles O1-Cu-N2 and O2-Cu-N1 *ca*. 176 degrees), with Cu(II) in a square planar geometry (angles N1-Cu-O1 and N2-Cu-O2 *ca*. 94.4 degrees).

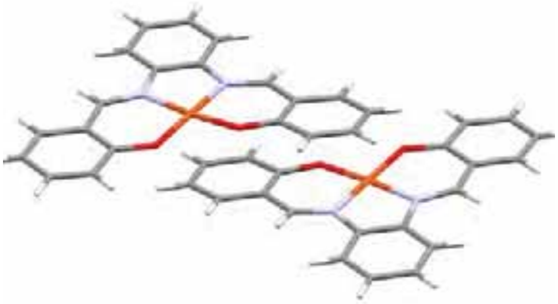

Figure 28: Crystal structure obtained for Cu(salophen).

II.1.c. EPR

Cu($\mathbf{L^1}$)$_2$ was submitted to X-band Electronic Paramagnetic Resonance (EPR) measurements. As reported for many hexacoordinate Cu(II) complexes, Cu($\mathbf{L^1}$)$_2$ displays a Jahn-Teller distortion [202]. In Cu($\mathbf{L^1}$)$_2$, this results in an axial elongation of the complex in solution. Unexpectedly, EPR spectrum of this complex is made of two components, whose contributions are shown to vary with temperature (Figure 29.A) [203]. Component **a**, predominant at low temperature, displays a signature consistent with an elongated D_{4h} symmetry, whereas component **b**, observed at higher temperature, seems to display a rhombic symmetry. Considering this, we have hypothesized an equilibrium between two distinct Jahn-Teller axially-elongated forms of the complex, as depicted on Figure 29.B. Parameters were calculated for component **a** as $g_{//} = 2.24$ and $A_{//} = 164\ e^{-4}\ cm^{-1}$.

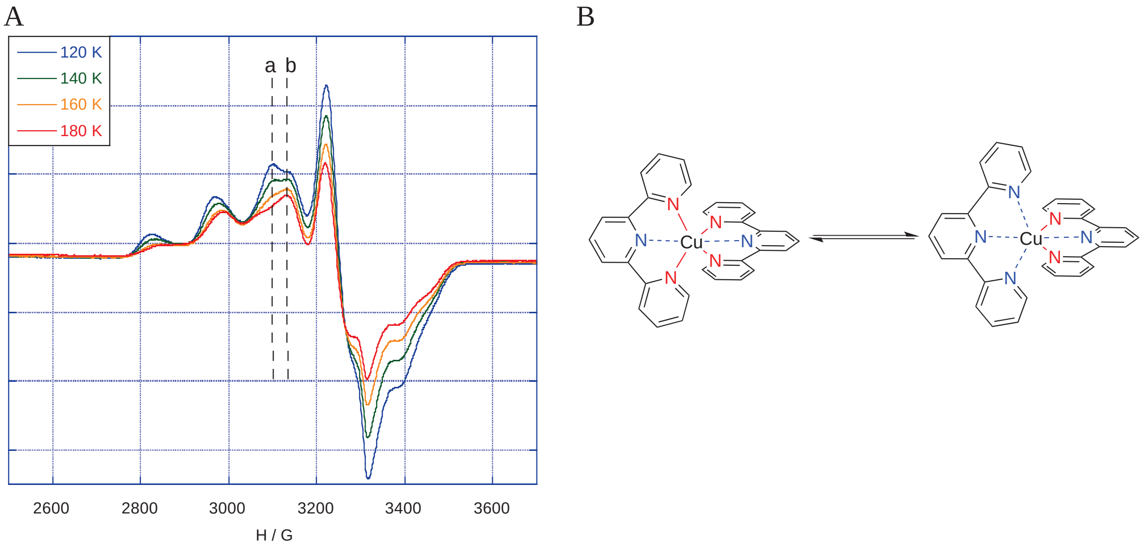

Figure 29: Jahn-Teller dynamic effect observed for Cu($\mathbf{L^1}$)$_2$ complex. A: *X-band EPR spectra (ν ca. 9.5 MHz) obtained for Cu($\mathbf{L^1}$)$_2$ in ACN at variable temperatures.* ***B:*** *Proposed equilibrium in Cu($\mathbf{L^1}$)$_2$. Atoms in red are close to Cu(II), atoms in blue are more distant.*

II.1.d. UV-Visible

UV-Vis spectra were recorded for the different complexes in ACN, showing different signatures: Cu($\mathbf{L^1}$)$_2$ and Cu(**salophen**) display intense bands in the visible region, whereas Cu($\mathbf{L^2}$)$_2$ and Cu(**bpy**)$_3$ absorb farther in the UV region.

Table 2: Absorption wavelengths and corresponding molar extinction coefficients of Cu(II) complexes in ACN. **: spectra recorded in H_2O.*

Complex	**λ_{max} (nm)**	**ε (L/mol/cm)**
Cu(**bpy**)$_3$	299	48,260

Cu(**L**^{1})$_2$	397	8,454
Cu(**L**^{2})$_2$*	334	11,200
Cu(**salophen**)	420	14,340

UV-Vis was also used to determine pH stability of terpyridine complexes. Acidification of a Cu(**L**^{1})$_2$ solution leads to a decrease of its UV band, presumably corresponding to a protonation of the amine group on terpyridines. This is consistent with the reported pKa of aniline *ca.* 4.6 [204]. Even at pH 2.2, the signature remains different from free ligand in acidic conditions, attesting that the complex is not degraded (Figure 30).

From these data, it is thus possible to work with Cu(II) bis terpyridine complexes in acidic conditions, which would be of interest for catalytic experiments.

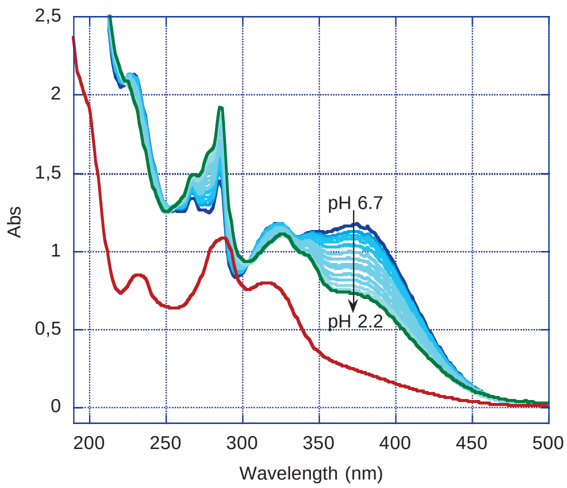

Figure 30: Decomposition of Cu(L^1)$_2$ in acidic conditions. *Red: free L^1 at pH ca. 2, blue: Cu(L^1)$_2$.**Conditions:** [Cu(L^1)$_2$] = 50 µM in H$_2$O + 10% ACN.*

II.1.e. Electrochemical characterization

To get a preliminary idea on the redox behaviour of our complexes, cyclic voltammetry measurements were run on Cu(**L**^{1})$_2$. In reduction, a quasi-reversible wave at -0.052 V *vs.* NHE is observed (ΔE^p = 89 mV), corresponding to the reduction of Cu(II) into Cu(I) (Figure 31, red curve). When scanning at much lower potential, irreversible peaks are observed, corresponding to the reduction of ligand aromatic rings. An intense peak is also observed on the reverse scan, corresponding to the deposition of Cu(0) onto the surface of the electrode (Figure 31, blue curve). In oxidation, an irreversible wave is observed, possibly corresponding to the oxidation of the amine groups (Figure 31, green curve).

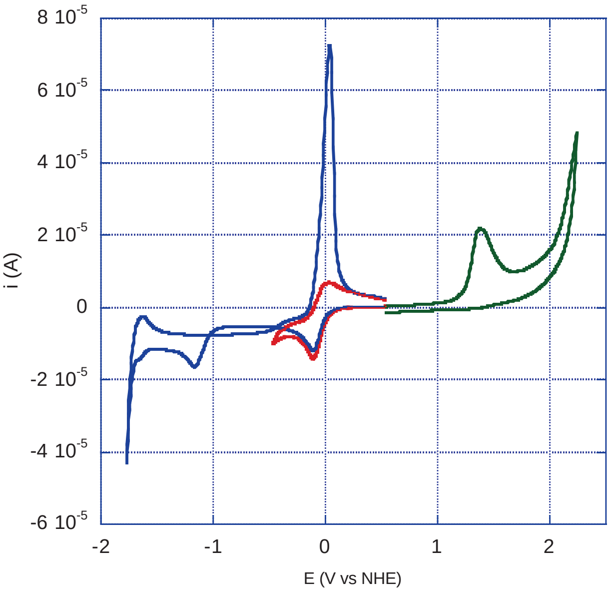

Figure 31: Cyclic voltamogrammes obtained for Cu(L^1)$_2$. Conditions: *[Cu(L^1)$_2$] = 1 mM, [TBAPF$_6$] = 0.1 mM in ACN, scan rate = 0.1 V/s, argon atmosphere. WE: glassy C, CE: Pt, RE: SCE.*

This study confirms that Cu(L^1)$_2$ is able to switch from Cu(II) to Cu(I) without important reorganisation of the coordination sphere.

II.1.f. Study of solution equilibriums

Working with [Cu($\mathbf{L}^1$)$_2$]$^{2+}$ complex, it seemed important to investigate the possible coordination/decoordination equilibriums in solution.

We started this study by completing a UV-Vis titration: Starting from a 50 μM solution of $\mathbf{L}^1$ in ACN, increasing amounts of $CuSO_4$ were added. This results in the apparition of a band at 397 nm, which increases in a linear manner until 1 eq Cu(II) (Figure 32). Changes are also observed in the 250-350 nm region, with an isobestic point *ca*. 350 nm.

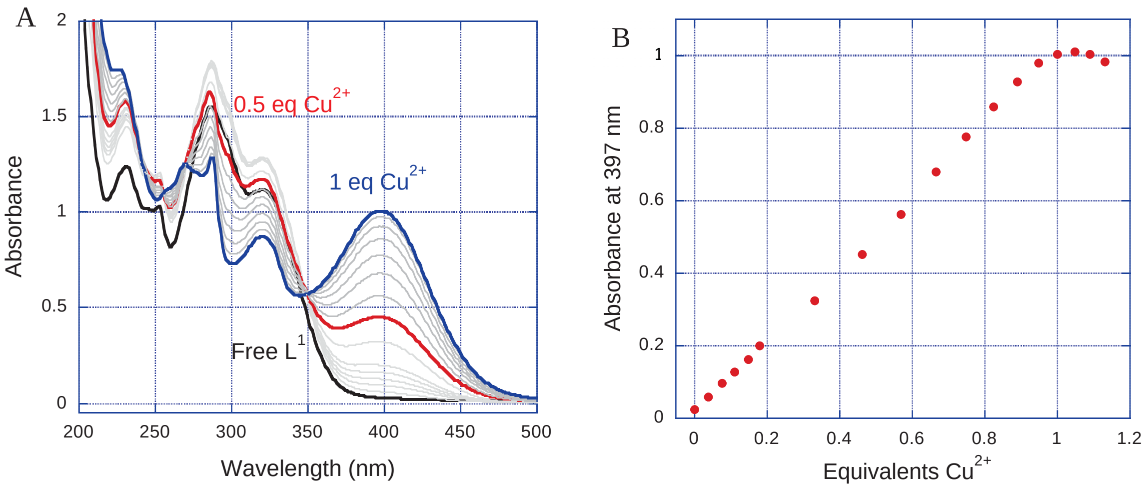

Figure 32: UV-Vis study of Cu(L^1)$_2$ formation in solution. A: *UV-Vis spectra obtained upon addition of $CuNO_3$ in a 50 μM solution of L^1 in ACN.* ***B:*** *Titration curve monitored at 397 nm.*

This titration does not allow to distinguish $[Cu(\mathbf{L^1})_2]^{2+}$ and $[Cu(\mathbf{L^1})]^{2+}$ from their UV-Vis signatures: a single MLCT band at 397 nm is observed for all Cu(II) equivalents. One hypothesis would be that CuL_2 is formed at substoichiometric ratios, that is then converted into CuL when above 0.5 eq Cu(II). In this case, CuL_2 and CuL would have similar molar absorption coefficients, considering the titration curve obtained. Another possibility would be that only CuL is formed in solution, if the addition of a second ligand on Cu(II) is not favourable.

To address this question, similar investigations were conducted in parallel by CV and solution EPR. To a 1 mM solution of $\mathbf{L^1}$ in ACN were added increasing amounts of $CuNO_3$. For each point, cyclic voltamogram was recorded (Figure 33.A), and solution was immediately sampled and shock-frozen to be submitted to EPR measurement (Figure 33.B).

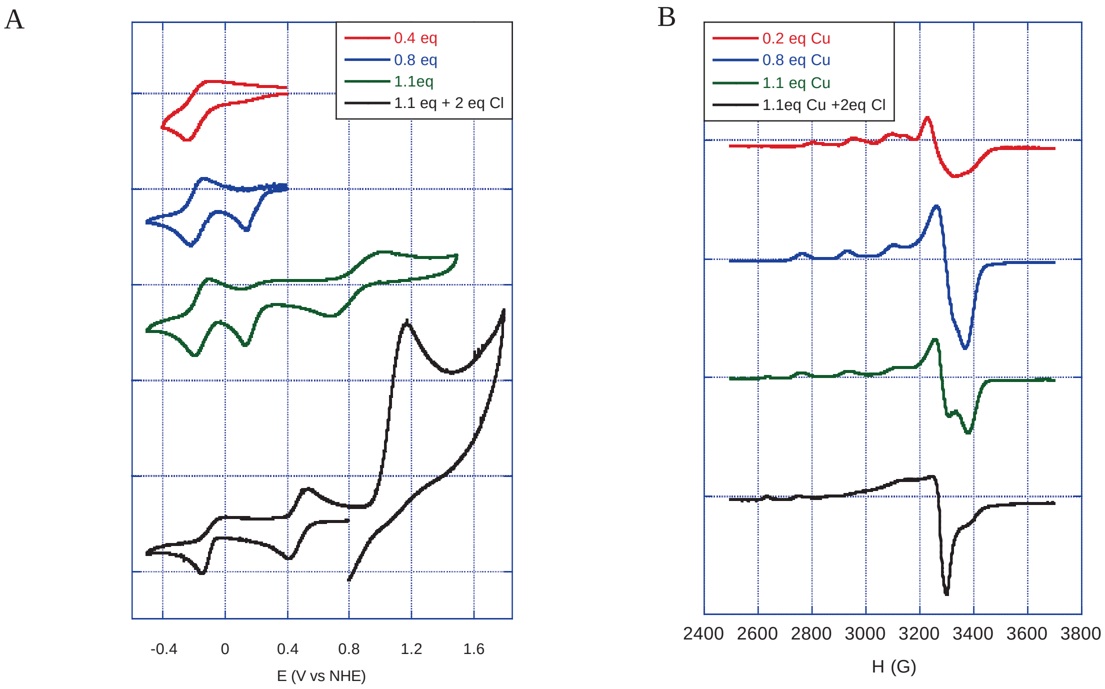

Figure 33: Formation of CuL complexes in solution. A. *Cyclic voltammogrammes of* $\mathbf{L^1}$ *upon addition of various equivalents of* $Cu(NO_3)_2$ *in ACN.* ***Conditions:*** $[L^1]$ *= 1 mM,* $[TBAPF_6]$ *= 0.1 mM, scan rate = 0.1 V/s, argon atmosphere. WE: glassy C, CE: Pt, RE: SCE.* ***B.*** *Species observed and corresponding reduction potentials.*

In sub-stoichiometric amounts of Cu(II) (red curves), a single specie is observed, which displays a splitting of signals due to a dynamic Jahn-Teller effect (see II.1.e). This specie is likely to be $[Cu(\mathbf{L^1})]^{2+}$.

For 0.8 eq of Cu(II) (blue curves), CV shows a peak *ca.* 0.15 V *vs.* NHE, and the previously observed reversible wave *ca.* -0.2 V *vs.* NHE. However, EPR spectrum attests of the presence of a single specie, different from $[Cu(\mathbf{L^1})]^{2+}$, likely $[Cu(\mathbf{L^1})]^{2+}$. We propose that this specie is irreversibly reduced at the electrode into $[Cu(\mathbf{L^1})]^{+}$. But since coordination with a planar tridentate ligand is not favourable for Cu(I), we hypothesize that $[Cu(\mathbf{L^1})]^{+}$ releases its ligand in solution. This ligand immediately coordinates to $[Cu(\mathbf{L^1})]^{2+}$, forming $[Cu(\mathbf{L^1})_2]^{2+}$. This last specie is then reduced, as attested by the reversible wave. According to this, $[Cu(\mathbf{L^1})_2]^{2+}$ would not be present in solution, but would be formed *in situ* following $[Cu(\mathbf{L^1})]^{2+}$ reduction.

Similar behaviour is observed at 1.1 eq of Cu(II) (green curves), with an extra reversible wave attributed to free Cu(II) *ca.* 0.8 V *vs.* NHE.

Finally, addition of chloride ions in solution results in a shift of the different waves at lower potential (black curves).

This parallel EPR/CV study confirms the successive formation of $[Cu(\mathbf{L^1})_2]^{2+}$ and $[Cu(\mathbf{L^1})]^{2+}$ in solution in the case of the titration of a ligand solution with Cu(II). Both species seem stable enough to be observed in solution, and a precise control of stoichiometry should enable to control the nature of species in solution. Importantly, when comparing these results with the ones obtained with solid $[Cu(\mathbf{L^1})_2](PF_6)_2$ dissolved in ACN (see II.1.e), it appears that the only specie detected from the powder is $[Cu(\mathbf{L^1})_2]^{2+}$. No partial decoordination is observed for this compound in ACN solution.

II.2. Iron (II) complexes

II.2.a. Synthesis

The synthesis of iron complexes is straightforward, consisting in a reaction between Fe(III) nitrate and the suitable stoichiometry of ligands. Ethanol plays a dual role, serving both as solvent and as reducing agent for Fe(III) [174]. The resulting complexes are formed within 1 h, and are soluble in ethanol. Upon anion exchange between NO_3^- and PF_6^-, the formation of a purple precipitate in ethanol is observed, while traces of ligands and salts remain in solution. Resulting Fe(II) complexes are soluble in ACN at the mM range.

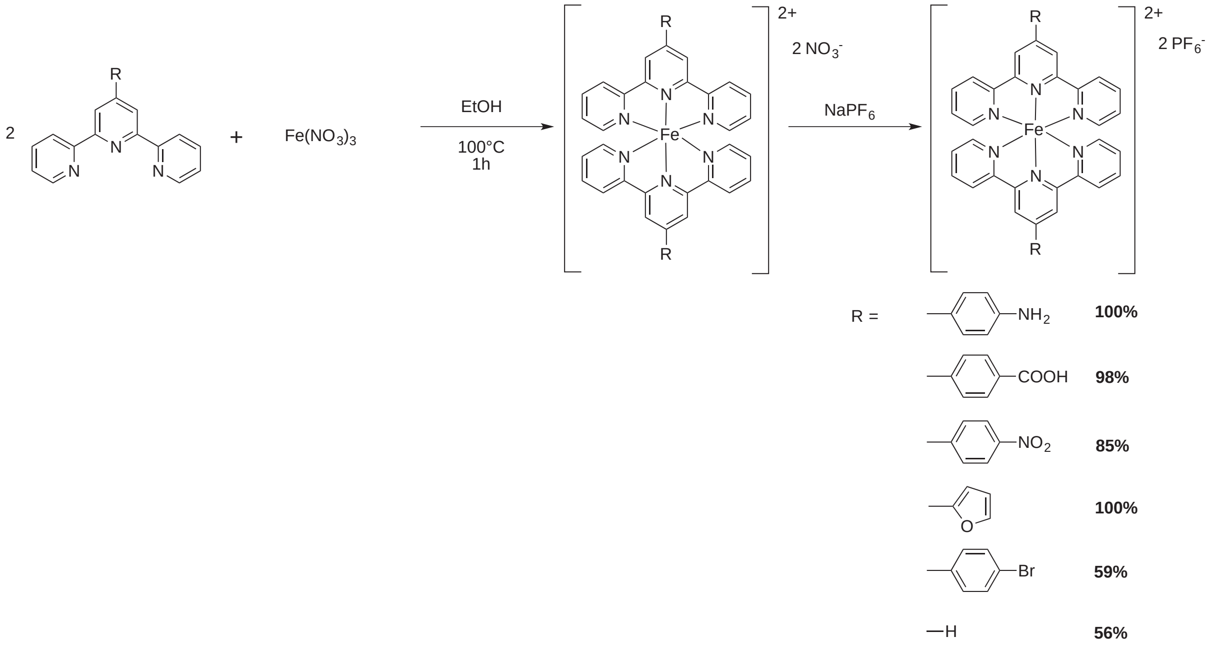

Scheme 25: Synthesis of $FeL_2(PF_6)_2$ complexes.

II.2.b. X-ray structures

Slow diffusion of diethyl ether into an ACN solution of Fe(**L**^{1})$_2$(PF$_6$)$_2$ yielded crystals suitable for X-ray diffraction. The resulting structure is close to the one obtained for Cu(**L**^{1})$_2$(PF$_6$)$_2$, the two terpyridine ligands being in perpendicular planes (angle N1-Fe-N5 of 75.91 degrees). Here again, distances between Fe(II) and central pyridine is shorter than for lateral pyridines (1.89 *vs.* 1.98 Å). Phenyl rings also display a small rotation from the central pyridine (dihedral angles of 16.53 and 37.67 degrees, respectively).

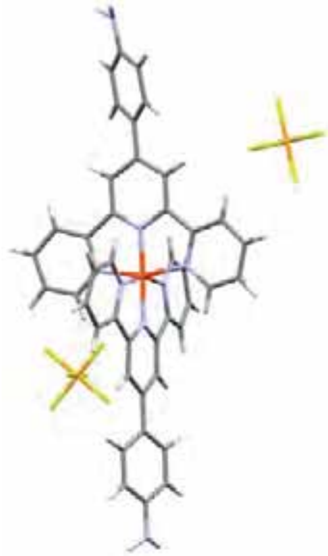

Figure 34: Crystal structure obtained for Fe(L^1)$_2$(PF$_6$)$_2$.

II.2.c. NMR

Fe(II) terpyridine complexes being diamagnetic (configuration 4s^0 3d^6 low-spin), ^{1}H NMR spectra of the complexes were recorded. Figure 35 shows the ^{1}H NMR spectra of **L**^{1} and Fe(**L**^{1})$_2$. It

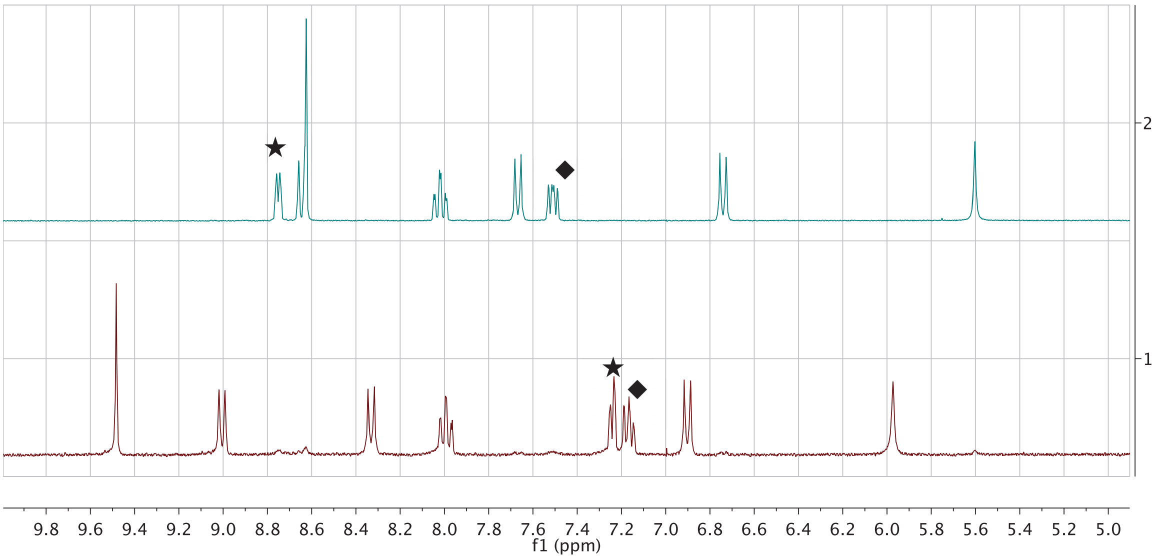

Figure 35: Modifications of ^{1}H NMR upon complexation of Fe(II) by L^1. *Green: L^1, Red: Fe(L^1)$_2$. Spectra were recorded on 300 MHz NMR in DMSO-d$_6$.*

appears that Fe(II) complexation results in a global deshielding of the NMR signals of terpyridine protons. The only exception are protons 6+6’’ (noted ★) and protons 5+5’’ (noted ◆) which undergo a shielding. This effect is likely due to the fact that these protons are situated in the anisotropy cone of the central pyridine of the facing ligand.

II.2.d. UV-Visible

UV-Vis spectra of Fe(II) bis-terpyridine complexes display several ligand-centred π→π* and n→π* transitions in the UV region, as well as a metal-to-ligand charge-transfer (MLCT) *ca.* 550-580 nm [205]. The corresponding bpy and phen complexes display MLCT bands at slightly higher energy (*ca* 510 nm) and ligand-centered transitions much more intense than for Fe(tpy)$_2$ complexes (Figure 36, red).

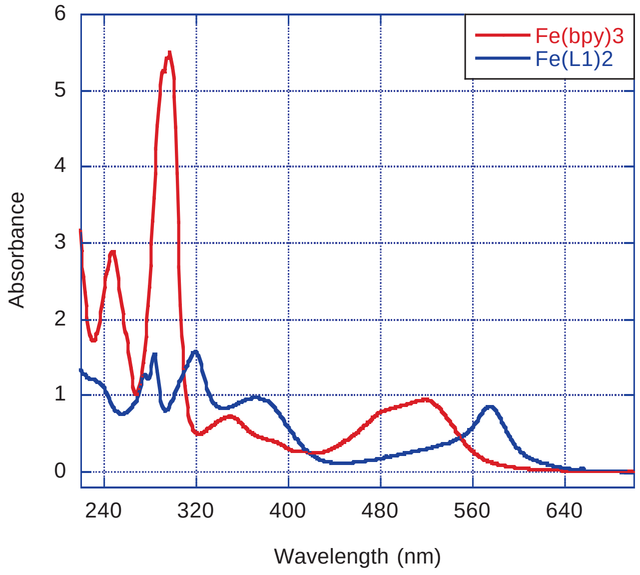

Figure 36: UV-Visible spectra of Fe(bpy)$_3$ (red) and Fe(L^1)$_2$ (blue).

Table 3 shows absorption wavelengths and molar extinction coefficients of the different Fe(II) complexes synthesized. These complexes were tested in fluorescence, but did not display any emissive properties.

Table 3: MLCT absorption wavelength and corresponding molar coefficient extinction of Fe(II) complexes in ACN.

Complex	**λ_{max} (nm)**	**ε (L/mol/cm)**
Fe(**bpy**)$_3$	520	9,400
Fe(**phen**)$_3$	509	9,820
Fe(**tpy**)$_2$	551	7,620
Fe(**L^1**)$_2$	576	32,700

Fe(**L**^{2})$_2$	568	24,400
Fe(**L**^{3})$_2$	574	34,700
Fe(**L**^{4})$_2$	576	32,000
Fe(**L**^{5})$_2$	567	21,830

II.3. Ruthenium (II) complexes

Ru(II) polypyridine complexes are reported in literature for their unique chemical, photophysical and electrochemical properties. In chemistry, their applications go from dye-sensitized solar cells [180], electron transfer [206] to catalysis [207]. Their biological applications cover anticancer therapy, DNA binding or imaging [208]. Interesting examples show the use of Ru complexes to monitor AD-related aggregation of tau protein [209] and to recognize insulin fibrils [210]. We thus got interested in Ru(II) polypyridine complexes, both for their use as probes to investigate their intercalation in amyloid fibres, and for their potential catalytic applications.

II.3.a. Synthesis

As for Fe(II), Ru(II) complexes were synthesized starting from Ru(III), reduction being promoted by EtOH. Upon 1 h reflux, the desired [RuL$_2$]Cl$_2$ complex is formed. For purification purpose, chloride ions are exchanged with hexafluorophosphate ions, leading to the precipitation of a purple solid corresponding to the complex.

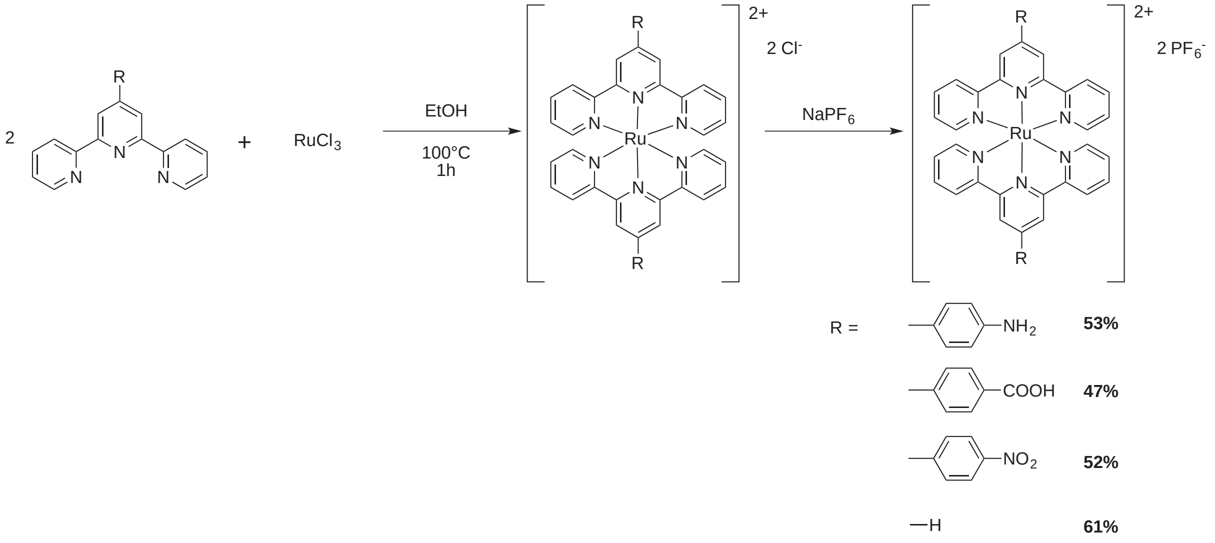

Scheme 26: Synthesis of $RuL_2(PF_6)_2$ complexes.

II.3.b. NMR characterization

Similarly to Fe(II), Ru(II) complexation leads to a global deshielding of terpyridine protons, the only exceptions being protons 5,5'' (noted ◆) and 6,6'' (noted ★) due to their presence in the anisotropy cone of the facing ligand (Figure 37). This effect is a bit lower than observed for Fe(II) complex.

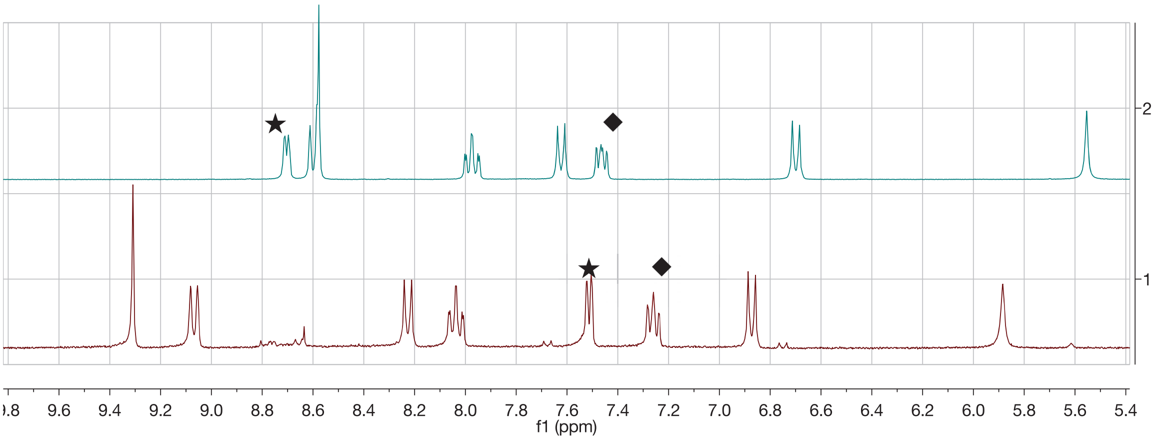

Figure 37: Modifications of ^{1}H NMR upon complexation of Ru(II) by L^{1}. *Spectra were recorded on 300 MHz NMR in DMSO-d^{6}.*

II.3.c. UV-Visible signatures

UV spectrum of Ru(II) polypyridine complexes displays to different types of transitions. In the UV region, different bands correspond to spin-allowed ligand-centred π→π* and n→π* transitions. In the visible region, a characteristic ^{1}MLCT band is observed, conferring to complexes an intense orange-red colour [180].

Absorption bands of phenyl-terpyridine complexes are slightly red-shifted compared to complexes of commercial ligands, certainly due to the presence of an extra aromatic ring. Ligand-centered bands are also much more intense (Figure 38).

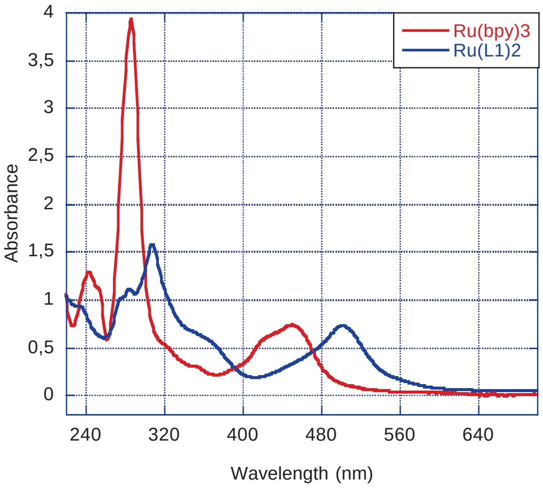

Figure 38: UV-Visible spectra of Ru(bpy)$_{3}$ (red) and Ru(L^{1})$_{2}$ (blue).

All absorption wavelengths and corresponding molar extinction coefficients were recorded and appear in Table 4.

Table 4: MLCT absorption wavelength and corresponding molar coefficient extinction of Ru(II) complexes in ACN.

Complex	λ_{max} (nm)	ε (L/mol/cm)
Ru(**bpy**)$_3$	451	15,575
Ru(**phen**)$_3$	444	15,280
Ru(**tpy**)$_2$	474	14,980
Ru(**L^1**)$_2$	502	24,100
Ru(**L^2**)$_2$	492	24,700
Ru(**L^3**)$_2$	494	25,100

II.3.d. Fluorescence properties

Ru(II) polypyridine complexes possess an emissive ^{3}MLCT state, which conveys them emissive properties at room temperature (Scheme 27). Their emission wavelength are *ca.* 600 nm in ACN [211].

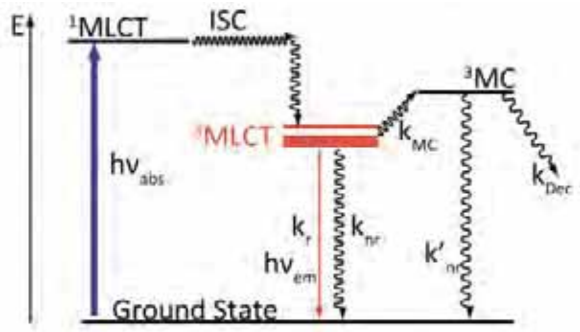

Scheme 27: Electronic diagram of Ru(bpy)$_3$. *MLCT = metal-to-ligand charge transfer excited state, MC = metal centre excited state, ISC = intersystem crossing.*

Ru(**bpy**)$_3$ is often used as a reference for quantum yield measurements, with a reported value of 1.8% in aerated ACN [212], and a corresponding fluorescence lifetimes *ca.* 800 ns. Contrariwise, Ru(**tpy**)$_2$ was found to display much lower fluorescence (Φ = 0.07%), together with a lower fluorescence lifetime (0.2 ns) [213]. This difference comes from the stabilisation of the ^{3}MC state in Ru(**tpy**)$_2$, which promotes a deactivation process (Scheme 27). Quantum yields of other Ru(II) complexes were determined using Ru(**bpy**)$_3$ as reference, fluorescence wavelengths and quantum yields appear in Table 5.

Table 5: Excitation and emission wavelengths and quantum yields of Ru(II) complexes in ACN. *Values in brackets are those reported in literature.*

Complex	λ_{exc} (nm)	λ_{em} (nm)	Φ (%)
Ru(**bpy**)$_3$	450	620	(1.8)
Ru(**phen**)$_3$	450	596	1.33
Ru(**tpy**)$_2$	475	550	0.053 (0.07)
Ru($\mathbf{L}^1$)$_2$	490	570	0.0174
Ru($\mathbf{L}^2$)$_2$	490	570	0.0169
Ru($\mathbf{L}^3$)$_2$	490	570	0.0130

Expectedly, Ru(**phen**)$_3$ displays similar characteristics as Ru(**bpy**)$_3$. Unfortunately, RuL$_2$ complexes are 100 times less fluorescent than Ru(**bpy**)$_3$, and their Stokes shift is also shorter. Compared with Ru(**tpy**)$_2$, it is likely that the presence of the phenyl ring linked with a rotatable bond partially quenches the fluorescence of the complex. Yet, the fluorescence can be observed for concentrations until 1 μM, which makes possible their use as fluorescent probes.

II.3.e. Electrochemical characterization

Electrochemical behaviour of Ru(II) complexes was assessed by cyclic voltammetry. To this aim, complexes were dissolved to 1 mM in ACN using 0.1 mM tetrabutylammonium hexafluorophosphate as support electrolyte. Figure 39 shows the cyclic voltamogrammes obtained for Fe($\mathbf{L}^1$)$_2$. A single oxidation wave is observed *ca.* 1.27 V *vs.* NHE, actually corresponding to two distinct processes: (a) the reversible oxidation of Ru^{2+} into Ru^{3+} and (b) the irreversible oxidation of the amine of $\mathbf{L}^{1'}$ as observed for the corresponding Cu($\mathbf{L}^1$)$_2$ complexes (Figure 31). In reduction,

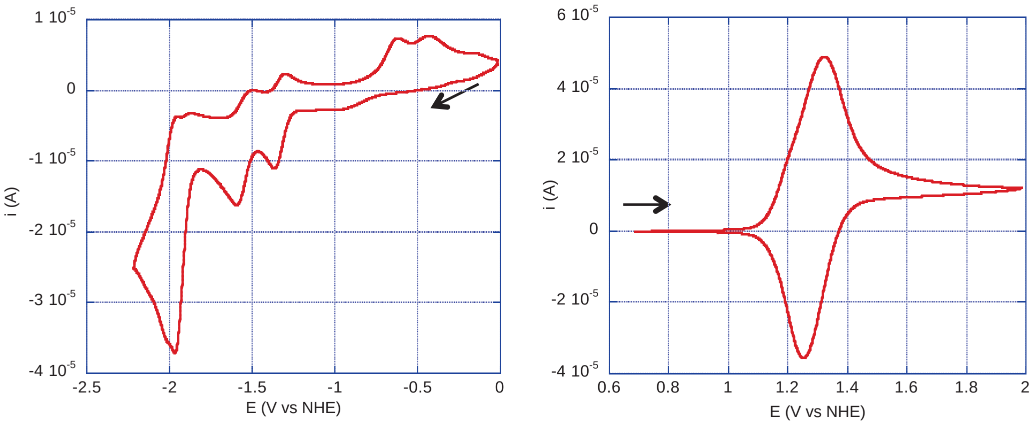

Figure 39: Cyclic voltamogrammes of Ru(L^1)$_2$ in ACN. Conditions: *[Ru(L^1)$_2$] = 1 mM, [TBAPF$_6$] = 0.1 mM, scan rate = 0.1 V/s, argon atmosphere. WE: glassy C, CE: Pt, RE: Ag/Ag$^+$.*

several quasi-irreversible waves and irreversible peaks are observed, corresponding to the reduction of the pyridyl and phenyl rings, consistently with literature [206].

Similar studies were conducted with other Ru(II) complexes, showing reversible Ru^{2+}/Ru^{3+} waves for all the complexes. Apparent redox potentials appear in Table 6, showing almost identical values for all the complexes. From these data, similar properties in terms of redox cycling can be expected for the different complexes, with no effect of the substituting group.

Table 6: Apparent redox potentials for Ru(II)/Ru(III) in various complexes.

Complex	**$E_{1/2}^{app}$ (V *vs.* NHE)**
Ru(**tpy**)$_2$	1.26
Ru($\mathbf{L^1}$)$_2$	1.27
Ru($\mathbf{L^2}$)$_2$	1.25
Ru($\mathbf{L^3}$)$_2$	1.28

Conclusion

In addition to commercially available **bpy**, **tpy** and **salophen**, we synthesized a series of six 4’-substituted terpyridines, using the Kröhnke method. The compounds are obtained in satisfying yields, and purified by simple filtration.

^{1}H NMR revealed that the nature of the substituent has no effect on the electronic properties of the terpyridine, the only affected protons being those of the phenyl ring. Their coordination properties should thus be similar.

A total of 18 metal complexes were synthesized, including four Cu(II) complexes, eight Fe(II) complexes, and six Ru(II) complexes.

A few crystal structures were obtained, confirming that terpyridine complexes are constituted of two perpendicular planes, whereas salophen remains planar. ^{1}H NMR showed consistent results, protons 5,5’’ and 6,6’’ being shielded due to the anisotropy cone of the other terpyridine.

The spectrophotometric characteristics of the different complexes were assessed, showing various properties. In particular, Ru$\mathbf{L}_2$ complexes revealed lower fluorescence properties than Fe(**tpy**)$_2$, possibly due to rotation of the phenyl ring. Yet, this could be sufficient to test them as probes for amyloid-β aggregation (see Chapter IV.I.1.c).

Finally, cyclic voltammetry confirmed that Cu(II) and Ru(II) complexes were able to cycle to Cu(I) and Ru(III) in a reversible way, making possible their use in catalysis.

Given all of this, the next step was to study the interaction of the different metal complexes and amyloid-β fibres.

Chapter IV. Study of metal complexes - amyloid fibres interaction

Introduction

Biologists dispose of a wide set of techniques to study protein-ligand interactions. In solid state, X-ray crystallography is widely used to resolve the three-dimensional structure of protein-ligand complexes and identify molecular determinants involved in molecular recognition. In solution, calorimetric techniques, such as Isothermal Titration Calorimetry, and hydrodynamic techniques, such as Dynamic Light Scattering, are powerful tools to obtain thermodynamic constants of the protein-ligand interaction. Spectrophotometric techniques, such as Infrared or Circular Dichroism also represent convenient techniques for this type of investigations.

Unfortunately, all these techniques require either soluble or crystalline proteins, which is not the case of amyloid fibres. They are also too large to be studied by solution NMR. To highlight the interaction between Aβ fibres and metal complexes, we propose to run indirect measurements looking for variations of metal complex or fibre properties upon interaction.

This chapter describes our investigations on complexes-fibre interaction. Because the development of recombinant peptide was still in progress at this time, these studies were conducted using commercial synthetic Aβ$_{1-40}$ peptide.

The first part describes experimental assessment of fibre-complex interaction. Firstly, qualitative results are obtained from spectrophotometric studies on metal complex in presence of fibres. More quantitative results are then obtained from indirect UV-Vis titration.

To investigate metal complexes binding site(s), studies were conducted on several truncated Aβ peptides, using solution NMR and UV-Vis titration. The nature of the interaction motif was also considered, using fragment molecules.

In a second part, docking studies were conducted on fibres models using selected complex candidates, seeking for insights on the nature of fibre-complex interaction.

All of this allowed finding complexes candidates that display good affinity for amyloid fibres, and gave clues on interaction determinants.

I. Interaction studies

I.1. Validation of metal complex-fibres interaction

Because we had no preliminary report on the binding of polypyridine metal complexes to amyloid fibres, a first step thus consisted in investigating the possible binding of the whole series of metal complexes synthesized (see Chapter III.II). To avoid interference with fibre formation, we chose to put aside Cu(II) complexes and to focus on Fe(II) and Ru(II) complexes (Scheme 28).

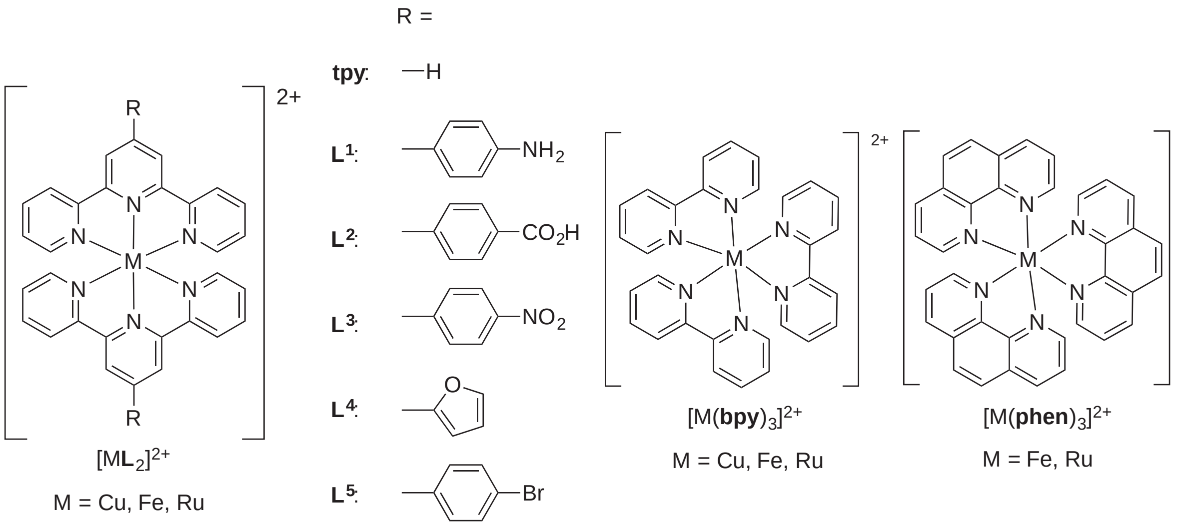

Scheme 28: Metal complexes used in this study.

I.1.a. Effect of metal complexes on aggregation kinetics

A first study to evaluate the interaction between $A\beta_{1-40}$ fibres and metal complexes consisted in looking for a variation of $A\beta_{1-40}$ aggregation kinetics. In the case of Th-T, which is used to monitor fibre formation (Chapter I.III.2.a), it was shown that its presence during the aggregation process was actually promoting aggregation, Th-T playing the role of template and pre-organizing peptides for a faster self-assembly [135]. To be able to detect aggregation, the presence of Th-T is mandatory. We thus proposed to run aggregation experiments in the presence of both Th-T and metal complexes. A significant modification of aggregation kinetics would be a first evidence of interaction between metal complexes and fibres.

Figure 40 shows the Th-T monitored aggregation curves obtained for $A\beta_{1-40}$ alone and in the presence of Fe(**L^1**)$_2$ or Fe(**bpy**)$_3$. Because stock solutions of complexes are in acetonitrile, a corresponding control with identical amount of acetonitrile was performed.

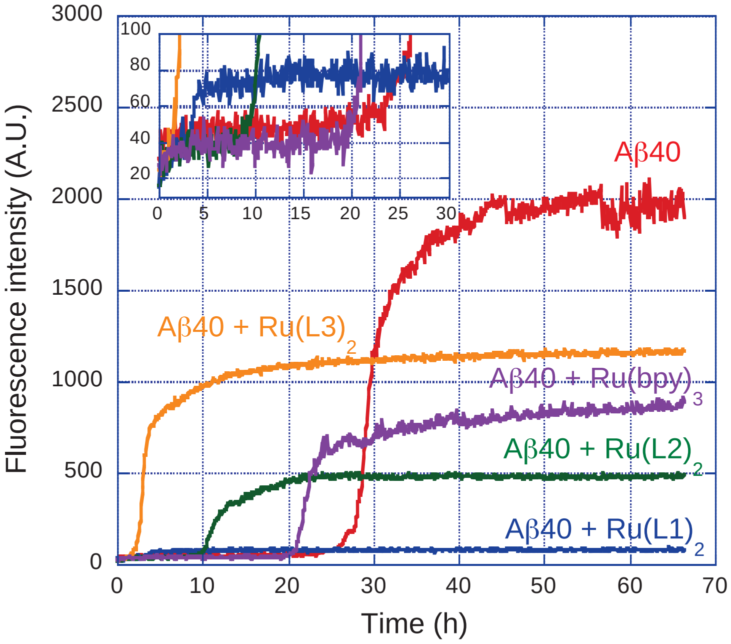

Figure 40: Effect of metal complexes on A$\beta_{1\text{-}40}$ aggregation kinetics. *Aggregation assay was performed with A$\beta_{1\text{-}40}$ alone or in the presence of Ru complexes. Insert shows a zoom on Ru(**L**^{1})$_2$ aggregation curve.* ***Conditions:*** *[A$\beta_{1\text{-}40}$] = 50 µM, [Th-T] = 10 µM, [PB] = 50 mM, [complex] = 50 µM, pH = 7, ACN 5%.*

It appears that the presence of Ru(**bpy**)$_3$ weakly affects aggregation kinetics, its aggregation half-times ($t_{1/2}$) being close to the peptide alone (*ca.* 22 h and *ca.* 29 h, respectively). Contrariwise, Ru(**L**^{1})$_2$ and Ru(**L**^{3})$_2$ drastically alters aggregation course, with a half-time around 4 h. Ru(**L**^{2})$_2$ has an intermediate effect. Fluorescence intensity of the plateau (I) is also drastically modified. Because this effect does not correlate with variations in $t_{1/2}$, we attribute this to an inner-filter effect of complexes that would absorb part of the light emitted by Th-T [133,214]. Differences between complexes would thus be due to their intrinsic spectrophotometric properties.

This aggregation experiment was reproduced with different available metal complexes. The variations in $t_{1/2}$ and I are shown in Table 7.

Table 7: Variation of the $t_{1/2}$ of A$\beta_{1\text{-}40}$ aggregation in presence of various coordination complexes. *Complexes displaying important effect are highlighted in bold.*

Compound	**Δ$t_{1/2}$ (%)**	**ΔI (%)**
Ru(**bpy**)$_3$	24	**95.2**
Ru(**phen**)$_3$	34	**95.5**
Ru(**tpy**)$_2$	25	**95.6**
Ru(**L**^{1})$_2$	**85**	**96.5**
Ru(**L**^{2})$_2$	56	**78.4**

$\mathrm{Ru}(\mathbf{L}^{3})_2$	**78**	42.5
$\mathrm{Fe}(\mathbf{bpy})_3$	0	5
$\mathrm{Fe}(\mathbf{L}^{1})_2$	**83**	**95.5**
$\mathrm{Fe}(\mathbf{L}^{2})_2$	19	38.9
$\mathrm{Fe}(\mathbf{L}^{3})_2$	**77**	49
$\mathrm{Fe}(\mathbf{L}^{4})_2$	**77**	**89**
$\mathrm{Fe}(\mathbf{L}^{5})_2$	**83**	**92**

It appears that only complexes of phenyl-terpyridine affect aggregation kinetics. Interestingly, $\mathrm{Ru}(\mathbf{L}^{1})_2$ has similar effect as $\mathrm{Fe}(\mathbf{L}^{1})_2$, as well as $\mathrm{Ru}(\mathbf{L}^{3})_2$ has similar effect as $\mathrm{Fe}(\mathbf{L}^{3})_2$. $\mathbf{L}^{4}$ and $\mathbf{L}^{5}$ complexes also seem to promote interaction, whereas the effect of $\mathbf{L}^{2}$ complexes is less defined. The lack of correlation is confirmed between $\Delta t_{1/2}$ and ΔI, confirming the hypothesis of inner-filter effect.

This study attests of an effect of some metal complexes on $A\beta_{1-40}$ aggregation, but is not sufficient to confirm an interaction. More quantitative experiments were thus designed to validate the incorporation of metal complexes into fibres.

I.1.b. Indirect quantification of bound species

Because it was not possible to directly quantify the amount of compound inserted into fibres, we proposed an indirect method based on spectrophotometric titration. At the end of the aggregation process, wells are sampled and centrifuged to separate fibres from soluble species. Complex concentration is then assessed by UV-Vis titration of the soluble fraction. Comparison with negative controls in absence of fibres allows the evaluation of the amount of metal complexes inserted into fibres. A schematic representation of this protocol is given in Scheme 29.

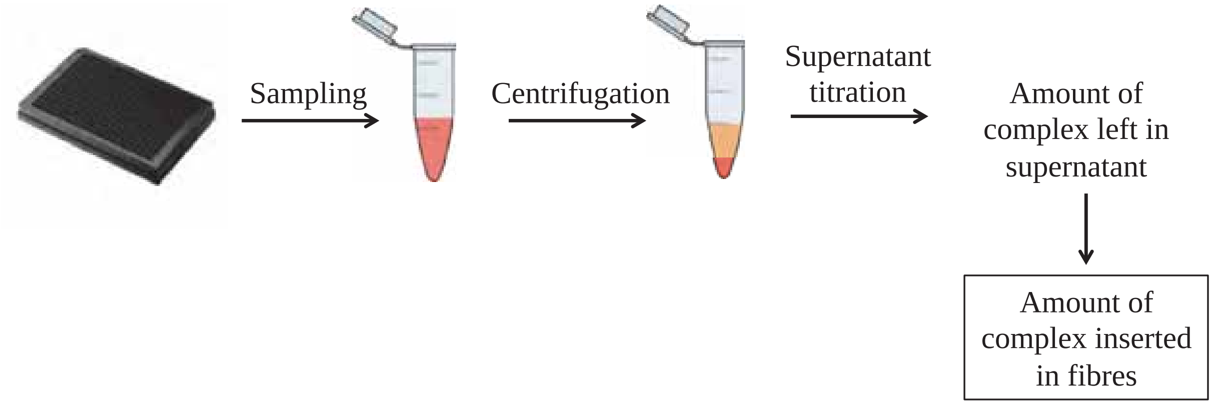

Scheme 29: Experimental protocol for quantification of inserted complex.

Several biases can arise from such an experiment. (a) First, a precipitation of complexes could be observed when diluted into buffered solution, or while incubating. To take this into account, negative controls were prepared in the exact same conditions. (b) Non-specific coprecipitation of complexes together with fibres could also be observed. To evaluate this, we have proposed to wash fibres with ACN, to remove unbound complexes. However, only traces of complexes were recovered, showing the limited extent of coprecipitation. (c) Competition between ligands and peptide to chelate metal ions could be envisaged. But we have shown that the UV-Vis signature of complexes was unchanged in presence of monomeric Aβ peptide. (d) Finally, it was mandatory to confirm the presence of fibres (oppositely to amorphous aggregates). To do so, Th-T control wells were systematically added, and samples were periodically submitted to atomic force microscopy. Considering all of this, we approximate in the following that the amount of complex disappearing from solution was equal to the amount of complex inserted into the fibres, although keeping in mind these potential biases.

Figure 41 shows fibre samples before and after centrifugation. A first visual estimation allows to conclude that **L**^{1} metal complexes (tubes 2 and 6) and **L**^{3} metal complexes (tubes 4 and 8) seem to insert into fibres, affording a colourful pellet upon centrifugation. **L**^{2} complexes seem to have moderate incorporation (tubes 3 and 7), while none is observed for Ru(**bpy**)$_3$ (tube 5). This correlates with the previously reported variations in aggregation kinetics of Aβ$_{1-40}$ (Figure 40). Corresponding controls in absence of fibres show no metal complex precipitation.

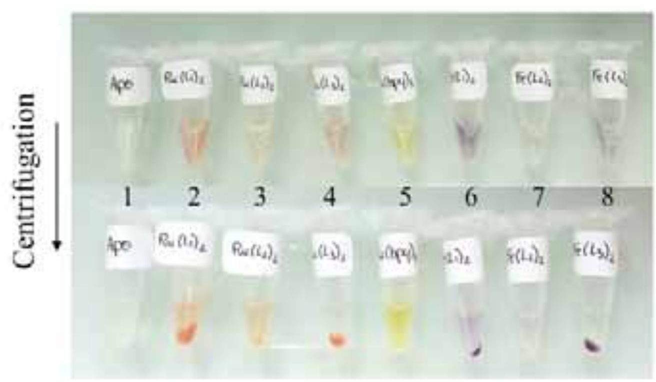

Figure 41: Tubes containing fibres mixtures before and after centrifugation.

The resulting supernatants were submitted to UV-Visible titration to quantify the amount of complexes in the soluble fraction. To take into account the possible precipitation of complexes in these buffered conditions, corresponding controls containing no Aβ were considered.

The amount of metal complexes inserted into fibres was deduced by difference between the initial amounts of metal complex minus the amount left in the supernatant. The results appear in Table 8, confirming the visual evidence: complexes of **L**^{1} and **L**^{3} get incorporated much better than others.

Table 8: Amount of metal complexes inserted into Aβ_{1-40} fibres during aggregation process.

Complex	**% Inserted complex**
Ru(**bpy**)$_3$	1
Ru(**phen**)$_3$	2
Ru(**tpy**)$_2$	3
Ru(**L^1**)$_2$	**55**
Ru(**L^2**)$_2$	0
Ru(**L^3**)$_2$	**100**
Fe(**bpy**)$_3$	10
Fe(**L^1**)$_2$	**81**
Fe(**L^2**)$_2$	0
Fe(**L^3**)$_2$	**99**
Fe(**L^4**)$_2$	**67**
Fe(**L^5**)$_2$	**93**

It seems that Fe(**L^3**)$_2$, Ru(**L^3**)$_2$ and Fe(**L^5**)$_2$ can incorporate one complex for one peptide. This ratio is slightly lower for Fe(**L^1**)$_2$, Ru(**L^1**)$_2$ and Fe(**L^4**)$_2$.

I.1.c. Spectrophotometric evidences of interaction

For small molecules, moving from solution to fibres constitutes a drastic change, comparable to a shift from aqueous to hydrophobic environment [215]. The solvation of the molecule is thus affected by this variation. Binding to fibres also decreases intramolecular rotations in the molecule, which results in modifications of fluorescence properties [216]. This affects the spectrophotometric properties of molecules, and thus constitutes a tool for investigating interaction.

(a) Effect of interaction on UV-Vis spectra

For a ligand, interaction with amyloid fibres is similar to a shift from an aqueous environment to a hydrophobic environment. This difference in solvation results in variations of their UV-Vis spectra. This is the case for Th-T, whose λ_{max} goes from 410 nm to 420 nm upon interaction with Aβ (Figure 42, red curves) [217].

In the same way, Ru($\mathbf{L^1}$)$_2$ displays a red shift upon incorporation into fibres, but of lower amplitude (λ_{max} = 495 nm to λ_{max} = 500 nm), as shown on Figure 42.

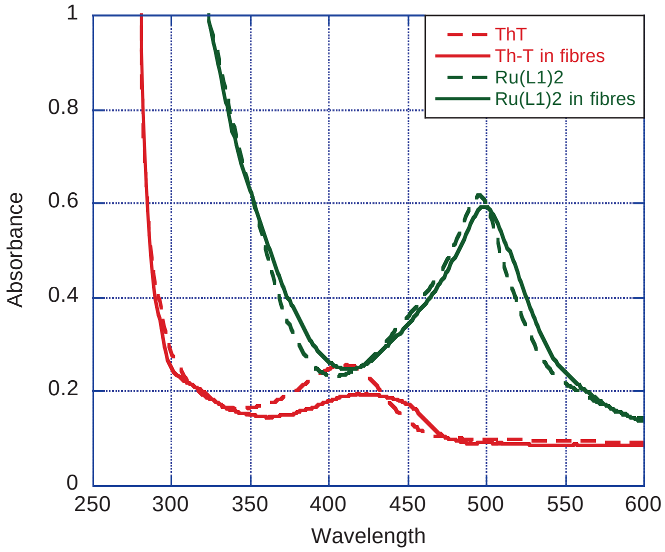

Figure 42: UV-Vis monitoring of absorption shift of metal complexes upon insertion in fibres. *Spectra were recorded for fibres containing only Th-T (red line) or in presence of 0.5 eq (green line). Corresponding negative controls without peptide appear in dashed lines.* ***Conditions:*** *[Aβ_{1-40}] = 50 µM, [Th-T] = 10 µM, [PB] = 50 mM, [complex] = 50 µM, pH = 7, aggregation for 4 days at 37°C.*

(b) Effect of interaction on fluorescence spectra

In the case of Th-T, interaction with fibres induces a shift in emission wavelength together with an increase in quantum yield. These effects are attributed to an immobilization of Th-T in fibres: the benzylamine ring and the benzothiazole ring are prevented from rotation, which results in the stabilization of Th-T fluorescence excited state, resulting in an enhanced fluorescence [132]. Investigations were conducted on fluorescent Ru($\mathbf{L^1}$)$_2$ complex, trying to see if similar effects can be observed.

Figure 43 displays emission spectra obtained for Ru($\mathbf{L^1}$)$_2$ alone (red) and in presence of Aβ_{1-40} fibres (green). Corresponding control containing only Aβ_{1-40} fibres appears in blue.

It appears that fluorescence of Ru($\mathbf{L^1}$)$_2$ at 660 nm is enhanced by approximately 50% in the presence of fibres. A slight shift of λ_{em} may be noted, but spectra resolution does not allow a precise determination.

The effect of interaction on Ru($\mathbf{L^1}$)$_2$ is considerably less important than for Th-T. Indeed, fluorescence comes from a MLCT state of Ru(tpy)$_2$ (see Chapter III.II.3.d), whose coordination is rather rigid. Although the immobilization of the *p*-amino phenyl ring could contribute to the observed fluorescence enhancement, its effect should be of limited extent.

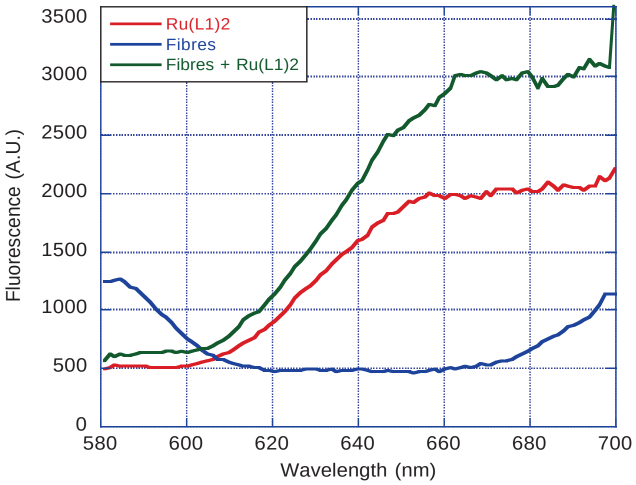

Figure 43: Enhanced fluorescence of Ru(L^1)$_2$ inserted in fibres. *Emission spectra were recorded at the end of aggregation for Aβ$_{1-40}$ 50 µM (blue line), Ru(L^1)$_2$ 50 µM (red line) and for a mixture of both (green line).* ***Conditions:*** *[Aβ$_{1-40}$] = [complex] = 50 µM, [PB] = 50 mM, pH = 7, aggregation for 4 days at 37°C, λ_{exc} = 490 nm.*

Yet, the enhanced fluorescence of Ru(**L^1**)$_2$ in the presence of fibres constitutes a proof of interaction. However, it does not give information on the strength of this interaction or on the nature of the binding site. NMR experiments were thus envisaged to answer these questions.

I.1.d. NMR experiments

Solution NMR being limited to proteins below 35 kDa, it cannot be applied to amyloid fibres [218]. In order to highlight its interaction with metal complexes, NMR experiments were run on monomeric Aβ$_{1-40}$. The existence of an interaction with monomeric peptide does not imply a similar interaction with fibres because peptide configuration in monomeric and fibrillary states are very different [139]. Yet, it gives preliminary information on the propensity of metal complexes to interact with peptides.

(a) ^{1}H NMR

^{1}H NMR spectra of Aβ$_{1-40}$ were recorded in the presence or absence of metal complexes, total amount of ACN being identical (Figure 44). In the aromatic region of the spectra, a broadening of the signals is observed, attesting of an interaction. Tyr (6.6 ppm) and His (7.0 and 7.6 ppm) signals become particularly large. In the aliphatic region, Ala signal (1.25 ppm) is also broadened. However, no splitting of peaks is observed, in line with a weak interaction. Expectedly, aromatic amino acids seem to be the most involved in the interaction.

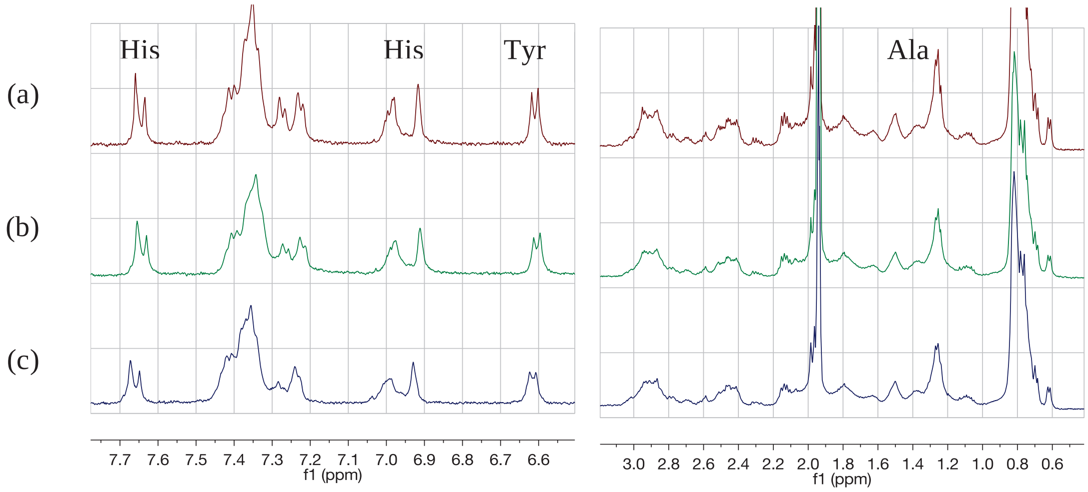

Figure 44: Effect of metal complexes on Aβ_{1-40} ^{1}H NMR spectrum. (a) *Aβ_{1-40} alone,* ***(b)*** *Aβ_{1-40} with Fe(**L**^{1})$_2$,* ***(c)*** *Aβ_{1-40} with Fe(**L**^{3})$_2$.* ***Experimental conditions:*** *[Aβ_{1-40}] = 200 μM, [PB] = 50 mM, [complex] = 200 μM, pH = 7, total ACN-d^3 content of 10% in each tube. Spectra recorded on 500 MHz NMR.*

(b) DOSY NMR

A typical experiment allowing highlighting the interaction between a protein and its ligand consists in measuring their diffusion coefficients. Upon interaction with the protein, the ligand loses mobility, and its diffusion coefficient decreases. To a certain extent, it is possible to extract a global binding constant of the system. In order to study diffusion coefficients, a DOSY NMR experiment was set up [219].

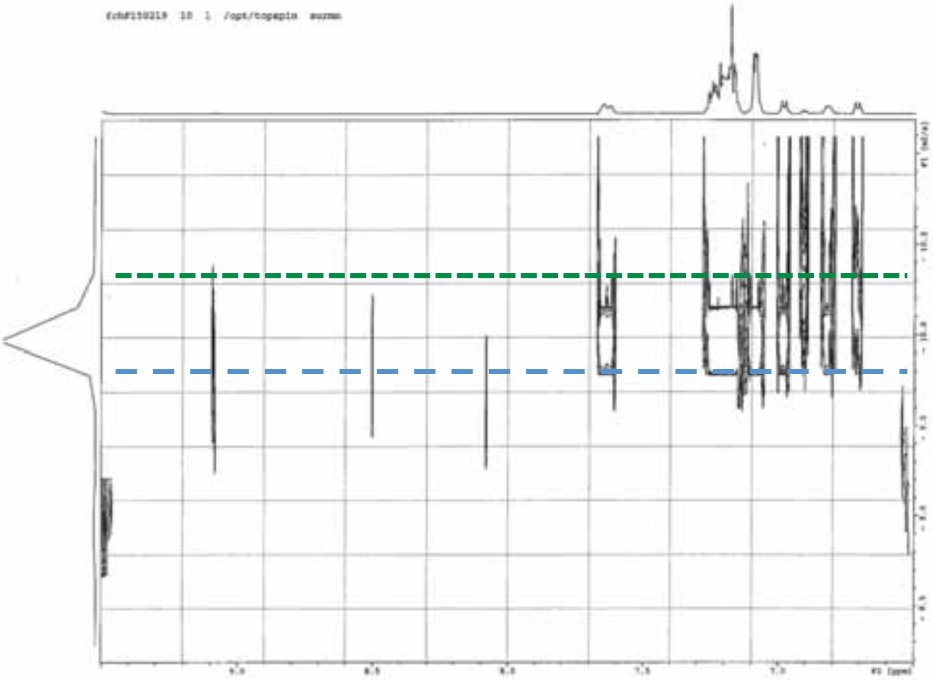

Figure 45: DOSY NMR spectrum evidencing Aβ_{1-28} - Fe(L^1)$_2$ interaction. *Blue line: diffusion of Fe(L^1)$_2$, green line: diffusion of Aβ_{1-28}.* ***Conditions:*** *[Aβ_{1-28}] = 200 μM, [PB] = 50 mM, [Fe(L^1)$_2$] = 200 μM, pH = 7. Spectrum recorded on 500 MHz NMR.*

Because this experiment requires long accumulation times (especially at low peptide concentration), it was not possible to proceed with Aβ_{1-40}, which aggregates too fast. We thus studied the variation of Fe(**L**^{1})$_2$ diffusion coefficient in the presence of monomeric Aβ_{1-28}. To do so, DOSY NMR spectra of Fe(**L**^{1})$_2$, Aβ_{1-28}, and of a mixture of both were recorded (Figure 45).

In the horizontal dimension appears the ^{1}H NMR signal of the mixture, and in the vertical dimension the diffusion coefficients of the different species. Two sets of spots are present, corresponding to Fe(**L**^{1})$_2$ (blue line) and to the peptide (green line). Precise diffusion coefficients were extracted from spectra and presented in Table 9.

Table 9: Diffusion coefficients obtained by DOSY NMR.

Compound	**Diffusion coefficient (m^2.s^{-1})**	
Aβ_{1-28}	0.76 e^{-10}	
Fe(**L**^{1})$_2$	3.10 e^{-10}	
Aβ_{1-28}+ Fe(**L**^{1})$_2$	1.78 e^{-10}	0.76 e^{-10}

As expected, the diffusion coefficient of Fe(**L**^{1})$_2$ is modified in presence of peptide, going from 3.1e^{-10} to 1.78e^{-10} m^2.s^{-1}. Yet, the diffusion coefficient of Fe(**L**^{1})$_2$ upon interaction remains different from the peptide's. This result is in line with a weak interaction between Fe(**L**^{1})$_2$ and Aβ_{1-28}, with an estimated K$_d$ of 10^{-4} M. The equations used for K$_d$ determination appear in Annex I.

Unfortunately, this experiment could not be reproduced with Fe(**L**^{3})$_2$ due to solubility issues.

I.1.e. Conclusion: Interacting species

These studies highlight that four species seem to interact with Aβ_{1-40} fibres: Fe(**L**^{1})$_2$, Fe(**L**^{3})$_2$, Ru(**L**^{1})$_2$ and Ru(**L**^{3})$_2$. All of them were shown to accelerate aggregation kinetics, possibly pre-organizing peptides and facilitating their auto-assembly, and all were shown to efficiently incorporate into Aβ_{1-40} fibres. **L**^{3} complexes seem to incorporate in stoichiometric ratios compared to the peptide, which could denote the existence of several binding sites according to the side-chain channel model. **L**^{1} complexes incorporate in lower ratios, which could be attributed to different binding sites or affinities. Solution NMR demonstrates a weak interaction between the monomeric form of peptide and Fe(**L**^{1})$_2$, but do not allow to conclude on interacting residues. Further studies were thus conducted to better understand interaction sites in fibres.

I.2. Investigation of metal complex binding sites

I.2.a. Investigation of Thioflavin-T binding site

Gaining insights on ligand binding sites in Aβ fibres is very difficult, and limited information is available on the amino acids involved in interactions with ligands. In the case of Th-T, experimental and computational studies have suggested that binding site(s) are located in side-chains channels, Th-T being parallel to the fibre axis (Chapter I.III.2.a), but no interaction with specific amino acids was reported [132].

A first investigation consisted in titrating unbound Th-T at the end of the aggregation process. As described before for metal complex quantification (Scheme 29), wells containing fibres were sampled and centrifuged, and supernatants were analysed by HPLC. Amount of unbound Th-T allowed determining the amount of Th-T inserted in fibres.

Table 10: Amount of Th-T inserted into $A\beta_{1-40}$ fibres during aggregation process in presence of various metal complexes.
Conditions: *$[A\beta_{1-40}]$ = 50 µM, [Th-T] = 10 µM, [PB] = 50 mM, [complex] = 50 µM, pH = 7, ACN 5%.*

Complex	**% Inserted Th-T**
Ru(**bpy**)$_3$	50
Ru(**L**^{1})$_2$	38
Ru(**L**^{2})$_2$	43
Ru(**L**^{3})$_2$	66
Fe(**bpy**)$_3$	36
Fe(**L**^{1})$_2$	31
Fe(**L**^{2})$_2$	39
Fe(**L**^{3})$_2$	45
Ø	43

Table 10 shows results obtained for Th-T quantification, showing limited variations. It seems that none of the complexes prevent Th-T from inserting into fibres.

To confirm this first result, a competition assay was set up between interacting complexes and Th-T. To address this objective, aggregation assays were run in presence of increasing amounts of metal complexes. At the end of aggregation, samples were centrifuged and soluble fractions were analysed by HPLC to evaluate the amount of unbound Th-T. Results are reported on Figure 46.

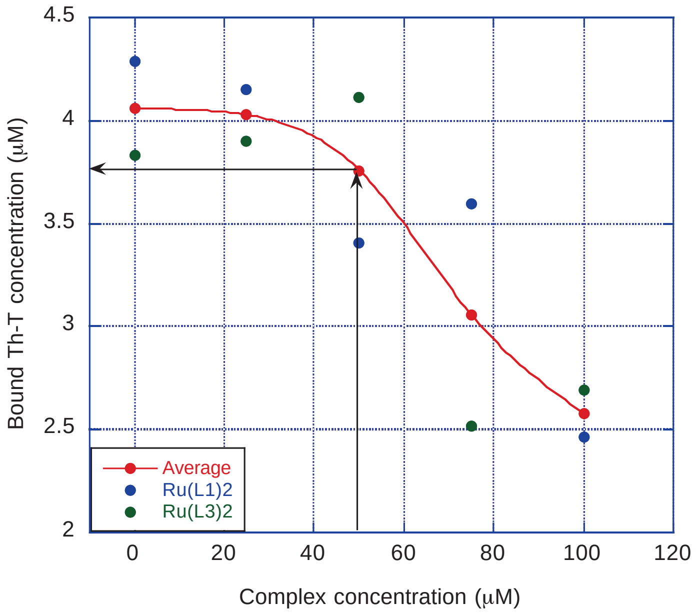

Figure 46: Th-T displacement by metal complexes. *Unbound Th-T was quantified in the end of A*$\beta_{1\text{-}40}$ *aggregation in the presence of Ru(*L^1*)*$_2$ *(blue) or Ru(*L^3*)*$_2$ *(green) in variable concentrations.* ***Conditions:*** *[A*$\beta_{1\text{-}40}$*] = 50 μM, [Th-T] = 10 μM, [PB] = 50 mM, [complex] = variable, pH = 7.*

It appears from these data that both metal complexes display low affinity for Th-T binding site. Indeed, 75 μM of metal complex are needed to displace 1 μM of Th-T. In other words, in the case of Ru(**L**^{3})$_2$, which fully incorporate in fibres at 50 μM, this means that among the 50 μM of complex inserted, only *ca.* 0.25 μM take the place of Th-T (Figure 46, black arrow). This amount can be considered as negligible, leading to the conclusion that Th-T and metal complexes bind A$\beta_{1\text{-}40}$ fibres in different sites.

I.2.b. Incorporation in fibres made of truncated peptides

Another experiment enabling to gain further insights into metal complex binding sites consists in studying their incorporation into fibres made of truncated Aβ peptides [220]. We focused on A$\beta_{11\text{-}28}$ peptide, which comprises the hydrophobic core of Aβ [221], and A$\beta_{1\text{-}28}$ which holds Aβ N-ter end [222] (Scheme 30). By comparison with results obtained with A$\beta_{1\text{-}40}$, some information could be retrieved on the residues involved in the interaction. For example, if metal complexes display affinity for the N-ter end of peptides, there should be no incorporation in A$\beta_{11\text{-}28}$, etc. Aggregation assays were thus run with A$\beta_{1\text{-}28}$ and A$\beta_{11\text{-}28}$, in the presence of stoichiometric amounts of metal complexes.

A$\beta_{11\text{-}28}$	EVHHQKLVFFAEDVGSNK
A$\beta_{1\text{-}28}$	DAEFRHDSGYEVHHQKLVFFAEDVGSNK
A$\beta_{1\text{-}40}$	DAEFRHDSGYEVHHQKLVFFAEDVGSNKGAIIGLMVGGVV

Scheme 30: Amino acid sequences of A*$\beta_{11\text{-}28}$*, A*$\beta_{1\text{-}28}$*, and A*$\beta_{1\text{-}40}$*.

Because they are less aggregation-prone compared with Aβ$_{1-40}$, aggregation parameters are slightly different for Aβ$_{11-28}$ and Aβ$_{1-28}$. Firstly, to work in comparable time frame, their aggregation has to be triggered by addition of 0.5 eq Zn(II) [223]. In the case of Aβ$_{1-28}$ concentration is also increased to 100 µM, to promote auto-assembling. Metal complex and Zn(II) concentrations were thus increased accordingly. Finally, their aggregation is monitored at 25°C. Aggregation curves obtained appear in Figure 47.

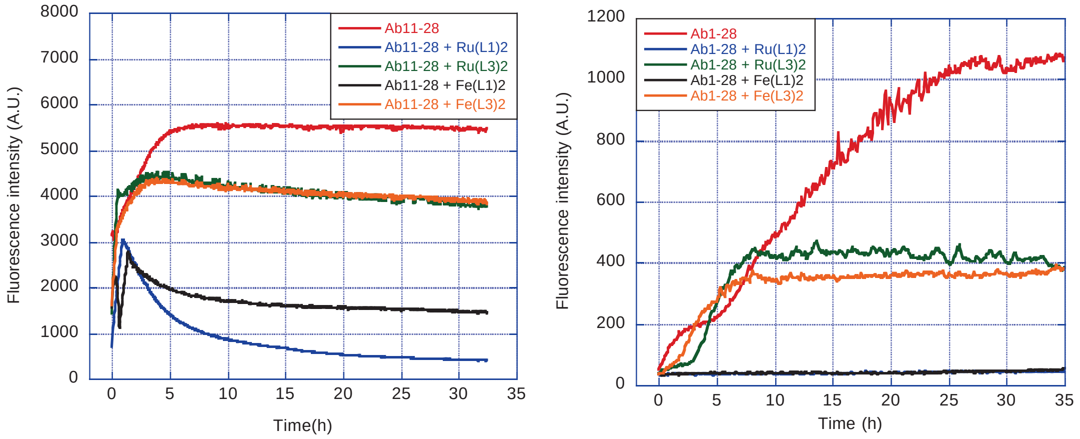

Figure 47: Aggregation curves obtained for Aβ$_{11-28}$ and Aβ$_{1-28}$ in presence of various metal complexes. A: *Curves obtained for Aβ$_{11-28}$.* ***Conditions:*** *[Aβ$_{11-28}$] = [complex] = 50 µM, [Th-T] = 10 µM, [ZnSO$_4$] = 25 µM, [PB] = 50 mM, pH = 7, 25°C.* ***B:*** *Curves obtained for Aβ$_{1-28}$.* ***Conditions:*** *[Aβ$_{1-28}$] = [complex] = 100 µM, [Th-T] = 10 µM, [ZnSO$_4$] = 25 µM, [PB] = 50 mM, pH = 7, 25°C.*

As for Aβ$_{1-40}$, a decrease of fluorescence intensity is observed in presence of metal complexes, particularly noted for **L^1** complexes. A variation in $t_{1/2}$ cannot be distinguished for Aβ$_{11-28}$ due to a very fast aggregation process. Despite differences in curve profiles, it seems that no variations in $t_{1/2}$ can be observed for Aβ$_{1-28}$. Unbound complexes were quantified at the end of aggregation following the previously described procedure (Scheme 29). Table 11 gathers the results obtained.

Table 11: Amount of metal complexes inserted into Aβ$_{11-28}$, Aβ$_{1-28}$, Aβ$_{1-40}$ fibres during aggregation process.

Complex	**Aβ$_{1-40}$**	**Aβ$_{1-28}$**	**Aβ$_{11-28}$**
Ru(**L^1**)$_2$	55%	0%	0%
Ru(**L^3**)$_2$	100%	4%	0%
Fe(**L^1**)$_2$	81%	0%	0%
Fe(**L^3**)$_2$	99%	17%	40%

These results indicate that metal complexes incorporation is very specific to Aβ_{1-40} fibres, and does not occur with Aβ_{1-28} or Aβ_{11-28}. An explanation could be the affinity of metal complexes for specific residues situated between Gly29 and Val40. However, a difference in the peptide conformation in fibres cannot be excluded [142]. As such, some amino acid side chains may be oriented outwards of the fibre in the case of Aβ_{1-40}, and inwards in truncated peptide fibres, which would explain the absence of interaction in the latter case.

To investigate this last hypothesis, an NMR study was carried out with the monomeric truncated peptides.

I.2.c. NMR evidence of binding sites

To compare the binding abilities of the different peptides, we propose to examine ^{1}H NMR spectra of peptides in the presence of ligands. The shift, enlargement, or splitting of certain peaks provide information on the amino acids interacting with the complexes.

Figure 48 shows aromatic region of ^{1}H NMR spectra of Aβ_{11-28}, Aβ_{1-28} and Aβ_{1-40} in the presence of Fe($\mathbf{L^1}$)$_2$ and Fe($\mathbf{L^3}$)$_2$. As region 29-40 does not contain any aromatic residues, we focused on aliphatic region of spectra. Although slight differences exist between spectra, no significant variation can be observed in presence of metal complexes, either in the aliphatic or in the aromatic region. It seems that ^{1}H NMR of monomeric peptide does not constitute an appropriate model for metal complex-fibres interaction. At this stage, an interaction with residues 29-40 thus cannot be confirmed or excluded.

I.2.d. Conclusion: Metal complex binding site

Even though these experiments do not allow concluding on the nature of binding site(s), they provide different pieces of information. First of all, we learnt that metal complexes bind very weakly to Th-T binding site in Aβ_{1-40}. Other binding sites might exist for metal complexes.

Metal complexes do not get incorporated within fibres made of truncated peptides. The difference of incorporation could be due either to a specific interaction with residues from segment 29-40, or to a difference in fibre structures. Unfortunately, ^{1}H NMR on monomeric peptide did not allow concluding on this point. ssNMR would constitute an appropriate alternative to investigate residues involved in interaction.

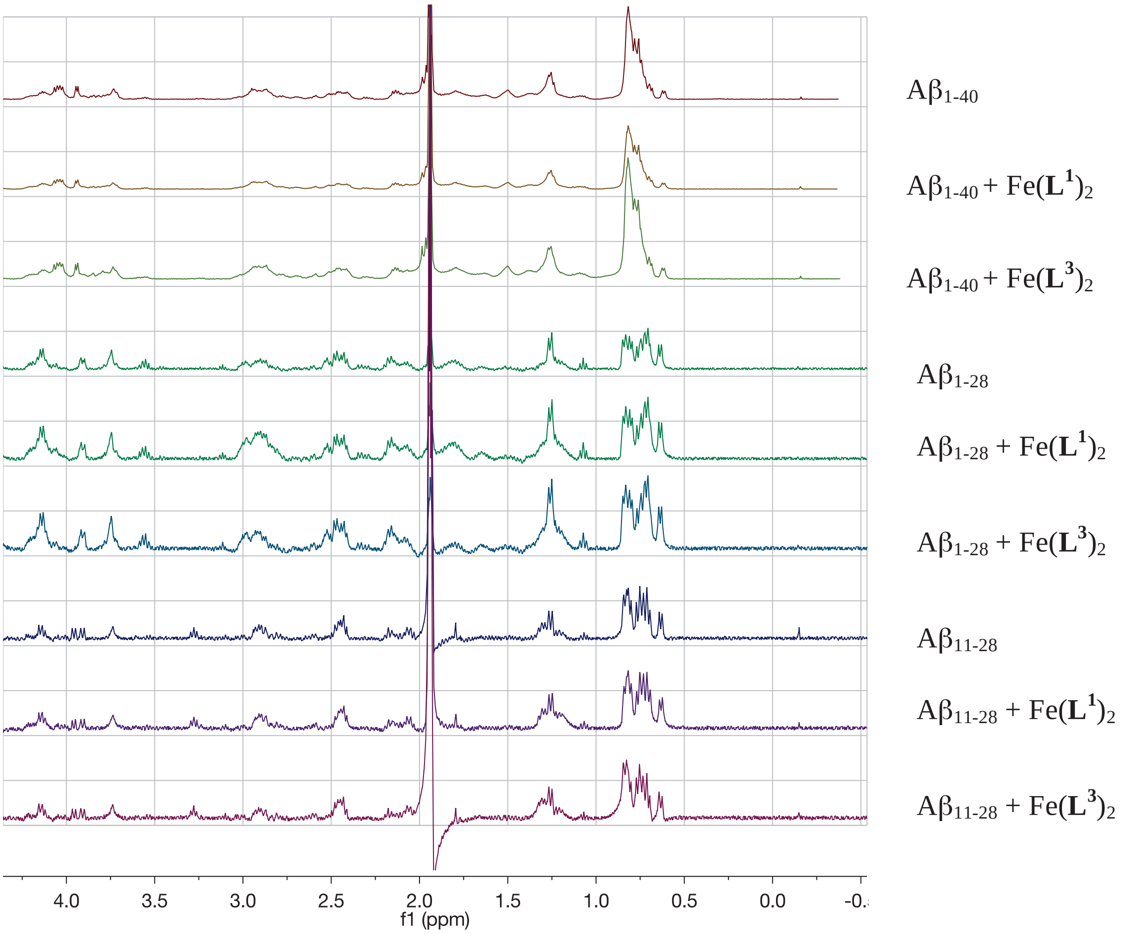

Figure 48: ^{1}H NMR spectra of $A\beta_{1\text{-}40}$, $A\beta_{1\text{-}28}$ and $A\beta_{11\text{-}28}$ in the presence of metal complexes. Experimental conditions: *For $A\beta_{1\text{-}40}$: [Aβ] = [complex] = 200 µM, [PB] = 50 mM, pH = 7, total ACN content of 10%. Spectra recorded on 500 MHz NMR. For $A\beta_{11\text{-}28}$ and $A\beta_{1\text{-}28}$: [Aβ] = [complex] = 500 µM, [PB] = 50 mM, pH = 7, total ACN content of 10%. Spectra recorded on 400 MHz NMR.*

I.3. Investigation of recognition patterns

Among the metal complexes tested, the best interaction with fibres seems to be achieved by **L**^{1} and **L**^{3} complexes. To better understand what the recognition motif in these structures is, we compared the interaction of different fragment molecules with Aβ$_{1\text{-}40}$ fibres.

I.3.a. Incorporation of fragment molecules

(a) Case of L^1 complexes

Table 12 displays the results obtained for incorporation of fragment molecules of **L**^{1} in Aβ$_{1\text{-}40}$ fibres.

Table 12: Insertion of fragment molecules from L^1 complexes in Aβ$_{1\text{-}40}$ fibres during aggregation process. Conditions: *[Aβ$_{1\text{-}40}$] = 50 μM, [Th-T] = 10 μM, [PB] = 50 mM, [compound] = 50 μM, pH = 7, ACN 5%.*

Compound	**Structure**	**% Inserted**
Fe(**L**^{1})$_2$	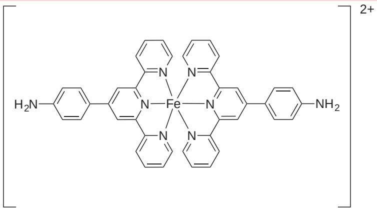	81
Ru(**L**^{1})$_2$	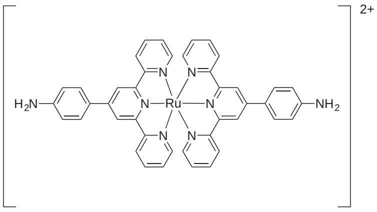	55
Ru(**tpy**)$_2$	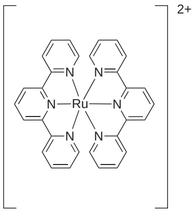	3
L^1	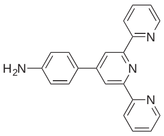	42
Aniline	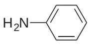	8

Several observations arise from these results. Firstly, the presence of *p*-amino phenyl on the terpyridine appears crucial for the interaction. Though, the result obtained with aniline shows that this motif is not sufficient to promote interaction. A hypothesis would be that the presence of three aromatic rings is required to promote interaction.

Secondly, the interaction of fibres with $\mathbf{L^1}$ metal complexes is similar to that with free $\mathbf{L^1}$. Because the ligands are in perpendicular planes, it is unlikely that they have additive contributions to the interaction. From this, one can conclude that interaction is predominantly promoted by ligand.

Finally, the shift from Fe(II) to Ru(II) seems to slightly decrease the interaction. These complexes being isostructural, there is no structural reason for this difference.

(b) Case of L^3 complexes

Similar experiments were run for $\mathbf{L^3}$ complexes, the results appear in Table 13.

Table 13: Insertion of fragment molecules from L^3 complexes in $A\beta_{1-40}$ fibres during aggregation process. Conditions:

$[A\beta_{1-40}]$ = 50 μM, [Th-T] = 10 μM, [PB] = 50 mM, [compound] = 50 μM, pH = 7, ACN 5%.

Compound	Structure	% Inserted
Fe($\mathbf{L^3}$)$_2$	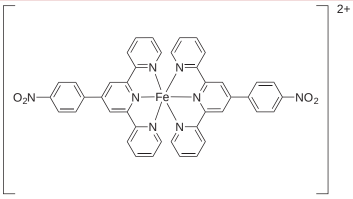	99
Ru($\mathbf{L^3}$)$_2$	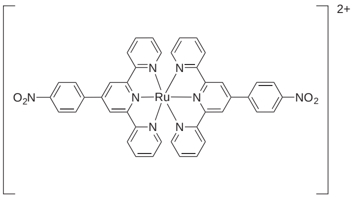	100
Ru(**tpy**)$_2$	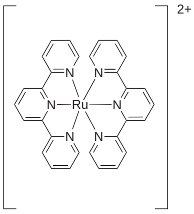	3
$\mathbf{L^3}$	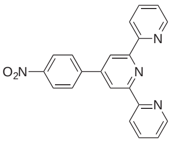	N/D

Here again, quantification of incorporated compounds seems to strongly rely on the presence of the *p*-nitro phenyl group on the pyridine, evidenced by the drop between Ru($\mathbf{L^3}$)$_2$ (100% inserted) and Ru(**tpy**)$_2$ (3% inserted). Contrariwise to $\mathbf{L^1}$ complexes, the switch from Fe($\mathbf{L^3}$)$_2$ to Ru($\mathbf{L^3}$)$_2$ does not affect the incorporation. Control experiment with $\mathbf{L^3}$ could not be achieved due to solubility issue.

I.3.b. STD NMR experiment

Another NMR experiment available to investigate peptide-complex interaction is Saturation Transfer Difference (STD). This technique relies on the fact that when a protein is irradiated to saturation, this saturation is transferred to its ligand by spin diffusion. In the case of weak-binding ligands (K_d from 10^{-8} to 10^{-3} M), the signal of bound ligands should then decrease. The STD spectrum is obtained by subtracting this saturation spectrum to a standard one (*i.e.* without protein saturation). The signals appearing on the STD spectrum correspond to hydrogen atoms of the molecule interacting with the protein [224]. Figure 49 displays spectra obtained for STD experiment with monomeric Aβ_{1-40} in the presence of Fe($\mathbf{L^1}$)$_2$. Three signals appear on the difference spectrum (middle) corresponding to Fe($\mathbf{L^1}$)$_2$. These peaks do not appear on control spectrum (bottom). This attests of a weak interaction between the complex and the peptide. Despite a low resolution, it seems that the signal of protons 3' and 5' (*ca*. 9 ppm) and of protons 5, 5", 6 and 6" (*ca*. 7.3 ppm) are the more intense, and would thus be the more involved in interaction. Figure 49.B shows the numbering scheme of $\mathbf{L^1}$, protons involved in interaction appearing in red. On this scheme, all the protons were represented on one ligand for simplification, but they could also be distributed on both ligands. However, because ligands are in perpendicular planes, it is unlikely that the same protons of both ligands interact in the same way with the fibre.

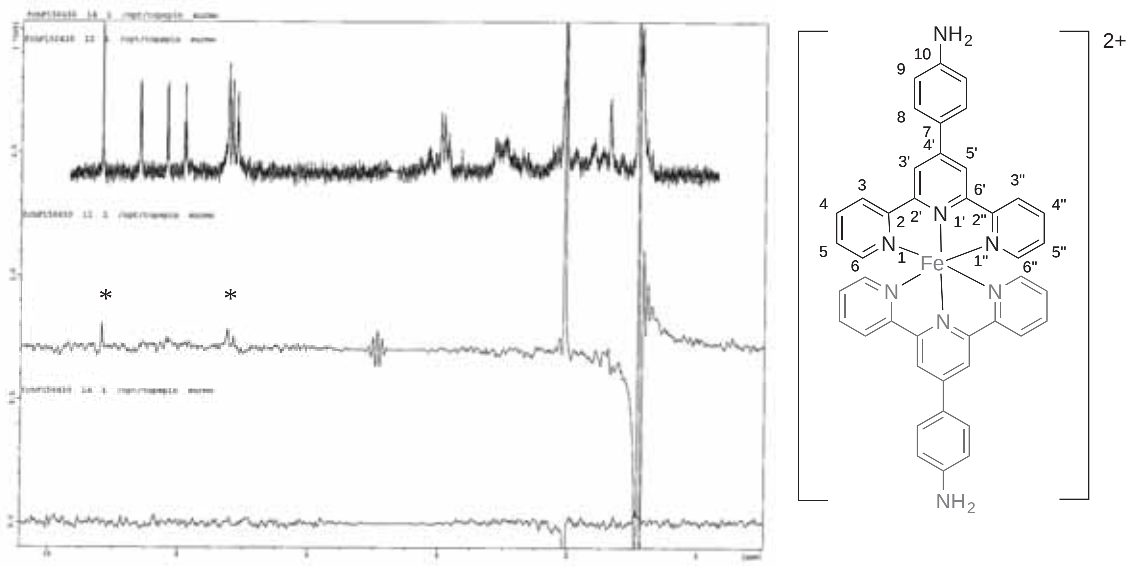

Figure 49: STD NMR experiment. A: *Top: ^{1}H NMR of Aβ_{1-40} with Fe(L^1)$_2$. Middle: STD difference spectrum.* indicates appearing signals. Bottom: control without Aβ_{1-40}.* ***B:*** *Numbering scheme of Fe(L^1)$_2$, atoms in red are those displaying signals on STD spectrum.* ***Conditions:*** *[Aβ_{1-40}] = 50 μM, [PB] = 50 mM, [Fe(L^1)$_2$] = 1 mM, pH = 7. Spectra recorded on 500 MHz NMR.*

I.3.c. Conclusion: Recognition pattern

Athought it is difficult to define a precise recognition pattern in our complexes, several points can be underlined. Firstly, the presence of a phenyl ring on the terpyridine ligand holding a *p*-amino or *p*-nitro group is mandatory to get interaction. However, phenyl amine alone is not sufficient to promote interaction. The presence of metal ion slightly modifies the interaction, indicating that interaction properties are mainly held by ligands. In complexes, the two *p*-amino phenyl terpyridine ligands are in perpendicular planes, centred on the metal ion (Scheme 31.A). It is thus unlikely that both side pyridines of a ligand could interact with fibres at the same time. All of this led us to consider the minimal recognition motif as constituted by a lateral pyridine, the central pyridine, and the phenyl ring, as appears in red on Scheme 31.B.

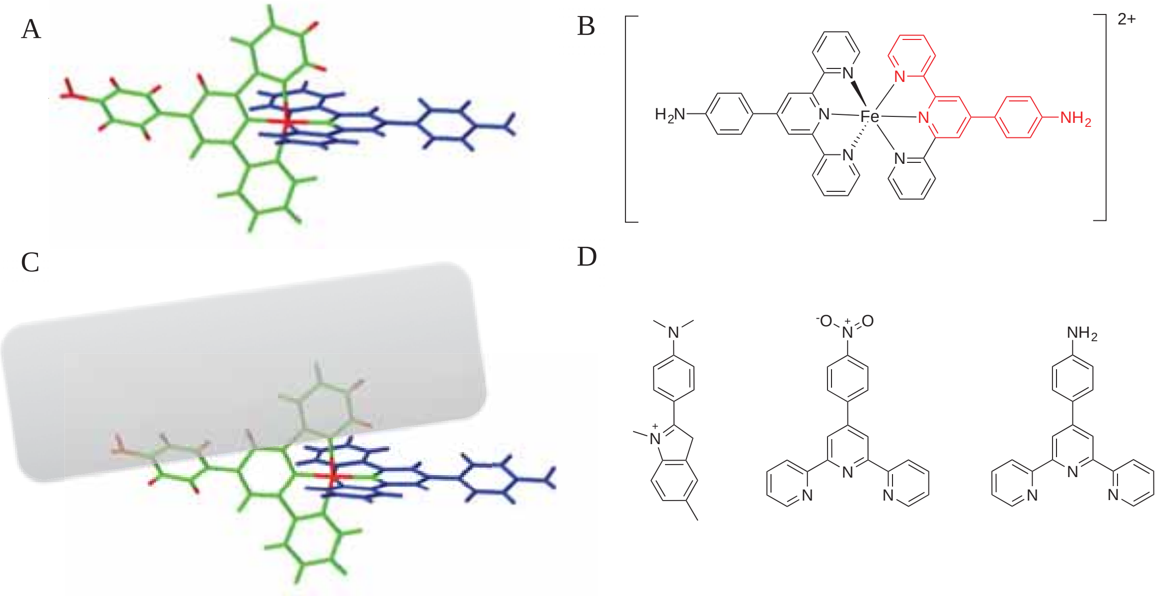

Scheme 31: Interaction pattern of metal complexes. A*: Fe(L^1)$_2$ crystal structure, atoms proved to be involved in interaction appear in red;* ***B:*** *Interaction pattern on Fe(L^1)$_2$.* ***C****: Proposed model for fibre binding. Grey rectangle represents amyloid fibre.* ***D****: structure similarities between Th-T, L^3 and L^1.*

From this, we imagined a binding model for Fe($\mathbf{L_1}$)$_2$ that encompasses the different interactions observed experimentally, *i.e.* with the amino group, the phenyl ring, and a side pyridine (Scheme 31.C). This model is very preliminar, considering fibres as linear channels.

When comparing structures, a similarity is observed between Th-T and $\mathbf{L^1}$ and $\mathbf{L^3}$, all of them being composed of a phenyl substituted by a nitrogen group (either nitro or amino) and by an aromatic heterocycle in para position (either pyridine or benzothiazole) (Scheme 31.D). This motif is found in various amyloid probes [173]. Both Th-T and metal complexes are also positively charged, the charge being higher (+II) but farther from the phenyl ring in the case of metal complexes.This motif could serve as a starting point for elaboration of probes for Aβ fibres (see Chap 5).

The only method that would enable concluding unambiguously on the location of metal complex binding sites on Aβ$_{1-40}$ fibres would be ssNMR. Unfortunately, we did not dispose of sufficient amounts of materials to run such experiment. To better understand this system, we performed computational studies, seeking to identify molecular determinants involved in interactions.

II. Modelling hybrid systems

II.1. General considerations

Computational approaches enable to overcome the lack of experimental data and provide insightful structural information. Among these techniques, molecular docking constitutes a convenient way to predict the possible binding sites of a ligand in a protein. It can also provide some indication regarding their binding affinity. However, the lack of crystallographic structure of amyloid fibres is a real issue. Because they are hierarchically assembled in one dimension, no crystal formation can be envisaged. To overcome this limitation, several studies proposed 3D structural models for $A\beta_{1\text{-}40}$ and $A\beta_{1\text{-}42}$ based on NMR experiments. These structures are of lower resolution compared with crystallographic structures, and are generally composed of 10 models, all satisfying experimental data.

Using the 10 models, docking experiments were first carried out using Th-T as ligand. Docking results, in terms of binding site location and binding energies were then used as reference for comparison with docking of complexes. Molecular docking experiments were run with metal complexes, seeking possible interaction sites. Because we had no presupposition on the location of binding site(s), the whole fibre was considered. The fibre being constituted of repeating units, we chose to consider amino acid side-chain channels as single binding sites. Docking protocol is described in Annex I.

II.2. Amyloid-β 1-40

II.2.a. Available structures

Among the available structures of $A\beta_{1\text{-}40}$ fibres in the Protein Data Bank (PDB), we chose to focus on the solid state NMR-structure of PDB code 2LMN [141], which was previously used for docking experiments [225,226]. Fibre is composed of two filaments, made of six peptides each. Structure 2LMN is constituted of 10 models, each fitting with experimental data.

Figure 50.A shows the model 1 of structure 2LMN. It is composed of two filaments, each of them having a β-turn shape. Hydrophobic residues (red) are mainly pointing inwards β-turns, whereas polar (green), acidic (blue) and basic (yellow) residues are pointing outwards. The two filaments are stacked by their most hydrophobic face (*i.e.* residues 31-37). Amino acids involved in β-turn stabilization are Phe19, Ile32 and Leu34, whereas residues Gly33 and Met35 promote inter-filament interaction.

When comparing all 10 models of 2LMN structure, it appears that both filaments contain some rigid regions, whereas other regions are more flexible (conformationally variable). Figure 50.B shows a superposition of models 1, 5 and 10 for the first peptides of each filament. It reveals that residues 17-22 and 31-36 (blue) are well superposed, indicating no conformational variability. Contrariwise, conformation of residues 9-16, 23-30 and 37-38 appears to vary significantly upon the model (red). This enables to distinguish two types of regions, either rigid or flexible.

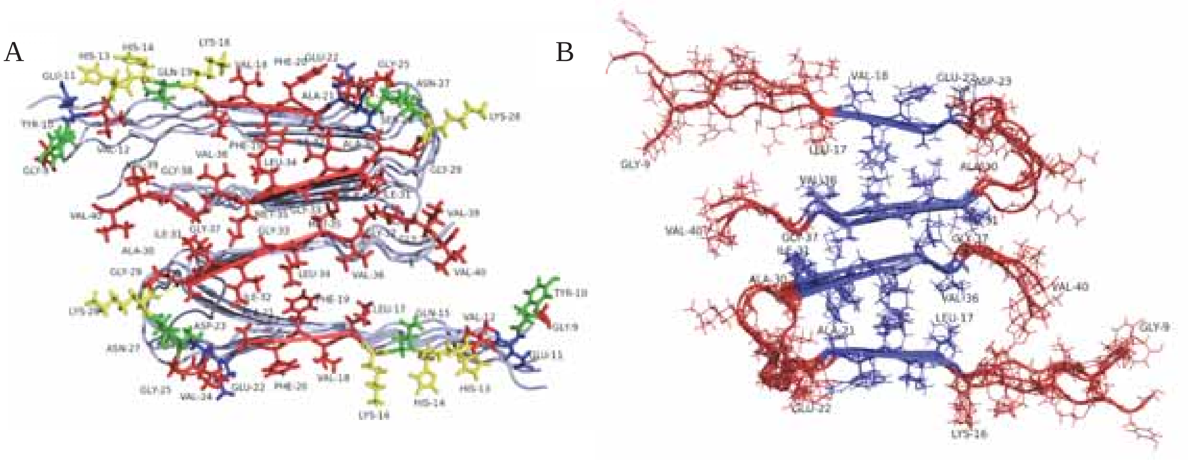

Figure 50: Solid-state NMR structure of ***Aβ_{1-40} fibres (PDB code: 2LMN). A:*** *2LMN model 1. Red: non-polar residues, green: polar residues, yellow: basic residues, blue: acidic residues. Side-chains of peptides 2-6 and 8-12 are omitted for clarity.* ***B:*** *Superposition of models 1, 5 and 10 of the first peptides each filament. Regions in blue are rather rigid, whereas regions in red are more flexible.*

II.2.b. Docking: Th-T

The first step of our docking study consisted in testing the different models of 2LMN to choose one that would be representative for further studies. To do so, we chose Th-T as a model ligand, as its interaction with fibres is experimentally validated (see Chapter I.III.2.a). The results obtained are summarized in Table 14. Three main sites are highlighted: in the channel delimited by Ala21 and Ile32 (site A), at the interface between filaments between Ile31 and Val39/40 (site B), and in the β-turn between Val36 and Gln15 (site C). The corresponding sites are highlighted in Figure 51.

Table 14: Percentages of docking solutions and corresponding energies obtained for the docking of Th-T on the different models of 2LMN. *Results in bold highlight the main binding site.*

Model	**Site A**		**Site B**		**Site C**	
	Percentage of solutions (%)	Lowest binding energy (kcal/mol)	Percentage of solutions (%)	Lowest binding energy (kcal/mol)	Percentage of solutions (%)	Lowest binding energy (kcal/mol)
1	28	-8.31	**64**	-7.17	7	-6.43
2	**42**	-7.62	9	-6.42	9	-6.35
3	20	-7.31	**71**	-7.30	3	-6.62
4	19	-8.18	33	-7.32	**46**	-6.87
5	14	-7.91	**50**	-7.68	22	-7.80
6	**53**	-8.61	3	-6.99	38	-7.72
7	**42**	-7.56	20	-7.47	21	-7.18
8	46	-8.39	0	/	**52**	-7.17
9	32	-8.36	0	/	**64**	-9.60
10	3	-7.23	**42**	-6.80	32	-6.83

The existence of three different binding sites for Th-T has been reported in literature, without evidence on the involved residues [227]. When comparing the three sites, it appears that the percentage of solutions for each site varies significantly from a model to another, and it seems that solutions are distributed along the three sites, with distinct populations. The important dynamic character of binding sites can explain this important variability. Indeed, the three sites reported are located at the interface between the “flexible regions” and the “rigid regions” previously described. The important mobility of the backbone in flexible regions can prevent Th-T insertion in some models, and promote binding into others. In all cases, Th-T is positioned into grooves parallel to the fibre axis, as reported in literature [132,228,229].

To be able to compare complexes and Th-T binding sites, we chose to work with a model in which the three binding sites for Th-T are accessible. For further studies with metal complexes, model 7 was thus chosen as an average model of 2LMN.

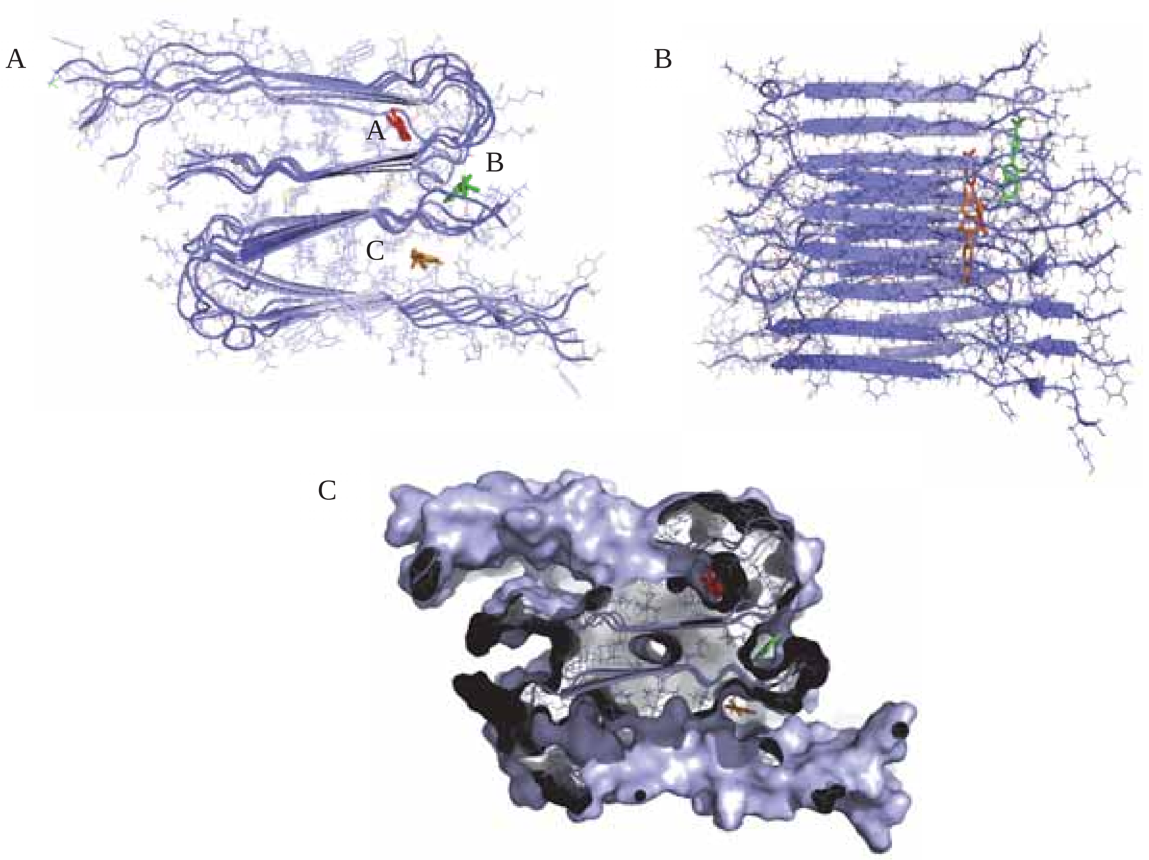

Figure 51: Representation of 3 distinct representative docking modes of Th-T in 2LMN model 1. A: *Top view,* ***B:*** *side view,* ***C:*** *molecular surface representation. Th-T binds either in site A (red), site B (green) or site C (yellow). Corresponding symmetric binding sites are omitted for clarity.*

II.2.c. Docking: Fe(L^1)$_2$ and Fe(L^3)$_2$

Docking experiments were run for Fe(**L^1**)$_2$ and Fe(**L^3**)$_2$ into 2LMN model 7. A vast majority of solutions (100% for Fe(**L^1**)$_2$, 87% for Fe(**L^3**)$_2$) positioned metal complexes at the end of the fibre (Figure 52). The corresponding binding energies are very favourable (-9.6 kcal/mol). This experiment thus confirms that unlike Th-T, metal complexes cannot intercalate in grooves of β-turns, or at the interface of filaments. Of note, no binding site on the external faces of fibre was observed. This could be due to the fact that the 2LMN structure is only constituted of six peptides, which is not enough to model the fibre amino-acid side-chain channels.

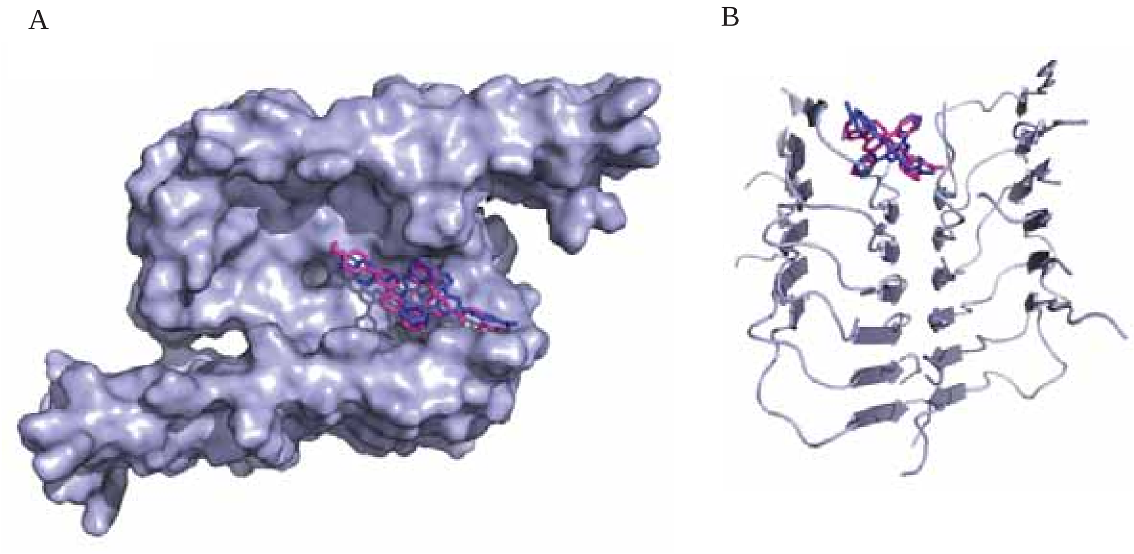

Figure 52: Representations of docking modes for Fe(L^1)$_2$ (blue) and Fe(L^3)$_2$ (pink) into 2LMN model 7. A: *molecular surface representation,* ***B:*** *side view.*

II.3. Amyloid-β 1-42

II.3.a. Available structures

Only two structures of Aβ_{1-42} fibres can be found in the Protein Data Bank, referred as 2MXU [145] and 2BEG [144]. 2MXU was preferred for our study, as it is more recent and better resolved, since benefitting from better technical advances than for 2BEG. It also consists of more peptide repeating units than 2BEG, which fits better the side chain channel model. Of note, the recent 2MXU structure has never been used for docking experiments in the literature. The docking of Th-T was performed to validate the use of 2MXU as fibre model.

Solid-state NMR structure 2MXU is composed of 12 assembled peptides forming two successive β-turns. As for Aβ_{1-40} model, non-polar amino acids are mostly pointing inwards β-turns, whereas polar, acidic and basic ones are mostly pointing outwards (Figure 53.A). A saline bridge between Lys28 and the C-term carboxylate further stabilizes the system. 2MXU is composed of 10 models, each of them satisfying NMR constraints. Figure 53.B shows the superposition of models 1, 5 and 10 of the first peptide chain. It appears that the conformation of the peptide remains quite similar among the 10 models, the only conformational differences were observed in regions being between Leu34 and Val36 and between Lys16 and Glu11 (residues in red). Overall, amino acid side-chains adopt similar orientations (residues in blue).

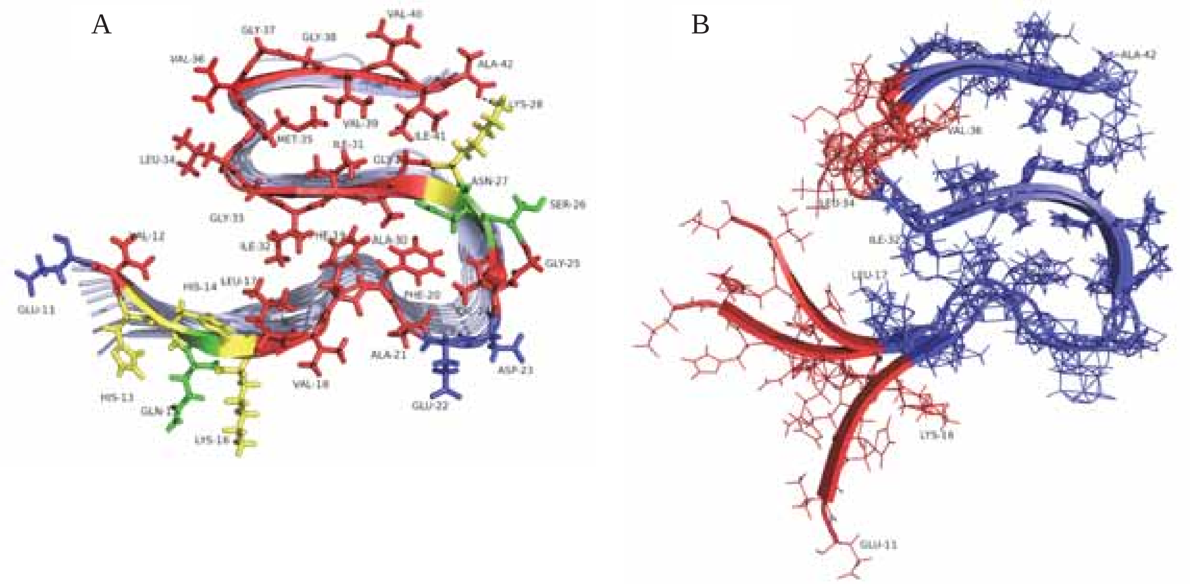

Figure 53: 2MXU model structures for Aβ_{1-42} fibres. A: *2MXU model 1. Red: non-polar residues, green: polar residues, yellow: basic residues, blue: acidic residues. Side-chains of peptides 2-10 are omitted for clarity.* ***B:*** *Superposition of models 1, 5 and 10 of the first peptide. Regions in blue are rather static, whereas regions in red are more dynamic.*

II.3.b. Docking: Thioflavin-T

Th-T was docked using the 10 models of 2MXU and considering the whole fibre as protein receptor. The results obtained are clear-cut, showing selectivity of Th-T for the channel formed by Ile32 and Leu34 (Table 15). Only two models (models 2 and 4) differ led to different results, what can be explained by important conformational changes: In model 2, the Ile32-Leu34 channel does not exist, Leu34 pointing inward the β-turn. In model 4, a large cavity is present between Ile31 and Val39, which hosts Th-T. All other models are in agreement to placeTh-T along the channel Ile32-Leu34.

This result validates the use of 2MXU for docking studies: A major solution is found for 8 models over 10, which is consistent with previously reported side-chain channels binding model of Th-T. Because all the models (except 2 and 4) afford similar binding sites of similar binding energies, we selected model 1 as an average model for the following studies of complex docking (Figure 54).

Table 15: Main docking mode observed for Th-T in the 10 different models of 2MXU and corresponding binding energies corresponding to channel Ile32-Leu34.

Model	**Ile32-Leu34**	
	Percentage of solutions (%)	Lowest binding energy (kcal/mol)
1	86	-7.57
2	37	-5.56
3	88	-6.80
4	15	-8.27
5	95	-6.29
6	75	-7.04
7	69	-7.04
8	79	-7.15
9	73	-7.60
10	99	-8.21

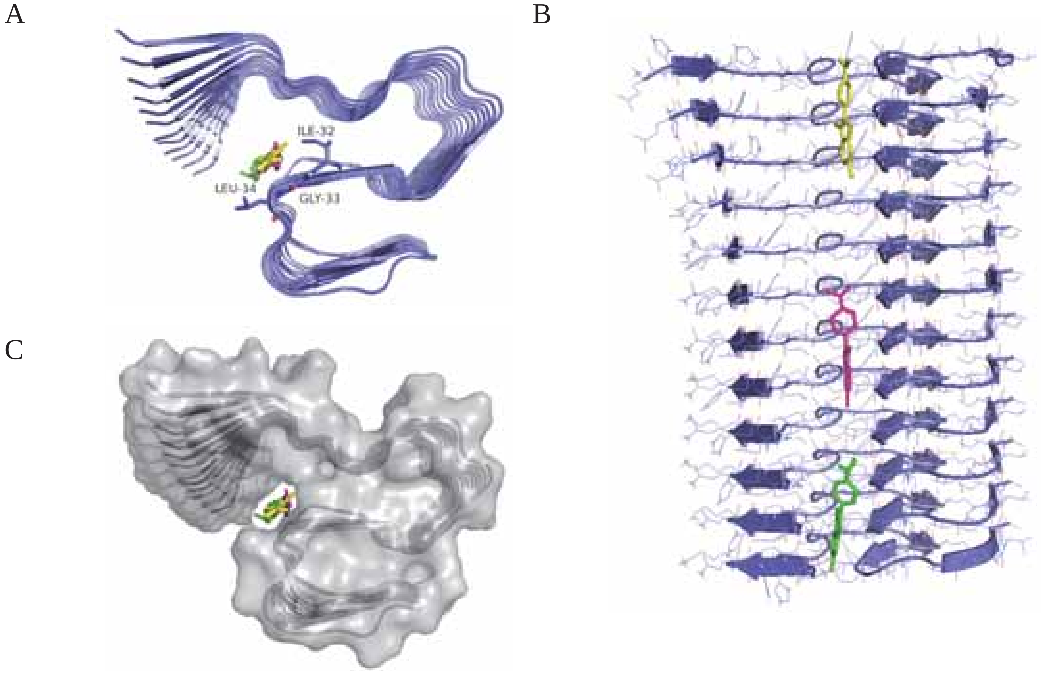

Figure 54: Representative docking modes of Th-T in 2MXU model 1. A: *Top view,* ***B:*** *Side view,* ***C:*** *molecular surface representation. Three representative docking poses of Th-T in the Ile32-Leu34 channel are depicted in yellow, pink, green, respectively.*

II.3.c. Docking: $Fe(L^1)_2$

Similar docking experiment was run with $Fe(L^1)_2$. Contrarily to Th-T, three different binding sites come apart: between Glu22 and Asp23 (site A), between Asp23 and Gly25 (site B), and between Ile32 and Leu34 (site C). Distribution of docking solutions among the three sites (A, B, and C) and associated lowest binding energies calculated at each site appear in Table 16, and corresponding representations are shown in Figure 55.

Table 16: Main docking sites identified by docking of $Fe(L^1)_2$ in 2MXU model 1.

	Site A (Glu22-Asp23)	**Site B (Asp23-Gly25)**	**Site C (Ile32-Leu34)**
Docking solutions (%)	53	25	18
Lowest binding energy (kcal/mol)	-6.47	-6.50	-7.05

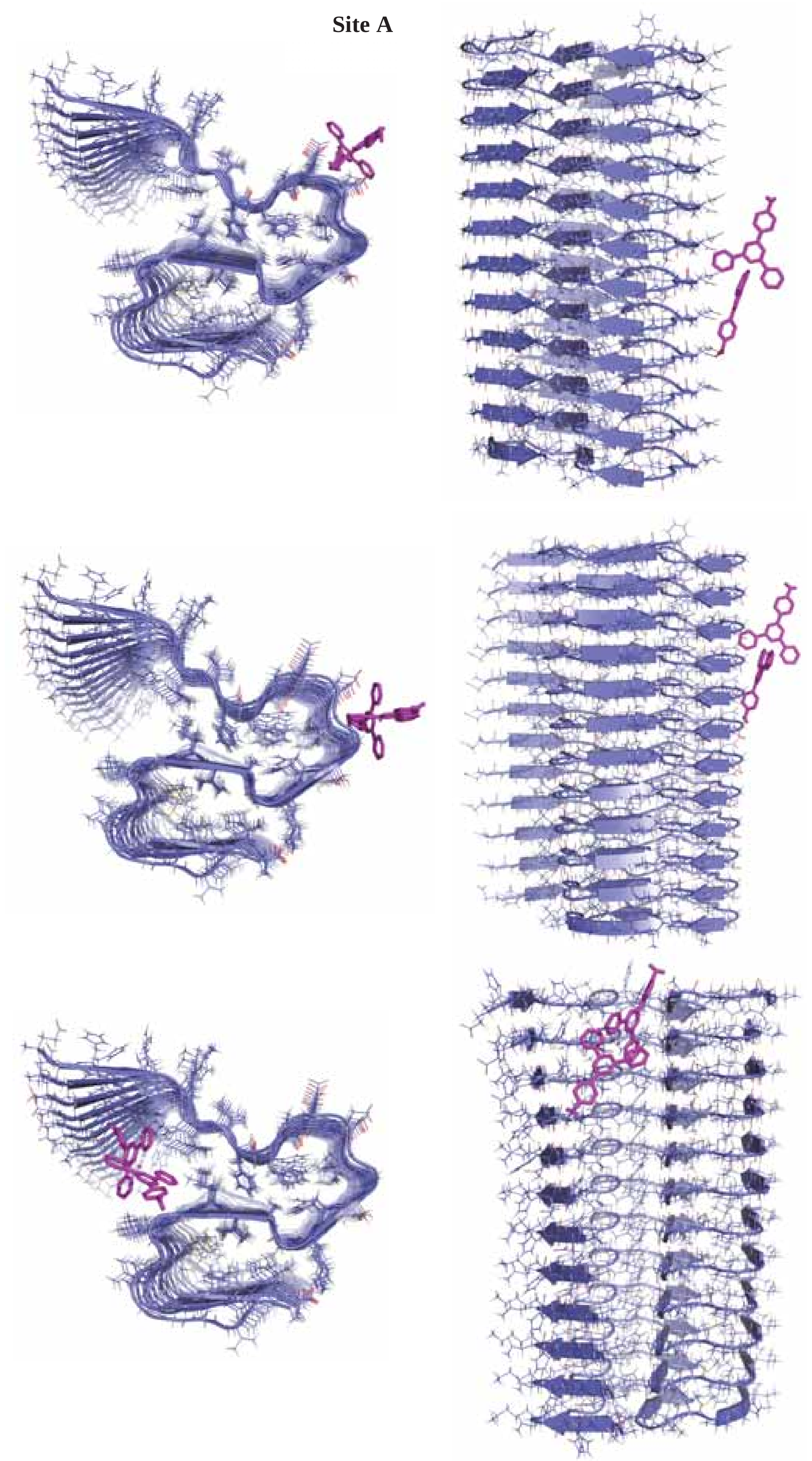

Figure 55: Representative docking poses obtained for Fe(L^1)$_2$ in 2MXU model 1.

Site A proposes a binding of Fe(**L^1**)$_2$ along the channel between Glu22 and Asp23. This site is stabilized by two hydrogen bonds between an amino group of Fe(**L^1**)$_2$ and the two carboxylate group side-chains of Glu22 and Asp23. The interaction involves the two terpyridine ligands of the metal complex, one interacting by the amino phenyl moiety, and the other one interacting by a lateral pyridine.

Site B is close to site A, Fe(**L^1**)$_2$ being positioned along the channel between Asp23 and Gly24. Here again, the two terpyridine ligands on Fe(**L^1**)$_2$ are involved in interaction, but only one hydrogen bonding interaction stabilizes the system. The binding energy is also comparable to result A. These two sites are located in regions where the conformation is maintained, and involve residues keeping similar orientation in the different models.

Contrariwise, site C constitutes an “energetically favoured” binding site, but not frequently observed. Unlike other results, complex is not distributed along the channel, but localized at the entrance of the fibre, and no polar contacts are evidenced between Fe(L^1)$_2$ and fibre. More importantly, some residues involved in interaction undergo significant conformational variability (region 11-16), and the interaction might be weakened if considering fibre dynamics.

This first docking experiment provides information on Fe(**L^1**)$_2$ binding: (a) Firstly, it validates that Fe(**L^1**)$_2$ can bind in side-chain channels of the fibre. (b) It also confirms the experimental evidence that the binding of Fe(**L^1**)$_2$ at Th-T site is not favourable. The main binding site for Fe(**L^1**)$_2$ is on one side or the other of Asp23, with similar predicted binding energy of -6.50 kcal/mol. From this, Fe(**L^1**)$_2$ seems to be a slightly weaker ligand than Th-T. (c) According to calculations, interaction between fibres and metal complexes is promoted by the amino phenyl moiety and one lateral pyridine. This is in good accordance with experimental observations.

II.3.d. Docking: Fe(L^3)$_2$

Similarly to Fe(**L^1**)$_2$, docking studies were conducted with Fe(**L^3**)$_2$ using 2MXU model 1 as receptor. Two main binding sites were observed, whose percentage of solutions and energies appear in Table 17.

Table 17: Main binding sites identified by docking of Fe(L^3)$_2$ in 2MXU model 1.

	Site A **(Ile32-Leu34)**	**Site B** **(Glu11-His13)**
Docking solutions (%)	69	13
Lowest binding energy (kcal/mol)	-8.08	-6.39

The main docking pose places Fe($\mathbf{L}^3$)$_2$ at the entrance of the first β-turn (Figure 56 site A). Metal complex is positioned slantwise, interacting with both sides of the β-turn motif. On one side, Fe($\mathbf{L}^3$)$_2$ is positioned in the channel Ile32-Leu34 (Th-T binding site). On the other side, stacking with His14 and H-bonding with NH_2 from Glu11 are observed. The predicted binding energy for this position is slightly better than for Th-T. However, it is to remind that His14 and Glu11 are highly flexible among the different models (see II.3.a). Furthermore, the N-ter amine on Glu11 does not exist on WT-A$\beta_{1\text{-}42}$. The interaction of Fe($\mathbf{L}^3$)$_2$ in this site is thus likely to be decreased if considering full-length A$\beta_{1\text{-}42}$. Molecular Dynamic simulations could be considered to validate this first result.

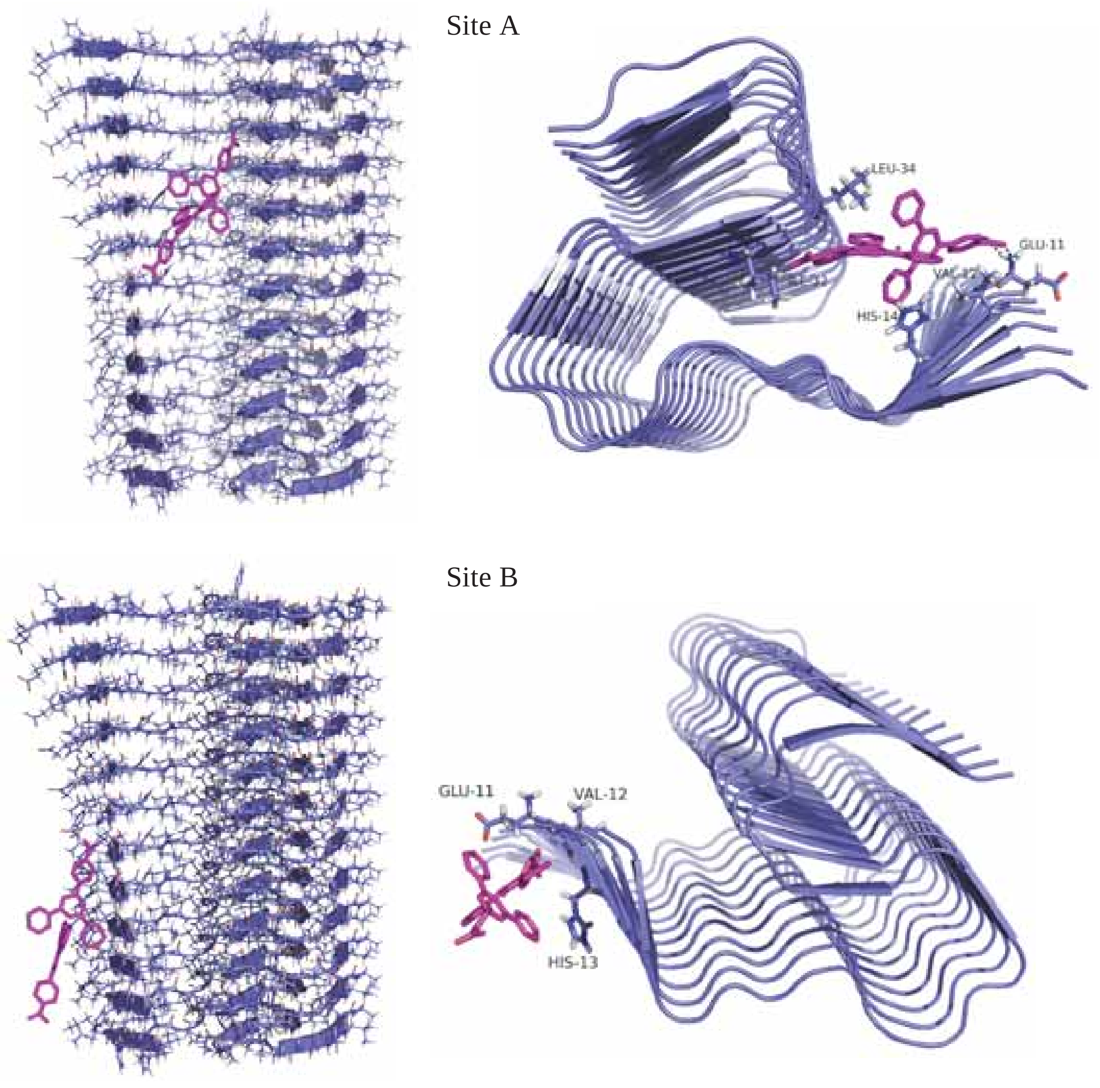

Figure 56: Representative docking poses of Fe(L^3)$_2$ in 2MXU model 1. A: *Fe(L^3)$_2$ binding in site A, interacting with Ile32, Leu34, His14 and Glu11.* ***B:*** *Fe(L^3)$_2$ binding in site B, interacting with Glu11 and His13.*

The other docking mode positions Fe(L^3)$_2$ in the channel between Glu11 and His13 (Figure 56 site B). The interaction being promoted by a single ligand, and no polar contact was found between the complex and the fibre. Expectedly, the calculated energy is thus weaker than for the main site A. Here again, the important dynamic character of the residues involved in the interaction has to be considered, and Molecular Dynamic simulations could be beneficial to further investigate this interaction.

From these results, it seems that Fe($\mathbf{L}^3$)$_2$ is able to bind A$\beta_{1\text{-}42}$ fibres, mainly interacting with residues of flexible character. Calculated binding energies are in the same range as for Th-T, but could potentially improve when considering the dynamic character of the fibre.

II.4. Conclusion: docking studies

- Th-T

These docking studies provide insightful information on Th-T binding with fibres. First of all, it confirms the experimental evidence that Th-T binds in side chain channels, its axis being parallel to the fibre axis in both fibre models. In the case of A$\beta_{1\text{-}40}$, molecular docking suggests that Th-T intercalates inside the β-turn motif, and between filaments, whereas with A$\beta_{1\text{-}42}$, the β-turn is too packed, and Th-T intercalates in a channel at the entrance of the main β-turn. In both models, Th-T binds at the interface between rigid and flexible regions, with estimated binding energies nearly similar.

- Fe($\mathbf{L}^1$)$_2$

Docking with A$\beta_{1\text{-}40}$ model only yielded binding sites at fibre extremities, probably due to too few repetition units in the fibre model. From study with A$\beta_{1\text{-}42}$ fibre model, Fe($\mathbf{L}^1$)$_2$ appears to be able to bind fibres in side-chain channels. The interaction is promoted by both ligands, and stabilized by H-bond interactions between the amino group on terpyridine and carboxylate side chains of amino acids. The calculated binding energy is slightly higher than for Th-T. This binding mode is fully compatible with experimental observations, interaction being promoted by amino-phenyl group and lateral pyridinyl rings of terpyridine (see Chapter IV.I.3.).

According to this study, Fe($\mathbf{L}^1$)$_2$ should also be able to bind at Th-T binding site with low binding energy. However, because amino acid residues involved in this interaction have important flexibility, this might be unfavoured when considering fibre dynamics. Here again, this is consistent with the experimental evidence of low affinity of metal complexes for Th-T binding sites (see Chapter IV.I.2.a).

- Fe($\mathbf{L}^3$)$_2$

Fe(L^3)$_2$ appears less prone to bind in side-chain channels, probably because of the lack of stabilizing H-bonds. Yet, a solution positioning Fe($\mathbf{L}^3$)$_2$ in the channel between Glu11 and His13 is obtained, with a moderate energy. But the main docking solution remains Th-T binding site, in which the binding is of low energy. Here again, both results involve amino acids with high dynamic character, interactions thus have to be confirmed by molecular dynamic simulations.

Docking studies thus enabled a first confirmation that metal complexes could bind fibres at binding sites different from Th-T. Interaction involves the phenyl ring and a pyridine ring, either from a single ligand or from both. Calculated binding energies are in the same range as Th-T. However, molecular dynamic simulations would be mandatory to explore in details inter-molecular interactions.

Conclusion

This study showed that some of the synthesized metal complexes were able to interact with Aβ_{1-40} fibres. Interestingly, their interaction is modulated by the substituting group on the phenyl terpyridine ligands: amine, nitro, and bromo groups seem to promote interaction, whereas carboxylate seems to prevent it. M(**tpy**)$_2$ complexes display no incorporation within fibres, confirming the importance of the extended aromaticity. Contrariwise, the nature of the metal ion has no effect on interaction, which is of interest for future catalytic applications. Upon interaction, Ru complexes display a shift in absorbance together with an increase of fluorescence, which is in accordance with a shift from aqueous to hydrophobic environment. These complexes could thus constitute new probes for Aβ aggregation.

Investigations on the precise localization of complexes within fibres remain tough, due to the insoluble nature of fibres and to their polymorphism. Yet, a first result shows a specificity of interacting metal complexes for Aβ_{1-40} fibres compared with shorter amyloid peptides. This suggests that our complexes might recognize specific binding site(s) on Aβ_{1-40}, and not only the general side-chain channel motif.

To further investigate this question, docking studies were performed with Fe($\mathbf{L}^1$)$_2$ and Fe($\mathbf{L}^3$)$_2$ on ssNMR models of Aβ_{1-40} and Aβ_{1-42} fibres. Results tend to show that metal complexes cannot intercalate into Th-T binding site, confirming experimental data. They also demonstrate the possible binding of metal complexes along the side-chain channels of fibres. To support these results, an experimental study with various mutants of Aβ_{1-40} would be of interest, seeking for residues that influence interaction.

Chapter V. Towards hybrid bioinorganic catalysts

Introduction

The objective of this thesis is the development of new hybrid catalysts made by incorporation of coordination complexes into amyloid fibres. In a first step, a library of complexes was synthesized and evaluated for their interaction with fibres (Scheme 32, arrow 1). The next step to progress towards our goal is to test metal complexes for their catalytic activity regarding benchmark reactions (Scheme 32, arrow 2). Once the reaction conditions optimized, the catalytic activity when incorporated into fibres must be demonstrated to make the proof of concept on the potential of the hybrid catalysts. Observations coming from interaction and catalytic studies provide clues for hybrid catalyst improvement, including modifications on the metal complex and on the peptide.

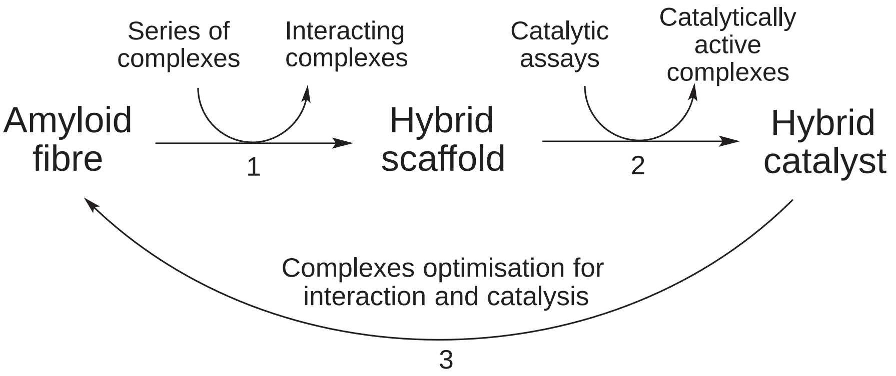

Scheme 32: Representation of the different steps for hybrid catalyst elaboration and optimisation.

This chapter describes preliminary results for our systems, and proposes evolution outlooks.

The first part describes the optimization of styrene epoxidation as catalytic benchmark reaction using our Fe(II) bis terpyridine complexes.

In a second part, preliminary results obtained in catalysis with our hybrid catalyst candidates are presented.

Lastly, different optimisation routes are proposed, considering requirements for both catalysis and fibre-complex interaction. This would constitute a first optimisation cycle for our hybrid catalysts (Scheme 32, arrow 3).

I. Iron terpyridine complexes as catalysts

I.1. State of art on iron terpyridine complexes in catalysis

Organic chemistry abounds with examples of Fe complexes used in catalysis. Reactions include substitutions, additions, eliminations, cycloadditions, metathesis, reductions and oxidations [230].

Among those, only a few reactions are described using Fe(tpy)$_2$-type complexes. In 2006, Beller and colleagues showed that acetophenone undergoes hydrogenation in the presence of iron salt together with tpy and phosphine ligands with perfect selectivity for the alcohol. This reaction occurs in refluxing iPrOH in the presence of base [189]. Subsequently, they showed that this system could also catalyze formic acid dehydrogenation in DMF with good TON [231]. But in these two examples, complexes are formed *in situ*, and without control experiments it is hard to conclude on the nature of the active catalytic species.

Yeung *et al.* also showed that Fe(tpy)Cl$_2$ catalyzed styrene cyclopropanation in the presence of ethyldiazoacetate in hot dichloromethane, with ee’s reaching 83% [232]. In 2012, Nakazawa’s group proposed to use Fe(tpy)X$_2$ complexes to catalyze alkene hydrosilylation. Reaction with 1-octene shows a TON of 1533 at 100°C for 24 h [233]. All these examples, although interesting, require mono terpyridine complexes, and work in harsh conditions *i.e.* in organic solvents at high temperature.

Alternatively, alkene epoxidation was shown to operate with bis terpyridine Fe complexes in biologically-compatible conditions. Che’s group developed 4,4’,4’’-substituted terpyridine Fe(II) complexes which catalyze epoxidation of alkenes using Oxone as oxidant (Scheme 33) [234]. The reaction operates in 5 mL of a ACN/water 2:1 mixture in the presence of 4 eq of ammonium bicarbonate, 1.3 eq Oxone and 5 mol% catalyst at room temperature, and is completed in 2 h. Conversion is obtained by GC analysis of the crude product or by ^{1}H NMR, after an extraction in diethyl ether. The control with Fe(**tpy**)$_2$ shows a decrease of conversion to 30%, whereas with FeSO$_4$ no conversion is observed. Reaction was tested on a series of 17 substrates, including electron-rich and electron-deficient aryl alkenes, steroids and allylic alkenes, showing conversions between 56% and 100%. Corresponding yields go from 42% to 96%, based on conversion. Although it is specified that

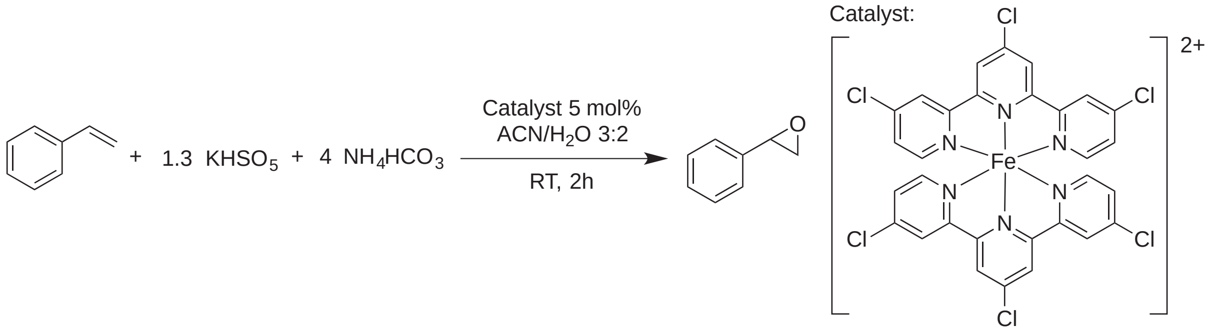

Scheme 33: Epoxidation reaction described by Che's group.

no diol formation is observed, there is no information on the nature of by-products observed. A subsequent study showed that this reactivity is conserved using oligopyridine Fe(II) complexes [235].

Because it was conducted under suitable conditions for our future hybrid catalysts, this reaction was chosen as a catalytic benchmark reaction to test on our FeL_2 complexes. The conditions proposed by Che's group were used as starting point, and the different parameters were optimized for our Fe(II) complexes.

I.2. Results

As a starting point, we chose to keep the same conditions as those reported by Che's group. We worked with styrene, to which we add 1.3 eq of Oxone, 4 eq of ammonium bicarbonate and 5 mol% $Fe(\mathbf{L^1})_2$ in 5 mL of a mixture ACN/H_2O 3:2. After 2 h shaking at RT, reaction medium was sampled and analysed by GC.

Preliminary results show 97% conversion after 2 h. Unexpectedly, a total of five products is detected: epoxide and diol, but also benzaldehyde, phenyl acetaldehyde, and 2-hydroxy 1-phenyl ethanone (Scheme 34).

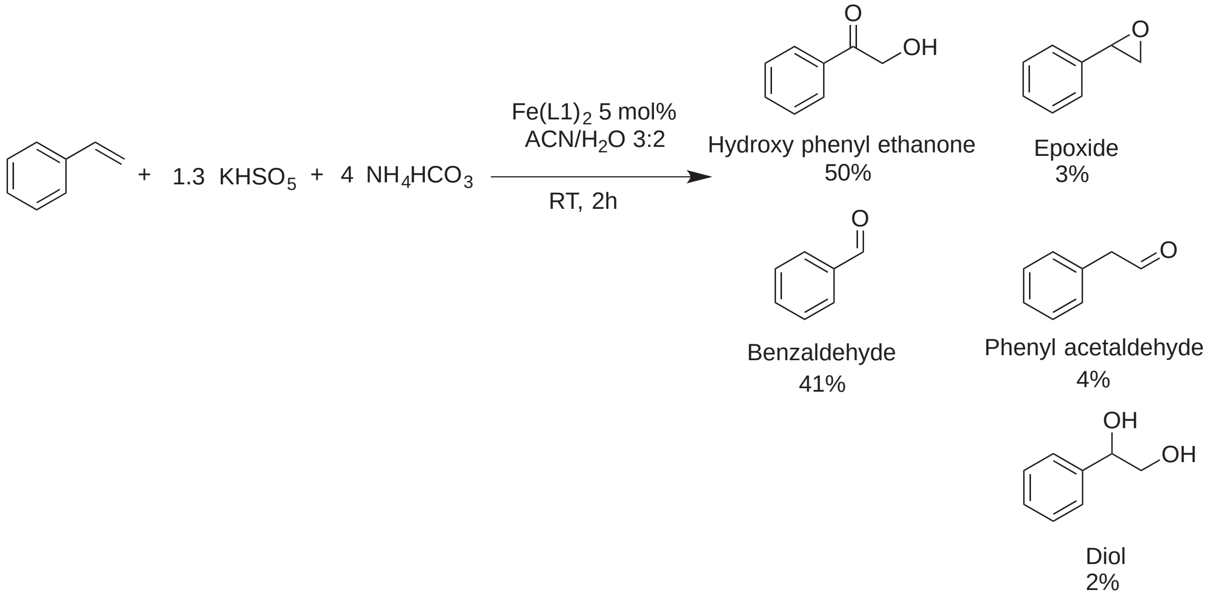

Scheme 34: Different products observed by GC for styrene epoxidation reaction.

Considering this result, we decided to study the effect of the different parameters of the reaction, trying to find conditions for which a single product would be obtained, if possible displaying an asymmetric carbon atom. To this aim, several points seemed of importance:

- **The catalytic charge required:** diminution of catalyst loading could be a way to limit substrate over-oxidation. Moreover, considering that amyloid fibres are available at μM scale, running reactions with low catalyst loadings would be of interest for hybrid catalysts.

- **The role of ammonium bicarbonate:** investigating the amount needed could allow concluding on its role in the reaction. In particular, its role of pH modulator should be considered.
- **Screening of oxidants:** studying various oxidative agents would allow finding the most suitable one for our specific reaction.
- **Screening of reaction conditions:** several reaction conditions, such as temperature or addition order could have an impact on product selectivity.

Those different points were investigated, looking for optimal reaction conditions. To this goal, we decided to scale down our experiments to 1 mL, enabling to run reaction in micro centrifuge tubes. Concentration of substrate was also lowered to 4 mM, which is in better accordance with the availability of our hybrid system (*ca* 50 μM metal complex). Reactions were run in a Thermomixer and samples were analysed by GC using toluene as internal standard (see Annex I).

I.2.a. Effect of ammonium bicarbonate

A first investigation consisted in determining the ideal amount of ammonium bicarbonate to perform epoxidation reaction. Reaction was run at 60°C for 4 h, in different tubes containing various amounts of ammonium bicarbonate. Results obtained show that it should be used in 1eq *vs.* styrene, any higher amount being detrimental for conversion rates (Table 18). Interestingly, this corresponds to substoichiometric amount *vs.* Oxone. This salt would thus play a role of additive in the reaction.

Table 18: Effect of ammonium bicarbonate on conversion. Conditions: *styrene (4 μmol), $Fe(L^1)_2$ (0.04 μmol), oxone (20 μmol) in 1 mL ACN/H_2O 3:2, 60°C, 4h.*

NH_4HCO_3 eq	Conversion (%)	Major product
1	100	Benzaldehyde
2	94	Benzaldehyde
4	78	Benzaldehyde
25	33	Traces

To assess this first observation, we tried to replace ammonium bicarbonate by phosphate buffer pH 7 at 100 mM, trying to see if the reaction was promoted by pH stabilization. It resulted in a drop of conversion below 10%, confirming that the promoting effect of NH_4HCO_3 was not due to a stabilization of pH.

I.2.b. Effect of oxidant

- Amount of Oxone

In a first experiment, we assessed the amount of oxidant needed to complete the reaction. Reaction was run at 60°C for 4 h, using different amounts of Oxone freshly solubilized in water. Results show that 5 eq Oxone are required to achieve full conversion, yielding benzaldehyde. If using higher amounts, styrene is oxidized into 2-hydroxy 1-phenyl ethanone (Table 19). A discoloration of the solution is also observed, probably corresponding to the decomposition of metal complexes.

Table 19: Effect of Oxone amount on conversion rates. Conditions: *styrene (4 µmol), $Fe(L^1)_2$ (0.04 µmol), ammonium bicarbonate (8 µmol) in 1 mL ACN/H_2O 3:2, 60°C, 4h.*

Oxone eq.	Conversion (%)	Major product
1.25	2.8	Traces
2.5	45.4	Benzaldehyde
5	100	Benzaldehyde
10	100	2-hydroxy 1-phenyl ethanone
15	100	2-hydroxy 1-phenyl ethanone

- Comparison with other oxidants

Other oxidants, namely hydrogen peroxide and tert-butyl hydroperoxide were tested in the same conditions. Temperature was lowered to 25°C to avoid oxidant decomposition. Unfortunately, none of

Table 20: Effect of the oxidant on conversion rates. Conditions: *styrene (4 µmol), $Fe(L^1)_2$ (0.04 µmol), ammonium bicarbonate (8 µmol), oxidant (20 µmol) in 1 mL ACN/H_2O 3:2, 25°C, 4h.*

Oxidant	Additive	Conversion (%)	Major product
Oxone	NH_4HCO_3	100	Benzaldehyde
H_2O_2	/	0	/
H_2O_2	NH_4HCO_3	2.6	Traces
H_2O_2	AcOH	26	Traces
tBuOOH	/	0	/
tBuOOH	NH_4HCO_3	0	/

them afforded satisfying conversions (Table 20). The use of Oxone in presence of ammonium bicarbonate thus seems to be the best combination to oxidize styrene.

I.2.c. Effect of catalyst

- Catalyst loading

Several loadings of catalyst were also tested, our aim being to lower the catalytic charge as much as possible in our hybrid systems. Results show that catalytic charge could be lowered to 0.5 mol% without altering conversion (Table 21).

Table 21: Effect of catalytic charge on conversion. Conditions: *styrene (4 µmol), Fe(L^1)$_2$ (variable), Oxone (20 µmol), ammonium bicarbonate (8 µmol) in 1 mL ACN/H_2O 3:2, 60°C, 4h.*

Catalytic charge	Conversion (%)	Major product
0.5 mol%	100	Benzaldehyde
1 mol%	100	Benzaldehyde
3 mol%	100	Benzaldehyde

- Screen for catalysts

Our different metal complexes were tested for their catalytic activity on styrene epoxidation. Reaction was run at 37°C overnight using identical amounts of various metal complexes. Luckily, results showed that the interacting Fe($\mathbf{L^1}$)$_2$ and Fe($\mathbf{L^3}$)$_2$ are the most efficient, converting all styrene

Table 22: Screen of metal complexes. Conditions: *styrene (4 µmol), catalyst (0.04 µmol), oxone (40 µmol), ammonium bicarbonate (8 µmol) in 1 mL ACN/H_2O 3:2, 37°C, overnight.*

Compound	Conversion (%)	Major product
Fe($\mathbf{L^1}$)$_2$	100	2-hydroxy 1-phenyl ethanone
Fe($\mathbf{L^2}$)$_2$	72.8	Benzaldehyde
Fe($\mathbf{L^3}$)$_2$	100	2-hydroxy 1-phenyl ethanone
Fe(**bpy**)$_3$	36.4	Benzaldehyde
Fe(**salophen**)	9.9	Benzaldehyde
Ru($\mathbf{L^1}$)$_2$	51.3	Benzaldehyde
Ru(**bpy**)$_3$	18.3	Benzaldehyde

into 2-hydroxy 1-phenyl ethanone. The non-interacting **L^2**, **bpy** and **salophen** complexes are poorly efficient, and oxidize styrene into benzaldehyde only with moderate conversions (Table 22).

I.2.d. Effect of reaction conditions

- Temperature

Even though amyloid fibres have high heat resistance, moderate reaction temperature would be more suitable to ensure stability of our hybrid catalysts. Temperatures of 4, 25 and 60°C were tested on 4 h reactions, showing a moderate improvement of conversion rates.

Table 23: Effect of temperature on conversion rates. Conditions: *styrene (4 µmol), $Fe(L^1)_2$ (0.04 µmol), Oxone (20 µmol), ammonium bicarbonate (8 µmol) in 1 mL ACN/H_2O 3:2, 4h.*

Temperature	Conversion (%)	Major product
4°C	80.5	Benzaldehyde
25°C	94	Benzaldehyde
60°C	100	Benzaldehyde

- Addition order

Through our experiments, we noticed that the order of addition had an effect on the reaction. In particular, addition of oxidant before substrate leads to a rapid discoloration of the reaction mixture, and corresponds to a drop of conversion. This effect is less noted when Oxone is added as a powder than when it is freshly solubilized in water. In any case, the major product formed is benzaldehyde (Table 24). We thus chose to systematically add Oxone solution last, to avoid catalyst deterioration.

Table 24: Effect of addition order on conversion rates. Conditions: *styrene (4 µmol), $Fe(L^1)_2$ (0.04 µmol), oxone (20 µmol), ammonium bicarbonate (8 µmol) in 1 mL ACN/H_2O 3:2, 60°C, 4h.*

Addition order	Conversion (%)	Major product
Solvent>NH_4HCO_3>cat>Oxone (solution)>styrene	38.6	Benzaldehyde
Solvent>NH_4HCO_3>cat>Oxone (solid)>styrene	73.6	Benzaldehyde
Solvent>NH_4HCO_3>cat>styrene>Oxone (solution)	100	Benzaldehyde

I.2.e. Reaction kinetics

A kinetic experiment was conducted, running reaction in parallel vials. The resulting curve shows a rapid increase of conversion during the first hour, followed by a slower increase. Final conversions are reached within 6-8 h (Figure 57). Replicates show identical results.

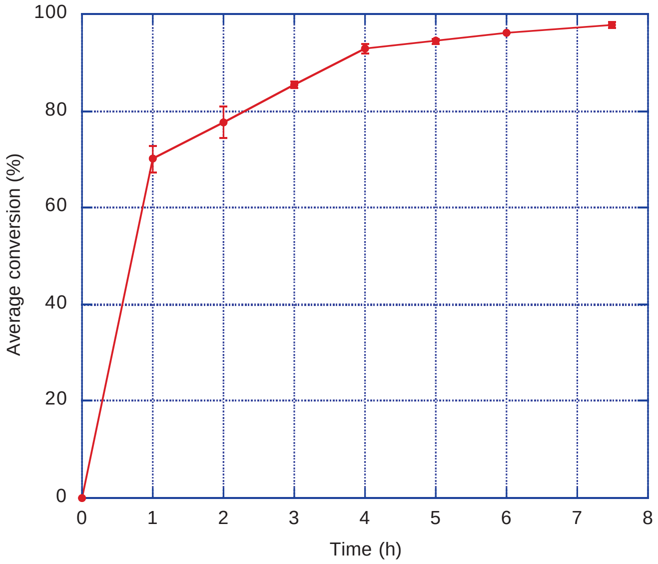

Figure 57: Kinetic curve of styrene conversion with time. Conditions: *styrene (4 µmol), Fe(L^1)$_2$ (0.04 µmol), oxone (20 µmol), ammonium bicarbonate (8 µmol) in 1 mL ACN/H_2O 3:2, 25°C. Each point is the average of triplicates, corresponding to separate vials.*

I.3. Conclusion: catalytic activity of FeL_2 complexes

This study enabled to determine the optimal conditions for styrene oxidation used our bis phenyl-substituted terpyridine Fe(II) complexes. Indeed, using 0.5 mol% catalyst, 1 eq of ammonium bicarbonate and 5 eq oxone provide 100 % conversion. However, in these conditions, benzaldehyde remains the major product. Increasing oxidant allows forming 2-hydroxy 1-phenyl ethanone as major product, but also leads to a discoloration of the solution, probably due to a degradation of the metal complex. Attempts with other oxidants have proven less successful, and variations of temperature showed limited effects.

Bis phenyl-substituted terpyridine Fe(II) complexes (that were proven to interact with fibres, see 0) are more active than their **bpy** and **salophen** analogues (that display no interaction). Ru(II) analogues also display promising properties. A preliminary catalytic experiment was thus conducted using Fe($\mathbf{L}^{\mathbf{1}}$)$_2$ incorporated into fibres.

II. Preliminary results: catalysis supported on fibres

After 3 days of A$\beta_{1\text{-}40}$ aggregation in the presence of metal complexes, fibres are harvested by centrifugation, and supernatant is titrated to determine the amount of inserted complex. Pellet of fibres is then redispersed in catalytic medium and used for oxidation reaction.

In normal conditions, A$\beta_{1\text{-}40}$ aggregation is monitored by Th-T. A control experiment was thus mandatory to assess the effect of the presence of Th-T on catalysis. For comparison, a control without fibres was also added.

Table 25: Results obtained for styrene epoxidation with Fe(L^1)$_2$ inserted in Aβ fibres. Conditions: *styrene (4 μmol), catalyst (0,04 μmol), ammonium bicarbonate (10 μmol), Oxone (variable), 25°C, 4h.*

Catalyst	**Oxone eq**	**Conversion (%)**	**Major product**
Fe($\mathbf{L}^1$)$_2$	4	93	Benzaldehyde
Fe($\mathbf{L}^1$)$_2$	8	100	Benzaldehyde
Fibres + Fe($\mathbf{L}^1$)$_2$	4	15	Traces
Fibres + Fe($\mathbf{L}^1$)$_2$	8	51	Benzaldehyde
Fibres + Fe($\mathbf{L}^1$)$_2$ + ThT	4	0	/
Fibres + Fe($\mathbf{L}^1$)$_2$ + ThT	8	63	Benzaldehyde

Results show a drop of conversion for catalysts inserted in fibres. This effect could be due to a difference in substrate accessibility to the active site. Yet, when using 8 eq of Oxone, satisfying conversions can be obtained. From this, it seems that Th-T does not disturb catalysis, which will be convenient for aggregation monitoring. In any case, benzaldehyde is formed as major product. A little difference is observed: in absence of fibres, traces of phenylacetaldehyde, epoxide and 2-hydroxy 1-phenyl ethanone are observed, whereas in presence of fibres only benzaldehyde is detected. This could be explained either by an incorporation of these side-products in fibres, or by a better selectivity of the hybrid system. To answer this question, a careful washing of fibres with an appropriate solvent could be envisaged.

This first result validates the concept of hybrid catalysts made of metal complexes inserted in amyloid fibres. Catalytic activity of coordination complexes is maintained through fibre intercalation, even though a small drop of conversion is observed. Investigations on the different parameters of this reaction would be required to optimize reaction conditions. In a next step, this system could be improved in many different ways, as presented in the next section.

III. Outlooks: how to improve our hybrid systems

III.1. Improving catalytic efficiency

III.1.a. Screening of metal ions

The interaction between fibres and metal complexes being mostly promoted by ligands, it enables to screen different metal ions. In addition to the Cu(II), Fe(II) and Ru(II), one could imagine the use of Mn(II), Ni(II), Pt(II) or Pd(II) for their catalytic properties.

In a preliminary study, [Mn(**L**^{1})$(OAc)_2$] and [Mn(**salophen**)Cl] were synthesized according to previously described procedures [60,82]. Both complexes were tested on thioanisole sulfoxidation reaction, in conditions reported by Pordea *et al*. [82] (Scheme 35).

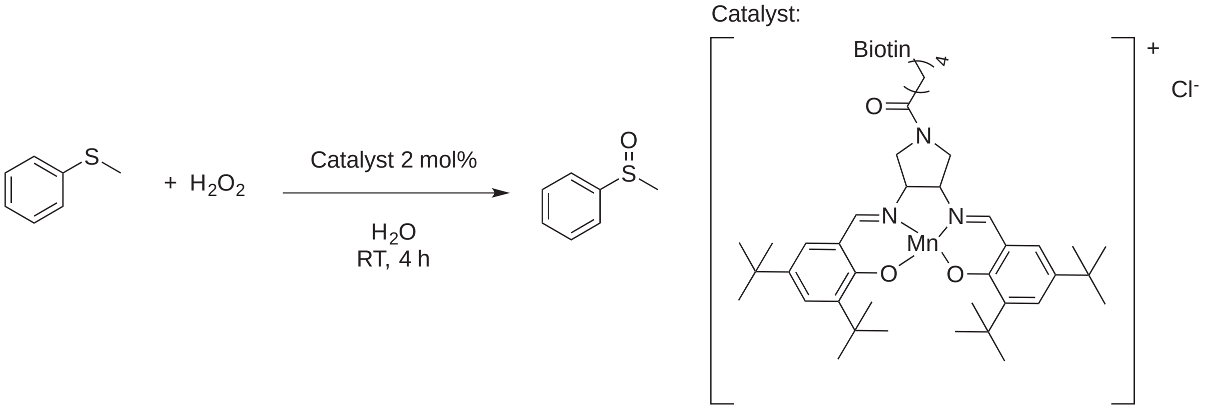

Scheme 35: Conditions for thioanisole sulfoxidation reported by Pordea et al.

Results obtained appear in Table 26, showing that good conversion rates can be obtained with salophen complex. However, according to GC, both sulfoxide and sulfone are formed in these conditions. Increasing catalyst loading allows formation of sulfone as major product. Further investigations on reaction time and temperature might help to isolate sulfoxide. Mn**L**^{1} complex displays poor conversion rates, that might be improved by using the corresponding Mn(III) complex.

Table 26: Results obtained for thioanisole sulfoxidation. Conditions: *Thioanisole (5 mmol), catalyst (variable), H_2O_2 (variable), 20°C, overnight.*

Catalyst	Catalyst loading (%)	H_2O_2 eq	Conversion (%)	GC ratio sulfoxide:sulfone
Mn(**salophen**)Cl	1	2	64	1:1
Mn(**salophen**)Cl	1	10	95	1:1
Mn(**salophen**)Cl	2	1	70	1:2
Mn(**L**^{1})$(OAc)_2$	2	1	11	1:1

Mn(**salophen**)Cl	2	2	85	1:2
Mn(**salophen**)Cl	2	10	95	1:1
Mn(**salophen**)Cl	4	2	91	1:9
Mn(**salophen**)Cl	4	10	96	1:2
Mn(**salophen**)Cl	2	0	0	/

Unfortunately, interaction studies showed a poor incorporation of salophen complexes into fibres. But modifications on the salophen scaffold could help to improve its affinity for fibres (see III.1.c).

III.1.b. Seeking for other reactivities

Despite epoxidation, other reactions were attempted with our metal complexes: aziridination, which was reported by Che to work under similar conditions as epoxidation [234], and cyclopropanation, which normally works in DCM with Cu(I) catalysts [236]. Conditions were slightly modified, as appearing in Scheme 36.

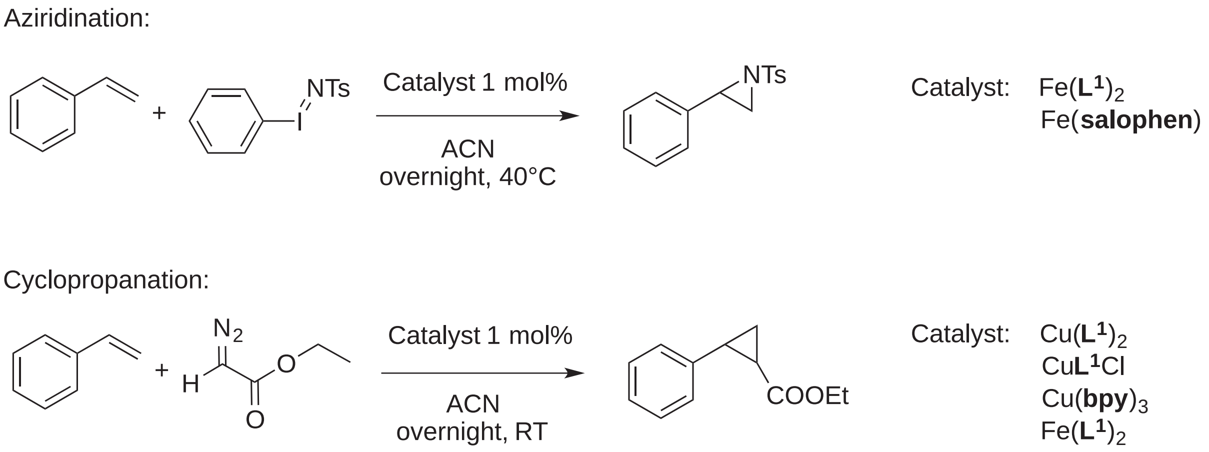

Scheme 36: Other catalytic reactions tested with Fe and Cu complexes.

Aziridination was tested using Fe($\mathbf{L^1}$)$_2$ and Fe(**salophen**), in air or under argon, showing maximum conversion of 15% by GC analysis. Traces of products were detected, but could not be analysed. The only variation from the article is the nature of the terpyridine ligands of the catalyst. As for epoxidation, it seems that this has a huge impact on catalytic activity (see Chapter I.I.).

Cyclopropanation was attempted with Cu($\mathbf{L^1}$)$_2$, Cu$\mathbf{L^1}$Cl$_2$, Cu(**bpy**)$_3$ and Fe($\mathbf{L^1}$)$_2$. Here again, conversion rates did not exceeded 10% by GC analysis. Such disappointing result can be explained by the use of Cu(II) instead of Cu(I), and by a difference in solvents.

Other reactions using Fe(tpy)X_2 complexes could also be attempted in future studies, but they are unlikely to be transposed to Fe(tpy)$_2$ complexes. To achieve good catalytic efficiency, it might be more efficient to operate modifications on ligands and complexes.

III.1.c. Ligand evolution

Going back to existing epoxidation catalysts, we notice that a huge majority display a vacant coordination site, which enables oxidant coordination to form an iron high-valent reactive specie. This was reported with enzymes (Scheme 37.A and 3.B) as well as with metal complexes [11] (Scheme 37.C).

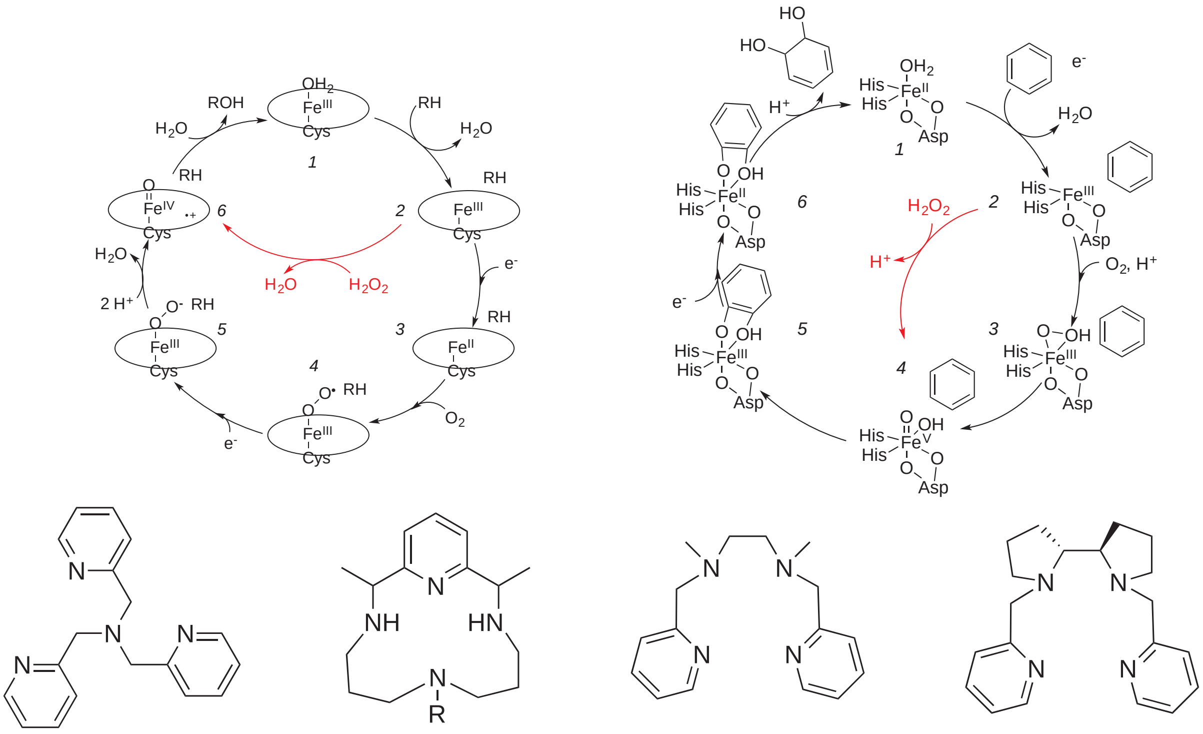

Scheme 37: Efficient iron-based catalysts. A: *Catalytic cycle of Cytochromes P450. Electrons come from NAD(P)H and transit through the electron transport system. Red: Peroxide shunt.* ***B:*** *Catalytic cycle of Rieske-type dioxygenases. The electron source is a Fe_2S_2 complex proximal to the active site. Red: Peroxide shunt.****C.*** *Ligands reported for hydrocarbons Fe(II)-catalysed epoxidation with H_2O_2. Reprinted from [11].*

With their chloro-substituted bis terpyridine Fe(II) complexes, Che and coll. showed that this rule could suffer exceptions. Yet, this requirement should be taken into account when developing a second generation of ligands, while keeping in mind requirements for supramolecular interaction.

Interesting examples would include the formation of heteroleptic [Fe(**L**)(**bpy**)]$^{2+}$ complexes, that would combine an interacting ligand (*i.e.* **L**^{1}, **L**^{3} or **L**^{5}) and would leave vacant a position on Fe. Their synthesis might be a little tricky compared to homoleptic complexes, possibly requiring isolation of the mono-ligand intermediate.

To go further into coordination sphere optimization, one could also imagine working with quaterpyridine scaffold substituted with the suitable phenyl moiety (Scheme 38, ligand 1). Ligands of this type were synthesized starting from bipyridine, the corresponding Ru(II) complexes displaying unique spectrophotometric properties [237]. In our case, Fe complex would combine the pyridinyl-pyridinyl-phenyl motif that seems required for interaction, together with the 4N coordination sphere important for catalysis. Replacing two pyridyl rings by phenol could also be of interest, considering the high efficiency of salen-type ligands in oxidation catalysis (Scheme 38, ligand 2).

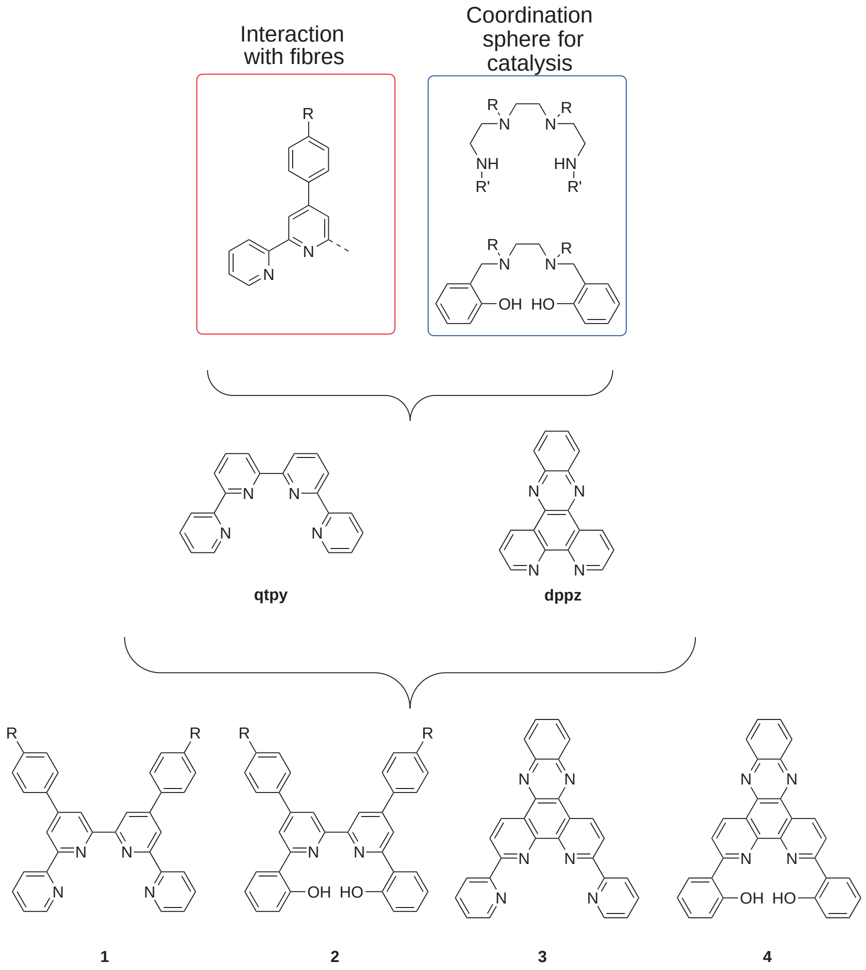

Scheme 38: Proposition for a second generation of ligands.

Another strategy could consist in starting from dipyridophenazine (**dppz**, Scheme 38), which was described as an efficient intercalating moiety. Substitution with pyridyl or phenol rings could provide **dppz** a 4N or 2N2O coordination sphere suitable for catalysis (Scheme 38, ligands **3** and **4**). Synthesis of ligand **3** has been described by Thummel *et al.* in three steps starting from dichloro phenanthroline [238]. Pyridinyl rings being coupled using Stille strategy, similar reaction could be envisaged using phenol rings.

This series could constitute a second generation of ligands that would encompass interaction and catalysis requirements. To further improve the hybrid system, modifications can also be operated on Aβ peptide.

III.1.d. Modifications of peptide

Different strategies can be applied to improve the peptide scaffold.

- **Directed mutagenesis on Aβ:** helped by experimental data together with calculations, it could be envisaged to operate some specific mutations on Aβ sequence to improve fibre-complex interaction. However, at this point, this option is limited by the lack of experimental data. Further experimentation with probe-modified terpyridine ligands might help to gain insights into residues implicated in interaction (see Chapter V.III.2).
- **Random mutagenesis on Aβ:** Considering the lack of experimental data, an alternative option could be to operate random mutagenesis on Aβ peptide. MAβ expression in *E. coli* being well managed, it would be possible to obtain mutant libraries. However, it would be mandatory to develop a straightforward screening assay to determine the potential of each mutant directly in bacteria. Screening for aggregation-prone mutants is already possible, using Th-S to stain inclusion bodies. One could imagine using a biocompatible Ru complex to screen for amyloid-complex interaction.
- **Moving to amyloid proteins:** Now that the interaction of our bis terpyridine complexes was assessed with Aβ, it could be interesting to see if it can be transposed to amyloid proteins. As an example, albumin proteins produce fibres in large amounts when heated and are easy to handle [239]. Their use could enable to run catalysis at synthetically relevant scale.
- **Moving to shorter amyloid peptides:** Finally, an opposite approach would consist in developing a library of amyloid-forming short peptides issued from solid-phase peptide synthesis. Such approach has been described in literature with seven residues peptides, enabling the rapid screening of catalytic efficiency [240].

III.2. Other possible strategies

Although not considered here, the grafting of an intercalating moiety onto the ligand could also constitute a convenient way to promote interaction. However, the chiral effect of amyloid fibre might be decreased, as described before for DNA based catalysts (see Chapter I.I.3.b).

In the same way, this project focused on non-covalent interaction between metal complexes and fibres; though, the covalent grafting of the complex also remains relevant. It could be achieved by bioconjugation using Lys or Cys residues, or by incorporation of non-natural amino acids. In that case, ligands could be reduced to the minimum, since having no impact on interaction, and the distance between catalyst and fibre would remain short. But that would require huge efforts of synthesis.

An alternative approach developed in our group consists in functionalizing terpyridine with diazirine moiety. Upon irradiation of ligand inserted into fibres, a carbene is formed, which reacts with neighbouring residues to form a covalent bond. Hence, the ligand is immobilized at its most favoured position [241].

All these approaches remain of interest, and should be kept in mind for further studies.

Conclusion

Our Fe(II) complexes were tested on styrene epoxidation reaction, which has been reported to work with Fe(tpy)$_2$-type complexes. Our complexes display high conversion rates; unfortunately, they do not form the expected epoxide, but benzaldehyde, which prevent the possible observation of chiral induction from the catalytic scaffold.

Yet, a preliminary catalytic assay using Fe($\mathbf{L^1}$)$_2$ inserted into A$\beta_{1\text{-}40}$ fibres was attempted, showing that the presence of fibres does not preclude the catalytic reaction, even though a little loss of conversion is noticed. This first result constitutes a proof of concept for hybrid catalyst elaboration from amyloid fibres. A screening of various substrates could be of interest, to conclude on the effect of the peptide environment on the substrate.

To improve this primary scaffold, we propose to operate chemogenetic optimisation, *i.e.* combining variations on the peptide and on the metal complex to reach an optimal system. In this view, developing a second generation of ligands is envisaged, which would encompass the requirements noted for both interaction and catalysis. Namely, interesting ligands would be constituted of four coordinating nitrogen atoms, while keeping the pyridyl-pyridyl-phenyl moiety that appeared crucial for interaction. Intercalating **dppz** scaffold could also be interesting.

Operating modifications on peptide is also to envisage. Considering the lack of structural information, random mutagenesis appears more appropriate. Future work would include the development of a new *in vivo* screening method for complex-fibre interaction.

General conclusion

Along this thesis, we have focused on the elaboration of hybrid bioinorganic catalysts, prepared by incorporation of coordination complexes in amyloid fibres. Three main points were to be considered: the production of peptide, the synthesis of metal complexes, and the study of their interaction, the ultimate goal being to study the catalytic activity of the final scaffold.

To this aim, amyloid-β recombinant production was attempted in *Escherichia coli*. First considered as more convenient, production of His-tagged Amyloid-β was abandoned in favour of untagged Met-Amyloid-β. Indeed, this peptide is produced as inclusion bodies in bacteria, which can be easily isolated from bacterial residues. Based on a previously published procedure, we have developed a new purification procedure for Met-Amyloid-β peptides, consisting in basic solubilisation followed by two ultrafiltration steps. This chromatography-free protocol afford pure peptide samples in good yields and with intact aggregative properties. This protocol constitutes a convenient procedure for routine Aβ sample production, and makes possible peptide variations by mutagenesis.

The next important point was to develop a series of metal complexes candidates that might display good interaction with amyloid fibres. Based on observation of known amyloid-β intercalating agents, we chose to focus on phenyl-functionalized terpyridine ligands. A series of five ligands was developed, each of them holding different functional groups, expected to modulate interaction with fibres. Corresponding Cu(II), Fe(II), and Ru(II) complexes were prepared and fully characterized. Fe(II) complexes caught our attention for its potential catalytic activity, whereas Ru(II) complexes had interesting luminescent properties.

These two series of complexes were thus tested for their interaction with amyloid fibres. Among the series, $\mathbf{L^1}$, $\mathbf{L^3}$ and $\mathbf{L^5}$ complexes showed high incorporation into $A\beta_{1\text{-}40}$ fibres. This comes together with an acceleration of $A\beta_{1\text{-}40}$ aggregation kinetics. Investigations on metal complex recognition pattern demonstrated that the pyridine-pyridine-phenyl was responsible for interaction, regardless the coordinated metal ion. Finally, experiments were conducted to binding site(s) of metal complexes in fibres. Results attest that metal complexes and Th-T have different binding sites. Unfortunately, no precise localization was obtained, although a clear difference of incorporation was observed with short peptides $A\beta_{11\text{-}28}$ and $A\beta_{1\text{-}28}$.

To get further insights on this last point, docking studies were conducted on ssNMR structures of $A\beta_{1\text{-}40}$ and $A\beta_{1\text{-}42}$ fibres. Results confirm that Th-T and metal complexes cannot bind in the same sites, due to geometric constraints. Docking of $Fe(\mathbf{L^1})_2$ into $A\beta_{1\text{-}42}$ model provides a first proof of concept for metal complexes binding in side-chain channels on the surface of fibres. This result is in accordance with the key role played by phenyl ring and lateral pyridine in interaction.

To conclude this study, a last step was to assess catalytic activity of coordination complexes when incorporated into fibres. To this aim, styrene epoxidation reaction was selected as benchmark reaction. Surprisingly, catalysis with our Fe(II) complexes afforded benzaldehyde as major product. Preliminary experiments in presence of fibres allowed us to validate that this catalytic activity of metal complexes is preserved upon insertion.

This result validates the proof of concept for bioinorganic hybrid catalysts based on amyloid fibres. Even though these systems already present advantages, such as their easy production and their biocompatibility, they will have to be improved to compete with existing catalysts. In this view, a chemogenetic optimization procedure could be applied, combining peptide mutagenesis and metal complex evolution to reach an optimised system.

References

1 Caserta G, Roy S, Atta M, Artero V & Fontecave M (2015) Artificial hydrogenases: biohybrid and supramolecular systems for catalytic hydrogen production or uptake. *Curr. Opin. Chem. Biol.* **25**, 36–47.

2 Onoda A & Hayashi T (2015) Artificial hydrogenase: biomimetic approaches controlling active molecular catalysts. *Curr. Opin. Chem. Biol.* **25**, 133–140.

3 Berggren G, Adamska A, Lambertz C, Simmons TR, Esselborn J, Atta M, Gambarelli S, Mouesca J-M, Reijerse E, Lubitz W, Happe T, Artero V & Fontecave M (2013) Biomimetic assembly and activation of [FeFe]-hydrogenases. *Nature* **499**, 66–69.

4 Eckenhoff WT, McNamara WR, Du P & Eisenberg R (2013) Cobalt complexes as artificial hydrogenases for the reductive side of water splitting. *Biochim. Biophys. Acta BBA - Bioenerg.* **1827**, 958–973.

5 Broering EP, Truong PT, Gale EM & Harrop TC (2013) Synthetic Analogues of Nickel Superoxide Dismutase: A New Role for Nickel in Biology. *Biochemistry (Mosc.)* **52**, 4–18.

6 Gale EM, Simmonett AC, Telser J, Schaefer HF & Harrop TC (2011) Toward Functional Ni-SOD Biomimetics: Achieving a Structural/Electronic Correlation with Redox Dynamics. *Inorg. Chem.* **50**, 9216–9218.

7 Riley DP (1999) Functional Mimics of Superoxide Dismutase Enzymes as Therapeutic Agents. *Chem. Rev.* **99**, 2573–2588.

8 Jackson TA, Gutman CT, Maliekal J, Miller A-F & Brunold TC (2013) Geometric and Electronic Structures of Manganese-Substituted Iron Superoxide Dismutase. *Inorg. Chem.* **52**, 3356–3367.

9 Artero V, Chavarot-Kerlidou M & Fontecave M (2011) Splitting Water with Cobalt. *Angew. Chem. Int. Ed.* **50**, 7238–7266.

10 Kärkäs MD, Verho O, Johnston EV & Åkermark B (2014) Artificial Photosynthesis: Molecular Systems for Catalytic Water Oxidation. *Chem. Rev.*, 141029100623006.

11 Que L & Tolman WB (2008) Biologically inspired oxidation catalysis. *Nature* **455**, 333–340.

12 Elgrishi N, Chambers MB, Artero V & Fontecave M (2014) Terpyridine complexes of first row transition metals and electrochemical reduction of CO2 to CO. *Phys. Chem. Chem. Phys.* **16**, 13635.

13 Rebilly J-N, Colasson B, Bistri O, Over D & Reinaud O (2015) Biomimetic cavity-based metal complexes. *Chem Soc Rev* **44**, 467–489.

14 Wiester MJ, Ulmann PA & Mirkin CA (2011) Enzyme Mimics Based Upon Supramolecular Coordination Chemistry. *Angew. Chem. Int. Ed.* **50**, 114–137.

15 Raynal M, Ballester P, Vidal-Ferran A & van Leeuwen PWNM (2014) Supramolecular catalysis. Part 2: artificial enzyme mimics. *Chem Soc Rev* **43**, 1734–1787.

16 Bos J & Roelfes G (2014) Artificial metalloenzymes for enantioselective catalysis. *Curr. Opin. Chem. Biol.* **19**, 135–143.

17 Lewis JC (2013) Artificial Metalloenzymes and Metallopeptide Catalysts for Organic Synthesis. *ACS Catal.* **3**, 2954–2975.

18 Steinreiber J & Ward TR (2008) Artificial metalloenzymes as selective catalysts in aqueous media. *Coord. Chem. Rev.* **252**, 751–766.

19 Letondor C & Ward TR (2006) Artificial Metalloenzymes for Enantioselective Catalysis: Recent Advances. *ChemBioChem* **7**, 1845–1852.

20 Thomas CM & Ward TR (2005) Artificial metalloenzymes: proteins as hosts for enantioselective catalysis. *Chem. Soc. Rev.* **34**, 337–346.

21 Collot J, Humbert N, Skander M, Klein G & Ward TR (2004) Artificial metalloenzymes for enantioselective catalysis: the phenomenon of protein accelerated catalysis. *J. Organomet. Chem.* **689**, 4868–4871.

22 Drienovská I & Roelfes G (2014) Artificial Metalloenzymes for Asymmetric Catalysis by Creation of Novel Active Sites in Protein and DNA Scaffolds. *Isr. J. Chem.*, n/a-n/a.

23 Marchi-Delapierre C, Rondot L, Cavazza C & Ménage S (2014) Oxidation Catalysis by Rationally Designed Artificial Metalloenzymes. *Isr. J. Chem.*, n/a-n/a.

24 Dürrenberger M & Ward TR (2014) Recent achievments in the design and engineering of artificial metalloenzymes. *Curr. Opin. Chem. Biol.* **19**, 99–106.

25 Ringenberg MR & Ward TR (2011) Merging the best of two worlds: artificial

metalloenzymes for enantioselective catalysis. *Chem. Commun.* **47**, 8470.

26 Yamamura K & Kaiser ET (1976) Studies on the oxidase activity of copper(II) carboxypeptidase A. *J. Chem. Soc. Chem. Commun.*, 830.

27 Fernández-Gacio A, Codina A, Fastrez J, Riant O & Soumillion P (2006) Transforming Carbonic Anhydrase into Epoxide Synthase by Metal Exchange. *ChemBioChem* **7**, 1013–1016.

28 Okrasa K & Kazlauskas RJ (2006) Manganese-Substituted Carbonic Anhydrase as a New Peroxidase. *Chem. - Eur. J.* **12**, 1587–1596.

29 Jing Q, Okrasa K & Kazlauskas RJ (2009) Stereoselective Hydrogenation of Olefins Using Rhodium-Substituted Carbonic Anhydrase-A New Reductase. *Chem. - Eur. J.* **15**, 1370–1376.

30 Jing Q & Kazlauskas RJ (2010) Regioselective Hydroformylation of Styrene Using Rhodium-Substituted Carbonic Anhydrase. *ChemCatChem* **2**, 953–957.

31 Fasan R (2012) Tuning P450 Enzymes as Oxidation Catalysts. *ACS Catal.* **2**, 647–666.

32 McIntosh JA, Coelho PS, Farwell CC, Wang ZJ, Lewis JC, Brown TR & Arnold FH (2013) Enantioselective Intramolecular C‐H Amination Catalyzed by Engineered Cytochrome P450 Enzymes In Vitro and In Vivo. *Angew. Chem. Int. Ed.* **52**, 9309–9312.

33 Mahy J-P, Ciesielski J & Dauban P (2014) Catalytic C‐H Amination: A Reaction Now Accessible to Engineered Natural Enzymes. *Angew. Chem. Int. Ed.* **53**, 6862–6864.

34 Coelho PS, Wang ZJ, Ener ME, Baril SA, Kannan A, Arnold FH & Brustad EM (2013) A serine-substituted P450 catalyzes highly efficient carbene transfer to olefins in vivo. *Nat. Chem. Biol.* **9**, 485–487.

35 Coelho PS, Brustad EM, Kannan A & Arnold FH (2013) Olefin Cyclopropanation via Carbene Transfer Catalyzed by Engineered Cytochrome P450 Enzymes. *Science* **339**, 307–310.

36 Köhler V & Ward TR (2010) Design of a Functional Nitric Oxide Reductase within a Myoglobin Scaffold. *ChemBioChem* **11**, 1049–1051.

37 Matzapetakis M, Farrer BT, Weng T-C, Hemmingsen L, Penner-Hahn JE & Pecoraro VL (2002) Comparison of the Binding of Cadmium(II), Mercury(II), and

Arsenic(III) to the de Novo Designed Peptides TRI L12C and TRI L16C. *J. Am. Chem. Soc.* **124**, 8042–8054.

38 Miner KD, Mukherjee A, Gao Y-G, Null EL, Petrik ID, Zhao X, Yeung N, Robinson H & Lu Y (2012) A Designed Functional Metalloenzyme that Reduces O2 to H2O with Over One Thousand Turnovers. *Angew. Chem. Int. Ed.* **51**, 5589–5592.

39 Chakraborty S, Touw DS, Peacock AFA, Stuckey J & Pecoraro VL (2010) Structural Comparisons of Apo- and Metalated Three-Stranded Coiled Coils Clarify Metal Binding Determinants in Thiolate Containing Designed Peptides. *J. Am. Chem. Soc.* **132**, 13240–13250.

40 Yu F, Penner-Hahn JE & Pecoraro VL (2013) De Novo-Designed Metallopeptides with Type 2 Copper Centers: Modulation of Reduction Potentials and Nitrite Reductase Activities. *J. Am. Chem. Soc.* **135**, 18096–18107.

41 Tegoni M, Yu F, Bersellini M, Penner-Hahn JE & Pecoraro VL (2012) Designing a functional type 2 copper center that has nitrite reductase activity within -helical coiled coils. *Proc. Natl. Acad. Sci.* **109**, 21234–21239.

42 Cangelosi VM, Deb A, Penner-Hahn JE & Pecoraro VL (2014) A De Novo Designed Metalloenzyme for the Hydration of CO_2. *Angew. Chem. Int. Ed.* **53**, 7900–7903.

43 Zastrow ML & Pecoraro VL (2014) Designing Hydrolytic Zinc Metalloenzymes. *Biochemistry (Mosc.)* **53**, 957–978.

44 Tebo AG & Pecoraro VL (2015) Artificial metalloenzymes derived from three-helix bundles. *Curr. Opin. Chem. Biol.* **25**, 65–70.

45 Tegoni M (2014) De Novo Designed Copper α-Helical Peptides: From Design to Function: Copper α-Helical Peptides. *Eur. J. Inorg. Chem.* **2014**, 2177–2193.

46 Zastrow ML & Pecoraro VL (2013) Designing functional metalloproteins: From structural to catalytic metal sites. *Coord. Chem. Rev.* **257**, 2565–2588.

47 Roelfes G & Feringa BL (2005) DNA-Based Asymmetric Catalysis. *Angew. Chem. Int. Ed.* **44**, 3230–3232.

48 Oelerich J & Roelfes G (2013) DNA-based asymmetric organometallic catalysis in water. *Chem. Sci.* **4**, 2013.

49 Boersma AJ, Coquière D, Geerdink D, Rosati F, Feringa BL & Roelfes G (2010)

Catalytic enantioselective syn hydration of enones in water using a DNA-based catalyst. *Nat. Chem.* **2**, 991–995.

50 Coquière D, Feringa BL & Roelfes G (2007) DNA-Based Catalytic Enantioselective Michael Reactions in Water. *Angew. Chem. Int. Ed.* **46**, 9308–9311.

51 Boersma AJ, de Bruin B, Feringa BL & Roelfes G (2012) Ligand denticity controls enantiomeric preference in DNA-based asymmetric catalysis. *Chem. Commun.* **48**, 2394.

52 Wang J, Benedetti E, Bethge L, Vonhoff S, Klussmann S, Vasseur J-J, Cossy J, Smietana M & Arseniyadis S (2013) DNA vs. Mirror-Image DNA: A Universal Approach to Tune the Absolute Configuration in DNA-Based Asymmetric Catalysis. *Angew. Chem. Int. Ed.* **52**, 11546–11549.

53 Park S, Zheng L, Kumakiri S, Sakashita S, Otomo H, Ikehata K & Sugiyama H (2014) Development of DNA-Based Hybrid Catalysts through Direct Ligand Incorporation: Toward Understanding of DNA-Based Asymmetric Catalysis. *ACS Catal.* **4**, 4070–4073.

54 Park S, Ikehata K, Watabe R, Hidaka Y, Rajendran A & Sugiyama H (2012) Deciphering DNA-based asymmetric catalysis through intramolecular Friedel–Crafts alkylations. *Chem. Commun.* **48**, 10398.

55 Park S & Sugiyama H (2012) DNA as a Chiral Scaffold for Asymmetric Synthesis. *Molecules* **17**, 12792–12803.

56 Oltra NS & Roelfes G (2008) Modular assembly of novel DNA-based catalysts. *Chem. Commun.*, 6039.

57 Fournier P, Fiammengo R & Jäschke A (2009) Allylic Amination by a DNA-Diene-Iridium(I) Hybrid Catalyst. *Angew. Chem. Int. Ed.* **48**, 4426–4429.

58 Carey JR, Ma SK, Pfister TD, Garner DK, Kim HK, Abramite JA, Wang Z, Guo Z & Lu Y (2004) A Site-Selective Dual Anchoring Strategy for Artificial Metalloprotein Design. *J. Am. Chem. Soc.* **126**, 10812–10813.

59 Ueno T, Koshiyama T, Ohashi M, Kondo K, Kono M, Watanabe Y, Suzuki A & Yamane T (2005) Coordinated Design of Cofactor and Active Site Structures in Development of New Protein Catalysts. *J. Am. Chem. Soc.* **127**, 6556–6562.

60 Zhang C, Srivastava P, Ellis-Guardiola K & Lewis JC (2014) Manganese terpyridine artificial metalloenzymes for benzylic oxygenation and olefin epoxidation. *Tetrahedron* **70**,

4245–4249.

61 Esmieu C, Cherrier MV, Amara P, Girgenti E, Marchi-Delapierre C, Oddon F, Iannello M, Jorge-Robin A, Cavazza C & Ménage S (2013) An Artificial Oxygenase Built from Scratch: Substrate Binding Site Identified Using a Docking Approach. *Angew. Chem. Int. Ed.* **52**, 3922–3925.

62 Cavazza C, Bochot C, Rousselot-Pailley P, Carpentier P, Cherrier MV, Martin L, Marchi-Delapierre C, Fontecilla-Camps JC & Ménage S (2010) Crystallographic snapshots of the reaction of aromatic C–H with O2 catalysed by a protein-bound iron complex. *Nat. Chem.* **2**, 1069–1076.

63 Philippart F, Arlt M, Gotzen S, Tenne S-J, Bocola M, Chen H-H, Zhu L, Schwaneberg U & Okuda J (2013) A Hybrid Ring-Opening Metathesis Polymerization Catalyst Based on an Engineered Variant of the β-Barrel Protein FhuA. *Chem. - Eur. J.* **19**, 13865–13871.

64 Abe S, Hirata K, Ueno T, Morino K, Shimizu N, Yamamoto M, Takata M, Yashima E & Watanabe Y (2009) Polymerization of Phenylacetylene by Rhodium Complexes within a Discrete Space of apo-Ferritin. *J. Am. Chem. Soc.* **131**, 6958–6960.

65 Pordea A, Creus M, Panek J, Duboc C, Mathis D, Novic M & Ward TR (2008) Artificial Metalloenzyme for Enantioselective Sulfoxidation Based on Vanadyl-Loaded Streptavidin. *J. Am. Chem. Soc.* **130**, 8085–8088.

66 Köhler V, Mao J, Heinisch T, Pordea A, Sardo A, Wilson YM, Knörr L, Creus M, Prost J-C, Schirmer T & Ward TR (2011) OsO4·Streptavidin: A Tunable Hybrid Catalyst for the Enantioselective cis-Dihydroxylation of Olefins. *Angew. Chem. Int. Ed.* **50**, 10863–10866.

67 Mahammed A & Gross Z (2005) Albumin-Conjugated Corrole Metal Complexes: Extremely Simple Yet Very Efficient Biomimetic Oxidation Systems. *J. Am. Chem. Soc.* **127**, 2883–2887.

68 Allard M, Dupont C, Muñoz Robles V, Doucet N, Lledós A, Maréchal J-D, Urvoas A, Mahy J-P & Ricoux R (2012) Incorporation of Manganese Complexes into Xylanase: New Artificial Metalloenzymes for Enantioselective Epoxidation. *ChemBioChem* **13**, 240–251.

69 Bos J, Fusetti F, Driessen AJM & Roelfes G (2012) Enantioselective Artificial Metalloenzymes by Creation of a Novel Active Site at the Protein Dimer Interface. *Angew. Chem. Int. Ed.* **51**, 7472–7475.

70 Mayer C, Gillingham DG, Ward TR & Hilvert D (2011) An artificial metalloenzyme for olefin metathesis. *Chem. Commun.* **47**, 12068.

71 Inaba H, Kanamaru S, Arisaka F, Kitagawa S & Ueno T (2012) Semi-synthesis of an artificial scandium(iii) enzyme with a β-helical bio-nanotube. *Dalton Trans.* **41**, 11424.

72 Srisa-Art M, Dyson EC, deMello AJ & Edel JB (2008) Monitoring of Real-Time Streptavidin−Biotin Binding Kinetics Using Droplet Microfluidics. *Anal. Chem.* **80**, 7063–7067.

73 Ward TR (2005) Artificial Metalloenzymes for Enantioselective Catalysis Based on the Noncovalent Incorporation of Organometallic Moieties in a Host Protein. *Chem. - Eur. J.* **11**, 3798–3804.

74 Collot J, Gradinaru J, Humbert N, Skander M, Zocchi A & Ward TR (2003) Artificial Metalloenzymes for Enantioselective Catalysis Based on Biotin−Avidin. *J. Am. Chem. Soc.* **125**, 9030–9031.

75 Pordea A & Ward TR (2008) Chemogenetic protein engineering: an efficient tool for the optimization of artificial metalloenzymes. *Chem. Commun.*, 4239.

76 Zimbron JM, Heinisch T, Schmid M, Hamels D, Nogueira ES, Schirmer T & Ward TR (2013) A Dual Anchoring Strategy for the Localization and Activation of Artificial Metalloenzymes Based on the Biotin–Streptavidin Technology. *J. Am. Chem. Soc.* **135**, 5384–5388.

77 Hyster TK, Knorr L, Ward TR & Rovis T (2012) Biotinylated Rh(III) Complexes in Engineered Streptavidin for Accelerated Asymmetric C-H Activation. *Science* **338**, 500–503.

78 Dürrenberger M, Heinisch T, Wilson YM, Rossel T, Nogueira E, Knörr L, Mutschler A, Kersten K, Zimbron MJ, Pierron J, Schirmer T & Ward TR (2011) Artificial Transfer Hydrogenases for the Enantioselective Reduction of Cyclic Imines. *Angew. Chem. Int. Ed.* **50**, 3026–3029.

79 Robles VM, Dürrenberger M, Heinisch T, Lledós A, Schirmer T, Ward TR & Maréchal J-D (2014) Structural, Kinetic, and Docking Studies of Artificial Imine Reductases Based on Biotin–Streptavidin Technology: An Induced Lock-and-Key Hypothesis. *J. Am. Chem. Soc.* **136**, 15676–15683.

80 Letondor C, Pordea A, Humbert N, Ivanova A, Mazurek S, Novic M & Ward TR (2006) Artificial Transfer Hydrogenases Based on the Biotin−(Strept)avidin Technology: Fine

Tuning the Selectivity by Saturation Mutagenesis of the Host Protein. *J. Am. Chem. Soc.* **128**, 8320–8328.

81 Quinto T, Häussinger D, Köhler V & Ward TR (2015) Artificial metalloenzymes for the diastereoselective reduction of NAD $^{+}$ to NAD ^{2} H. *Org Biomol Chem* **13**, 357–360.

82 Pordea A, Mathis D & Ward TR (2009) Incorporation of biotinylated manganese-salen complexes into streptavidin: New artificial metalloenzymes for enantioselective sulfoxidation. *J. Organomet. Chem.* **694**, 930–936.

83 Matsuo T, Imai C, Yoshida T, Saito T, Hayashi T & Hirota S (2012) Creation of an artificial metalloprotein with a Hoveyda–Grubbs catalyst moiety through the intrinsic inhibition mechanism of α-chymotrypsin. *Chem. Commun.* **48**, 1662.

84 Sansiaume-Dagousset E, Urvoas A, Chelly K, Ghattas W, Maréchal J-D, Mahy J-P & Ricoux R (2014) Neocarzinostatin-based hybrid biocatalysts for oxidation reactions. *Dalton Trans.* **43**, 8344.

85 Mahy J-P, Maréchal J-D & Ricoux R (2015) From “hemoabzymes” to “hemozymes”: towards new biocatalysts for selective oxidations. *Chem Commun* **51**, 2476–2494.

86 Quilez R, de Lauzon S, Desfosses B, Mansuy D & Mahy J-P (1996) Artificial peroxidase-like hemoproteins based on antibodies constructed from a specifically designed ortho-carboxy substituted tetraarylporphyrin hapten and exhibiting a high affinity for iron-porphyrins. *FEBS Lett.* **395**, 73–76.

87 Ricoux R, Sauriat-Dorizon H, Girgenti E, Blanchard D & Mahy J-P (2002) Hemoabzymes: towards new biocatalysts for selective oxidations. *J. Immunol. Methods* **269**, 39–57.

88 Ricoux R, Girgenti E, Sauriat-Dorizon H, Blanchard D & Mahy J-P (2002) Regioselective nitration of phenol induced by catalytic antibodies. *J. Protein Chem.* **21**, 473–477.

89 Ricoux R, Lukowska E, Pezzotti F & Mahy J-P (2004) New activities of a catalytic antibody with a peroxidase activity: Formation of Fe(II)-RNO complexes and stereoselective oxidation of sulfides. *Eur. J. Biochem.* **271**, 1277–1283.

90 Sansiaume E, Ricoux R, Gori D & Mahy J-P (2010) Oxidation of organic molecules in homogeneous aqueous solution catalyzed by hybrid biocatalysts (based on the Trojan

Horse strategy). *Tetrahedron Asymmetry* **21**, 1593–1600.

91 Zhang Z, Yang H, Zhang C & Lewis JC (2012) Synthesis and Catalytic Activity of Amino Acids and Metallopeptides with Catalytically Active Metallocyclic Side Chains. *Organometallics* **31**, 7328–7331.

92 Christensen CA & Meldal M (2005) Efficient Solid-Phase Synthesis of Peptide-Based Phosphine Ligands: Towards Combinatorial Libraries of Selective Transition Metal Catalysts. *Chem. - Eur. J.* **11**, 4121–4131.

93 Christensen CA & Meldal M (2007) Solid-Phase Synthesis of a Peptide-Based P,S-Ligand System Designed for Generation of Combinatorial Catalyst Libraries. *J. Comb. Chem.* **9**, 79–85.

94 Gilbertson SR, Collibee SE & Agarkov A (2000) Asymmetric Catalysis with Libraries of Palladium β-Turn Phosphine Complexes. *J. Am. Chem. Soc.* **122**, 6522–6523.

95 Ueno T, Tabe H & Tanaka Y (2013) Artificial Metalloenzymes Constructed From Hierarchically-Assembled Proteins. *Chem. - Asian J.* **8**, 1646–1660.

96 Inaba H, Kitagawa S & Ueno T (2014) Protein Needles as Molecular Templates for Artificial Metalloenzymes. *Isr. J. Chem.*, n/a-n/a.

97 Seeman P & Seeman N (2011) Alzheimer’s disease: β-amyloid plaque formation in human brain. *Synapse* **65**, 1289–1297.

98 Hardy JA & Higgins GA (1992) Alzheimer’s disease: the amyloid cascade hypothesis. *Science* **256**, 184–185.

99 Sakono M & Zako T (2010) Amyloid oligomers: formation and toxicity of Aβ oligomers. *FEBS J.* **277**, 1348–1358.

100 Tipping KW, van Oosten-Hawle P, Hewitt EW & Radford SE (2015) Amyloid Fibres: Inert End-Stage Aggregates or Key Players in Disease? *Trends Biochem. Sci.* **40**, 719–727.

101 Anand R, Gill KD & Mahdi AA (2014) Therapeutics of Alzheimer’s disease: Past, present and future. *Neuropharmacology* **76**, 27–50.

102 Marzban L, Park K & Verchere CB (2003) Islet amyloid polypeptide and type 2 diabetes. *Exp. Gerontol.* **38**, 347–351.

103 Pithadia A, Brender JR, Fierke CA & Ramamoorthy A (2016) Inhibition of IAPP

Aggregation and Toxicity by Natural Products and Derivatives. *J. Diabetes Res.* **2016**, 2046327.

104 Fraser PE (2014) Prions and Prion-like Proteins. *J. Biol. Chem.* **289**, 19839–19840.

105 Perrin C (2009) Implication et r´egulation de la production des curli dans la r´esistance au nickel au sein de biofilms d'Escherichia coli K-12. .

106 Bayry J, Aimanianda V, Guijarro JI, Sunde M & Latgé J-P (2012) Hydrophobins—Unique Fungal Proteins. *PLoS Pathog.* **8**, e1002700.

107 Hamodrakas SJ, Hoenger A & Iconomidou VA (2004) Amyloid fibrillogenesis of silkmoth chorion protein peptide-analogues via a liquid-crystalline intermediate phase. *J. Struct. Biol.* **145**, 226–235.

108 Fowler DM, Koulov AV, Alory-Jost C, Marks MS, Balch WE & Kelly JW (2005) Functional Amyloid Formation within Mammalian Tissue. *PLoS Biol.* **4**, e6.

109 McGlinchey RP, Shewmaker F, McPhie P, Monterroso B, Thurber K & Wickner RB (2009) The repeat domain of the melanosome fibril protein Pmel17 forms the amyloid core promoting melanin synthesis. *Proc. Natl. Acad. Sci.* **106**, 13731–13736.

110 Chiti F, Webster P, Taddei N, Clark A, Stefani M, Ramponi G & Dobson CM (1999) Designing conditions for in vitro formation of amyloid protofilaments and fibrils. *Proc. Natl. Acad. Sci. U. S. A.* **96**, 3590–3594.

111 Guijarro JI, Sunde M, Jones JA, Campbell ID & Dobson CM (1998) Amyloid fibril formation by an SH3 domain. *Proc. Natl. Acad. Sci. U. S. A.* **95**, 4224–4228.

112 Pearce FG, Mackintosh SH & Gerrard JA (2007) Formation of Amyloid-like Fibrils by Ovalbumin and Related Proteins under Conditions Relevant to Food Processing. *J. Agric. Food Chem.* **55**, 318–322.

113 Sawaya MR, Sambashivan S, Nelson R, Ivanova MI, Sievers SA, Apostol MI, Thompson MJ, Balbirnie M, Wiltzius JJW, McFarlane HT, Madsen AØ, Riekel C & Eisenberg D (2007) Atomic structures of amyloid cross-β spines reveal varied steric zippers. *Nature* **447**, 453–457.

114 Greenwald J & Riek R (2010) Biology of Amyloid: Structure, Function, and Regulation. *Structure* **18**, 1244–1260.

115 Smith JF, Knowles TPJ, Dobson CM, Macphee CE & Welland ME (2006)

Characterization of the nanoscale properties of individual amyloid fibrils. *Proc. Natl. Acad. Sci. U. S. A.* **103**, 15806–15811.

116 Westermark GT, Johnson KH & Westermark P (1999) [1] Staining methods for identification of amyloid in tissue. In (Enzymology B-M in, ed), pp. 3–25. Academic Press.

117 Scheibel T, Parthasarathy R, Sawicki G, Lin X-M, Jaeger H & Lindquist SL (2003) Conducting nanowires built by controlled self-assembly of amyloid fibers and selective metal deposition. *Proc. Natl. Acad. Sci.* **100**, 4527–4532.

118 Reches M & Gazit E (2003) Casting Metal Nanowires Within Discrete Self-Assembled Peptide Nanotubes. *Science* **300**, 625–627.

119 Lu K, Guo L, Mehta AK, Childers WS, Dublin SN, Skanthakumar S, Conticello VP, Thiyagarajan P, Apkarian RP & Lynn DG (2007) Macroscale assembly of peptide nanotubes. *Chem. Commun.*, 2729.

120 Baxa U, Speransky V, Steven AC & Wickner RB (2002) Mechanism of inactivation on prion conversion of the Saccharomyces cerevisiae Ure2 protein. *Proc. Natl. Acad. Sci.* **99**, 5253–5260.

121 Baldwin AJ, Bader R, Christodoulou J, MacPhee CE, Dobson CM & Barker PD (2006) Cytochrome Display on Amyloid Fibrils. *J. Am. Chem. Soc.* **128**, 2162–2163.

122 Zhang Y, Gu H, Yang Z & Xu B (2003) Supramolecular Hydrogels Respond to Ligand−Receptor Interaction. *J. Am. Chem. Soc.* **125**, 13680–13681.

123 Hureau C (2012) Coordination of redox active metal ions to the amyloid precursor protein and to amyloid-β peptides involved in Alzheimer disease. Part 1: An overview. *Coord. Chem. Rev.* **256**, 2164–2174.

124 Cassagnes L-E, Hervé V, Nepveu F, Hureau C, Faller P & Collin F (2013) The Catalytically Active Copper-Amyloid-Beta State: Coordination Site Responsible for Reactive Oxygen Species Production. *Angew. Chem. Int. Ed.* **52**, 11110–11113.

125 Rufo CM, Moroz YS, Moroz OV, Stöhr J, Smith TA, Hu X, DeGrado WF & Korendovych IV (2014) Short peptides self-assemble to produce catalytic amyloids. *Nat. Chem.* **6**, 303–309.

126 Friedmann MP, Torbeev V, Zelenay V, Sobol A, Greenwald J & Riek R (2015) Towards Prebiotic Catalytic Amyloids Using High Throughput Screening. *PLOS ONE* **10**,

e0143948.

127 Bolisetty S, Arcari M, Adamcik J & Mezzenga R (2015) Hybrid Amyloid Membranes for Continuous Flow Catalysis. *Langmuir* **31**, 13867–13873.

128 Faller P, Hureau C, Dorlet P, Hellwig P, Coppel Y, Collin F & Alies B (2012) Methods and techniques to study the bioinorganic chemistry of metal–peptide complexes linked to neurodegenerative diseases. *Coord. Chem. Rev.* **256**, 2381–2396.

129 Alies B, Bijani C, Sayen S, Guillon E, Faller P & Hureau C (2012) Copper Coordination to Native N-Terminally Modified versus Full-Length Amyloid-β: Second-Sphere Effects Determine the Species Present at Physiological pH. *Inorg. Chem.* **51**, 12988–13000.

130 Bousejra-ElGarah F, Bijani C, Coppel Y, Faller P & Hureau C (2011) Iron(II) Binding to Amyloid-β, the Alzheimer's Peptide. *Inorg. Chem.* **50**, 9024–9030.

131 Noël S, Cadet S, Gras E & Hureau C (2013) The benzazole scaffold: a SWAT to combat Alzheimer's disease. *Chem. Soc. Rev.* **42**, 7747–7762.

132 Biancalana M & Koide S (2010) Molecular mechanism of Thioflavin-T binding to amyloid fibrils. *Biochim. Biophys. Acta BBA - Proteins Proteomics* **1804**, 1405–1412.

133 Hudson SA, Ecroyd H, Kee TW & Carver JA (2009) The thioflavin T fluorescence assay for amyloid fibril detection can be biased by the presence of exogenous compounds. *FEBS J.* **276**, 5960–5972.

134 Hackl EV, Darkwah J, Smith G & Ermolina I (2015) Effect of acidic and basic pH on Thioflavin T absorbance and fluorescence. *Eur. Biophys. J. EBJ* **44**, 249–261.

135 Di Carlo MG, Minicozzi V, Foderà V, Militello V, Vetri V, Morante S & Leone M (2015) Thioflavin T templates amyloid β(1–40) conformation and aggregation pathway. *Biophys. Chem.* **206**, 1–11.

136 Hamley IW (2012) The Amyloid Beta Peptide: A Chemist's Perspective. Role in Alzheimer's and Fibrillization. *Chem. Rev.* **112**, 5147–5192.

137 Faller P, Hureau C & Berthoumieu O (2013) Role of Metal Ions in the Self-assembly of the Alzheimer's Amyloid-β Peptide. *Inorg. Chem.* **52**, 12193–12206.

138 Roychaudhuri R, Yang M, Hoshi MM & Teplow DB (2009) Amyloid β-Protein Assembly and Alzheimer Disease. *J. Biol. Chem.* **284**, 4749–4753.

139 Fu Z, Aucoin D, Davis J, Van Nostrand WE & Smith SO (2015) Mechanism of Nucleated Conformational Conversion of Aβ42. *Biochemistry (Mosc.)* **54**, 4197–4207.

140 Petkova AT, Leapman RD, Guo Z, Yau W-M, Mattson MP & Tycko R (2005) Self-Propagating, Molecular-Level Polymorphism in Alzheimer’s ß-Amyloid Fibrils. *Science* **307**, 262–265.

141 Petkova AT, Yau W-M & Tycko R (2006) Experimental constraints on quaternary structure in Alzheimer’s β-amyloid fibrils. *Biochemistry (Mosc.)* **45**, 498–512.

142 Paravastu AK, Leapman RD, Yau W-M & Tycko R (2008) Molecular structural basis for polymorphism in Alzheimer’s beta-amyloid fibrils. *Proc. Natl. Acad. Sci. U. S. A.* **105**, 18349–18354.

143 Lu J-X, Qiang W, Yau W-M, Schwieters CD, Meredith SC & Tycko R (2013) Molecular Structure of β-Amyloid Fibrils in Alzheimer’s Disease Brain Tissue. *Cell* **154**, 1257–1268.

144 Luhrs T, Ritter C, Adrian M, Riek-Loher D, Bohrmann B, Dobeli H, Schubert D & Riek R (2005) 3D structure of Alzheimer’s amyloid- (1-42) fibrils. *Proc. Natl. Acad. Sci.* **102**, 17342–17347.

145 Xiao Y, Ma B, McElheny D, Parthasarathy S, Long F, Hoshi M, Nussinov R & Ishii Y (2015) Aβ(1–42) fibril structure illuminates self-recognition and replication of amyloid in Alzheimer’s disease. *Nat. Struct. Mol. Biol.* **22**, 499–505.

146 Butterfield DA (2002) Amyloid β-peptide (1-42)-induced Oxidative Stress and Neurotoxicity: Implications for Neurodegeneration in Alzheimer’s Disease Brain. A Review. *Free Radic. Res.* **36**, 1307–1313.

147 Butterfield DA, Swomley AM & Sultana R (2013) Amyloid *β* -Peptide (1–42)-Induced Oxidative Stress in Alzheimer Disease: Importance in Disease Pathogenesis and Progression. *Antioxid. Redox Signal.* **19**, 823–835.

148 Soto C, Castaño EM, Asok Kumar R, Beavis RC & Frangione B (1995) Fibrillogenesis of synthetic amyloid-β peptides is dependent on their initial secondary structure. *Neurosci. Lett.* **200**, 105–108.

149 Zagorski MG, Yang J, Shao H, Ma K, Zeng H & Hong A (1999) [13] Methodological and chemical factors affecting amyloid β peptide amyloidogenicity. In *Methods in Enzymology* pp. 189–204. Elsevier.

150 Finder VH, Vodopivec I, Nitsch RM & Glockshuber R (2010) The Recombinant Amyloid-β Peptide Aβ1–42 Aggregates Faster and Is More Neurotoxic than Synthetic Aβ1–42. *J. Mol. Biol.* **396**, 9–18.

151 Voet D & Voet JG (2005) *Biochimie* De Boeck, Bruxelles.

152 Shen M, Wang Q, Mu X, Xu H & Yan W (2009) Expression, purification and characterization of recombinant human β-amyloid 1–42 in Pichia pastoris. *Protein Expr. Purif.* **63**, 84–88.

153 Bockhorn JJ, Lazar KL, Gasser AJ, Luther LM, Qahwash IM, Chopra N & Meredith SC (2010) Novel semisynthetic method for generating full length β-amyloid peptides. *Biopolymers* **94**, 511–520.

154 Lee EK, Hwang JH, Shin DY, Kim DI & Yoo YJ (2005) Production of recombinant amyloid-β peptide 42 as an ubiquitin extension. *Protein Expr. Purif.* **40**, 183–189.

155 Garai K, Crick SL, Mustafi SM & Frieden C (2009) Expression and purification of amyloid-β peptides from Escherichia coli. *Protein Expr. Purif.* **66**, 107–112.

156 Alies B, LaPenna G, Sayen S, Guillon E, Hureau C & Faller P (2012) Insights into the Mechanisms of Amyloid Formation of Zn ^{II} -Ab11-28: pH-Dependent Zinc Coordination and Overall Charge as Key Parameters for Kinetics and the Structure of Zn ^{II} -Ab11-28 Aggregates. *Inorg. Chem.* **51**, 7897–7902.

157 Szczepankiewicz O, Linse B, Meisl G, Thulin E, Frohm B, Sala Frigerio C, Colvin MT, Jacavone AC, Griffin RG, Knowles T, Walsh DM & Linse S (2015) N-Terminal Extensions Retard Aβ42 Fibril Formation but Allow Cross-Seeding and Coaggregation with Aβ42. *J. Am. Chem. Soc.* **137**, 14673–14685.

158 Liao Y-H & Chen Y-R (2015) A novel method for expression and purification of authentic amyloid-β with and without 15N labels. *Protein Expr. Purif.* **113**, 63–71.

159 Wiesehan K, Funke SA, Fries M & Willbold D (2007) Purification of recombinantly expressed and cytotoxic human amyloid-beta peptide 1–42. *J. Chromatogr. B* **856**, 229–233.

160 Sharma SC, Armand T, Ball KA, Chen A, Pelton JG, Wemmer DE & Head-Gordon T (2015) A facile method for expression and purification of 15N isotope-labeled human Alzheimer's β-amyloid peptides from E. coli for NMR-based structural analysis. *Protein*

Expr. Purif. **116**, 82–89.

161 Chhetri G, Pandey T, Chinta R, Kumar A & Tripathi T (2015) An improved method for high-level soluble expression and purification of recombinant amyloid-beta peptide for in vitro studies. *Protein Expr. Purif.* **114**, 71–76.

162 Walsh DM, Thulin E, Minogue AM, Gustavsson N, Pang E, Teplow DB & Linse S (2009) A facile method for expression and purification of the Alzheimer’s disease-associated amyloid β-peptide: Expression and purification of the amyloid β-peptide. *FEBS J.* **276**, 1266–1281.

163 Espargaró A, Sabate R & Ventura S (2012) Thioflavin-S staining coupled to flow cytometry. A screening tool to detect in vivo protein aggregation. *Mol. Biosyst.* **8**, 2839.

164 Vignaud H, Bobo C, Lascu I, Sörgjerd KM, Zako T, Maeda M, Salin B, Lecomte S & Cullin C (2013) A Structure-Toxicity Study of Aß42 Reveals a New Anti-Parallel Aggregation Pathway. *PLoS ONE* **8**, e80262.

165 Carrió M, González-Montalbán N, Vera A, Villaverde A & Ventura S (2005) Amyloid-like Properties of Bacterial Inclusion Bodies. *J. Mol. Biol.* **347**, 1025–1037.

166 Villar-Piqué A, Espargaró A, Sabaté R, de Groot NS & Ventura S (2012) Using bacterial inclusion bodies to screen for amyloid aggregation inhibitors. *Microb. Cell Factories* **11**, 55.

167 Allen SP, Polazzi JO, Gierse JK & Easton AM (1992) Two novel heat shock genes encoding proteins produced in response to heterologous protein expression in Escherichia coli. *J. Bacteriol.* **174**, 6938–6947.

168 Neerathilingam M, Mysore S & Gandham SHA (2014) Soni-removal of nucleic acids from inclusion bodies. *Biochem. Biophys. Res. Commun.* **448**, 45–49.

169 Beaven GH & Holiday ER (1952) Ultraviolet Absorption Spectra of Proteins and Amino Acids. In *Advances in Protein Chemistry* (M.L. Anson KB and JTE, ed), pp. 319–386. Academic Press.

170 Long F, Cho W & Ishii Y (2011) Expression and purification of 15N- and 13C-isotope labeled 40-residue human Alzheimer’s β-amyloid peptide for NMR-based structural analysis. *Protein Expr. Purif.* **79**, 16–24.

171 Kim E-K, Moon JC, Lee JM, Jeong MS, Oh C, Ahn S-M, Yoo YJ & Jang HH

(2012) Large-scale production of soluble recombinant amyloid-β peptide 1–42 using cold-inducible expression system. *Protein Expr. Purif.* **86**, 53–57.

172 Zhang L, Yu H, Song C, Lin X, Chen B, Tan C, Cao G & Wang Z (2009) Expression, purification, and characterization of recombinant human β-amyloid42 peptide in Escherichia coli. *Protein Expr. Purif.* **64**, 55–62.

173 Xu M, Ren W, Tang X, Hu Y & Zhang H (2016) Advances in development of fluorescent probes for detecting amyloid-β aggregates. *Acta Pharmacol. Sin.* **37**, 719–730.

174 Hofmeier H & Schubert US (2004) Recent developments in the supramolecular chemistry of terpyridine?metal complexes. *Chem. Soc. Rev.* **33**, 373.

175 Madhu V, Diskin-Posner Y & Neumann R (2011) Copper(I) Complexes of Bipyridine and Terpyridine with Fluorous Tails and the Formation of Crystalline Materials with Fluorous Layers. *Eur. J. Inorg. Chem.* **2011**, 1792–1796.

176 Feng H, Zhou X-P, Wu T, Li D, Yin Y-G & Ng SW (2006) Hydrothermal synthesis of copper complexes of 4′-pyridyl terpyridine: From discrete monomer to zigzag chain polymer. *Inorganica Chim. Acta* **359**, 4027–4035.

177 Dalla Cort A, De Bernardin P, Forte G & Yafteh Mihan F (2010) Metal–salophen-based receptors for anions. *Chem. Soc. Rev.* **39**, 3863.

178 Amini MK, Khorasani JH, Khaloo SS & Tangestaninejad S (2003) Cobalt(II) salophen-modified carbon-paste electrode for potentiometric and voltammetric determination of cysteine. *Anal. Biochem.* **320**, 32–38.

179 Cozzi PG (2004) Metal Salen Schiff base complexes in catalysis: practical aspects. *Chem. Soc. Rev.* **33**, 410.

180 Adeloye A & Ajibade P (2014) Towards the Development of Functionalized PolypyridineLigands for Ru(II) Complexes as Photosensitizers inDye-Sensitized Solar Cells (DSSCs). *Molecules* **19**, 12421–12460.

181 Butsch K, Günther T, Klein A, Stirnat K, Berkessel A & Neudörfl J (2013) Redox chemistry of copper complexes with various salen type ligands. *Inorganica Chim. Acta* **394**, 237–246.

182 Yam VW-W, Ko C-C & Zhu N (2004) Photochromic and Luminescence Switching Properties of a Versatile Diarylethene-Containing 1,10-Phenanthroline Ligand and Its

Rhenium(I) Complex. *J. Am. Chem. Soc.* **126**, 12734–12735.

183 Germain ME, Vargo TR, Khalifah PG & Knapp MJ (2007) Fluorescent Detection of Nitroaromatics and 2,3-Dimethyl- 2,3-dinitrobutane (DMNB) by a Zinc Complex: (salophen)Zn. *Inorg. Chem.* **46**, 4422–4429.

184 Constable EC, Lewis J, Liptrot MC & Raithby PR (1990) The coordination chemistry of 4′-phenyl-2,2′:6′, 2″-terpyridine; the synthesis, crystal and molecular structures of 4′-phenyl-2,2′:6′,2″-terpyridine and bis(4′-phenyl-2,2′:6′,2″-terpyridine)nickel(II) chloride decahydrate. *Inorganica Chim. Acta* **178**, 47–54.

185 Sauvage JP, Collin JP, Chambron JC, Guillerez S, Coudret C, Balzani V, Barigelletti F, De Cola L & Flamigni L (1994) Ruthenium(II) and Osmium(II) Bis(terpyridine) Complexes in Covalently-Linked Multicomponent Systems: Synthesis, Electrochemical Behavior, Absorption Spectra, and Photochemical and Photophysical Properties. *Chem. Rev.* **94**, 993–1019.

186 Dobrawa R, Ballester P, Saha-Möller CR & Würthner F (2006) Thermodynamics of 2,2′:6′,2″-Terpyridine-Metal Ion Complexation. In *Metal-Containing and Metallosupramolecular Polymers and Materials* pp. 43–62. American Chemical Society.

187 Henderson IM & Hayward RC (2012) Kinetic stabilities of bis-terpyridine complexes with iron(II) and cobalt(II) in organic solvent environments. *J. Mater. Chem.* **22**, 21366–21369.

188 Uma V, Elango M & Nair BU (2007) Copper(II) Terpyridine Complexes: Effect of Substituent on DNA Binding and Nuclease Activity. *Eur. J. Inorg. Chem.* **2007**, 3484–3490.

189 Enthaler S, Hagemann B, Erre G, Junge K & Beller M (2006) An Environmentally Benign Process for the Hydrogenation of Ketones with Homogeneous Iron Catalysts. *Chem. – Asian J.* **1**, 598–604.

190 Hvasanov D, Mason AF, Goldstein DC, Bhadbhade M & Thordarson P (2013) Optimising the synthesis, polymer membrane encapsulation and photoreduction performance of Ru(ii)- and Ir(iii)-bis(terpyridine) cytochrome c bioconjugates. *Org. Biomol. Chem.* **11**, 4602.

191 Constable EC, Ward MD & Corr S (1988) A convenient, high yield synthesis of 2,2′:6′,2″-terpyridine and its iron(II) complex. *Inorganica Chim. Acta* **141**, 201–203.

192 Kröhnke pyridine synthesis (2006) In *Name Reactions* pp. 343–344. Springer

Berlin Heidelberg.

193 Harzmann GD, Neuburger M & Mayor M (2013) 4,4″-Disubstituted Terpyridines and Their Homoleptic Fe ^{II} Complexes. *Eur. J. Inorg. Chem.* **2013**, 3334–3347.

194 Wang J & Hanan GS (2005) A Facile Route to Sterically Hindered and Non-Hindered 4′-Aryl-2,2′:6′,2″-Terpyridines. *Synlett*, 1251–1254.

195 Sasaki I, Daran JC & Balavoine GGA (1999) An Effective Route to Polysubstituted Symmetric Terpyridines. *Synthesis* **1999**, 815–820.

196 Constable EC & Lewis J (1982) The preparation and coordination chemistry of 2,2′:6′,2″-terpyridine macrocycles—1. *Polyhedron* **1**, 303–306.

197 Potts KT, Usifer DA, Guadalupe A & Abruna HD (1987) 4-Vinyl-, 6-vinyl-, and 4’-vinyl-2,2’:6’,2"-terpyridinyl ligands: their synthesis and the electrochemistry of their transition-metal coordination complexes. *J. Am. Chem. Soc.* **109**, 3961–3967.

198 Fallahpour R-A, Neuburger M & Zehnder M (1999) Homoleptic and heteroleptic iron(II) and ruthenium(II) complexes of novel 4′-nitro-2,2′:6′,2″-terpyridines and 4′-amino-2,2′:6′,2″-terpyridines. *New J. Chem.* **23**, 53–61.

199 Schubert US & Eschbaumer C (1999) New Synthetic Strategy toward Pyridine-Based Ligands for Supramolecular Chemistry Utilizing 2,6-Bis(trimethyltin)pyridine as the Central Building Block. *Org. Lett.* **1**, 1027–1029.

200 Koohmareh GA & Sharifi M (2009) Synthesis, characterization, and coordination behavior of copoly(styrene-maleimide) functionalized with terpyridine. *J. Appl. Polym. Sci.*, NA-NA.

201 Constable EC, Dunphy EL, Housecroft CE, Neuburger M, Schaffner S, Schaper F & Batten SR (2007) Expanded ligands: bis(2,2′:6′,2″-terpyridine carboxylic acid)ruthenium(ii) complexes as metallosupramolecular analogues of dicarboxylic acids. *Dalton Trans.*, 4323.

202 Halcrow MA (2013) Jahn–Teller distortions in transition metal compounds, and their importance in functional molecular and inorganic materials. *Chem. Soc. Rev.* **42**, 1784–1795.

203 Meyer A, Schnakenburg G, Glaum R & Schiemann O (2015) (Bis(terpyridine))copper(II) Tetraphenylborate: A Complex Example for the Jahn–Teller

Effect. *Inorg. Chem.* **54**, 8456–8464.

204 Perrin DD, Dempsey B & Serjeant EP (1981) Prediction of pK a Values for Phenols, Aromatic Carboxylic Acids and Aromatic Amines. In *pK a Prediction for Organic Acids and Bases* pp. 44–52. Springer Netherlands.

205 Constable EC & Thompson AMWC (1992) Ligand reactivity in iron(II) complexes of 4?-(4?-pyridyl)-2,2? : 6?,2?-terpyridine. *J. Chem. Soc. Dalton Trans.*, 2947.

206 Encinas S, Flamigni L, Barigelletti F, Constable EC, Housecroft CE, Schofield ER, Figgemeier E, Fenske D, Neuburger M, Vos JG & Zehnder M (2002) Electronic energy transfer and collection in luminescent molecular rods containing ruthenium(II) and osmium(II) 2,2’:6’,2"-terpyridine complexes linked by thiophene-2,5-diyl spacers. *Chem. Weinh. Bergstr. Ger.* **8**, 137–150.

207 Delgado J, Zhang Y, Xu B & Epstein IR (2011) Terpyridine- and Bipyridine-Based Ruthenium Complexes as Catalysts for the Belousov−Zhabotinsky Reaction. *J. Phys. Chem. A* **115**, 2208–2215.

208 Chao H, Li G-Y, Sun L & Ji L-N (2016) Ruthenium(II) complexes with dppz: From molecular photoswitch to biological applications. *Dalton Trans.*

209 Gao X, Wang L, Huang H-L, Wang L-L, Yao J-L, Shi S & Yao T-M (2015) Molecular “light switch” [Ru(phen) $_2$ dppzidzo] $^{2+}$ monitoring the aggregation of tau. *The Analyst* **140**, 7513–7517.

210 Hanczyc P (2014) Binuclear ruthenium(II) complexes for amyloid fibrils recognition. *Chem. Phys.* **445**, 1–4.

211 White TA, Arachchige SM, Sedai B & Brewer KJ (2010) Emission Spectroscopy as a Probe into Photoinduced Intramolecular Electron Transfer in Polyazine Bridged Ru(II),Rh(III) Supramolecular Complexes. *Materials* **3**, 4328–4354.

212 Ishida H, Tobita S, Hasegawa Y, Katoh R & Nozaki K (2010) Recent advances in instrumentation for absolute emission quantum yield measurements. *Coord. Chem. Rev.* **254**, 2449–2458.

213 Breivogel A, Kreitner C & Heinze K (2014) Redox and Photochemistry of Bis(terpyridine)ruthenium(II) Amino Acids and Their Amide Conjugates – from Understanding to Applications. *Eur. J. Inorg. Chem.* **2014**, 5468–5490.

214 Fonin AV, Sulatskaya AI, Kuznetsova IM & Turoverov KK (2014) Fluorescence of Dyes in Solutions with High Absorbance. Inner Filter Effect Correction. *PLOS ONE* **9**, e103878.

215 Sulatskaya AI, Maskevich AA, Kuznetsova IM, Uversky VN & Turoverov KK (2010) Fluorescence Quantum Yield of Thioflavin T in Rigid Isotropic Solution and Incorporated into the Amyloid Fibrils. *PLOS ONE* **5**, e15385.

216 Stsiapura VI, Maskevich AA, Kuzmitsky VA, Uversky VN, Kuznetsova IM & Turoverov KK (2008) Thioflavin T as a Molecular Rotor: Fluorescent Properties of Thioflavin T in Solvents with Different Viscosity. *J. Phys. Chem. B* **112**, 15893–15902.

217 Maskevich AA, Stsiapura VI, Kuzmitsky VA, Kuznetsova IM, Povarova OI, Uversky VN & Turoverov KK (2007) Spectral Properties of Thioflavin T in Solvents with Different Dielectric Properties and in a Fibril-Incorporated Form. *J. Proteome Res.* **6**, 1392–1401.

218 Yu H (1999) Extending the size limit of protein nuclear magnetic resonance. *Proc. Natl. Acad. Sci. U. S. A.* **96**, 332–334.

219 Macchioni A, Ciancaleoni G, Zuccaccia C & Zuccaccia D (2012) Diffusion Ordered NMR Spectroscopy (DOSY). In *Supramolecular Chemistry* John Wiley & Sons, Ltd.

220 Kummer MP & Heneka MT (2014) Truncated and modified amyloid-beta species. *Alzheimers Res. Ther.* **6**, 28.

221 Juszczyk P, Kołodziejczyk AS & Grzonka Z (2009) FTIR spectroscopic studies on aggregation process of the beta-amyloid 11-28 fragment and its variants. *J. Pept. Sci. Off. Publ. Eur. Pept. Soc.* **15**, 23–29.

222 Rojas AV, Liwo A & Scheraga HA (2011) A Study of the α-Helical Intermediate Preceding the Aggregation of the Amino-Terminal Fragment of the β Amyloid Peptide (Aβ $_{1–28}$). *J. Phys. Chem. B* **115**, 12978–12983.

223 Esler WP, Stimson ER, Jennings JM, Ghilardi JR, Mantyh PW & Maggio JE (1996) Zinc-Induced Aggregation of Human and Rat β-Amyloid Peptides In Vitro. *J. Neurochem.* **66**, 723–732.

224 Viegas A, Manso J, Nobrega FL & Cabrita EJ (2011) Saturation-Transfer Difference (STD) NMR: A Simple and Fast Method for Ligand Screening and Characterization of Protein Binding. *J. Chem. Educ.* **88**, 990–994.

225 Huy PDQ & Li MS (2014) Binding of fullerenes to amyloid beta fibrils: size matters. *Phys. Chem. Chem. Phys.* **16**, 20030.

226 DeToma AS, Krishnamoorthy J, Nam Y, Lee HJ, Brender JR, Kochi A, Lee D, Onnis V, Congiu C, Manfredini S, Vertuani S, Balboni G, Ramamoorthy A & Lim MH (2014) Synthetic Flavonoids, Aminoisoflavones: Interaction and Reactivity with Metal-Free and Metal-Associated Amyloid-β Species. *Chem. Sci. R. Soc. Chem. 2010* **5**, 4851–4862.

227 Lockhart A, Ye L, Judd DB, Merritt AT, Lowe PN, Morgenstern JL, Hong G, Gee AD & Brown J (2005) Evidence for the Presence of Three Distinct Binding Sites for the Thioflavin T Class of Alzheimer's Disease PET Imaging Agents on β-Amyloid Peptide Fibrils. *J. Biol. Chem.* **280**, 7677–7684.

228 Biancalana M, Makabe K, Koide A & Koide S (2009) Molecular Mechanism of Thioflavin-T Binding to the Surface of β-Rich Peptide Self-Assemblies. *J. Mol. Biol.* **385**, 1052–1063.

229 Khurana R, Coleman C, Ionescu-Zanetti C, Carter SA, Krishna V, Grover RK, Roy R & Singh S (2005) Mechanism of thioflavin T binding to amyloid fibrils. *J. Struct. Biol.* **151**, 229–238.

230 Bauer I & Knölker H-J (2015) Iron Catalysis in Organic Synthesis. *Chem. Rev.* **115**, 3170–3387.

231 Boddien A, Loges B, Gärtner F, Torborg C, Fumino K, Junge H, Ludwig R & Beller M (2010) Iron-Catalyzed Hydrogen Production from Formic Acid. *J. Am. Chem. Soc.* **132**, 8924–8934.

232 Yeung C-T, Sham K-C, Lee W-S, Wong W-T, Wong W-Y & Kwong H-L (2009) Cobalt and iron complexes of chiral C1- and C2-terpyridines: Synthesis, characterization and use in catalytic asymmetric cyclopropanation of styrenes. *Inorganica Chim. Acta* **362**, 3267–3273.

233 Kamata K, Suzuki A, Nakai Y & Nakazawa H (2012) Catalytic Hydrosilylation of Alkenes by Iron Complexes Containing Terpyridine Derivatives as Ancillary Ligands. *Organometallics* **31**, 3825–3828.

234 Liu P, Wong EL-M, Yuen AW-H & Che C-M (2008) Highly Efficient Alkene Epoxidation and Aziridination Catalyzed by Iron(II) Salt + 4,4′,4″-Trichloro-2,2′:6′,2″-terpyridine/4,4″-Dichloro-4′- *O* -PEG-OCH $_3$ -2,2′:6′,2″-terpyridine. *Org. Lett.* **10**, 3275–

3278.

235 Liu P, Liu Y, Wong EL-M, Xiang S & Che C-M (2011) Iron oligopyridine complexes as efficient catalysts for practical oxidation of arenes, alkanes, tertiary amines and N-acyl cyclic amines with Oxone. *Chem. Sci.* **2**, 2187.

236 García JI, López-Sánchez B & Mayoral JA (2008) Linking Homogeneous and Heterogeneous Enantioselective Catalysis through a Self-Assembled Coordination Polymer. *Org. Lett.* **10**, 4995–4998.

237 Renouard T, Fallahpour R-A, Nazeeruddin MK, Humphry-Baker R, Gorelsky SI, Lever ABP & Grätzel M (2002) Novel ruthenium sensitizers containing functionalized hybrid tetradentate ligands: synthesis, characterization, and INDO/S analysis. *Inorg. Chem.* **41**, 367–378.

238 Zhang G, Zong R, Tseng H-W & Thummel RP (2008) Ru(II) Complexes of Tetradentate Ligands Related to 2,9-Di(pyrid-2‘-yl)-1,10-phenanthroline. *Inorg. Chem.* **47**, 990–998.

239 Pearce FG, Mackintosh SH & Gerrard JA (2007) Formation of Amyloid-like Fibrils by Ovalbumin and Related Proteins under Conditions Relevant to Food Processing. *J. Agric. Food Chem.* **55**, 318–322.

240 Makhlynets OV, Gosavi PM & Korendovych IV (2016) Short Self-assembling Peptides are Able to Bind to Copper and Activate Oxygen. *Angew. Chem. Int. Ed.*

241 Dubinsky L, Krom BP & Meijler MM (2012) Diazirine based photoaffinity labeling. *Bioorg. Med. Chem.* **20**, 554–570.

242 Rambaran RN & Serpell LC (2008) Amyloid fibrils: Abnormal protein assembly. *Prion* **2**, 112–117.

243 Cherny I & Gazit E (2008) Amyloids: Not Only Pathological Agents but Also Ordered Nanomaterials. *Angew. Chem. Int. Ed.* **47**, 4062–4069.

244 Pan Q-J, Guo Y-R, Li L, Odoh SO, Fu H-G & Zhang H-X (2011) Structures, spectroscopic properties and redox potentials of quaterpyridyl Ru(II) photosensitizer and its derivatives for solar energy cell: a density functional study. *Phys. Chem. Chem. Phys.* **13**, 14481–14489.

Annexes

- Annex I. Experimental procedures
- Annex II. Products characterization
- Annex III. Articles

Annex I. Experimental procedures

Experimental procedures for Chapter II

General remarks

All experiments were run at room temperature unless otherwise noted. All experiments were run using fresh ultrapure water (Synergy). All chemicals and solvents were purchased from Sigma-Aldrich and used without further purification. pET28a plasmid was purchased from Novagen. NcoI, XhoI and BamHI restriction enzymes Antarctic phosphatase and T4 DNA Ligase were purchased from New England Biolabs and used with the provided buffer according to supplier’s recommendations. pET28a_His_Thromb_Ab42 plasmid was synthesized by Genecust. *E. coli* TOP10 cells and *E. coli* BL21 (DE3) cells were obtained from Invitrogen. QIAprep spin MiniPrep kit was purchased from Qiagen. Sequence analyses of the constructions were performed by GATC Biotech.

Vectors construction and cloning procedure

The commercial pET28a plasmid was digested by NcoI and XhoI restriction enzymes, dephosphorylated using Antarctic phosphatase, and gel purified on an agarose 0.8% Tris acetate EDTA (TAE) gel. The pET28a_His-Thromb-Ab1-42 plasmid was used as template for PCR amplification of the Aβ_{1-42} coding sequence using pR_pET28_Ab42: AGCGGTGGCAGCAGCCAACTCAGCT and pF_pET28_Ab42: GACCTACCCATGGACGCTGAATTTCGCCACGACTCCGGCTAT as primers. The PCR product was digested by NcoI and XhoI, gel purified on an agarose 1.2% TAE gel and ligated in the NcoI/XhoI digested pET28a yielding the desired pET28a_MAb42 plasmid. The construction was used to transform chimiocompetent *E.coli* TOP10 cells that were grown on solid Luria-Bertani (LB) medium (10 g/L tryptone, 10 g/L NaCl, 5 g/L yeast extract) containing 50 mg/L kanamycin (1X). One colony was used to inoculate 5 mL LB kanamycin 1X at 37 °C. Cells were grown overnight, harvested before plasmid extraction using a MiniPrep kit.

The pET28a_MAb40 was obtained from pET28a_MAb42 using a similar procedure except that the sequence coding for Aβ_{1-40} was PCR-amplified with pR_pet28_Ab40: AATGGATCCTAATTAAACAACGCCGCCAACCATCAGACCGATG and pF_pet28_Ab40: AATTGTGAGCGGATAACAATTCCCCTCTAG as primers. The PCR-product was digested using NcoI and BamHI, and ligated into NcoI/BamHI digested and dephosphorylated pET28_MAb42.

Expression of His-Thromb-Aβ_{1-42}, MAβ_{1-40} and MAβ_{1-42}

Chemically competent *E. coli* BL21 (DE3) cells transformed with corresponding plasmids were used for peptide production. One single colony was used to inoculate 10 mL LB kanamycin 1X medium. The cells were grown for 16 h. 100 mL of LB medium containing kanamycin 1X were inoculated to an OD_{600} of 0.05 with an overnight pre-culture performed from one single clone in 10 mL LB-Kana medium. Cells were grown at 37 °C under agitation to an OD_{600} of 0.8. Expression was induced with 0.5 mM Isopropyl β-*D*-1-thiogalactopyranoside (IPTG) during for 4 additional hours of culture at 37 °C.

His-Thromb-A$\beta_{1\text{-}42}$ purification

Cells are harvested by centrifugation (8,000 g, 10 min) and re-suspended to an OD_{600} of 80 in lysis buffer (50 mM Tris-HCl, 100 mM NaCl, pH 8) containing 1% Tergitol-type NP40 detergent. Cells were then lysed by 30 s sonication on ice and the lysate was centrifuged (12,000 g, 10 min). Pellet was resuspended in 8 M urea under slow agitation until the solution turns clear. Solution is then applied on TALON resin in batch mode equilibrated with lysis buffer and incubated 30 min at RT. Supernatent is discarded, and resin is washed twice with lysis buffer. Peptide is finally eluted with imidazole solutions of increasing concentration (25, 50, 100, 200, 300, 400 mM, respectively). Samples were analysed by SDS-PAGE.

MA$\beta_{1\text{-}40}$ and MA$\beta_{1\text{-}42}$ inclusion bodies isolation

Cells were harvested by centrifugation (8,000 g, 10 min, 4°C) and re-suspended to an OD_{600} of 80 in lysis buffer (50 mM Tris-HCl, 100 mM NaCl, pH 8) containing 1% Tergitol-type NP40 detergent. Cells were then lysed by 30 s sonication on ice and the lysate was centrifuged (12,000 g, 10 min, 10°C). From then, pellets of IBs can be stored at -20°C at least for a few days. The insoluble fraction was re-suspended in 1 mL lysis buffer, containing phenylmethanesulfonyl fluoride (15 mM) and lysozyme (300 μg/mL), and incubated for 1 h at room temperature. IBs were harvested by centrifugation (12,000 g, 10 min, 10°C), washed with Triton X100 0.5% and twice with phosphate saline buffer (PBS) 1X pH 8. IBs were finally resuspended in PBS buffer and submitted to 10 cycles of 10 s sonication followed by centrifugation to remove nucleic acid contaminants that could be stacked on their surface, according to a previously reported procedure. Samples can then be combined.

MAβ peptides purification

IBs were denatured by 2 h incubation in 500 μL of NaOH 50 mM under smooth shaking at room temperature. Solution must be almost perfectly translucent and pale yellow. The resulting mixture was centrifuged (12,000 g, 5 min, 10°C), and the supernatant neutralized to pH 7 by addition of 500 mM HCl. The formation of a white precipitate was observed. The mixture was centrifuged once again, and the supernatant was collected. To optimize recovery, this denaturation/neutralisation cycle was applied twice. Supernatants were mixed and passed through a 30-kDa Amicon-Ultra centrifugal device, to remove high molecular weight contaminant proteins, and then concentrated on a 3-kDa Amicon-Ultra centrifugal device. Final volume should be below 500 μL to enable SEC purification (see below).

For short-term storage purpose (not more than a few hours/days), it is possible to add NaOH to final concentration 50 mM. This can be done either before 30-kDa filtration (if filtrations are extended to a long period of time), or after concentration (operating a “buffer exchange” on the 3-kDa membrane). Samples can then be stored at 4°C. NaOH addition is mandatory for SEC purification in our elution conditions (see below). No solution has been found yet for long-term storage (weeks/months).

SDS-PAGE analysis

15 μL protein samples were mixed with 5 μL Laemli Sample buffer (Bio-Rad) containing 10% β-mercaptoethanol, and denatured at 95 °C for 10 min. Samples were then loaded on a Mini-protean TGX Stain-Free Any Kd Precast Gel (Bio-Rad) and electrophoresis was run for 30 min at 150 V in Tris/Glycine/SDS buffer (Bio-Rad). Gel was then stained using PageBlue Protein Staining solution (Bio-Rad).

Thioflavin-S staining

Samples of Aβ peptide producing cells or purified IBs are centrifuged (12,000 g, 10 min) and resuspended in 200 μL Thioflavin-S 125 μM in PBS 1X pH 8. After 15 min incubation, cells or IBs were harvested by centrifugation, washed with 200 μL PBS, and re-suspended in PBS, and submitted to fluorescence experiments.

Fluorescence microscopy

50 μL samples of Th-S stained cells or IBs were dispensed on a microscope glass slide and imaged using a Leica microscope with a 63x lens with a DAPI filter (λ_{exc} = 340-380 nm, dichroic = 400, λ_{em} = 425 nm).

Fluorescence spectrophotometry

1 mL samples of Th-S stained cells or IBs were placed in a quartz cuvette and their emission spectra were recorded using a Jasco fluorimeter (λ_{exc} = 375 nm). Right after each measurement, OD_{600} was measured, to normalize the signal.

^{1}H NMR

Pure samples of peptides in water were diluted to 100 μM in phosphate buffer 50 mM pH 7 in D_2O. ^{1}H NMR spectra were recorded on a 500 MHz NMR (Bruker) at 25 °C using solvent as reference. As a control, synthetic $A\beta_{1-40}$ was dissolved in NaOD and diluted to 100 μM in the same conditions.

LC-MS

Peptide samples were analysed by LC-MS on an Agilent 1200 HPLC fitted with a Macherey Nagel Nucleodur 300-5 C4 ec 250 mm x 2 mm 5 μm at 30 °C coupled with a Thermo Fisher Scientific LCQ Fleet mass spectrometer fitted with an H-ESI II Probe.

Samples were eluted at 0.33 mL/min using a gradient of acetonitrile going from 5% to 90% in aqueous formic acid 0.1% in 12 min. Multiply-charged peptides were detected by mass spectrometry (ESI +).

Thioflavin-T aggregation assay

To ensure of the homogeneity of the starting sample, monomeric peptides were isolated by steric exclusion chromatography (SEC). An Aktä Purifier system equipped with a Superdex 75 10/300 column was equilibrated with 2 column volumes of 15 mM NaOH. Peptide samples in NaOH 50 mM (volume below 500 μL) were then eluted at RT using NaOH 15 mM at 1 mL/min, with UV monitoring at 220 and 293 nm. Monomeric MAβ peptides display retention times around 9 min. Fractions containing peptides were collected, centrifuged, and their concentration was assessed by UV-Vis at pH 12 (λ = 293 nm, ε = 2400 $L.mol^{-1}.cm^{-1}$).

In a 384-wells microplate (Greiner) were added phosphate buffer (50 mM), thioflavin-T (10 μM) and freshly SEC-purified peptide (20 μM or 50 μM). Fluorescence intensity was recorded every 5 min for a total duration of 4 days using a ClarioStar plate reader (BMG Labtech) set at 37 °C. Fluorescence parameters were set as follows: λ_{exc} = 440 nm, λ_{em} = 490 nm, gain = 650, shaking at 200 rpm for 12 s before each measurement. Aggregation curves were fitted using KaleidaGraph software.

Experimental procedures for Chapter III

Synthesis of 4-(*p*-nitrophenyl)- 2,6- (2’,2’’-pyridyl)pyridine (L^3)

(E)-3-(4”-nitrophenyl)-1-(pyridine-2’-yl)prop-2-enone (0.4 g, 1.57 mmol) and 9-(2-pyridinylcarbonyl)pyridinium iodide (0.51 g, 1.57 mmol) are dissolved in methanol (20 mL) and the mixture is heated to reflux for 6 h, leading to a thick grey precipitate. The mixture is allowed to cool at room temperature, then in ice. The precipitate is filtered, washed with cold methanol, and dried with diethyl ether, affording the desired compound as a light grey solid (0.37 g, 68%).

Synthesis of 4-*p*-carboxyphenyl—2,6 (2’,2’’-pyridyl)pyridine (L^2)

Terephtaldehydic acid (2.46 g, 16.4 mmol) and KOH (5.52 g, 98.4 mmol) are dispersed in 50 mL of ethanol. 4-acetyl pyridine (3.67 mL, 32.8 mmol) is added, followed by 60 mL of NH_4OH, leading to a clear yellow solution. The mixture is heated at 75°C and stirred overnight. The mixture is cooled to RT, and resulting white solid is filtered off, rinsed with ethanol, diethyl ether, and dried under vacuum. Recrystallization in ethanol affords the desired product as a white solid (1.82 g, 30%).

Synthesis of 4-furyl-2,6 (2’,2’’-pyridyl)pyridine (L^4)

Furaldehyde (1.66 mL, 20 mmol), 2-acetyl pyridine (4.48 mL, 40 mmol) and KOH (3.08 g, 55 mmol) are dissolved together in ethanol (100 mL). Ammoniac is added (60 mL) and the mixture is heated at 60 °C for 24 h, forming a precipitate. The solution is cooled at RT and part of the solvent is evaporated. The solid is filtered off, washed with ethanol and dried under vacuum to afford the desired compound (3 g, 51 %).

Synthesis of 4-*p*-bromophenyl-2,6 (2’,2’’-pyridyl)pyridine (L^5)

4-bromobenzaldehyde (1.65 g, 9 mmol), 2-acetyl pyridine (2 mL, 18 mmol) and KOH (2.76 g, 50 mmol) are dissolved together in ethanol (50 mL). Aqueous ammoniac (25 %) is added (30 mL) and the mixture is heated at 60 °C for 24 h, forming a white precipitate. The solution is cooled at RT and part of the solvent is evaporated. The solid is filtered off, washed with methanol and dried under vacuum to afford the desired compound (2.38 g, 70 %).

Synthesis of 4-*p*-aminophenyl-2,6- (2’,2’’-pyridyl)pyridine (L^1)

Synthesis 1: L^3 (0.43 g, 1.21 mmol) and Pd/C 10% (0.06 g, cat.) are dissolved in ethanol (15 mL) and heated to reflux for 45 min. Hydrazine (1.47 mL, 47.3 mmol) is then added dropwise, and the resulting solution is refluxed for 3 additional hours. The resulting mixture is cooled at room temperature, filtered over Celite and washed with DCM (75 mL). The supernatant is washed with

$NaHCO_3$ sat. (100 mL), brine (100 mL), dried over Na_2SO_4, filtered and dried under reduced pressure, leading to the desired ligand as a bright yellow powder (0.2g, 52%).

Synthesis 2: **L^3** (2 g, 5.63 mmol) and tin (II) chloride (4.28 g, 22.5 mmol) are dissolved in HCl 37% and the mixture is heated at 70°C for 5 h. The resulting mixture is then cooled to RT, and 40 mL of 20% NaOH are added. The mixture is stirred for 30 min. pH is then set to 10 by addition of concentrated NaOH, which afford a brown precipitate. After 15 min stirring, the solid is filtrated, washed with ether, and dried under vacuum. The solid is then dispersed in acetonitrile and heated to reflux. The resulting mixture is filtrated hot over Celite, and evaporated, affording a yellow solid (0.7 g, 30%).

General procedure: CuL_2 complexes synthesis

Copper (II) nitrate (36.4 mg, 0.154 mmol) and L (100 mg, 0.3 mmol) are dissolved separately in methanol and warmed at 50°C. The copper solution is then added drop wise to the ligand solution, resulting in an instantaneous change of colour. The solution is cooled to RT, and a concentrated $NaPF_6$ solution is added drop wise, forming a precipitate. The solid is then filtered, washed with methanol, and dried *in vacuo* (87-98% average yield).

General procedure: FeL_2 complexes synthesis

Iron (III) nitrate (60 mg) and L (100 mg, 2 eq) are dissolved separately in ethanol and refluxed. The iron solution is then added dropwise to the ligand solution, resulting in an instantaneous change of colour, from light yellow to dark purple. The solution is refluxed for 1 h, and cooled to RT. A concentrated $NaPF_6$ solution is added drop wise, forming a light purple precipitate. The solid is collected by centrifugation, washed with ethanol, and dried *in vacuo*. Desired complexes are afforded as purple solids (56-72% average yield).

General procedure: RuL_2 complexes synthesis

Ruthenium (III) chloride (80 mg) and L (2 eq) are dissolved separately in methanol and refluxed. The ruthenium solution is then added dropwise to the ligand solution, resulting in an instantaneous change of colour, from light yellow to dark brown. A spatula of sodium ascorbate is added and the solution is refluxed for 1 h. The mixture is cooled to RT, then on ice. Subsequently the solution is filtered, and the volume of supernatant is reduced under low pressure. A concentrated $NaPF_6$ solution is added drop wise, forming a light red precipitate. The solid is collected by centrifugation, washed with methanol, and dried *in vacuo*. Desired complexes are afforded as red solids (42-61% yield).

Nuclear Magnetic Resonance (NMR)

Dried samples were dissolved in 500 μL of deuterated solvent and placed in a 5 mm borosilicate NMR tube. ^{1}H and ^{13}C NMR spectra were recorded either on a 300 MHz or a 400 MHz NMR (Bruker) at 298 K using solvent as reference. Spectra were processed using MestReNova software.

Electron Paramagnetic Resonance (EPR)

Metal complex was dissolved to 1 mM in ACN containing 0.1 mM tetrabutylammonium hexafluoro phosphate and 10% glycerol. Samples were placed in a 2 mm quartz EPR tubes and frozen in liquid nitrogen. Band X EPR spectra (9,5 GHz) were recorded on a Elexsys E500 machine (Brucker). Spectra were processed using Kaleidagraph software.

Following formula were applied to calculate EPR parameters:

$$B_{\parallel} = \frac{h \times \nu}{g_{\parallel} \times \beta} \quad \text{with } \nu \text{ in GHz and B in mT.}$$

$$A_{\parallel}\,(cm) = A_{\parallel}\,(G) \times 4.6686.10^{-5} \times g_{\parallel}$$

Cyclic voltammetry (CV)

Cyclic voltammetry experiments were run with a three electrodes system in a 2 mL cylindrical cell at room temperature. The working electrode is in glassy carbon, and was polished using a colloidal silica suspension between each measurement. The counter electrode is a platinum wire. In the case of Cu complexes, reference electrode was SCE, isolated from the cell by a salt bridge ended with a frit. In the case of Ru complexes, reference electrode was Ag/Ag+ in 0.01 M $AgNO_3$ in ACN, directly connected to the system. Dissolved dioxygen was removed by sparging Ar before each measurement.

Complex samples were dissolved in ACN containing 0.1 M tetrabutylammonium tetrafluoro borate, and cyclic voltamogrammes were recorded at 0.1 V/s scan rate, with ohmic resistance was set to 300 Ω. Data were collected, and all potentials were converted into V *vs.* NHE, using the following relations:

$$E\ (V\ vs. NHE)\ =\ E\ (V\ vs. SCE)\ +\ 0.241$$

$$E\ (V\ vs. NHE)\ =\ E\ (V\ vs. Ag/Ag+)\ +\ 0.288$$

UV-Visible measurements

UV-Vis spectra were recorded on a Spectro Star Nano spectrophotometer (BMG Labtech) in a 100 μL 1 cm pathlength quartz cuvette at room temperature.

Fluoresence measurements

Fluoresence spectra were recorded on a Optima ClarioStar plate reader (BMG Labtech) in a 384-well plate (Greiner) at 25°C.

Quantum Yield determination

In a 384-well plate (Greiner) were prepared six solutions of 0, 1, 2, 3, 4, and 5 mM of compound in ACN. Similar solutions were prepared with $Ru(bpy)_3$ which are used as reference.

UV-Vis and emission of solutions at suitable wavelength were recorded on a Optima ClarioStar plate reader (BMG Labtech) at 25°C. Quantum yields were calculated for each solution using the following formula:

$$\phi(x) = \frac{F(x)A(ref)}{F(ref)A(x)}\left(\frac{n(x)}{n(ref)}\right)^2 \phi(ref)$$

with Φ: fluorescence quantum yield, F: fluorescence intensity at λ_{em}, A: absorbance at λ_{max}, n: refractive index of the medium.

Experimental procedures from Chapter IV

Aβ$_{1\text{-}40}$ aggregation assay

To ensure of the homogeneity of the starting sample, commercial synthetic Aβ$_{1\text{-}40}$ (Genecust) is purified by steric exclusion chromatography. Lyophilized Aβ$_{1\text{-}40}$ is gently dissolved in 50 mM NaOH to a concentration of 10 mg/mL. The solution is then injected on a Aktä system equipped with a Superdex 75 10/300 column previously equilibrated with 2 column volumes of 15 mM NaOH. Peptide sample is eluted using NaOH 15 mM at 1 mL/min, with UV monitoring at 220 and 293 nm. Monomeric Aβ$_{1\text{-}40}$ displays retention times around 10 min. Fractions containing peptides are collected, centrifuged, and their concentration was assessed by UV-Vis at pH 12 (λ = 293 nm, ε = 2400 L.mol^{-1}.cm^{-1}).

In a 384-wells microplate (Greiner) were added water, phosphate buffer pH 7 (50 mM), thioflavin-T (10 μM), metal complex (50 μM) and freshly purified Aβ$_{1\text{-}40}$ (50 μM). Final ACN content is of 5%. Fluorescence intensity was recorded every 5 min for a total duration of 4 days using a ClarioStar plate reader (BMG Labtech) set at 37 °C. Fluorescence parameters were set as follows: λ_{exc} = 440 nm, λ_{em} = 490 nm, gain = 650, 200 rpm shaking for 12 s before each measurement. $t_{1/2}$ values were obtained by sigmoidal curve fitting using Kaleidagraph software.

Aβ$_{11\text{-}28}$ aggregation assay

Because it is less aggregation prone than Aβ$_{1\text{-}40}$, Aβ$_{11\text{-}28}$ was used without further purification. Lyophilized synthetic Aβ$_{11\text{-}28}$ was dissolved in 50 mM NaOH at 10 mg/mL. In a 384-wells microplate (Greiner) were added water, phosphate buffer pH 7 (50 mM), thioflavin-T (10 μM), metal complex (50 μM), $ZnSO_4$ (25 μM) and Aβ$_{11\text{-}28}$ (50 μM). Final ACN content was of 5%. Fluorescence intensity was recorded every 5 min for a total duration of 40 h using a ClarioStar plate reader (BMG Labtech) set at 25 °C. Fluorescence parameters were set as follows: λ_{exc} = 440 nm, λ_{em} = 490 nm, gain = 2000, 200 rpm shaking for 12 s before each measurement. Aggregation curves were fitted using KaleidaGraph software.

Aβ$_{1\text{-}28}$ aggregation assay

Lyophilized synthetic Aβ$_{1\text{-}28}$ was dissolved in 50 mM NaOH at 10 mg/mL. In a 384-wells microplate (Greiner) were added water, phosphate buffer pH 7 (50 mM), thioflavin-T (10 μM), metal complex (100 μM), $ZnSO_4$ (50 μM) and Aβ$_{1\text{-}28}$ (100 μM). Final ACN content was of 5%. Fluorescence intensity was recorded every 5 min for a total duration of 40 h using a Optima plate reader (BMG Labtech) set at 25 °C. Fluorescence parameters were set as follows: λ_{exc} = 440 nm, λ_{em} =

490 nm, gain = 1000, 200 rpm shaking for 12 s before each measurement. Aggregation curves were fitted using KaleidaGraph software.

UV-Vis and Emission spectra of fibres samples

See Experimental procedures for Chapter III.

UV-Vis quantification of unbound metal complexes

In the end of aggregation assay, wells containing fibres are gently sampled, gathering replicates. Samples are then centrifuged (10,000 g, 5 min) and the top fraction of supernatant is analysed by UV-Vis spectrophotometry using a SpectroStar Nano reader (BMG Labtech). Negative controls (*i.e.* without peptide) are processed similarly, to consider potential precipitation or degradation issues. Quantification of metal complexes is achieved by comparing absorbance at complexes λ_{max} versus negative controls.

HPLC quantification of unbound Th-T

In the end of aggregation assay, wells containing fibres are gently sampled, gathering replicates. Samples are then centrifuged (10,000 g, 5 min) and the top fraction of supernatant is analysed on Agilent 1200 HPLC fitted with a Nova-Pak C18 column, 4 mM, 3.9 mm x 75 mm (Waters). Elution method was set as follows: Isocratic elution for 1 min in 10% ACN in H_2O+0.1% TFA, followed by a gradient from 10 to 100% ACN in 10 min, and isocratic elution in 100% ACN for 5 min. Elution is monitored at 220 nm and 250 nm. In these conditions, Th-T comes out around 6.9 min. Quantification is achieved by comparing integrations at 250 nm versus negative controls.

NMR experiments: preparation of samples

In a microtube are added D_2O, phosphate buffer pH 7 in D_2O (50 mM), metal complex in CD_3CN (variable), and Aβ peptide solubilized in NaOD (variable). For control experiments in absence of complex, corresponding amount of CD_3CN is added. The mixture is carefully transferred in an NMR tube and NMR spectra are promptly recorded on a 500 MHz NMR (Bruker).

DOSY NMR: calculations of K_d

This calculation is based on the idea that if a ligand is strongly bound to a protein, their diffusion coefficients become identical. Contrariwise, if the ligand does not bind the protein, its diffusion coefficient is unchanged. Considering this, a linear equation can be written, considering the fraction of ligand bound to the protein, noted x_{bound}.

$$D_{\text{protein}} \,.\, x_{\text{bound}} + D_{\text{free ligand}} \,.\, x_{\text{unbound}} = D_{\text{bound ligand}}$$

$$D_{\text{protein}} \,.\, x_{\text{bound}} + D_{\text{free ligand}} \,.\, (1 - x_{\text{bound}}) = D_{\text{bound ligand}}$$

Upon simplification, we obtain:

$$x_{\text{bound}} = \frac{D_{\text{bound ligand}} - D_{\text{free ligand}}}{D_{\text{protein}} - D_{\text{free ligand}}}$$

It is now possible to get the bound ligand concentration:

$$[bound\ ligand] = [ligand]_0 \, . \, x_{\text{bound}}$$

Finally, a K_d can be calculated:

$$K_d = \frac{[Free\ ligand].[free\ protein]}{[complex]} = \frac{([ligand]_0 - [bound\ ligand]).([protein]_0 - [bound\ ligand])}{[bound\ ligand]}$$

Molecular Docking

Docking was achieved using AutoDock 4 program. Protein and ligand files were prepared using AutoDock Tools software. Numbers of torsions were set to 2 for Th-T and to 4 for metal complexes.

Grid bow parameters were set as follows:

For 2LMN:

Number of points in the x-dimension = 126

Number of points in the y-dimension = 96

Number of points in the z-dimension = 126

Spacing = 0.65 Å

For 2MXU:

Number of points in the x-dimension = 126

Number of points in the y-dimension = 126

Number of points in the z-dimension = 126

Spacing = 0.608 Å

Centre of Grid Box was modulated according to the model used to encompass the whole fibre.

Atomic map files were generated using the AutoGrid4 program. Docking was then run using the AutoDock4 program with Lamarckian Genetic Algorithm 4.2 parameters set as follows:

Number of GA runs = 100

Population size = 300

Maximum number of evals = 2,500,000 (medium)

Maximum number of generations = 27,000

Maximum number of top individuals that automatically survive = 1

Rate of gene mutation = 0.02

Rate of Crossover = 0.8

GA Crossover mode: twopt

Mean of Cauchy distribution for gene mutation = 0

Variance of Cauchy distribution for gene mutation = 1

Number of generations for picking worst individual = 10

Solutions were analysed using AutoDock Tools, clustering solutions using a rmsd-tolerance of 2.0 Å. Binding energies and Ki were automatically calculated by AutoDock Tools.

Experimental procedures for Chapter V

General procedure: catalytic experiment

In a 1.5 mL microcentrifuge tube were added ACN (550 μL), water (220 μL), aqueous solution of ammonium bicarbonate (100 mM, 80 μL), catalyst dissolved in ACN (1 mM, 40 μL), styrene diluted in ACN (400 mM, 10 μL), and finally Oxone dissolved in water (200 mM, 100 μL). Tube was placed in a Thermomixer and incubated at 25°C shaking at 1500 rpm for 4 h.

At the end of the reaction, 100 μL of reaction medium are sampled and mixed with 2 mL of toluene (internal standard). Samples were analysed by GC, using a method sets as follows: 50°C for 2 min, temperature gradient going from 50 to 300°C over 10 min, then 300°C for 1 min.

Retention times and attribution methods for each product described appear in the following table.

Compound	Retention time (min)	Attribution
Toluene	4.4	Commercial reference
Styrene	5.5	Commercial reference
Benzaldehyde	6.0	Commercial reference
Phenyl acetaldehyde	6.6	Commercial reference
Epoxide	6.8	Commercial reference
2-hydroxy 1-phenyl ethanone	7.9	Detected by GC-MS
Diol	8.3	Synthesized and isolated

General procedure: catalytic experiment on fibres

Fibres were obtained by aggregation of 200 μM A$\beta_{1\text{-}40}$ in the presence of 200 μM Fe($\mathbf{L^1}$)$_2$. In the end of aggregation, wells containing fibres were combined and centrifuged (10,000 g, 5 min). Supernatant was carefully sampled and submitted to UV-Vis titration to determine the amount of Fe($\mathbf{L^1}$)$_2$ inserted into fibres. Complex content in fibres was determined to be 6.3 e^{-8} mol. To the fibre pellet were added ACN (590 μL), water (220 μL), aqueous solution of ammonium bicarbonate (100 mM, 80 μL), styrene diluted in ACN (400 mM, 10 μL), and finally Oxone dissolved in water (200 mM, 100 μL). Catalytic loading is of 1.6 mol%. Corresponding controls were modified accordingly. Tubes were placed in a Thermomixer and incubated at 25°C shaking at 1500 rpm for 4 h.

GC monitoring of the reaction was completed similarly as in absence of fibres (see above).

Annex II. Products characterization

4-*p*-aminophenyl-2,6- (2’,2’’-pyridyl)pyridine (L^1)

^{1}**H NMR** (300 MHz, DMSO-d_6) δ (ppm) = 8.75 (ddd, *J* = 4.8, 1.7, 0.9 Hz, 2H, H6 + H6’’), 8.64 (m, 2H, H3 + H3’’), 8.62 (s, 2H, H3’ + H5’), 8.02 (ddd, *J* = 7.9, 7.7, 1.8 Hz, 2H, H4 + H4’’), 7.66 (d, J_{ortho} = 8.5 Hz, 2H, H9 + H9’), 7.51 (ddd, *J* = 7.7, 4.8, 1.2 Hz, 2H, H5 + H5’’), 6.74 (d, J_{ortho} = 8.5 Hz, 2H, H8 + H8’), 5.60 (s, 2H, H11). (cf MH-1-24)

^{13}**C NMR** (300 MHz, DMSO-d_6) δ (ppm) = 155.38 (C2’ + C2’’), 155.35 (C2 + C6), 150.54 (C10), 149.61 (C4), 149.30 (C6’ + C6’’), 137.42 (C4’ + C4’’), 127.63 (C8 + C8’), 124.37 (C5’ + C5’’), 123.75 (C7), 120.87 (C3’ + C3’’), 116.16 (C3 + C5), 114.30 (C9 + C9’). (cf MH-1-24)

MS (ESI+): calculated for $C_{21}H_{16}N_4$: 324.14, found: 325.18 ($[M+H]^+$).

IR (ν in cm^{-1}): 3482 (N-H asymmetrical stretching), 3387 (N-H symmetrical stretching), 1583 (N-H bending), 1183 (C-N stretching).

4-p-carboxyphenyl—2,6 (2’,2’’-pyridyl)pyridine (L^2)

^{1}**H NMR** (300 MHz, DMSO-d_6): δ (ppm) = 8.78 (ddd, *J* = 4.8, 1.8, 0.8 Hz, 2H, H6 + H6’’), 8.74 (s, 2H, H3’ + H5’), 8.69 (dt, *J* = 8.0, 1.2 Hz, 2H, H3’ + H3’’), 8.04 (m, 4H, H9 + H9’ + H4 + H4’’), 7.80 (dt, *J* = 8.0, 1.1 Hz, 2H, H8 + H8’), 7.54 (ddd, *J* = 7.6, 4.7, 1.2 Hz, 2H, H5 + H5’’).

^{13}**C NMR** (300 MHz, DMSO-d_6): δ (ppm) = 168.57, 156.07, 155.45, 152.29, 150.10, 149.83, 137.94, 137.45, 130.45, 126.09, 124.98, 121.38, 118.32.

MS (ESI+): calculated for $C_{22}H_{15}N_3O_2$: 353.12, found: 353.9 ($[M+H]^+$).

IR: ν (cm^{-1}) =3201, 1585, 1553, 1385, 777.

4-(*p*-nitrophenyl)- 2,6- (2’,2’’-pyridyl)pyridine (L^3)

^{1}**H NMR** (400 MHz, $CDCl_3$): δ (ppm) = 8.76 (s, 2H, H3’ + H5’), 8.74 (ddd, *J* = 4.8, 1.8, 0.9 Hz, 2H, H6 + H6’’), 8.69 (m, 2H, H3 + H3’’), 8.37 (d, *J* = 8.7 Hz, 2H, H9 + H9’), 8.05 (d, *J* = 8.7 Hz, 2H, H8 + H8’), 7.91 (td, *J* = 8.0, 7.6, 1.8 Hz, 2H, H4 + H4’’), 7.39 (ddd, *J* = 7.6, 4.8, 1.2 Hz, 2H, H5 + H5’’).

^{13}**C NMR** (300 MHz, $CDCl_3$) δ (ppm) = 156.40 (C2 + C2”), 155.68 (C2’ + C6’), 149.21 (C10), 137.02 (C4 + C4”), 128.31 (C8 + C8’), 124.20 (C5 + C5’’), 124.18 (C7), 121.41 (C3 + C3’’), 118.94 (C6 + C6”).

MS (ESI+): $[M + H]^+$ calculated for $C_{21}H_{15}N_4O_2$, 355.12; found, 355.18.

IR (ν in cm^{-1}): 3080 (aromatic C-H stretching), 1510 (N=O asymmetrical stretching), 1350 (N=O symmetrical stretching), 855 (C-N stretching).

4-furyl-2,6 (2’,2’’-pyridyl)pyridine (L^4)

^{1}**H NMR** (300 MHz, DMSO-d_6): δ (ppm) = 8.78 (ddd, *J* = 4.8, 1.8, 0.9 Hz, 2H, H6 + H6’’), 8.71 (s, 2H, H3’ + H5’), 8.66 (ddd, *J* = 8.0, 1.2, 0.9 Hz, 2H, H3 + H3’’), 8.05 (ddd, *J* = 8.0, 7.5, 1.8 Hz, 2H, H4 + H4’’), 7.99 (dd, *J* = 1.7, 0.7 Hz, 2H, H10), 7.55 (ddd, *J* = 7.5, 4.8, 1.2 Hz, 2H, H5 + H5’’), 7.50 (dd, *J* = 3.6, 0.7 Hz, 2H, H8), 6.76 (dd, *J* = 3.5, 1.8 Hz, 2H, H9).

^{13}**C NMR (400 MHz,** DMSO-d_6): δ (ppm) = 155.67, 154.76, 150.71, 149.29, 145.05, 138.97, 137.41, 124.56, 120.82, 114.08, 112.75, 110.31.

MS (ESI+): calculated for $C_{19}H_{13}N_3O$: 299.11, found: 300.6 ($[M+H]^+$).

IR: ν (cm^{-1}) = 1607, 1587, 1544, 1466, 789, 730.

4-*p*-bromophenyl-2,6 (2’,2’’-pyridyl)pyridine (L^5)

^{1}**H NMR** (300 MHz, DMSO-d_6): δ (ppm) = 8.73 (ddd, *J* = 4.8, 1.7, 0.9 Hz, 2H, H6 + H6’’), 8.71 (s, 2H, H3’ + H5’), 8.64 (ddd, *J* = 8.0, 1.2, 0.9 Hz, 2H, H3’ + H3’’), 8.01 (ddd, *J* = 8.0, 7.5, 1.8 Hz, 2H, H4 + H4’’), 7.87 (d, J = 8.5 Hz, 2H, H9 + H9’), 7.75 (d, J = 8.5 Hz, 2H, H8 + H8’), 7.50 (ddd, *J* = 7.5, 4.8, 1.2 Hz, 2H, H5 + H5’’)

^{13}**C NMR** (300 MHz, DMSO-d_6): δ (ppm) = 155.80, 154.83, 149.38, 148.30, 137.53, 136.68, 132.34, 129.08, 124.65, 123.12, 121.00, 117.79.

$Cu(L^1)_2(PF_6)_2$

MS (ESI+): calculated for $[C_{42}H_{32}CuN_8]^{2+}$: 355.60; 356.60, found: 355.60 ($[M]^{2+}$), 356.60 ($[M+H]^{2+}$).

IR: ν (cm^{-1}) = 3639, 3569 (N-H asymmetrical stretching), 3397 (N-H symmetrical stretching), 1597 (N-H bending), 1189 (C-N stretching), 826 (PF_6), 555 (PF_6).

UV-Visible: λ = 397 nm (MLCT), ε = 8454 L.mol^{-1}.cm^{-1}

X-rays:

Empirical formula	C42 H32 Cu N8, 2(F6 P)
Formula weight	1002.25
Temperature	180(2) K
Wavelength	0.71073 A
Crystal system, space group	orthorhombic, P 21 21 21

Unit cell dimensions	a = 9.0216(5) A alpha = 90 deg.
	b = 13.5996(8) A beta = 90 deg.
	c = 32.9658(19) A gamma = 90 deg.
Volume	4044.6(4) A^3
Z, Calculated density	4, 1.646 Mg/m^3
Absorption coefficient	0.720 mm^-1
F(000)	2028
Crystal size	0.20 x 0.06 x 0.02 mm
Theta range for data collection	2.57 to 25.33 deg.
Limiting indices	-10<=h<=10, -16<=k<=15, -37<=l<=39

$Cu(L^2)_2(PF_6)_2$

MS (ESI+): calculated for $[C_{42}H_{32}CuN_8]^{2+}$: 768.1546, found: 768.1573 ($[M+H]^+$); 384.5812, found 384.5828 ($[M+2H]^{2+}$).

IR: ν (cm^{-1}) = 3271 (O-H stretching), 1594, 1557, 1366.

Cu(salophen)

IR: ν (cm^{-1}) = 3053, 3011, 1603, 1574, 1518, 742.

UV-Visible: λ = 420 nm (MLCT), ε = 14340 L.mol^{-1}.cm^{-1}

X-Rays:

Empirical formula	C20 H14 Cu N2 O2
Formula weight	377.88
Temperature	180(2) K
Wavelength	0.71073 A
Crystal system, space group	orthorhombic, P 21 21 21
Unit cell dimensions	a = 9.1051(4) A alpha = 90 deg.
	b = 17.9213(8) A beta = 90 deg.
	c = 18.8494(9) A gamma = 90 deg.
Volume	3075.8(2) A^3

Z, Calculated density	8, 1.632 Mg/m^3
Absorption coefficient	1.437 mm^-1
F(000)	1544
Crystal size	0.60 x 0.08 x 0.02 mm
Theta range for data collection	1.57 to 26.59 deg.
Limiting indices	-10<=h<=11, -22<=k<=22, -23<=l<=23

$Fe(L^1)_2(PF_6)_2$

^{1}H NMR: (300 MHz, DMSO-d_6): δ (ppm) = 9.49 (s, 4H), 9.01 (dd, *J* = 7.9, 1.3 Hz, 4H), 8.34 (d, *J* = 8.6 Hz, 4H), 8.00 (ddd, *J* = 7.9, 7.5, 1.5 Hz, 4H), 7.25 (dd, *J* = 5.7, 1.5 Hz, 4H), 7.17 (ddd, *J* = 7.5, 5.7, 1.3 Hz, 4H), 6.91 (d, *J* = 8.6 Hz, 4H), 5.98 (s, 4H).

^{13}C NMR: (400 MHz, DMSO-d_6): δ (ppm) = 159.40, 158.25, 152.71, 151.80, 149.43, 138.50, 128.93, 127.36, 123.72, 122.00, 118.83, 114.07.

MS (ESI+): calculated for $[C_{42}H_{32}FeN_8]^{2+}$: 352.10, 352.61; found: 352.1049, 352.6065 ($[M]^{2+}$), calculated for $[C_{42}H_{32}FeN_8PF_6]^+$: 849.1742, 850.1770, found: 849.1750, 850.1770 ($[M]^+$).

IR: ν (cm^{-1}) = 3650 (N-H asymmetrical stretching), 3386 (N-H symmetrical stretching), 1595 (N-H bending), 1191 (C-N stretching), 820 (PF_6), 554 (PF_6).

UV-Visible: λ = 576 nm (MLCT), ε = 32,700 $L.mol^{-1}.cm^{-1}$ in ACN.

X-rays:

Empirical formula	C42 H32 Fe N8, 2(F6 P)
Formula weight	994.55
Temperature	180(2) K
Wavelength	0.71073 A
Crystal system, space group	orthorhombic, P 21 21 21
Unit cell dimensions	a = 8.8873(3) A alpha = 90 deg.
	b = 13.3727(4) A beta = 90 deg.
	c = 32.9736(11) A gamma = 90 deg.
Volume	3918.8(2) A^3

Z, Calculated density	4, 1.686 Mg/m^3
Absorption coefficient	0.570 mm^-1
F(000)	2016
Crystal size	0.16 x 0.12 x 0.04 mm
Theta range for data collection	2.40 to 28.53 deg.
Limiting indices	-11<=h<=11, -16<=k<=17, -44<=l<=44

$Fe(L^2)_2(PF_6)_2$

^{1}H NMR: (300 MHz, DMSO-d_6): δ (ppm) = 9.71 (s, 4H), 9.11 (dd, *J* = Hz, 4H), 8.56 (d, *J* = Hz, 4H), 8.28 (dd, *J* = Hz, 4H), 8.05 (dd, *J* = Hz, 4H), 7.30 (, *J* = Hz, 4H), 7.20 (, *J* = Hz, 4H).

MS (ESI+): calculated for $[C_{44}H_{30}FeN_6O_4]^{2+}$: 381.0840, 381.5854; found: 381.0842, 381.5857 ($[M]^{2+}$).

IR: ν (cm^{-1}) = 3358 (O-H stretching), 1341 (NO_3), 1159 (C-N stretching), 781 (NO_3).

UV-Visible: λ = 568 nm (MLCT), ε = 24,400 L.mol^{-1}.cm^{-1} in ACN.

$Fe(L^3)_2(PF_6)_2$

^{1}H NMR: (300 MHz, ACN-d_3): δ (ppm) = 9.24 (s, 4H), 8.65 (m, 4H), 8.63 (m, 4H), 8.51 (d, J = 8.9 Hz, 4H), 7.93 (ddd, J = 7.9, 7.6, 1.5 Hz, 4H), 7.19 (d, J = 5.1 Hz, 4H), 7.10 (m, 4H).

^{13}C NMR: (400 MHz, ACN-d_3): δ (ppm) = 161.50, 158.70, 154.03, 139.89, 130.18, 128.44, 125.72, 125.03, 123.01.

MS (ESI+): calculated for $[C_{42}H_{28}FeN_8O_4]^{2+}$: 382.08; found: 382.56 ($[M]^{2+}$).

UV-Visible: λ = 574 nm (MLCT), ε = 34,700 L.mol^{-1}.cm^{-1} in ACN.

$Fe(L^4)_2(PF_6)_2$

^{1}H NMR: (400 MHz, DMSO-d_6): d (ppm) = 9.49 (s, 4H), 8.96 (d, 4H), 8.25 (d, *J* = 1.9 Hz, 2H), 8.01 (ddd, 4H), 7.96 (d, *J* = 3.5 Hz, 2H), 7.30 (d, 4H), 7.17 (ddd, 4H), 7.03 (dd, *J* = 3.5, 1.9 Hz, 2H).

^{13}C NMR: (400 MHz, ACN-d_3): δ (ppm) = 161.21, 158.79, 154.06, 147.20, 139.68, 128.28, 124.75, 114.52, 113.75.

IR: ν (cm^{-1}) = 1707, 1614, 1483, 826, 556.

MS (ESI): Calculated for $C_{38}H_{26}FeN_6O_2^{2+}$: 327.07, found: 327.1 ($[M]^{2+}$)

UV-Visible: λ = 576 nm (MLCT), ε = 32,000 L.mol^{-1}.cm^{-1} in ACN.

$Fe(L^5)_2(NO_3)_2$

^{1}H NMR: (400 MHz, ACN-d_3): δ (ppm) = 9.17 (s, 4H, H3'+H5'), 8.60 (d, *J* = 8.1 Hz, 4H, H9+H9'), 8.23 (d, *J* = 8.1 Hz, 4H, H8+H8'), 7.99 (d, *J* = 8.2 Hz, 4H, H3+H3''), 7.91 (ddd, *J* = 8.2, 7.4 Hz, 4H, H4+H4''), 7.17 (d, *J* = 5.6 Hz, 4H, H6+H6''), 7.09 (d, *J* = 7.4, 5.6 Hz, 4H, H5+H5'').

^{13}C NMR: (400 MHz, ACN-d_3): δ (ppm) = 153.96, 139.70, 133.74, 130.63, 128.24, 124.79, 122.38.

IR: ν (cm^{-1}) = 1707, 1614, 1483, 826, 556.

MS (ESI): Calculated for $C_{42}H_{28}Br_2FeN_6^{2+}$: 830.01, found: ($[M]^{2+}$)

UV-Visible: λ = 567 nm (MLCT), ε = 21,830 L.mol^{-1}.cm^{-1} in ACN.

$Fe(bpy)_3(PF_6)_2$

^{1}H NMR: (300 MHz, ACN-d3): δ (ppm) = 8.50 (dt, *J* = 8.3, 1.0 Hz, 3H), 8.10 (m, 3H), 7.38 (m, 6H).

^{13}C NMR: (300 MHz, ACN-d3): δ (ppm) = 160.10, 155.14, 139.61, 128.38, 124.88.

MS (ESI+): calculated for $[C30H24FeN6]^{2+}$: 262.07 ($[M]^{2+}$); found: 262.1.

UV-Visible: λ = 520 nm (MLCT), ε = 9,400 L.mol^{-1}.cm^{-1} in ACN.

$Fe(tpy)_2(PF_6)_2$

^{1}H NMR: (300 MHz, ACN-d3): δ (ppm) = 8.86 (d, *J* = 8.0 Hz, 4H), 8.64 (t, *J* = 8.0 Hz, 2H), 8.43 (d, *J* = 8.0 Hz, 4H), 7.85 (dd, *J* = 8.0, 4.4 Hz, 4H), 7.03 (d, *J* = 4.4 Hz, 8H).

^{13}C NMR: (400 MHz, ACN-d_3): δ (ppm) = 161.17, 158.72, 154.00, 139.66, 138.90, 128.26, 124.67, 124.59.

MS (ESI+): calculated for $[C_{30}H_{22}FeN_6]^{2+}$: 261.06; found: 261.08 ($[M]^{2+}$).

UV-Visible: λ = 551 nm (MLCT), ε = 7,620 L.mol^{-1}.cm^{-1} in ACN.

$Fe(phen)_3(PF_6)_2$

^{1}H NMR: (300 MHz, ACN-d_3): δ (ppm) = 8.59 (d, *J* = 8.0 Hz, 6H), 8.23 (s, 6H), 7.59 (m, 12 H).

^{13}C NMR: (400 MHz, ACN-d_3): δ (ppm) = 157.01, 150.65, 138.21, 131.40, 128.94, 126.78.

MS (ESI+): calculated for $[C_{36}H_{24}FeN_6]^{2+}$: 298.07 ($[M]^{2+}$), 741.10 ($[M](PF_6)^+$); found: 298.08, 740.58.

UV-Visible: λ = 509 nm (MLCT), ε = 9,820 L.mol^{-1}.cm^{-1} in ACN.

$Ru(L^1)_2(PF_6)_2$

^{1}H NMR: (300 MHz, DMSO-d_6): δ (ppm) = 9.31 (s, 4H), 9.07 (d, J = 8.1 Hz, 4H), 8.23 (d, J = 8.6 Hz, 4H), 8.04 (ddd, J = 7.9, 1.5 Hz, 4H), 7.51 (d, J = 5.5 Hz, 4H), 7.25 (ddd, J = 7.6, 5.6, 1.3 Hz, 4H), 6.87 (d, j = 8.6 Hz, 4H), 5.88 (s, 4H).

^{13}C NMR: (400 MHz, ACN-d_3): δ (ppm) = 159.46, 156.14, 153.29, 151.77, 149.38, 138.75, 129.76, 128.17, 125.33, 125.16, 120.75, 115.73.

MS (ESI+): calculated for $[C_{42}H_{32}RuN_8]^{2+}$: 375.09; found: 375.42 ($[M]^{2+}$)

UV-Visible: λ = 502 nm (MLCT), ε = 24,100 L.mol^{-1}.cm^{-1} in ACN.

$Ru(L^2)_2(PF_6)_2$

^{1}H NMR: (300 MHz, ACN-d_3): δ (ppm) = 9.07 (S, 4H), 8.68 (dd, *J* = 8.3, 1.3 Hz, 4H), 8.39 (d, *J* = 8.3 Hz, 4H), 8.33 (d, *J* = 8.3 Hz, 4H), 8.00 (ddd, *J* = 8.3, 7.6, 1.4 Hz, 4H), 7.49 (dd, *J* = 5.6, 1.4 Hz, 4H), 7.24 (ddd, *J* = 7.6, 5.6, 1,3 Hz, 4H).

^{13}C NMR: (400 MHz, DMSO-d_6): δ (ppm) = 158.99 (C_q), 156.50 (C_q), 153.43, 139.10, 131.70, 129.01, 128.51, 125.61, 122.90.

MS (ESI+): calculated for $[C_{44}H_{30}RuN_6O_4]^{2+}$: 404.07 ($[M]^{2+}$); found: 404.0.

UV-Visible: λ = 492 nm (MLCT), ε = 24,700 L.mol^{-1}.cm^{-1}

$Ru(L^3)_2(PF_6)_2$

^{1}H NMR: (300 MHz, ACN-d_3): δ (ppm) = 9.03 (s, 4H), 8.63 (ddd, *J* = 8.1, 1.4, 0.7 Hz, 4H), 8.56 (d, *J* = 8.8 Hz, 4H), 8.37 (d, *J* = 8.8 Hz, 4H), 7.94 (ddd, *J* = 8.1, 7.8, 1.5 Hz, 4H), 7.40 (ddd, *J* = 5.6, 1.5, 0.7 Hz, 4H), 7.17 (ddd, *J* = 7.8, 5.6, 1.3 Hz, 4H).

^{13}C NMR: (400 MHz, DMSO-d_6): δ (ppm) = 153.45, 139.19, 130.02, 128.58, 125.67, 125.61, 123.09.

MS (ESI+): calculated for $[C_{42}H_{28}RuN_8O_4]^{2+}$: 405.06; found: 405.36 ($[M]^{2+}$).

UV-Visible: λ = 494 nm (MLCT), ε = 25,100 L.mol^{-1}.cm^{-1} in ACN.

$Ru(bpy)_3(PF_6)_2$

^{1}H NMR: (400 MHz, ACN-d_3): δ (ppm) = 8.48 (ddd, *J* = 8.2, 1.2, 0.8 Hz, 6H), 8.04 (ddd, *J* = 8.2, 7.6, 1.5 Hz, 6H), 7.71 (ddd, *J* = 5.6, 1.5, 0.8 Hz, 6H), 7.37 (ddd, *J* = 7.6, 5.6, 1.2, 6H).

^{13}C NMR: (400 MHz, DMSO-d_6): δ (ppm) = 157.93, 152.63, 138.74, 128.51, 125.20.

MS (ESI+): calculated for $[C_{30}H_{24}FeN_6]^{2+}$: 285.05 ($[M]^{2+}$), 715.07 ($[M](PF_6)^+$); found: 284.98, 715.0.

UV-Visible: λ = 451 nm (MLCT), ε = 15,575 L.mol^{-1}.cm^{-1} in ACN.

$Ru(tpy)_2(PF_6)_2$

^{1}H NMR: (300 MHz, ACN-d_3): δ (ppm) = 8.72 (d, *J* = 8.1 Hz, 4H), 8.46 (d, *J* = 8.1 Hz, 4H), 8.38 (t, *J* = 8.2 Hz, 2H), 7.89 (dd, *J* = 8.1, 7.8 Hz, 4H), 7.31 (d, *J* = 5.2 Hz, 4H), 7.13 (dd, *J* = 7.8, 5.4 Hz, 4H).

^{13}C NMR: (300 MHz, ACN-d_3): δ (ppm) = 158.02 (C_q), 156.10 (C_q), 152.44, 138.05, 137.52, 127.43, 124.38, 123,69.

MS (ESI+): calculated for $[C_{30}H_{22}RuN_6]^{2+}$: 284.05 ($[M]^{2+}$), 713.06 ($[M](PF_6)^+$); found: 284.15, 713.03.

UV-Visible: λ = 474 nm (MLCT), ε = 14,980 L.mol^{-1}.cm^{-1} in ACN.

$Ru(phen)_3(PF_6)_2$

^{1}H NMR: (300 MHz, ACN-d_3): δ (ppm) = 8.57 (dd, *J* = 8.3, 3.1 Hz, 6H), 8.23 (s, 6H), 8.00 (dd, *J* = 5.3, 3.1 Hz, 6H), 7.60 (dd, *J* = 8.3, 5.3 Hz, 6H).

^{13}C NMR: (400 MHz, ACN-d_3): δ (ppm) = 152.96, 148.94, 136.74, 131.94, 128.02, 125.84.

MS (ESI+): calculated for $[C_{36}H_{24}RuN_6]^{2+}$: 321.05 ($[M]^{2+}$), 787.07 ($[M](PF_6)^+$); found: 321.17, 786.92.

UV-Visible: λ = 444 nm (MLCT), ε = 15,280 L.mol^{-1}.cm^{-1} in ACN.

Annex III. Articles

Coordination Chemistry Reviews 308 (2016) 445–459

Contents lists available at ScienceDirect

Coordination Chemistry Reviews

journal homepage: www.elsevier.com/locate/ccr

Review

Coordination complexes and biomolecules: A wise wedding for catalysis upgrade

Marie Hoarau[a,b], Christelle Hureau[a,b,*], Emmanuel Gras[a,b,**], Peter Faller[a,b]

[a] *CNRS, LCC (Laboratoire de Chimie de Coordination), 205 Route de Narbonne, 31077 Toulouse, France*
[b] *Université de Toulouse, UPS, INPT, LCC, 31077 Toulouse, France*

Contents

Dedicated to the memory of our colleague and friend Dr Guy Lavigne (deceased April 23th 2015).

Abbreviations: A, adenine; Bipyridine, 2-Pyridin-2-ylpyridine; BPMCN, N ;*N*′-bis(2-pyridylmethyl)-*N* ;*N*′-dimethyl-trans-1 ;2-diaminocyclohexane; BPMEN, N ;*N*′-dimethyl-*N* ;*N*′-bis-(pyridin-2-ylmethyl)-1 ;2-diaminoethane; C, cytosine; Conv., conversion; Cp, cyclopentadienyl; Cyt, cytochrome; DNA, deoxyribonucleic acid; EDTA, 2-({2-[bis(carboxymethyl)amino]ethyl}(carboxymethyl)amino)acetic acid; ee, enantiomeric excess; er, enantiomeric ratio; G, guanine; h, hour; His, histidine; min, minute; NAD, nicotinamide adenine nucleotide; NikA, periplasmic nickel-binding protein; phenanthroline, 1 ;10-phenanthroline; Ref, reference; salen, 2 ;2′-ethylenebis(nitrilomethylidene)diphenol; salophen, *N* ;*N*′-bis(3 ;5-di-*tert*-butylsalicylidene)-1 ;2-diaminobenzene; St-DNA, Salmon testes deoxyribonucleic acid; SWOT, Strength weakness, opportunities and threats; T, thymine; terpyridine, 2 ;6-bis(2-pyridyl)pyridine; TO, turnover; TON, turnover number; WT, wild-type.

[*] Corresponding author at: Tel.: +33 5 61 33 31 62.

[**] Corresponding author at: Tel.: +33 5 61 33 31 56.

E-mail addresses: christelle.hureau@lcc-toulouse.fr (C. Hureau), emmanuel.gras@lcc-toulouse.fr (E. Gras).

http://dx.doi.org/10.1016/j.ccr.2015.05.011

ARTICLE INFO

Article history:
Received 24 March 2015
Received in revised form 13 May 2015
Accepted 25 May 2015
Available online 8 June 2015

Keywords:
Hybrid catalyst
Coordination complexes catalysis
Artificial metalloenzymes
Biomolecules
Enantiospecificity

ABSTRACT

Artificial metalloenzymes, with their high selectivity and specificity combined with a wide scope of reactivity and substrates, constitute an original approach for catalyst development. Different strategies have been proposed for their elaboration, proceeding from modification of natural enzymes using bioengineering methods to *de novo* protein design. Another bio-inspired methodology for the development of hybrid catalysts consists in the incorporation of coordination complexes into biomolecules, with the aim to upgrade their catalytic abilities. In these systems, the reaction performed by the naked catalyst is modulated by the well-defined structure of the host biomolecule. This conveys added value to the catalyst, such as enantioselectivity or chemoselectivity. DNA, apo-enzymes, proteins and peptides have been engaged in this approach, affording a wide diversity of reactivities and substrates. The resulting systems can then be improved by combined chemical and bioengineering optimization, allowing access to powerful catalysts. Because this approach can virtually be applied to any biomolecule or coordination complex, the elaboration of bio-based hybrid catalysts seems promising for advance in catalysis.

1. Introduction

Over the last 15 years, the three Nobel Prizes associated with organic synthesis have been awarded to Knowles, Noyori and Sharpless for metal-catalyzed asymmetric hydrogenation and oxidation in 2001, Chauvin, Grubbs and Schrock for the work on olefin metathesis, based on the use of ruthenium, molybdenum and tungsten complexes as catalysts, and in 2005 Heck, Negishi and Suzuki for palladium catalysed cross coupling in 2010.

This exemplifies the importance of coordination complexes (noted as such in the present review to define a metallic centre bound to synthetic ligands) in organic synthesis. From a general view, coordination catalysis utilises a large selection of metallic ions, ligands and substrates to achieve a large set of reactivities.

The reactivity of a coordination complex is mainly based on the tuning of its redox properties, substrate accessibility and/or Lewis acidity of its metallic centre. This is achieved by modulating the donor/acceptor character of the ligands, and by controlling their geometry and arrangement around the metallic centre. For instance, steric hindrance can be used to induce substrate selectivity. Chemists excel at developing very sophisticated ligands that confer to the complexes the desired properties. But this has several bottlenecks, among which the multi-step synthesis of the targeted ligands which potentially represents a significant economical concern and might hamper its accessibility.

By observing metalloenzymes, it appears that the first, second and outer coordination spheres play a crucial role in tuning the reactivity of the metallic centre. Indeed within enzymes, the reactivity is not only driven by steric control of the metal site by the ligands (proteic and/or non-proteic) but also *via* remote interactions (H bonding, electrostatic, stacking *etc.*) that guide the substrate into the active site, position it to ease the reaction, and help the release of the products.

In other words, the strength of enzymes resides in the combination of inner and outer sphere effects, which confers rate enhancement, specificity and selectivity to the enzyme. Moreover the mobility, dynamics and/or conformational changes of the proteic chain can help to adopt the most suitable geometry for the active site. All of this makes enzymes very powerful catalysts, but only considering a single reactivity and substrate. Chemists thus developed synthetic analogues of enzymes active sites, to better understand the structure-properties relationships. The ultimate goal would be to select the crucial parameters for powerful catalysis, getting rid of the less pertinent ones. Such mimics (structural, functional or both) were thus developed for hydrogenases [1–4], superoxide dismutases [5–9], photosynthetic system [10,11], oxygenases [12] *etc.* These systems go from the simplest, using very usual metallic ions and ligands [13] to the most sophisticated ones [14–16]. Even though models of metalloenzymes are very helpful for investigation purposes, these models are often poor catalysts (with respect to their loadings).

To overcome these two drawbacks, namely the cost and time consuming production of the ligands involved in the coordination catalysts while achieving the very high selectivity of enzymes, chemists have recently developed two convergent strategies: (i) Protein re-design, based on their knowledge of the natural systems and (ii) *de novo* design of biomolecules, seeking for perfectly defined metal ion environment. In the first approach, shown in Fig. 1 artificial metalloenzymes are re-designed by modification of the native metal ion (panel B) or of the ligands (panel C) using bioengineering. In the second approach, depicted in the panel D of Fig. 1, host cavities are rationally formed from scratch.

This review covers an alternative approach, which cannot be classified into those previously defined categories. It relies on the insertion of a simple coordination catalyst into a host biomolecule (Fig. 1, panel A). The guest coordination complex already possesses its own reactivity, which is modulated by the environment provided by the host biomolecule. The appealing nature of this approach is that it truly takes advantage of the knowledge of the two fields (biochemistry and coordination chemistry driven catalysis). The coordination complex can be chosen among the wide library of catalysts, according to the desired reactivity, and can be tuned easily. Obviously the chosen system should be able to operate under condition compatible with biomolecules (*i.e.* solvent and temperature compatibility). On the other hand, biomolecules can be engineered to host the complex in the most suitable way. This strategy is exemplified by a Cu(bipy) complex, into a host biomolecule, namely DNA, proteins and peptides, which is anticipated to confer selectivity properties to the guest complex.

Therefore, this review will focus on highlighting how a coordination complex could have its activity upgraded by its interaction with a biomolecule. Using selected examples, we are trying to exemplify this concept and to highlight the different methodologies used. We may try to foresee the opened perspectives and future development of this approach.

2. The artificial metalloenzyme approach

Before covering the main topic of this review, *i.e.* incorporation of coordination complexes into biomolecules (Panel A Fig. 1), we will give a concise overview of the other approaches (Panels B–D). They all share the same ultimate goal: development of systems able to catalyse synthetically relevant reactions with the exquisite rates and selectivities of enzymes, and with an extended set of substrates. This goal seems very ambitious, and the path to this target appears still long and tough. Still, huge progresses have been made in the

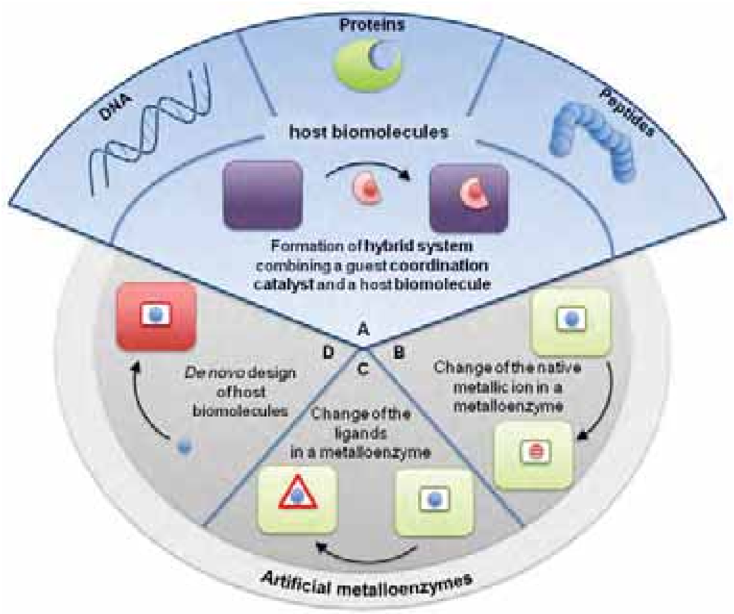

Fig. 1. Strategies to develop bio-supported catalysts based either on the insertion of a *simple* catalyst into a biomolecule (panel A) or to the elaboration of artificial metalloenzymes (panels B–D), including modification of the natural metallic ion of an enzyme (panel B); the modification of the natural active site of an enzyme, generally by mutagenesis (panel C); and the elaboration of new metallic ion coordinating biomolecules (panel D).

development of such systems, both in terms of methodology and results.

Over the years, different approaches have been explored to develop such artificial enzymes, and these methods have been widely reviewed [17–26]. As a consequence, we will only summarize the most prominent and latest results in the following (sections 2.1 to 2.4).

2.1. *Replacement of the native metallic ion*

The replacement of the native metallic ion of an enzyme represents a first strategy, relatively easy to develop. It consists in replacing the native metallic ion of an enzyme by another. Kaiser and co-workers first exemplified this approach in 1976. By changing Zn(II) with Cu(II) in carboxypeptidase A, they showed that the native activity was completely inhibited, and substituted by oxidizing properties [27]. Subsequent studies from Soumillion and colleagues showed that Mn(II)-substituted carbonic anhydrase was active in epoxidation reactions [28]. In parallel, Kazlauskas et al. showed that replacing Zn(II) by Mn(II) could also afford a new peroxidase activity [29]. Fig. 2 shows the X-ray structure of the active site of a Mn(II)-substituted human carbonic anhydrase. It appears that the same amino acids are involved in the coordination of Zn(II) and of Mn(II) (*i.e.* His 94, His 96, and His 119), showing that the overall organization of the active site is not distorted by the substitution of the metallic ion. Some mutagenesis studies showed that several other amino acids within the catalytic pocket (white circles in Fig. 2) influence catalysis, further confirming the crucial importance of the whole environment.

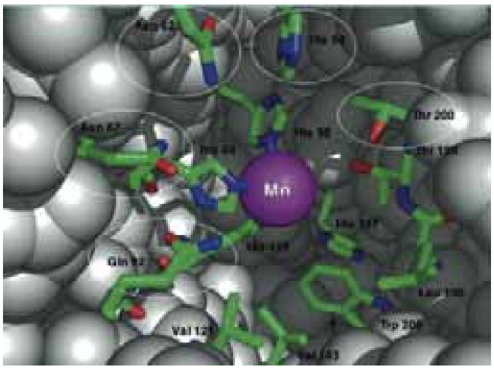

Fig. 2. X-ray crystal structure of Mn(II) replacing Zn(II) in human carbonic anhydrase II. The amino acids involved in metallic ion coordination (His 94, His 96 and His 119) are the same for Mn and Zn. The circled amino acids affect catalysis efficiency and selectivity. Reprinted with permission from [29].

Another step forward was the replacement of Zn(II) with a metallic ion of low natural abundance. This was achieved by incorporating Rh(I) into human carbonic anhydrase. This system catalyzed olefin hydrogenation and styrene hydroformylation with moderate to good yields and selectivities [30,31].

This constitutes a typical illustration of how a simple swap of metallic ion in an enzyme can dramatically modify its reactivity. Unfortunately, this strategy can only be applied to a few, rather exceptional, enzymes, and in most cases, more significant modifications are required.

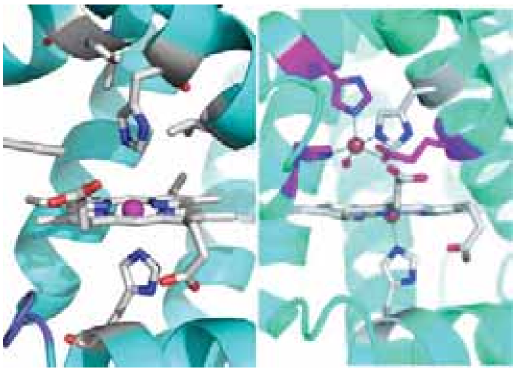

Fig. 3. Left panel: Native active site of myoglobin (PDB 1JP6), right panel: Engineered active site of myoglobin, showing the mutated residues (pink) and the Fe centres in red. The resulting enzyme displays NO reductase activity [32,33]. Reprinted with permission from [33].

2.2. Mutations of the amino-acid involved in the active site

Another strategy aiming at modifying the native function of enzymes was to facilitate some amino-acid mutations in order to alter their reactivity. This approach usually benefits from the support of molecular modelling. Mutations, for instance, can impact either the coordination of the metallic centre or remote amino acids in order to favour active site access towards a wider range of substrates.

A representative example, which encompasses these two aspects, is the engineering of cytochrome P450, an iron hemoprotein which catalyzes mono-oxygenation of substrates using molecular dioxygen. By performing some mutations on its active site, either site-directed or random, it is possible to enlarge the set of substrates of cytochrome P450, keeping its good oxidizing properties [34]. The Cys apical ligand of the heme centre of cytochrome P450 was replaced by Ser, removing the “thiolate push”, and thus preventing the native monooxygenase activity (*i.e.* C—O bond formation). Combination with other mutations was also needed to reach specific reactivities, such as intramolecular amination (C—N bond formation) [35,36] and carbene transfer to olefins [37,38], showing good yields and selectivities.

Another possibility is the creation of a host site for a metallic ion from scratch. For instance, Lu and co-workers gave WT-myoglobin (Fig. 3, left panel) a nitric oxide reductase activity, by mutating three residues of the natural active site and thus inducing the coordination of a second Fe ion (Fig. 3, right panel) [32,33]. The mutated amino acids appear in pink in Fig. 3, right panel (mutations L29H, F43H, and V68E) and the Fe(II) ions in red. Similarly, WT-myoglobin was implemented to coordinate Cu ion, thus displaying a 4-electrons dioxygen reductase activity [39].

A final opportunity would be to induce a new reactivity in the enzyme by modifying the peptidic ligands of the metallic centre. Although this straightforward approach is frequently used to decipher the essential residues bound to the catalytic ion, or to modulate the native reactivity of enzymes [40], there is to the best of our knowledge, no report on mutations to induce a non-native reactivity.

The use of bioengineering to form artificial metalloenzymes, although very interesting, can become highly laborious, and requires an exceptional combination of advanced knowledge in molecular and structural biology, molecular modelling and chemistry.

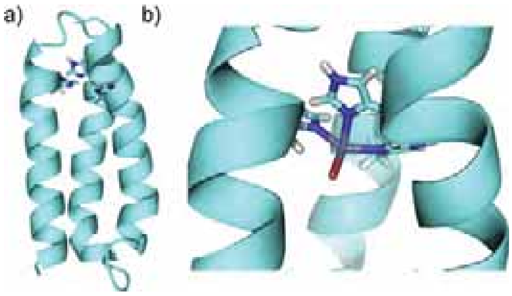

Fig. 4. The three stranded coiled coils coordinating Zn, developed by Pecoraro's group reproduced by courtesy of V. Pecoraro [41].

2.3. De novo design of artificial metalloenzymes

De novo protein design, which consists in the rational design of new proteins to get a specific 3D structure is of central interest for artificial enzymes elaboration [42]. A typical example is the triple helix bundle developed by the Pecoraro's group (Fig. 4), formed by hydrophobic interactions between amphiphilic helices. These systems, first developed to study the binding of toxic heavy metals [43], have required huge effort to control the geometry of the binding site [44]. These systems were then transposed for Cu [45,46] and Zn coordination [41,47] showing promising results as artificial metalloenzymes [48–50] such as nitrite reductase [46] and hydrolase [47] or hydratase [41].

2.4. Conclusions

All of this shows the abundant and diverse ways to generate artificial enzymes, both in terms of approaches and techniques. The coordination complex incorporation approach caught our attention, as it combines the use of inorganic and organic chemistry as well as biology.

In the following sections, we will focus on this approach, which consists in the insertion of a guest catalyst into a host biomolecule. This will be split into three subsections depending on the nature of the biomolecule: DNA, 3D-structured proteins, antibodies and flexible peptides.

3. Incorporation of coordination complexes into DNA

3.1. Anchoring strategies

With their structure in double helix, nucleic acids are one of the most elegant natural examples of chirality. The DNA double helix constitutes a rare example of switch from central molecular chirality to helical supramolecular chirality. Nature only uses RNA for metal-driven catalysis in ribozymes, but its known low stability so far prevented its use for catalytic applications. DNA was thus logically a privileged scaffold for asymmetric catalysis.

Fig. 5 depicts the different strategies reported in literature to anchor a catalyst to a DNA molecule. Three main possibilities have been investigated: (a) weak but additive interactions (stacking, electrostatic, hydrogen bonds) with DNA, (b) covalent linkage with a base form synthetic DNA and (c) covalent linkage to a known intercalant of DNA.

In the former case, the coordination complex is thus in close vicinity to the DNA chiral environment, although no experimental structural investigations on the exact mode of binding has been reported to date (Fig. 5a). In the latter case, the linkage to a

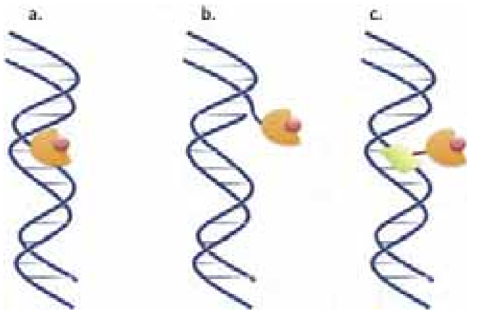

Fig. 5. The three strategies to anchor coordination complexes on DNA double helix. Additive weak interactions anchoring (a), covalent binding to an oligonucleotide followed by hybridization with another DNA strand (b) and DNA intercalant linked to a coordination complex (c).

DNA-intercalant, decreases the impact of the chiral environment on the catalytic centre due to the increased distance between the host molecule and the guest coordination complex (Fig. 5c). Finally, it is also possible to covalently bioconjugate coordination complexes to oligonucleotides, then re-forming the helix (second case). This strategy is less straightforward, requiring oligonucleotide synthesis, but it allows a better rationalization of the effect of the oligonucleotide sequence in the vicinity of the anchoring site, as more detailed in Section 3.3 (Fig. 5b).

These three strategies were successfully applied, either using natural or synthetic DNA. Some examples, considered as representative, are further detailed in this review, and appear in Table 1.

3.2. Intercalation of coordination complexes into natural double-strand DNA

In their seminal paper, Roelfes and Feringa presented the first example of a direct transfer of chirality from natural DNA to a Cu(II) complex involved in Diels–Alder reaction [51]. It was promoted by stacking interactions between DNA and a DNA-intercalant linked to an achiral Cu(II) complexes (Scheme 1, ligand amino pyridine and Fig. 5c). When tested for catalytic Diels–Alder reaction, these systems showed a strong predominance for the expected *endo* product (entry 1a, Table 1 and Scheme 2 (i)). The enantiomeric composition was dependent on linker length, and, moreover, when the linker becomes too long, ee values dropped dramatically. Later on, the same authors showed that this strategy is less efficient with respect to the cyclopropanation reaction than when simple Cu(II) complexes interact directly with the DNA (entries 1b and 2a in Table 1) *via* stacking with aromatic ligands (Scheme 1, ligands bipy, terpy, phen, and phenazine) [52]. This second anchoring approach (Fig. 5a) was thus used in subsequent studies, where these Cu(II) complexes afforded ee's up to 99% when involved in Diels–Alder reaction, Friedel–Crafts, *syn*-Hydratation of enones or Michael additions (entry 2b, Table 1) [53–55]. Interestingly, they showed that in the Friedel–Crafts and Diels–Alder reactions, the replacement of a bipyridine by a terpyridine causes a swap of enantiopreference [55]. The Cu(II) to ligand ratio was also investigated with respect to the cyclopropanation reaction and increasing the Cu(II):L ratio to 1:1 from 1:2 leads to an improvement in the ee values. In the meantime, Wang et al. showed the crucial role of the helix chirality by studying *L*- and *D*-DNA interacting with a Cu(II) bipyridine complex [56]. The *L*- and *D*-hybrid systems, tested on Friedel–Crafts and Michael addition, showed "mirror" selectivities, the switch from *L* to *D* inducing a switch of chiral induction (entry 3, Table 1).

Lastly, Park and colleagues demonstrated the dramatic influence of the oligonucleotide sequence: the ee values strongly depend on

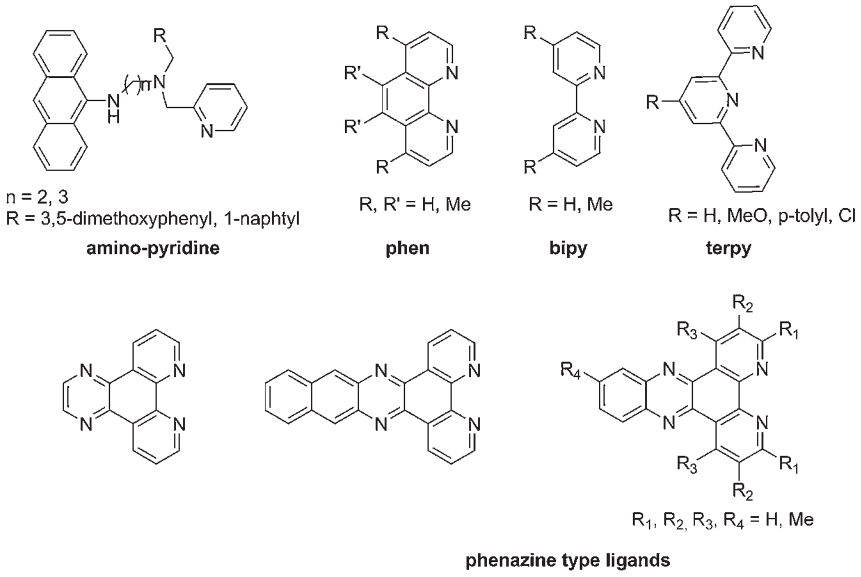

Scheme 1. Typical intercalating ligands used in DNA-based hybrid catalysts.

Table 1
Some representative examples of DNA-based hybrid catalysts.

Entry	Biomolecule	Ligand type	Metallic ion	LLink type according to Fig. 5	Reaction	Conv. max (%)	ee max (%)	Ref.
1a	St-DNA	(aminomethyl)-Pyridine	Cu(II)	c	Diels–Alder	80	82	[51]
1b					Cyclopropanation	42	0	
2a		Bipyridine	Cu(II)	a	Cyclopropanation	100	84	[52]
2b		Terpyridine Phenanthroline Phenazine			Michael addition, Syn-hydratation of enones Diels–Alder Friedel–Crafts	100	99	[53–55]
3	Artificial *L*- and *D*-DNA	Bipyridine	Cu(II)	a	Friedel–Crafts Michael Addition	89	99	[56]
4	Artificial DNA	Bipyridines Phenanthrolines	Cu(II)	b	Friedel–Crafts	91	82	[57]
5	Functionalized DNA	Bipyridine	Cu(II)	b	Diels–Alder	76	93	[58]
6	Functionalized DNA	Diene	Ir(I)	b	Allylic Amination Kinetic resolution of phenyl allyl acetate	92	28	[59]
7	Functionalized DNA	Bipyridine	Cu(II)	b	Friedel–Crafts	80	86	[60]

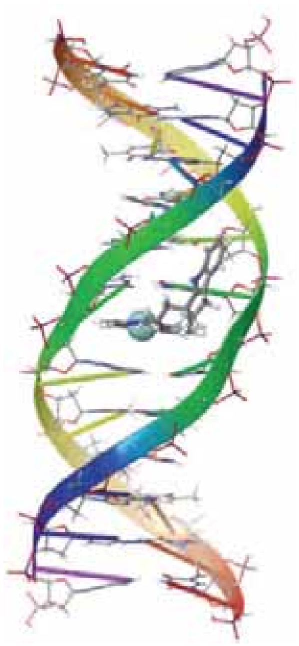

Fig. 6. A binding model proposed by Park et al. for coordination complex intercalation into double-helix DNA. The product of the reaction is also present. Reprinted with permission from [57].

the nucleotide GC or TA content and whether the A, T or G, C bases are alternated (entry 4, Table 1). The oligonucleotide length is also significant [57]. They also propose a model of the catalyst binding together with the product of the reaction buried in the DNA helix (Fig. 6) [57,61].

This case study highlights the fundamental importance of both the chiral environment of the host molecule and the nature of ligand in the guest catalysts, each of them influencing selectivity. The results obtained here are remarkably clear-cut since it is possible to commute from one enantiomer to the other by changing either the chirality of the DNA [56] or the ligand used [55]. The simplicity of this system enables a thorough evaluation of key parameters although no deep investigation on the exact nature of the catalytic entities has been performed yet. This would have fostered a rapid and rational improvement of key features. The use of solid-phase supported DNA was recently reported, allowing the development of such catalysis at synthetically relevant scale and enabling recycling of the catalyst [62,63].

3.3. *Covalently-functionalized oligonucleotides*

Another strategy proposed by Roelfes' group was to covalently functionalize an oligonucleotide with a ligand. Upon hybridization with a DNA template and coordination of the Cu(II) ion, a helix DNA duplex is formed with the coordination complex in its vicinity (Fig. 5b). This approach is convenient, allowing the screening of different nucleotides, linkers and ligands. When tested for Diels–Alder cycloaddition, the different systems displayed ee's up to 93% (entry 5, Table 1). Expectedly this effect is substantially dependent on the nucleotides surrounding the anchoring position [58]. Similar studies were conducted on synthetic DNA functionalized with a diene–Ir(I) complex (entry 6, Table 1). The resulting catalysts only yielded 28% ee in kinetic resolution of phenyl allyl acetate [59]. Finally, Sugiyama and colleagues proposed to graft DNA strands on two points of a bipyridine (Table 1, entry 7 and Scheme 3, middle). Upon metallation and hybridization, the resulting catalyst showed 86% ee for Friedel–Crafts alkylation [60]. The high reaction-specific nature of this strategy is clearly highlighted by the significant differences of enantioselectivities. Despite the variable efficiency of these catalysts, they constitute the first examples of covalently functionalized DNA operating catalysis. The wholeness of this kind of hybrid systems should be more easily preserved than those where the coordination catalyst is bound to DNA by non-covalent interactions.

3.4. *Conclusions*

All these examples confirm the value of DNA as host biomolecule for asymmetric catalysis. According to these results, all anchoring strategies seem to afford good to excellent efficiencies. On the one hand, covalent linkage of catalysts to DNA allows one to drive the position of the complex relative to the DNA sequence, depending on the linker length. It is thus anticipated an easier rationalization of different parameters. However, production of these systems requires delicate solid phase synthesis. On the other hand, the use of non-covalent anchoring has the advantage to be very easy to set up, enabling one to test various ligands, but the lack of insight on the

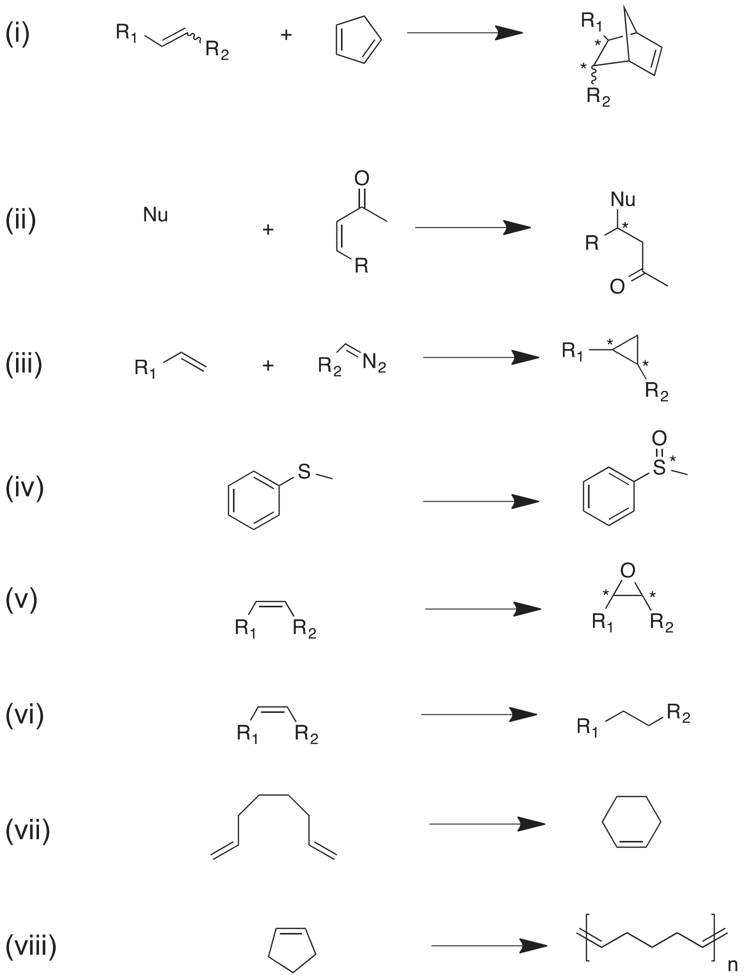

Scheme 2. Typical reactions operated by hybrid catalysts. (i) Diels–Alder, (ii) Michael addition (Friedel–Craft reaction corresponds to Michael addition with Nu = indole), (iii) cyclopropanation, (iv) sulfoxidation, (v) epoxidation, (vi) hydrogenation, (vii) Ring-closing metathesis, (viii) Ring opening metathesis polymerization.

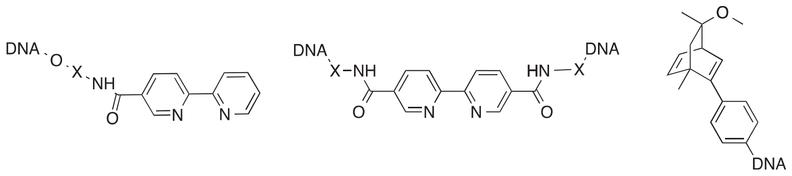

Scheme 3. Typical covalently linked ligands used in DNA-based hybrid catalysts (X = linker).

exact position and interactions in the system is still to be explored. Roelfes' group proposed an intermediate strategy, using a cisplatin link to anchor the catalyst to DNA, but here again the positioning remains unclear [64]. The choice of the anchoring strategy must be considered according to the targeted reaction.

4. Incorporation of coordination complexes into proteins

Virtually any of the 35,000 known proteins might exhibit some level of interaction with a coordination complex, thus becoming a potential catalyst. Nevertheless in order to significantly enhance

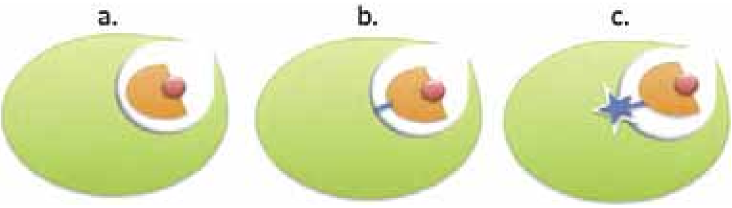

Fig. 7. The three existing strategies for the incorporation of a coordination complex inside a protein.

the catalytic activity of the coordination complex, this interaction has to be optimized. Therefore the first criterion for selection of an appropriate host candidate is the presence of a large enough vacant space buried inside the protein. This could serve as a reaction pocket, conferring selectivity and even specificity to substrates.

As for the DNA host biomolecule, three anchoring methods are possible, as depicted in Fig. 7.

(a) Non-covalent anchoring, taking advantage of weak but additive interactions between proteins and the coordination complex (electrostatic, hydrophobic, H-bonding...). This method is very convenient, but requires investigating the location of the complex.
(b) Covalent attachment of the coordination complex in the pocket of a protein. This strategy is more time-demanding and consists in the covalent attachment of the complex by bioconjugation, using natural or synthetic amino-acids.
(c) Functionalization of a natural guest of a protein with a coordination complex.

Each of these strategies has been successfully explored, depending to the targeted protein and will be exemplified in more detail below.

4.1. *Incorporation of a coordination complex into an apo-protein*

4.1.1. *Insertion of planar coordination complexes*

A straightforward strategy for the elaboration of hybrid catalysts is the insertion of a synthetic catalyst into a protein from which the native Fe hemic group (entries 1a–1d, Table 2) or Ni(II) metallophore (entry 2a, in Table 2) has been removed, thus taking advantage of the cavity left vacant.

The first example is the incorporation of coordination complexes into apo-myoglobin, which naturally hosts an iron porphyrin. Because of their planar structure and their high catalytic efficiency, Schiff base complexes were considered as good candidates to replace the hemic group. The first approach was envisaged by Carey et al. consisting in the covalent dual anchoring of functionalized Mn(III) or Cr(III) salen complexes (Scheme 4) into the hydrophobic pocket of apo-myoglobin. To do so, a covalent link was made by the creation of two disulfide bridges using methane thio-sulfonate salen derivatives and Cys mutations, which positions were determined by molecular modelling. The corresponding Cys mutants were expressed, produced and purified, then bioconjugated to the Schiff base complex. Modelling studies showed that the complex was positioned in the active site exactly at the same place as the hemic group in the wild type myoglobin, as depicted in Fig. 8.

The interest of the double anchoring of the coordination catalyst has been established by comparison with a single-point attached counterpart in the sulfoxidation of thioanisole: both the ee values and the rate have been improved (entries 1a and 1b, Table 2). This is fully consistent with a better immobilisation of the complex inside the cavity, taking thus full advantage of a better defined environment [65]. These systems could now be further improved by directed evolution, or applied to a wider set of reactivities, but the overall process might represent a rather time-consuming approach.

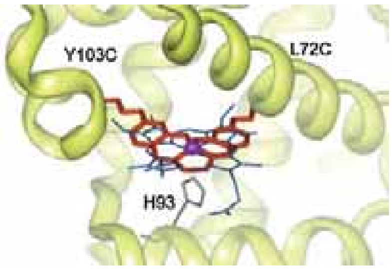

Fig. 8. Modelling of the myoglobin active centre with Mn(salen)-type complex covalently attached on the two L72C and Y103C mutated positions. The position of the hemic group in wild-type myoglobin is shown in blue showing the correct positioning of the coordination complex. Reprinted with permission from [65].

Another possibility, potentially easier but also probably less topologically defined, consists in anchoring the complex *via* non-covalent interactions (Fig. 7a). The direct incorporation of Schiff base complexes into apo-myoglobin mutants was tried because incorporation into wild-type myoglobin was less successful [66]. The crystal structures obtained showed that the complexes were positioned in pertinent mutants at the exact same place as the hemic group in the wild-type myoglobin. Even if the rate was improved by optimising the ligand, the ee obtained for thioanisole sulfoxidation did not exceed 33% (entry 1c, Table 2).

Comparison with the previous example leads to the observation of three general remarks (although drawing trends with only two examples is uncertain): (i) Imposing a fixed position using covalent anchorage may precludes the most suitable location of the catalysts for catalytic enhancement, whereas more freedom is given to the system in non-covalent anchoring, (ii) in contrast, regarding the ee values a much more dynamic interaction leads to a loss of influence of the proteic environment and thus to a lower chiral induction, (iii) combining the two approaches, *i.e.*, mutations to covalently anchor the catalyst and to optimize the binding pocket could be more appropriate.

In this context, Lewis and co-workers found a good compromise: allowing the complex to choose its best position, and then covalently grafting it *in situ* [67]. To do so, they functionalized their Mn-terpyridine complex with a maleimide group. The resulting coordination complex was incubated with cysteine mutants of nitrobindin. Once the complex is set at its most suitable place inside the protein, the formation of a carbon-sulfur covalent bond allows the immobilization of the complex. The mutants displaying the most efficient bioconjugation were considered as the most appropriate, and were tested for several catalytic oxidation reactions

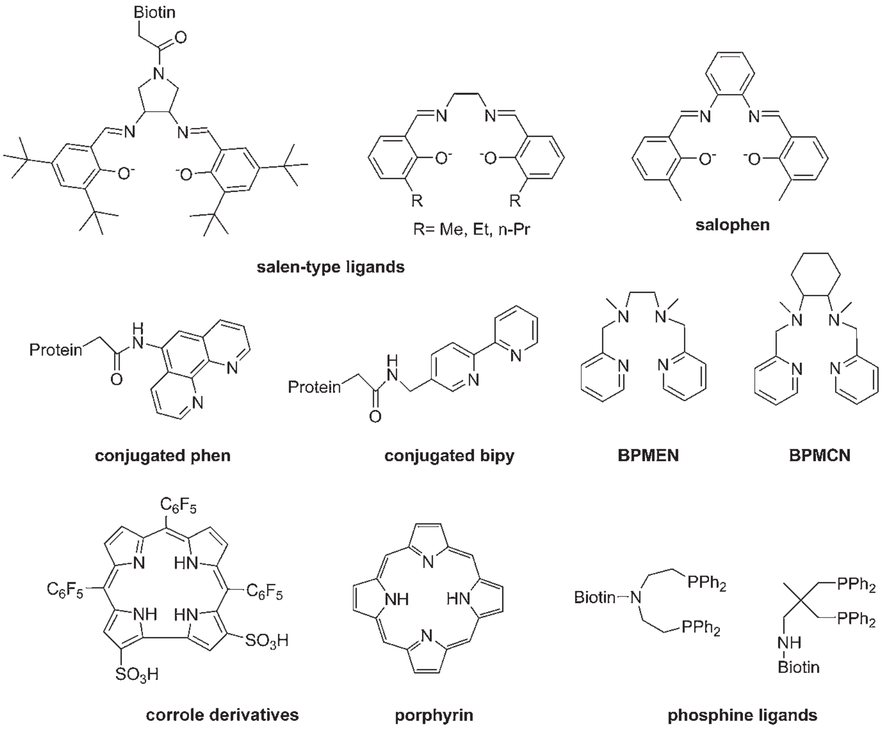

Scheme 4. Typical ligands used in protein-based hybrid catalysts.

(entry 1d, Table 2). In the best case, the product was obtained with 99% yield. Yet the ee's obtained remain low (7%) indicating that the most suitable positioning of the metallic complex in the protein may not efficiently transfer the chiral information from the environment to the reaction product. The topology of the edifice still needs to be improved for example allowing the metallic cofactor to choose its most favourable position inside the protein. The reactivity of the maleimide allows its permanent binding at the right position, limiting dynamic exchanges; but the precise positioning into a chiral pocket might require a thorough screening to allow a significant chiral induction to be achieved.

4.1.2. *Insertion of non-planar coordination complexes*

4.1.2.1. Metallic complexes transport proteins. Non-planar coordination complexes can be inserted into proteins involved in the transport of metallic complexes. They have the advantage to exist natively in the apo-form and are able to bind coordination complexes easily. Thus, Fe(II) complexes of the diamino-pyridine BPMEN and BPMCN ligands were incorporated into the apo-form of the periplasmic nickel-binding protein NikA (where NikA binds Ni(II) in form of a coordination complex). They display sulfoxidation activity with good to moderate yields (entry 2a, Table 2). In that case, suitable substrates were determined by docking studies [68].

Table 2
Some representative examples of hybrid catalysts made by incorporation of a coordination complex in the active site of an apo-protein.

Entry	Biomolecule	Ligand	Metallic ion	Link type according to Fig. 7.	Reaction	Conv. max (%)	ee max (%)	Ref.
1a	Apo-Myoglobin	Schiff base	Mn(III), Cr(III)	b	Asymmetric sulfoxidation	0.4 TO/min	51	[65]
1b						0.05 TO/min	12	
1c				a		2.7 TO/min	33	[66]
1d	Apo-nitrobindin	Terpy	Mn(II)	b	Benzylic oxygenation, Olefin epoxidation	89 99	7	[67]
2a	Periplasmic nickel-binding protein	BPMEN BPMCN	Fe(III)	a	Selective sulfoxidation	85	Sel. 100	[68]
2b	FhuA	Hoveyda–Grubbs catalyst	Ru(III)	b	ROMP	98	Cis 70%	[69]
2c	Apo-nitrobindin	Cp	Rh(I)	b	Polymerization of phenylacetylene		Cis 95%	[70]
2d	Apo-ferritin	Norbornadiene	Rh(I)	b	Polymerization of phenylacetylene			[71]

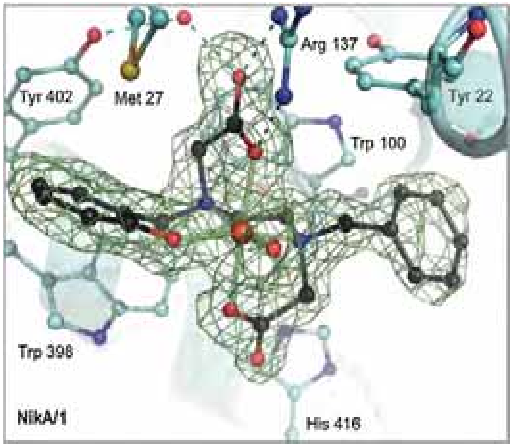

Fig. 9. Crystal structure of the FeL complex [L = 5 *N*-benzyl-*N′*-(2-hydroxybenzyl)-*N*,*N′*-ethylenediaminediacetic acid] incorporated into periplasmic nickel-binding protein (NikA) and electron density map of FeL. Reprinted with permission from [72].

To illustrate this, Fig. 9 shows the crystal structure obtained for the incorporation of an analogous Fe(II) complex into NikA, which was involved in arene dihydroxylation of the ligand itself [72].

The other example is FhuA that incorporates the Hoveyda–Grubbs catalyst (entry 2b, Table 2). This system showed efficient polymerization with a preference for the *cis* form [69]. This was assigned to the cavity effect of FhuA, which has a β-barrel structure and hence a confined space. Similar results, *i.e.* efficient polymerization and preference for the *cis* form, were also reported for another hybrid system namely the β-barrel protein aponitrobindin functionalized with CpRh(I) (entry 2c, Table 2). These examples nicely illustrate the fundamental effect of the confinement to force the reaction even to its less favoured stereochemical outcome.

4.1.2.2. Ferritin. An even more pronounced confinement can be obtained with apo-ferritin, a hollow protein with several relatively small access-channels. A Rh(I)-norbornadiene complex was inserted in the cavity of apo-ferritin, where it reacted to form a covalent bond with a cysteine. The Rh complex catalyzes the polymerization of phenyl acetylene with restricted molecular weight and a narrow molecular weight distribution due to the cavity effect (entry 2d, Table 2) [71].

From these examples, one can conclude that the native pocket of an apo-enzyme can efficiently host a coordination complex, thus displaying new catalytic activities. The conversion rates obtained are mostly high, but the selectivity/specificity fluctuate depending on the reactions tested, potentially requiring some optimization. Another potential approach is to consider naturally non-metallic proteins.

4.2. Incorporation of a coordination complex into a non-metallic protein

A more chancy strategy is to consider proteins which do not natively host metallic complex but possess cavities, for instance for the transport of organic molecules. Different proteins were considered, as summarized in Table 3. Even though cavities are not naturally used for catalysis, they remain an asymmetric environment, allowing stereoselectivity to be expected. When the cavity is sufficiently small, using of non-covalent anchoring approach was preferred.

A very simple strategy to form hybrid catalyst was introduced by Ward and co-workers, who incorporated vanadium oxide [78] or osmium oxide [79] into streptavidin. The resulting systems displayed selectivities up to 95% ee for olefins dihydroxylation. However, these examples exceed the scope of this review, in so far as metallic oxides may not be considered as true coordination complexes. Anyway, they are neat illustrations of how a catalytic moiety can be upgraded by a proteic environment.

4.2.1. The host cavity is made by a monomeric protein

An elegant biomimetic oxidation system was developed by incorporating a corrole metallic complex into albumins. The complex was buried inside the protein *via* interaction with the sulfonato and pentafluorophenyl groups that decorated the corrole central group. The system was tested for thioanisole sulfoxidation using hydrogen peroxide, showing efficient reactivity and promising ee's (Entry 1a, Table 3) [70].

Another example, using the same strategy, was the incorporation of manganese complexes into xylanase (entry 1b, Table 3), a protein displaying affinity for synthetic Fe(II) porphyrins [80]. When tested for styrene oxidation, the system displayed moderate yields, but good selectivities (up to 80%) [74].

4.2.2. The host cavity is made by supramolecular interaction of proteins

In a recent study, Roelfes and co-workers showed that the hydrophobic interface formed upon dimerization of proteins could also be used as an active site. Copper complexes grafted onto dimerized Lactococcal multidrug resistance regulator were used to catalyse Diels–Alder cycloaddition with excellent efficiency and selectivity (entry 2a, Table 3) [75].

In a similar way, Hilvert developed a system based on a small heat shock protein, able to form spherical capsids, functionalized with Grubbs–Hoveyda catalyst. This system demonstrated good properties for olefin metathesis (entry 2b, Table 3) [76].

These two studies represent good examples of reconversion of protein activity. This methodology could beneficially be extended to other proteins.

4.2.3. Grafting of coordination complex outside a cavity

An hybrid system with coordination complexes, namely a bipy-Sc(III) species, in which the ligand is covalently anchored onto the surface of proteins has been developed. The species exhibit moderate results both in terms of conversion and ee values (entry 3, Table 3). Although this strategy seems less convincing compared with the previously detailed ones and to the corresponding DNA covalent functionalization (Section 3.3), this proof of concept study shows that there is some ability for induction of asymmetry. This should stimulate further studies along this approach [77].

4.2.4. Concluding remarks

The previously described results provide evidence for the expected importance of the cavity effect. If this strategy is at this point of limited extent, it could at least conceptually be applied to a wide range of hollow proteins; yet the optimization required to achieve an efficient catalysis remains the main source of uncertainty, and might require significant screening capabilities.

4.3. Functionalization of a natural cofactor of a protein

4.3.1. (Strept)avidin/biotin system

In an effort to simplify the elaboration of hybrid catalysts, some groups proposed to attach the coordination complex onto

Table 3
Some representative examples of hybrid catalysts prepared by incorporation of a coordination complex into non-enzymatic proteins.

Entry	Biomolecule	Ligand	Metal	Link type according to Fig. 7	Reaction	Conv. max (%)	ee max (%)	Ref.
1a	Serum albumins	Corrole	Fe(III), Mn(III)	a	Asymmetric sulfoxidation	98	74	[73]
1b	Xylanase A	Salen, porphyrin	Mn	a	Asymmetric epoxidation	23	80	[74]
2a	Lactococcal multidrug resistance Regulator (LmrR)	Bipyridine, phenanthroline	Cu(II)	b	Asymmetric Diels–Alder	100	97	[75]
2b	Small heat shock protein	Hoveyda–Grubbs catalyst	Ru(III)	b	RCM	TON = 33	/	[76]
3	Tubular protein	Bipyridine	Sc(III)	b	Epoxide ring-opening	42	17	[77]

Table 4
Representative examples of hybrid catalysts formed by functionalization of natural cofactors of proteins.

Entry	Biomolecule	Ligand	Metal	Link type according to Fig. 7	Reaction	Conv. max (%)	ee max (%)	Ref.
1a	Avidin, streptavidin	Phosphines	Rh(I)	c	Asymmetric hydrogenation	100	96	[81,82]
1b	Streptavidin (S112H)	Cp functionalized	Rh(III)		Asymmetric transfer hydrogenation	100	79	[83]
1c	Streptavidin mutants				Asymmetric C—H activation	99	82	[84]
1d	Streptavidin S112 mutants				Imine reduction	100	96	[85]
1e	Streptavidin	Salen	Mn(III)		Asymmetric sulfoxidation	50	11	[86]
2a	Chymotrypsin	Hoveyda–Grubbs catalyst	Ru(III)		Ring closing metathesis	TN = 20 (2 h)	/	[87]
2b	Neocarzinostatin mutant	Porphyrin	Fe(III)		Thioanisole sulfoxidation	/	13	[88]

natural cofactors of proteins, taking advantage of the strong host–guest interaction to incorporate the complex at a precise place in the protein (Fig. 7c). The most common example is the biotin-(strept)avidin couple, in which the interaction is very strong ($K_D \approx 10^{-15}$ M) and fast (binding rate constant of biotin-streptavidin is in a range of 3.0×10^6–4.5×10^7 M^{-1} s^{-1}) [89]. Conjugation of catalysts onto biotin, followed by interaction with avidin or streptavidin, affords highly reliable systems [90]. This also permits one to get rid of the complicated step of bioconjugation with a protein (Fig. 7b). But some other protein-cofactor systems can be used as well, as illustrated in Table 4.

In 2003, Ward and co-workers developed a phosphine functionalized biotin which upon metallation with Rh(I) and incorporation into avidin and streptavidin was able to catalyse asymmetric hydrogenation with 96% ee after 15 h (entry 1a, Table 4). Interestingly, avidin and streptavidin offered opposite enantiopreference [81]. Much effort was made in subsequent studies to improve this system, considering different optimization parameters. Chemically, different anchoring positions, metallic ions and ligands were tested. Different mutants of the host protein were also considered. Finally, a library of substrates was tested. This “chemogenetic” optimization allowed determination of a system with good to very good selectivity. After the chemogenetic selection, a careful study of crystal structures allowed one to point out other mutations of interest, further improving the catalysts [82]. This constitutes a very elegant example of combined chemical and genetic optimization, showing the full potential of this yet simple system.

In subsequent studies, Ward and colleagues showed that a unique mutated position (112 or 121) into histidine allowed a dual anchoring, both by biotin/streptavidin interaction and by Rh coordination by histidine, as shown on Fig. 10. This appeared highly beneficial to the system: conversion is increased from 60 to 100%, and ee values from 0 to 79% for transfer hydrogenation of a prochiral imine compared with the wild type protein (entry 1b, Table 4) [83]. This study only considered the transfer hydrogenation, but other reactivities were also demonstrated. As such, biotinylated Rh(III) complexes were efficient for C—H activation (entry 1c, Table 4) [84] and imine reduction (entry 1d, Table 4) [85,91]. In a very comprehensive study, the same group investigated several parameters with respect to the hydrogen transfer reaction, including the nature of the coordination complex and the influence of the mutants at position 112. Interestingly, the nature of the complex impacted strongly the transfer of chirality, with the two enantiomers being detected depending on the catalysts used. Also, with a given catalyst, the two enantiomers can be obtained depending on the nature of the mutants at position 112 [92]. More recently, Cp-Ir(III) complexes were also successfully used for NAD^+ reduction [93].

Mn salen complexes were also tested for asymmetric sulfoxidation, displaying somewhat low yields and selectivities (entry 1e, Table 4), therefore illustrating that this strategy cannot be systematically generalized, and requires cautious optimization [86].

4.3.2. Other host–guest systems

Still within this context, an original example is the use of a natural protein inhibitor to constitute hybrid catalysts proposed by Matsuo and co-workers. They functionalized an inhibitor of chymotrypsin with a linker and a catalytic entity. The inhibitor goes into the active site of the enzyme and the coordination complex is thus positioned inside the hydrophobic pocket, and can intercept the incoming substrates. In the present case, the functionalized Grubbs–Hoveyda complex was able to catalyze ring-closing metathesis with good rates (entry 2a, Table 4) [87].

Finally Mahy and co-workers used neocarzinostatin, a cytotoxic protein known to recognize specifically enediyne derivatives. Since these compounds are of limited stability, the authors used a formerly established mutant that binds tightly testosterone. An

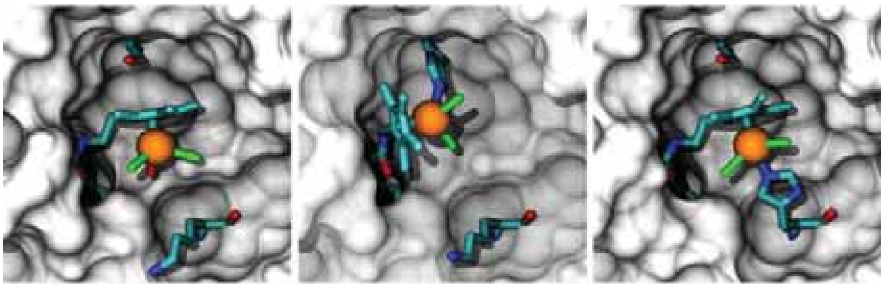

Fig. 10. Docking studies of Rh-functionalized biotin into WT-streptavidin (left), S112H (middle) and K121H streptavidin (right). The double anchoring of the coordination complex improves the catalytic properties of the system. Reprinted with permission from [83].

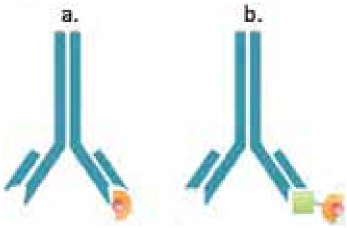

Fig. 11. Schematic representation of antibody–coordination complex recognition (a) and antibody–antigen recognition, where the antigen is linked to the coordination complex. (b).

iron–porphyrin complex was then decorated with a testosterone moiety and inserted into the cavity. The resulting system was subsequently tested for thioanisole sulfoxidation, but showed only low enantioselectivity (entry 2b, Table 4) [88].

4.3.3. Concluding remarks

These examples show the high convenience of this approach, which affords efficient catalysts with a single bioconjugation step. Directed evolution enables one to further improve the systems, virtually both in terms of rate and selectivity. This represents a powerful example of combining chemical and biological methods for hybrid catalysts development and optimization.

5. Incorporation of a coordination complex into an antibody

An original example of hybrid catalyst development is the use the antibody–antigen recognition. The presence of exogeneous species in a body leads to the production of antibodies directed against it, forming a very stable duplex. In the case of an exogeneous metallic complex, the association with an antibody would modify the environment of the metallic centre in an asymmetric manner (Fig. 11a).

For example, Mahy's group aimed at developing cytochrome P450 mimics by raising antibodies against natural or synthetic porphyrins [94]. In this precise case, the proteic environment also serves as a protection against heme oxidative degradation.

A first example using Fe(III)–porphyrin and the corresponding antibody showed good peroxidase activity, using a large scope of peroxide sources and substrates [95]. Looking for a system bearing an axial ligand on the metallic centre, antibodies were then directed against Microperoxidase 8. The resulting scaffold was tested for peroxidase activity [96], nitration of phenol [97] and thioanisole sulfoxidation [98]. This study constitutes a proof of concept for the use of antibody–metal complex system as hydrid catalysts. But despite the clear improvement due to the presence of an axial ligand, these systems remain much less efficient than natural heme peroxidases. A way to further improve the system, could be the use of monoclonal antibodies, combined with site directed mutagenesis and structural analysis. Yet, this would represent a tough approach.

Nevertheless, an attempt was made using the so-called “Trojan horse strategy”. The porphyrin group was attached to an estradiol molecule which allowed binding to an anti-estradiol antibody (Fig. 11b). The catalytic rates were thus improved, but the ee's remained low, witnessing the low influence of the proteic environment [99]. This seems to show the limitations of this antibody strategy, at least for heme complexes.

6. Incorporation of coordination complexes into peptides

Because of their shorter length, and hence the possibility to produce them by chemical synthesis, peptides were first considered as a more convenient opportunity for elaboration of hybrid catalysts. Efforts of synthesis and functionalization are less substantial than for proteins and their handling is less sensitive. But their conformational dynamic makes the chiral environment less defined, diminishing the effect on the metallic centre. Predictions are also more difficult to make, which contrasts with the *de novo* approach used for proteins and presented in Section 2.3. In a first trial to design a catalyst-peptide hybrid, Lewis et al. developed tetrapeptides bearing Pd or Ir metallacycle on their N-terminal end (Fig. 12a, Scheme 5). These constructions conserved the reactivity of the free complexes, but unfortunately no selectivity was observed. The authors proposed that in its favoured conformation, the peptide scaffold is too far from the metallic centre to influence its reactivity (entry 1, Table 5) [100].

To get a stronger influence, the coordination complex was grafted along the peptidic chain, using a non-natural amino acid as the anchor. Christensen and colleagues proposed to position the ligands either in the middle (Fig. 12b) or on each side (Fig. 12c) of the peptide backbone. In this way, peptidic environment surrounds the coordination complexes. A first attempt with phosphine ligands displayed high yields but mild selectivities [101]. Interestingly, the doubly coordinated complex (Fig. 12e) showed better yields and selectivity than its single-point attachment analogue (Fig. 12d). This is consistent with an increasing burying of the catalytic centre in the peptidic scaffold. In a subsequent work, a second generation of [P,S] ligands enabled the remarkable improvement of selectivities. Although not discussed in the publication, a reason for the improvement could be the closer proximity of the chiral centre

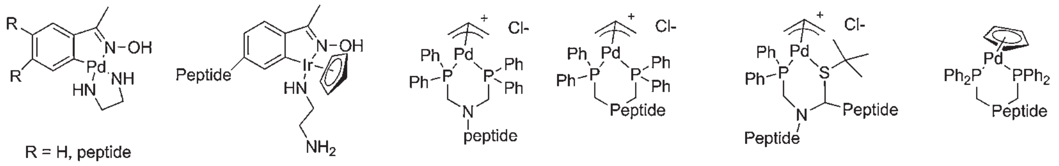

Scheme 5. [Pd] and [Ir]-peptide hybrid catalysts.

Table 5
Some examples of peptides bearing a catalytically active coordination complex detailed in this review.

Entry	Biomolecule	Ligand	Metal	Link type according to Fig. 12	Reaction	Conv.max (%)	ee max (%)	Ref.
1	Tetra-peptide	Metallacycle	Pd(II), Ir (II)	a	Transfer hydrogenation Imidate rearrangement	70	0	[100]
2	Peptide	Phosphines	Pd (II)	b–c	Asymmetric allylic substitution	98	60	[101,102]
2	β-Turn peptide	Phosphines	Pd (II)	c	Asymmetric addition	99	85	[103]

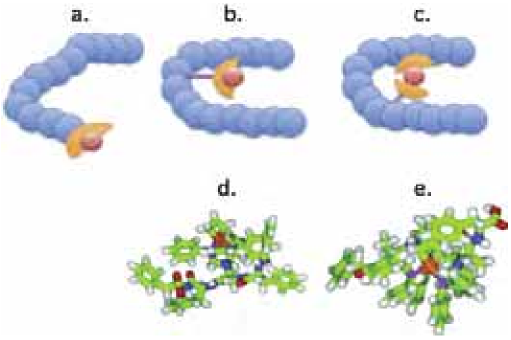

Fig. 12. Top: Schematic representations of the different types of coordination complex decorated peptides. The complexes can be either in the terminal end (a), or along the peptidic chain, either by single (b) or double-point attachment (c). Bottom: the corresponding molecular dynamics modelling obtained by Christensen et al. (d and e). Reprinted with permission from [101].

of the amino acids and the fact that the backbone is part of the metallacycle, which is expected to increase the rigidity. They also demonstrated that inverting the stereochemistry of the amino acids induces an inversion of the stereochemistry of the products [102].

The use of three-dimensionally ordered peptides was also proposed, in order to reduce the dynamic issue. In a paper of Gilbertson, a library of β-turn peptides was decorated with phosphine ligands. The corresponding Pd complex turned efficient for Michael addition, with ee's up to 85% [103].

A final strategy is the coordination of Rh catalysts to carboxylate groups from side chains of amino-acids of host peptides [104]. However, this is at the edge of the central approach described in this review (*i.e.* a combination of a coordination complex with a host biomolecule), since the host peptide itself participates in the metal centre binding.

Table 5 summarizes the results obtained for these different examples. It appears that conversion rates are excellent, showing that good results can still be expected from peptide-based catalysts. Enantiomeric excesses vary a lot according to the systems, highlighting a new issue: here, there is no risk of steric hindrance, contrariwise it seems that the peptidic backbone should surround the catalytic moiety as much as possible. The somewhat easy development of libraries should strongly help to improve the systems, even though the results may be not fully predictable.

7. Conclusion and outlooks

7.1. SWOT analysis

All these examples highlight the wide diversity of applications that can arise from this area of hybrid catalysts prepared from coordination complexes host in biomolecules: chiral scaffolds can be constituted from a large scope of biomolecules and used to target a wide range of reactivities. The simple change of ligands or metals usually constitutes the first optimization step, affording moderate efficiencies. For protein-based systems, genetic optimization might be performed for further improvement. In all cases, the help of molecular modelling and the resolution of crystal (or NMR) structures are crucial for the determination of relevant mutations. This overall process affords catalysts with high selectivity. The rates are still remaining more difficult to improve, sometimes requiring several optimization cycles.

Even if at this point, none of these systems can compete with naturally occurring enzymes in terms of speed rates (all the processes presented above being complete in a few hours to a few days). Their main interest is that they clearly establish that the catalytic properties of a coordination complex can be highly enriched by the stereochemical induction brought by biomolecules.

Compared with standard coordination catalysts they offer interesting alternative as they can induce enantioselectivity without requiring production of sophisticated ligands, which is expensive and generates waste. In contrast, the use of biosynthesized biomolecules further increases the sustainability factor brought by catalysis.

Further development of the field can be expected and would take advantage of the methodological improvement. First of all, control experiments should never be omitted (in particular, comparison with the catalyst in absence of the host biomolecule). In addition, although having a unique reaction as universal control is hardly achievable, having a set of test reactions depending on the nature of the catalysts appears reasonable.

Similarly, the metrics used to assess catalytic efficiency (yield, conversion, speed rates, TON. . .) might also be standardized [105]. These would bring a more convenient comparison of the different approaches. A relation between the catalytic efficiency (k_{cat}) and the catalyst stability under the reaction conditions (TON usually used in catalysis based on transition metals) would also be beneficial.

Related to this, one can also regret that mainly highly efficient strategies are reported. Indeed poorly efficient systems, when properly characterized, represent important and interesting results, which can shed light on unexpected effects of the biomolecule when interacting with the coordination complex. This can help to understand the rational behind these systems, and to develop new optimization strategies.

Still, the development of hybrid catalysts seems to have a bright future. First, because it relies on a truly multidisciplinary approach, it can take advantage of the technological developments from the two fields, enabling a faster advance. The constantly increasing understanding of protein-substrate interactions should help to move towards a more rational method for proteins optimization. Among the efforts made to facilitate the elaboration of the systems, one can especially consider the improvement of the anchoring methods [106–108]. Thanks to the support of computational modelling and directed evolution [40], virtually all of the existing systems can be further optimized.

7.2. Perspectives: Other bio- or bioinspired molecules as potential host

Finally, it appears that many biomolecules are still to be explored. This includes:

(i) *Auto-assembling structures:* Some promising examples involving auto-assembling proteins, including fibres, needles, disc and rod structures obtained with amphiphilic proteins and peptides recently appeared in literature, showing interesting extension of this research field to heterogeneous catalysis [109,110]. This approach using amyloid type fibres has been recently developed for hydrolytic purpose [111]. It is currently under investigation in our group for application to more synthetically relevant catalytic reactions.

(ii) *Foldamers:* The emerging use of foldamers, *i.e.* artificial folded molecular architectures inspired by the structures and functions of biopolymers (glycoproteins [112,113] and peptide analogues [114]), is also of great potential [115]. Foldamers are already being used for organocatalysis [116–118], and can coordinate metallic ions [119], or form cavities [120]. Yet, to the best of our knowledge, no example was described for chemistry-based catalysis hosted by foldamer scaffolds, but this is likely to appear in a very close future. Another direction of research is also consisting in the generation of catalysts inside cells, which gives a new dimension to the field [36].

Acknowledgements

We thank the Région Midi-Pyrénées and the Université de Toulouse for financial support of M. H. (APR-PRES 2013, project EVOLCAT).

References

[1] G. Caserta, S. Roy, M. Atta, V. Artero, M. Fontecave, Curr. Opin. Chem. Biol. 25 (2015) 36.
[2] A. Onoda, T. Hayashi, Curr. Opin. Chem. Biol. 25 (2015) 133.
[3] G. Berggren, A. Adamska, C. Lambertz, T.R. Simmons, J. Esselborn, M. Atta, S. Gambarelli, J.-M. Mouesca, E. Reijerse, W. Lubitz, T. Happe, V. Artero, M. Fontecave, Nature 499 (2013) 66.
[4] W.T. Eckenhoff, W.R. McNamara, P. Du, R. Eisenberg, Biochim. Biophys. Acta 1827 (2013) 958.
[5] O. Iranzo, Bioorg. Chem. 39 (2011) 73.
[6] E.P. Broering, P.T. Truong, E.M. Gale, T.C. Harrop, Biochemistry 52 (2013) 4.
[7] E.M. Gale, A.C. Simmonett, J. Telser, H.F. Schaefer, T.C. Harrop, Inorg. Chem. 50 (2011) 9216.
[8] D.P. Riley, Chem. Rev. 99 (1999) 2573.
[9] T.A. Jackson, C.T. Gutman, J. Maliekal, A.-F. Miller, T.C. Brunold, Inorg. Chem. 52 (2013) 3356.
[10] V. Artero, M. Chavarot-Kerlidou, M. Fontecave, Angew. Chem. Int. Ed. 50 (2011) 7238.
[11] M.D. Kärkäs, O. Verho, E.V. Johnston, B. Åkermark, Chem. Rev. 114 (2014) 11863.
[12] L. Que, W.B. Tolman, Nature 455 (2008) 333.
[13] N. Elgrishi, M.B. Chambers, V. Artero, M. Fontecave, PCCP 16 (2014) 13635.
[14] J.-N. Rebilly, B. Colasson, O. Bistri, D. Over, O. Reinaud, Chem. Soc. Rev. 44 (2015) 467.
[15] M.J. Wiester, P.A. Ulmann, C.A. Mirkin, Angew. Chem. Int. Ed. 50 (2011) 114.
[16] M. Raynal, P. Ballester, A. Vidal-Ferran, P.W.N.M. van Leeuwen, Chem. Soc. Rev. 43 (2014) 1734.
[17] J. Bos, G. Roelfes, Curr. Opin. Chem. Biol. 19 (2014) 135.
[18] J.C. Lewis, ACS Catal. 3 (2013) 2954.
[19] J. Steinreiber, T.R. Ward, Coord. Chem. Rev. 252 (2008) 751.
[20] C. Letondor, T.R. Ward, ChemBioChem 7 (2006) 1845.
[21] C.M. Thomas, T.R. Ward, Chem. Soc. Rev. 34 (2005) 337.
[22] J. Collot, N. Humbert, M. Skander, G. Klein, T.R. Ward, J. Organomet. Chem. 689 (2004) 4868.
[23] I. Drienovská, G. Roelfes, Isr. J. Chem. 55 (2014) 21.
[24] C. Marchi-Delapierre, L. Rondot, C. Cavazza, S. Ménage, Isr. J. Chem. 55 (2014) 61.
[25] M. Dürrenberger, T.R. Ward, Curr. Opin. Chem. Biol. 19 (2014) 99.
[26] M.R. Ringenberg, T.R. Ward, Chem. Commun. 47 (2011) 8470.
[27] K. Yamamura, E.T. Kaiser, J. Chem. Soc., Chem. Commun. 20 (1976) 830.
[28] A. Fernández-Gacio, A. Codina, J. Fastrez, O. Riant, P. Soumillion, ChemBioChem 7 (2006) 1013.
[29] K. Okrasa, R.J. Kazlauskas, Chem. Eur. J. 12 (2006) 1587.
[30] Q. Jing, K. Okrasa, R.J. Kazlauskas, Chem. Eur. J. 15 (2009) 1370.
[31] Q. Jing, R.J. Kazlauskas, ChemCatChem 2 (2010) 953.
[32] N. Yeung, Y.-W. Lin, Y.-G. Gao, X. Zhao, B. Russell, L. Lei, K. Miner, H. Robinson, Y. Lu, Nature 462 (2009) 1079.
[33] V. Köhler, T.R. Ward, ChemBioChem 11 (2010) 1049.
[34] R. Fasan, ACS Catal. 2 (2012) 647.
[35] J.A. McIntosh, P.S. Coelho, C.C. Farwell, Z.J. Wang, J.C. Lewis, T.R. Brown, F.H. Arnold, Angew. Chem. Int. Ed. 52 (2013) 9309.
[36] J.-P. Mahy, J. Ciesielski, P. Dauban, Angew. Chem. Int. Ed. 53 (2014) 6862.
[37] P.S. Coelho, Z.J. Wang, M.E. Ener, S.A. Baril, A. Kannan, F.H. Arnold, E.M. Brustad, Nat. Chem. Biol. 9 (2013) 485.
[38] P.S. Coelho, E.M. Brustad, A. Kannan, A.H. Frances, Science 339 (2013) 307.
[39] K.D. Miner, A. Mukherjee, Y.-G. Gao, E.L. Null, I.D. Petrik, X. Zhao, N. Yeung, H. Robinson, Y. Lu, Angew. Chem. Int. Ed. 51 (2012) 5589.
[40] I.D. Petrik, J. Liu, Y. Lu, Curr. Opin. Chem. Biol. 19 (2014).
[41] V.M. Cangelosi, A. Deb, J.E. Penner-Hahn, V.L. Pecoraro, Angew. Chem. Int. Ed. 53 (2014) 7900.
[42] F. Yu, V.M. Cangelosi, M.L. Zastrow, M. Tegoni, J.S. Plegaria, A.G. Tebo, C.S. Mocny, L. Ruckthong, H. Qayyum, V.L. Pecoraro, Chem. Rev. 114 (2014) 3495.
[43] M. Matzapetakis, B.T. Farrer, T.-C. Weng, L. Hemmingsen, J.E. Penner-Hahn, V.L. Pecoraro, J. Am. Chem. Soc. 124 (2002) 8042.
[44] S. Chakraborty, D.S. Touw, A.F.A. Peacock, J. Stuckey, V.L. Pecoraro, J. Am. Chem. Soc. 132 (2010) 13240.
[45] F. Yu, J.E. Penner-Hahn, V.L. Pecoraro, J. Am. Chem. Soc. 135 (2013) 18096.
[46] M. Tegoni, F. Yu, M. Bersellini, J.E. Penner-Hahn, V.L. Pecoraro, Proc. Natl. Acad. Sci. U.S.A. 109 (2012) 21234.
[47] M.L. Zastrow, V.L. Pecoraro, Biochemistry 53 (2014) 957.
[48] M.L. Zastrow, V.L. Pecoraro, Coord. Chem. Rev. 257 (2013) 2565.
[49] A.G. Tebo, V.L. Pecoraro, Curr. Opin. Chem. Biol. 25 (2015) 65.
[50] M. Tegoni, Eur. J. Inorg. Chem. 13 (2014) 2177.
[51] G. Roelfes, B.L. Feringa, Angew. Chem. Int. Ed. 44 (2005) 3230.
[52] J. Oelerich, G. Roelfes, Chem. Sci. 4 (2013) 2013.
[53] A.J. Boersma, D. Coquière, D. Geerdink, F. Rosati, B.L. Feringa, G. Roelfes, Nat. Chem. 2 (2010) 991.
[54] D. Coquière, B.L. Feringa, G. Roelfes, Angew. Chem. Int. Ed. 46 (2007) 9308.
[55] A.J. Boersma, B. de Bruin, B.L. Feringa, G. Roelfes, Chem. Commun. 48 (2012) 2394.
[56] J. Wang, E. Benedetti, L. Bethge, S. Vonhoff, S. Klussmann, J.-J. Vasseur, J. Cossy, M. Smietana, S. Arseniyadis, Angew. Chem. Int. Ed. 52 (2013) 11546.
[57] S. Park, K. Ikehata, R. Watabe, Y. Hidaka, A. Rajendran, H. Sugiyama, Chem. Commun. 48 (2012) 10398.
[58] N.S. Oltra, G. Roelfes, Chem. Commun. 45 (2008) 6039.
[59] P. Fournier, R. Fiammengo, A. Jäschke, Angew. Chem. Int. Ed. 48 (2009) 4426.
[60] S. Park, L. Zheng, S. Kumakiri, S. Sakashita, H. Otomo, K. Ikehata, H. Sugiyama, ACS Catal. 4 (2014) 4070.
[61] S. Park, H. Sugiyama, Molecules 17 (2012) 12792.
[62] E. Benedetti, N. Duchemin, L. Bethge, S. Vonhoff, S. Klussmann, J.-J. Vasseur, J. Cossy, M. Smietana, S. Arseniyadis, Chem. Commun. 51 (2015) 6076.
[63] S. Park, K. Ikehata, H. Sugiyama, Biomater. Sci. 1 (2013) 1034.
[64] L. Gjonaj, G. Roelfes, ChemCatChem 5 (2013) 1718.
[65] J.R. Carey, S.K. Ma, T.D. Pfister, D.K. Garner, H.K. Kim, J.A. Abramite, Z. Wang, Z. Guo, Y. Lu, J. Am. Chem. Soc. 126 (2004) 10812.
[66] T. Ueno, T. Koshiyama, M. Ohashi, K. Kondo, M. Kono, Y. Watanabe, A. Suzuki, T. Yamane, J. Am. Chem. Soc. 127 (2005) 6556.
[67] C. Zhang, P. Srivastava, K. Ellis-Guardiola, J.C. Lewis, Tetrahedron 70 (2014) 4245.

[68] C. Esmieu, M.V. Cherrier, P. Amara, E. Girgenti, C. Marchi-Delapierre, F. Oddon, M. Iannello, A. Jorge-Robin, C. Cavazza, S. Ménage, Angew. Chem. Int. Ed. 52 (2013) 3922.
[69] F. Philippart, M. Arlt, S. Gotzen, S.-J. Tenne, M. Bocola, H.-H. Chen, L. Zhu, U. Schwaneberg, J. Okuda, Chem. Eur. J. 19 (2013) 13865.
[70] A. Onoda, K. Fukumoto, M. Arlt, M. Bocola, U. Schwaneberg, T. Hayashi, Chem. Commun. 48 (2012) 9756.
[71] S. Abe, K. Hirata, T. Ueno, K. Morino, N. Shimizu, M. Yamamoto, M. Takata, E. Yashima, Y. Watanabe, J. Am. Chem. Soc. 131 (2009) 6958.
[72] C. Cavazza, C. Bochot, P. Rousselot-Pailley, P. Carpentier, M.V. Cherrier, L. Martin, C. Marchi-Delapierre, J.C. Fontecilla-Camps, S. Ménage, Nat. Chem. 2 (2010) 1069.
[73] A. Mahammed, Z. Gross, J. Am. Chem. Soc. 127 (2005) 2883.
[74] M. Allard, C. Dupont, V. Muñoz Robles, N. Doucet, A. Lledós, J.-D. Maréchal, A. Urvoas, J.-P. Mahy, R. Ricoux, ChemBioChem 13 (2012) 240.
[75] J. Bos, F. Fusetti, A.J.M. Driessen, G. Roelfes, Angew. Chem. Int. Ed. 51 (2012) 7472.
[76] C. Mayer, D.G. Gillingham, T.R. Ward, D. Hilvert, Chem. Commun. 47 (2011) 12068.
[77] H. Inaba, S. Kanamaru, F. Arisaka, S. Kitagawa, T. Ueno, Dalton Trans. 41 (2012) 11424.
[78] A. Pordea, M. Creus, J. Panek, C. Duboc, D.B. Mathis, M. Novic, T.R. Ward, J. Am. Chem. Soc. 130 (2008) 8085.
[79] V. Köhler, J. Mao, T. Heinisch, A. Pordea, A. Sardo, Y.M. Wilson, L. Knörr, M. Creus, J.-C. Prost, T. Schirmer, T.R. Ward, Angew. Chem. Int. Ed. 50 (2011) 10863.
[80] T. Komatsu, S. Ishihara, E. Tsuchida, H. Nishide, C. Morokuma, S. Nakamura, Biomacromolecules 6 (2005) 1489.
[81] J. Collot, J. Gradinaru, N. Humbert, M. Skander, A. Zocchi, T.R. Ward, J. Am. Chem. Soc. 125 (2003) 9030.
[82] A. Pordea, T.R. Ward, Chem. Commun. 36 (2008) 4239.
[83] J.M. Zimbron, T. Heinisch, M. Schmid, D. Hamels, E.S. Nogueira, T. Schirmer, T.R. Ward, J. Am. Chem. Soc. 135 (2013) 5384.
[84] T.K. Hyster, L. Knorr, T.R. Ward, T. Rovis, Science 338 (2012) 500.
[85] M. Dürrenberger, T. Heinisch, Y.M. Wilson, T. Rossel, E. Nogueira, L. Knörr, A. Mutschler, K. Kersten, M.J. Zimbron, J. Pierron, T. Schirmer, T.R. Ward, Angew. Chem. Int. Ed. 50 (2011) 3026.
[86] A. Pordea, D. Mathis, T.R. Ward, J. Organomet. Chem. 694 (2009) 930.
[87] T. Matsuo, C. Imai, T. Yoshida, T. Saito, T. Hayashi, S. Hirota, Chem. Commun. 48 (2012) 1662.
[88] E. Sansiaume-Dagousset, A. Urvoas, K. Chelly, W. Ghattas, J.-D. Maréchal, J.-P. Mahy, R. Ricoux, Dalton Trans. 43 (2014) 8344.
[89] M. Srisa-Art, E.C. Dyson, A.J. deMello, J.B. Edel, Anal. Chem. 80 (2008) 7063.
[90] T.R. Ward, Chem. Eur. J. 11 (2005) 3798.
[91] V.M. Robles, M. Dürrenberger, T. Heinisch, A. Lledós, T. Schirmer, T.R. Ward, J.-D. Maréchal, J. Am. Chem. Soc. 136 (2014) 15676.
[92] C. Letondor, A. Pordea, N. Humbert, A. Ivanova, S. Mazurek, M. Novic, T.R. Ward, J. Am. Chem. Soc. 128 (2006) 8320.
[93] T. Quinto, D. Häussinger, V. Köhler, T.R. Ward, Org. Biomol. Chem. 13 (2015) 357.
[94] J.-P. Mahy, J.-D. Maréchal, R. Ricoux, Chem. Commun. 51 (2015) 2476.
[95] R. Quilez, S. de Lauzon, B. Desfosses, D. Mansuy, J.-P. Mahy, FEBS Lett. 395 (1996) 73.
[96] R. Ricoux, H. Sauriat-Dorizon, E. Girgenti, D. Blanchard, J.-P. Mahy, J. Immunol. Met. 269 (2002) 39.
[97] R. Ricoux, E. Girgenti, H. Sauriat-Dorizon, D. Blanchard, J.-P. Mahy, J. Protein Chem. 21 (2002) 473.
[98] R. Ricoux, E. Lukowska, F. Pezzotti, J.-P. Mahy, Eur. J. Biochem. 271 (2004) 1277.
[99] E. Sansiaume, R. Ricoux, D. Gori, J.-P. Mahy, Tetrahedron: Asymmetry 21 (2010) 1593.
[100] Z. Zhang, H. Yang, C. Zhang, J.C. Lewis, Organometallics 31 (2012) 7328.
[101] C.A. Christensen, M. Meldal, Chem. Eur. J. 11 (2005) 4121.
[102] C.A. Christensen, M. Meldal, J. Comb. Chem. 9 (2007) 79.
[103] S.R. Gilbertson, S.E. Collibee, A. Agarkov, J. Am. Chem. Soc. 122 (2000) 6522.
[104] Z. Ball, Acc. Chem. Res. 46 (2012) 560.
[105] I.V. Korendovych, W.F. DeGrado, Curr. Opin. Struct. Biol 27 (2014) 113.
[106] J.M. Palomo, Org. Biomol. Chem. 10 (2012) 9309.
[107] I. Drienovská, A. Rioz-Martínez, A. Draksharapu, G. Roelfes, Chem. Sci. 6 (2015) 770.
[108] H. Yang, P. Srivastava, C. Zhang, J.C. Lewis, ChemBioChem 15 (2014) 223.
[109] T. Ueno, H. Tabe, Y. Tanaka, Chem. Asian J. 8 (2013) 1646.
[110] H. Inaba, S. Kitagawa, T. Ueno, Isr. J. Chem. 53 (2013) 1.
[111] C.M. Rufo, Y.S. Moroz, O.V. Moroz, J. Stöhr, T.A. Smith, X. Hu, W.F. DeGrado, I.V. Korendovych, Nat. Chem 6 (2014) 303.
[112] C. Bonduelle, J. Huang, T. Mena-Barragán, C. Ortiz Mellet, C. Decroocq, E. Etamé, A. Heise, P. Compain, S. Lecommandoux, Chem. Commun. 50 (2014) 3350.
[113] C. Bonduelle, S. Lecommandoux, Biomacromolecules 14 (2013) 2973.
[114] L. Sebaoun, B. Kauffmann, T. Delclos, V. Maurizot, I. Huc, Org. Lett. 16 (2014) 2326.
[115] G. Guichard, Y. Huc, Chem. Commun. 47 (2011) 5933.
[116] M.M. Müller, M.A. Windsor, W.C. Pomerantz, S.H. Gellman, D. Hilvert, Angew. Chem. Int. Ed. 48 (2009) 922.
[117] C. Mayer, M.M. Müller, S.H. Gellman, D. Hilvert, Angew. Chem. Int. Ed. 53 (2014) 6978.
[118] G. Maayan, M.D. Ward, K. Kirshenbaum, Proc. Natl. Acad. Sci. U.S.A. 106 (2009) 13679.
[119] G. Maayan, M.D. Ward, K. Kirshenbaum, Chem. Commun. (2009) 56.
[120] M.L. Singleton, G. Pirotte, B. Kauffmann, Y. Ferrand, I. Huc, Angew. Chem. Int. Ed. 53 (2014) 13140.

PLOS | ONE

RESEARCH ARTICLE

A Robust and Efficient Production and Purification Procedure of Recombinant Alzheimers Disease Methionine-Modified Amyloid-β Peptides

Marie Hoarau[1,2], Yannick Malbert[1☯], Romain Irague[1☯¤a], Christelle Hureau[2‡], Peter Faller[2¤b‡], Emmanuel Gras[2‡], Isabelle André[1‡], Magali Remaud-Siméon[1‡*]

1 Laboratoire d'Ingénierie des Systèmes Biologiques et Procédés, Université de Toulouse, CNRS, INRA, INSA, Toulouse, France, **2** Laboratoire de Chimie de Coordination, CNRS, Université de Toulouse, INPT, Toulouse, France

☯ These authors contributed equally to this work.
‡ These authors also contributed equally to this work.
¤a Current address: Unité Fonctionnalité et Ingénierie des Protéines, CNRS, Université de Nantes, Nantes, France
¤b Current address: Institut de Chimie, UMR 7177, Université de Strasbourg, Strasbourg, France
* remaud@insa-toulouse.fr

Abstract

An improved production and purification method for Alzheimer's disease related methionine-modified amyloid-β 1–40 and 1–42 peptides is proposed, taking advantage of the formation of inclusion body in *Escherichia coli*. A Thioflavin-S assay was set-up to evaluate inclusion body formation during growth and optimize culture conditions for amyloid-β peptides production. A simple and fast purification protocol including first the isolation of the inclusion bodies and second, two cycles of high pH denaturation/ neutralization combined with an ultrafiltration step on 30-kDa cut-off membrane was established. Special attention was paid to purity monitoring based on a rational combination of UV spectrophotometry and SDS-PAGE analyses at the various stages of the process. It revealed that this chromatography-free protocol affords good yield of high quality peptides in term of purity. The resulting peptides were fully characterized and are appropriate models for highly reproducible *in vitro* aggregation studies.

Citation: Hoarau M, Malbert Y, Irague R, Hureau C, Faller P, Gras E, et al. (2016) A Robust and Efficient Production and Purification Procedure of Recombinant Alzheimers Disease Methionine-Modified Amyloid-β Peptides. PLoS ONE 11(8): e0161209. doi:10.1371/journal.pone.0161209

Editor: Koichi M Iijima, National Center for Geriatrics and Gerontology, JAPAN

Received: May 12, 2016

Accepted: August 1, 2016

Published: August 17, 2016

Data Availability Statement: All relevant data are within the paper and its Supporting Information files.

Funding: This work was funded within the frame of APR-PRES 2013, project EVOLCAT.

Competing Interests: The authors have declared that no competing interests exist.

Introduction

With a worldwide incidence of millions people, Alzheimer's disease is considered as a major health issue, and much research effort is currently being devoted to better understand the causes and mechanisms of the disease. Diverse therapeutic approaches are being explored, including hormonotherapy [1], immunotherapy [2], genetics [3] or pharmaceutics [4].

Although their implication in the disease remains unclear, the presence of amyloid plaques and oligomers in the synaptic cleft is widely considered as one of the hallmarks of Alzheimer's disease, and were found to be highly deleterious for neuron plasticity [5]. These aggregates are mainly constituted of amyloid-β (Aβ) peptides, namely $A\beta_{1-40}$ and $A\beta_{1-42}$, resulting from the abnormal proteolytic cleavage of the amyloid precursor protein. Understanding the mechanism of formation and the behavior of these aggregates could pave the way to new therapeutic approaches against Alzheimer's disease, promoting multiple investigations on Aβ peptide aggregation process [6].

For *in vitro* experimentation, disposing of Aβ samples displaying reproducible behaviours is a key issue. Indeed, aggregation was shown to be highly sensitive to many factors, such as temperature, concentration, agitation, but also storage or sample preparation [7,8]. But most importantly, the presence of both contaminants and pre-aggregated forms of the peptide were shown to strongly alter the course of aggregation, either inhibiting it or yielding no fibrillary material. In this regard, the easy access to pure and homogeneous Aβ samples is still challenging and essential for *in vitro* experimentation.

Most investigations are usually performed with chemically synthesized peptides. Although convenient and easily accessible, solid phase peptide synthesis can be complex in terms of purification. Indeed, the presence of peptides with altered sequence caused by non-quantitative synthetic steps or of racemized peptides is observed, which can hardly be removed, even by up-to-date purification methods. Traces of salts or metal ions were also reported [9]. Finally, presence of pre-formed aggregates due to storage conditions is frequent. All of this induce significant variations of aggregation properties from batch to batch. This has been recently exemplified in a study, which showed that the recombinant peptide is more aggregation-prone and more neurotoxic than its synthetic analogue, demonstrating a deleterious effect of synthetic procedures on peptide properties [10]. This has encouraged the exploration of various biological routes to access recombinant Aβ, getting rid of such issues.

Aβ peptide recombinant production was attempted in yeast [11] or by combining recombinant and synthetic procedures [12] but, to date, the most common expression system remains *Escherichia coli*. Most often, peptides are appended to a fusion protein that enhance their solubility and ease their isolation and purification using affinity chromatography. However, such strategies raised several issues. First of all, despite the increased solubility of the fusion proteins, a significant amount of the peptide frequently remains insoluble, thus requiring an extra denaturation step to achieve full recovery [13,14]. Moreover, a cleavage site has to be installed, its position being critical; indeed if not carefully chosen, upon cleavage amino-acids will be introduced at the terminal end of the peptide, potentially modifying its aggregation and metal-binding properties [15,16]. The same drawback is also observed with smaller affinity tags [17,18]. This problem has been solved through the use of proteolytic enzymes whose cleavage sites enable the formation of native Aβ (Factor Xa, Enterokinase. . .) [19,20]. Still such methods are time-consuming and require many purification steps, including long affinity chromatography purification procedures that induce in a loss of peptide. A representative example was described by Zhang and co-workers, showing that only 24% of Glutathione S-transferase-tagged peptide is recovered in the soluble fraction after cell lysis. This yield is weakly affected by affinity chromatography (21%), but drops to 5.1% after thrombin cleavage. To overcome this drawback, it was proposed to express Aβ in its native form in *E. coli* [21,22]. Notably, Aβ forms insoluble inclusion bodies (IBs) when expressed in *E. coli* in their native form. This was exploited by Walsh and co-workers to isolate pure recombinant methionine-modified Aβ peptides $MA\beta_{1-40}$ and $MA\beta_{1-42}$ in five purification steps [21].

We describe here an alternative and straightforward procedure of recombinant $MA\beta_{1-40}$ and $MA\beta_{1-42}$ production and purification. First, expression conditions were optimized using Thioflavin-S (Th-S), a known fluorescent probe for *in vivo* imaging of IBs. We subsequently established a rapid purification process based on inclusion body treatment with NaOH followed by an ultrafiltration step that has proven remarkably efficient to remove protein and nucleic acid contaminants. Finally, a detailed monitoring of the purification process was conducted, showing that only a combination of characterization techniques can ensure sample reliability.

Materials and Methods

All chemicals were purchased from Sigma-Aldrich (St. Louis, USA). pET28a plasmid was purchased from Novagen (Darmstadt, Germany). NcoI, XhoI and BamHI restriction enzymes Antarctic phosphatase and T4 DNA Ligase were purchased from New England Biolabs (Ipswich, USA) and used with the provided buffer according to supplier's recommendations. pET28a_His-Thromb-Aβ_{1-42} plasmid was synthesized by Genecust (Dudelange, Luxembourg). *E. coli* TOP10 cells and *E. coli* BL21 (DE3) cells were obtained from Invitrogen (Carlsbad, USA). QIAprep spin MiniPrep kit was purchased from Qiagen (Hilden, Germany). Sequence analyses of the constructions were performed by GATC Biotech (Constance, Germany).

Vectors construction and cloning procedure

The commercial pET28a plasmid was digested by NcoI and XhoI restriction enzymes, dephosphorylated using Antarctic phosphatase, and gel purified on an agarose 0.8% Tris acetate EDTA (TAE) gel. The pET28a_His-Thromb-Aβ_{1-42} plasmid was used as template for PCR amplification of the Aβ_{1-42} coding sequence using pR_pET28_Ab42: AGCGGTGGCAGCAG CCAACTCAGCT and pF_pET28_Ab42: GACCTACCCATGGACGCTGAATTTCGCCAC GACTCCGGCTAT as primers. The PCR product was digested by NcoI and XhoI, gel purified on an agarose 1.2% TAE gel and ligated in the NcoI/XhoI digested pET28a yielding the desired pET28a_MAβ_{1-42} plasmid. The construction was used to transform chimiocompetent *E.coli* TOP10 cells that were grown on solid Luria-Bertani (LB) medium (10 g/L tryptone, 10 g/L NaCl, 5 g/L yeast extract) containing 50 mg/L kanamycin (1X). One colony was used to inoculate 5 mL LB kanamycin 1X at 37°C. Cells were grown overnight, harvested before plasmid extraction using a MiniPrep kit.

The pET28a_MAβ_{1-40} was obtained from pET28a_MAβ_{1-42} using a similar procedure except that the sequence coding for Aβ_{1-40} was PCR-amplified with pR_pet28_Ab40: AATGG ATCCTAATTAAACAACGCCGCCAACCATCAGACCGATG and pF_pet28_Ab40: AATT GTGAGCGGATAACAATTCCCCTCTAG as primers. The PCR-product was digested using NcoI and BamHI, and ligated into NcoI/BamHI digested and dephosphorylated pET28a.

Expression of MAβ_{1-40} and MAβ_{1-42} and inclusion body isolation

Chemically competent *E. coli* BL21 (DE3) cells transformed with pET28a_MAβ_{1-40} or pET28a_MAβ_{1-42} plasmids were used for peptide production. One single colony was used to inoculate 10 mL LB kanamycin 1X medium. The cells were grown for 16 h. 100 mL of LB medium containing kanamycin 1X were inoculated to an OD_{600} of 0.05 with an overnight preculture performed from one single clone in 10 mL LB-Kana medium. Cells were grown at 37°C under agitation to an OD_{600} of 0.8. Expression was induced with 0.5 mM Isopropyl β-*D*-1-thiogalactopyranoside (IPTG) during for 4 additional hours of culture at 37°C. Cells were harvested by centrifugation (8,000 g, 10 min) and re-suspended to an OD_{600} of 80 in lysis buffer (50 mM Tris-HCl, 100 mM NaCl, pH 8) containing 1% Tergitol-type NP40 detergent. Cells were then lysed by 30s sonication on ice and the lysate was centrifuged (12,000 g, 10 min). The insoluble fraction was re-suspended in 1 mL lysis buffer, containing phenylmethanesulfonyl fluoride (15 mM) and lysozyme (300 μg/mL), and incubated for 1 h at room temperature. IBs were harvested by centrifugation (12,000 g, 10 min), washed with Triton X100 0.5% and twice with phosphate saline buffer (PBS) 1X pH 8. IBs were finally resuspended in PBS buffer and submitted to 10 cycles of 10 s sonication followed by centrifugation to remove nucleic acid contaminants contained in the supernatant and that could be stacked on their surface, according to a previously reported procedure [23].

Peptide purification

IBs were denatured by 2 h incubation in 500 μL of NaOH 50 mM under smooth shaking at room temperature. The resulting mixture was centrifuged (12,000 g, 5 min), and the supernatant neutralized by addition of 500 mM HCl. The formation of a white precipitate was observed. The mixture was centrifuged once again, and the supernatant was collected. To optimize recovery, this denaturation/neutralisation cycle was applied twice. Supernatants were passed through a 30-kDa Amicon-Ultra centrifugal device, to remove high molecular weight contaminant proteins, and then concentrated on a 3-kDa Amicon-Ultra centrifugal device.

SDS-PAGE analysis

15 μL protein samples were mixed with 5 μL Laemli Sample buffer (Bio-Rad) containing 10% β-mercaptoethanol, and denatured at 95°C for 10 min. Samples were then loaded on a Mini-protean TGX Stain-Free Any Kd Precast Gel (Bio-Rad) and electrophoresis was run for 30 min at 150 V in Tris/Glycine/SDS buffer (Bio-Rad). Gel was then stained using PageBlue Protein Staining solution (Bio-Rad).

Thioflavin-S staining

Samples of Aβ peptide producing cells or purified IBs are centrifuged (12,000 g, 10 min) and resuspended in 200 μL Thioflavin-S 125 μM in PBS 1X pH 8. After 15 min incubation, cells or IBs were harvested by centrifugation, washed with 200 μL PBS, re-suspended in PBS, and submitted to fluorescence experiments.

Fluorescence microscopy

50 μL samples of Th-S stained cells or IBs were dispensed on a microscope glass slide and imaged using a Leica microscope with a 63x lens with a DAPI filter (λ_{exc} = 340–380 nm, dichroic = 400, λ_{em} = 425 nm).

Fluorescence spectrophotometry

1 mL samples of Th-S stained cells or IBs were placed in a quartz cuvette and their emission spectra were recorded using a Jasco fluorimeter (λ_{exc} = 375 nm). Right after each measurement, OD_{600} was measured, to normalize the signal.

^{1}H NMR

Pure samples of peptides in water were diluted to 100 μM in phosphate buffer 50 mM pH 7 in D_2O. ^{1}H NMR spectra were recorded on a 500 MHz NMR (Bruker) at 25°C using solvent as reference. As a control, synthetic $A\beta_{1-40}$ was dissolved in NaOD and diluted to 100 μM under the same conditions.

LC-MS

Peptide samples were analysed by LC-MS on an Agilent 1200 HPLC fitted with a Macherey Nagel Nucleodur 300–5 C4 ec 250 mm x 2 mm 5 μm at 30°C coupled with a Thermo Fisher Scientific LCQ Fleet mass spectrometer fitted with an H-ESI II Probe.

Samples were eluted at 0.33 mL/min using a gradient of acetonitrile going from 5% to 90% in aqueous formic acid 0.1% in 12 min. Multiply-charged peptides were detected by mass spectrometry (ESI +).

Thioflavin-T aggregation assay

To ensure of the homogeneity of the starting sample, monomeric peptides were isolated by steric exclusion chromatography (SEC). An Aktä Purifier system equipped with a Superdex 75 10/300 column was equilibrated with 2 column volumes of 15 mM NaOH. Peptide samples in NaOH 50 mM were then eluted using NaOH 15 mM at 1 mL/min, with UV monitoring at 220 and 293 nm. Monomeric MAβ peptides display retention times around 9 min. Fractions containing peptides were collected, centrifuged, and their concentration was assessed by UV-Vis at pH 12 ($\lambda = 293$ nm, $\varepsilon = 2400$ $L.mol^{-1}.cm^{-1}$).

In a 384-wells microplate (Greiner) were added phosphate buffer (50 mM), Thioflavin-T (10 μM) and freshly SEC-purified peptide (20 μM or 50 μM). Fluorescence intensity was recorded every 5 min for a total duration of 4 days using a ClarioStar plate reader (BMG Labtech) set at 37°C. Fluorescence parameters were set as follows: $\lambda_{exc} = 440$ nm, $\lambda_{em} = 490$ nm, gain = 650, shaking at 200 rpm for 12 s before each measurement. Aggregation curves were fitted using KaleidaGraph software.

Results and Discussion

Optimization of $MA\beta_{1-40}$ and $MA\beta_{1-42}$ expression

The genes encoding $MA\beta_{1-40}$ and $MA\beta_{1-42}$ were first cloned in pET28. They were then expressed by growing *E. coli* BL21 (DE3) transformed with the recombinant plasmids on LB broth supplemented with kanamycin. To determine optimal conditions for peptide expression, we envisioned a procedure based on Th-S monitoring.

Indeed, Th-S is usually used for staining amyloid plaques but was also recently shown to stain bacterial IBs formed by MAβ peptides, both *in vivo* and *in vitro*. Hence, Th-S was used to detect protein aggregation in bacteria [22], or to screen *in vivo* aggregation inhibitors [24]. In order to use Th-S staining as a tool for the optimization of peptide expression, the correlation between IB content and the Th-S fluorescence level had to be established. For this purpose, cultures expressing $MA\beta_{1-42}$ were stopped at different induction times. The cells were sampled, incubated with Th-S, and their emission spectra were recorded. As shown in Fig 1A, the fluorescence level increased during the first 4 hours of induction and then reached a plateau. The corresponding cultures were lysed and peptide was purified and analysed by SDS-PAGE. A good correlation was observed between the amount of purified peptide and the fluorescence level (Fig 1B). Similar results were obtained with $MA\beta_{1-40}$, showing that Th-S staining is very useful to estimate MAβ IB content in cells. Based on these results, a 4 h induction was considered as adapted and applied throughout the rest of the study.

Th-S monitoring was then used to screen for the optimal concentration of IPTG inducer. No significant variations of IB production was observed with IPTG concentration comprised between 0.5 and 1.5 mM (Fig 1C). Contrariwise, increased levels of protein contaminants were observed when using 1 or 1.5 mM IPTG, which could be due to the overexpression of *E. coli* chaperones [25]. Induction at 0.5 mM IPTG was thus found optimal. Finally, the optimal temperature of cell growth was investigated. As shown in Fig 1D, the best temperature allowing the formation of a maximal amount of IBs was 37°C.

This preliminary work allowed us to establish the optimal conditions of MAβ peptide recombinant production as corresponding to recombinant cell cultures carried out at 37°C and

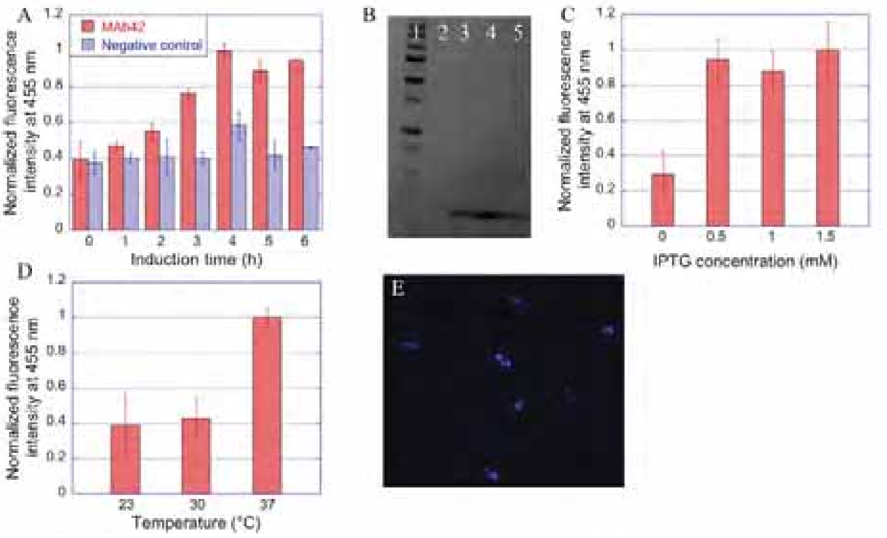

Fig 1. MAβ_{1-42} expression monitoring using Thioflavin-S. A. Variations of normalized fluorescence of Th-S-treated *E. coli* cells expressing MAβ_{1-42} with culture induction time. **B**. SDS-PAGE of inclusion bodies formed during *E. coli* cultures expressing MAβ_{1-42}; lane 1: 10–250 kDa protein ladder, lane 2 to 5: samples taken at 0, 2, 4, and 6 hours of growth, respectively. **C.** Normalized fluorescence intensity of Th-S-treated *E. coli* cells expressing MAβ_{1-42} as a function of IPTG concentration used for induction. **D**. Normalized fluorescence intensity of Th-S-treated *E. coli* cells expressing MAβ_{1-42} during 4h at various temperatures. **E**. Fluorescence microscopy of *E. coli* cells expressing MAβ_{1-42} as IBs after 4 h culture.

doi:10.1371/journal.pone.0161209.g001

induced for 4 h with 0.5 mM IPTG. Under these conditions, both visible and fluorescence microscopy confirmed the presence of IBs located at the poles of the cells (Fig 1E).

Purification of MAβ_{1-40} and MAβ_{1-42}

As Aβ peptides were produced as IBs, the first step of the purification procedure consisted in isolating and purifying IBs. The main challenge of this approach was to succeed in removing proteins and nucleic acids that could be trapped in the IBs or stacked on their surface.

First, the previously reported "soni-removal" method, which consists in multiple sonication and centrifugation cycles, was performed to roughly eliminate nucleic acids and proteins stacked at the IB surface [23]. At this stage, Th-S fluorescence visualization of isolated IBs confirmed that their average size remained unchanged, showing no deterioration due to sonication.

The protocol shown in Fig 2A was then applied. Aβ peptides are soluble at high pH, since their isoelectric point is about 5–6. The IBs were thus first incubated with 50 mM sodium hydroxide, to solubilize MAβ. Upon pH neutralization, a large amount of proteins is removed by precipitation, while MAβ peptides remain in the supernatant (Fig 2B, lanes S1 and P2). The high pH denaturation/neutralization cycle was applied twice to maximize MAβ recovery (Fig 2B, lane S2). Further completion of contaminant elimination was carried out by ultrafiltration of the solubilized peptides followed by concentration, respectively on a 30-kDa and a 3-kDa molecular weight cut-off membranes. As shown on the electrophoresis gel (Fig 2B, lane F), the

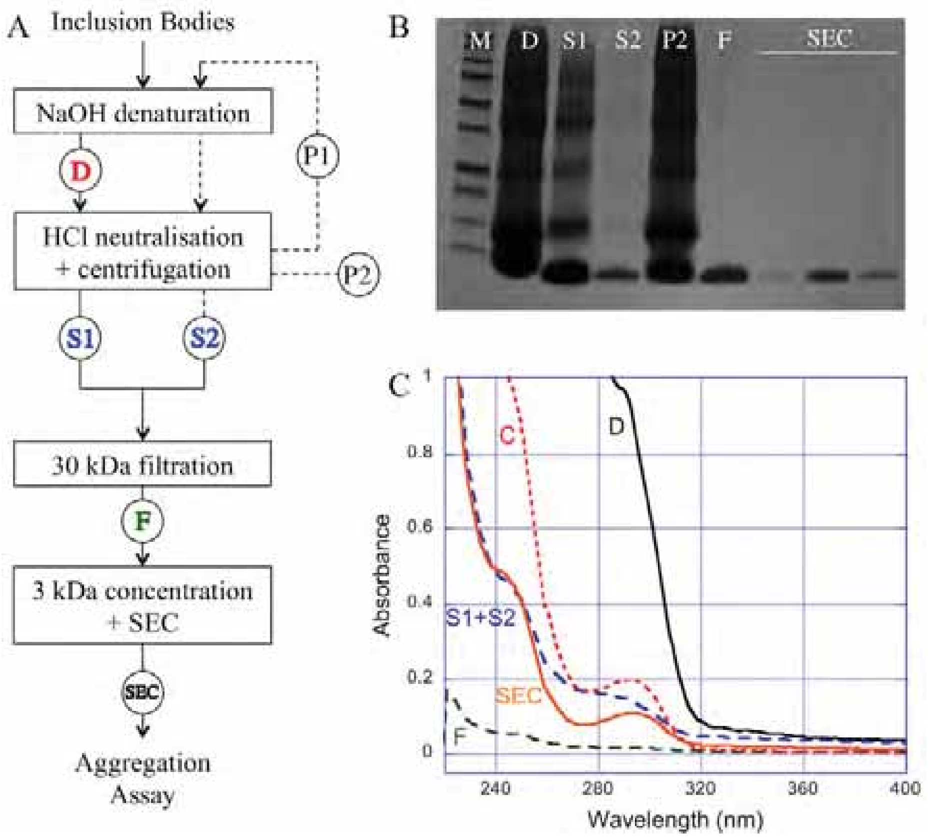

Fig 2. Purification monitoring of MAβ. A. Simplified scheme of the purification procedure. Circled letters correspond to samples collected for either UV/Vis measurements or gel analysis. Supernatant S1 and S2, and pellet P1 and P2 correspond to the supernatant and the precipitate obtained for the two cycles of denaturation/neutralisation. **B.** SDS-PAGE at different steps of purification, compared with 10–250 kDa protein marker (lane M). **C.** UV-Vis spectra at pH 12 after IBs denaturation (D), after denaturation/neutralisation cycles (S1+S2), after 30-kDa ultrafiltration (F), after concentration (C), and after size exclusion chromatography (SEC).

doi:10.1371/journal.pone.0161209.g002

ultrafiltration step allowed getting one single band around 5 kDa, the presence of any protein contaminant being excluded.

In parallel, the MAβ_{1-42} IBs were also solubilized using 8M urea and then passed through a DEAE Sepharose ion-exchange resin to remove NA traces. As seen in Fig 3, this protocol did not allow the elimination of a 13 kDa protein contaminant, regardless of IPTG concentration used for induction. Furthermore, this protein could not be eliminated by ultrafiltration indicating that the urea treatment did not allow breaking the interaction probably existing between the 13 kDa protein and the peptide (Fig 3 lanes 4 and 5). This clearly showed the limitation of the denaturation with urea and emphasizes the interest of the NaOH treatment with to eliminate proteins and nucleic acids.

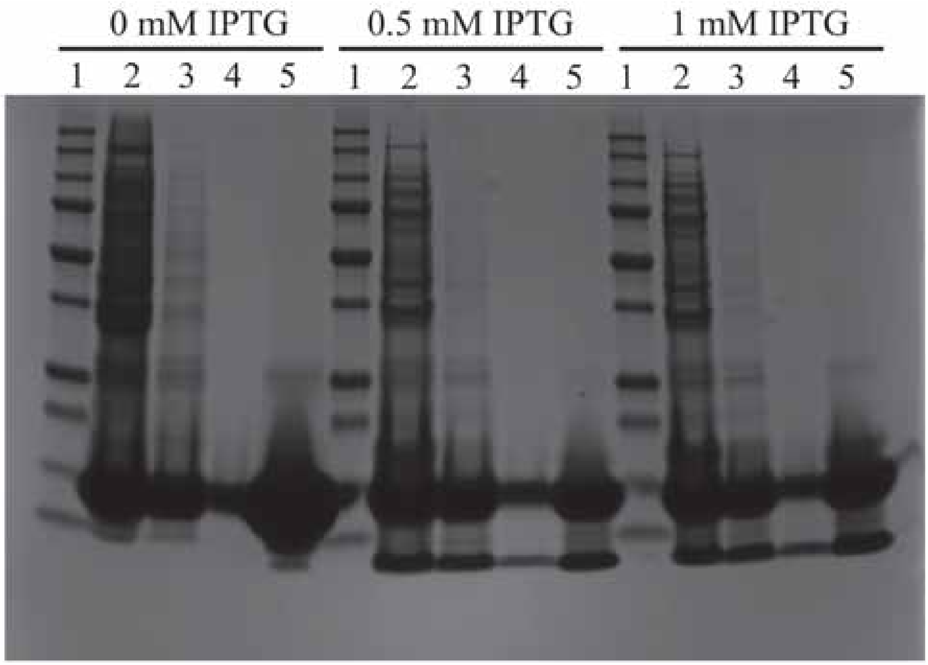

Fig 3. Purification protocol of MAβ_{1-42} IBs dissolved in 8M urea. Lane 1: 10–250 kDa protein marker, lane 2: IBs after urea denaturation, lane 3: after passing through DEAE resin, lane 4: after 30-kDa ultrafiltration, lane 5: after 3-kDa concentration.

doi:10.1371/journal.pone.0161209.g003

At this point, one important issue was the monitoring of the sample purity at the various stages of the purification procedure. The Bradford protein assay was eliminated because it does not give any information on sample purity and only allows the determination of a global protein content. Combination of UV-Vis spectrophotometry with gel electrophoresis was clearly preferred. Indeed, SDS-PAGE permits to visualize the presence of protein contaminants while UV-Vis analyses inform on the predominant presence of either nucleic acids ($\lambda = 260$ nm) or specific amino acids, namely tryptophan ($\lambda = 280$ nm), tyrosine/tyrosinate ($\lambda = 274$ nm/$\lambda =$ 293 nm), phenylalanine ($\lambda = 257$ nm) [26]. Both methods were thus combined to assess the purity level of the peptide samples depending on the purification steps as shown in Fig 2C. After denaturation (Fig 2C, spectrum D), a lot of species are evidenced. The supernatant harvested after neutralization (Fig 2C, spectrum S1+S2), still contain proteins but is already devoid of nucleic acids. After ultrafiltration, the sample was too diluted to give an informative UV spectrum (Fig 2C, spectrum F). Finally, the concentration step yielded a pure sample showing a UV signature with the typical UV band at $\lambda = 293$ nm corresponding to the tyrosinate form (Fig 2C, spectrum C). This typical profile is conserved after size exclusion chromatography, which was performed to isolate only monomeric peptide before aggregation assays (Fig 2C, spectrum SEC). Overall, these analyses confirmed the high level of purity of the peptide preparation.

As the sample was devoid of any protein contaminants, the pH-dependent absorption of Tyr was used to estimate the peptide yield. Absorption spectra of the peptides were thus recorded at pH 12 (showing the absorption band of tyrosinate at 293 nm) and at pH 2 (displaying no tyrosinate band). The precise quantification of the tyrosine content of the sample was performed by subtracting spectra. This enabled the estimation of the peptide yield as being around 4 mg/L of culture, which is in the same range as those previously reported, comprised between 3 and 7 mg/L [13,14,19,27,28].

Characterization of $MA\beta_{1-40}$ and $MA\beta_{1-42}$

To further characterize the peptides, LC-MS and NMR analyses were conducted right after the concentration step on both peptides. $MA\beta_{1-40}$ displays a clean chromatographic trace with a major peak at 10.8 min. The mass spectrum associated to this peak is in good agreement with the expected masses (Fig 4A and 4C). $MA\beta_{1-42}$ chromatogram is less resolved, the main peak being shouldered (Fig 4B and 4D). The masses detected for both the shoulder and the peak are consistent with the calculated masses of $MA\beta_{1-42}$, indicating that oligomeric forms of $MA\beta_{1-42}$ could be present. This is consistent with the high propensity of $A\beta_{1-42}$ to aggregate.

^{1}H NMR spectra of both peptides were then recorded, and compared with commercially available synthetic $A\beta_{1-40}$ (Fig 5). They display the typical signals usually observed for $A\beta_{1-40}$ peptide. In the aromatic region, signals corresponding to the Hδ and Hε of aromatic residues are well defined. As such, Phe 19 and 20 (*ca*. 7.2 ppm and *ca*. 7.3 ppm) and Tyr 10 (*ca*. 7.95 ppm and *ca*. 6.8 ppm) can be distinguished. Slight shifts are observed for His 6, 13 and 14

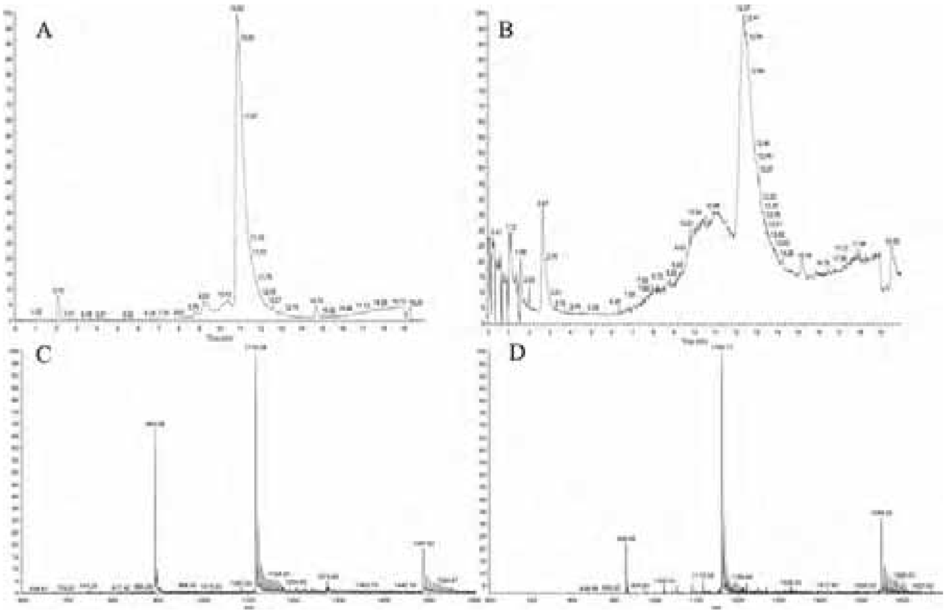

Fig 4. LC-MS analysis of $MA\beta_{1-40}$ and $MA\beta_{1-42}$. A. LC trace of $MA\beta_{1-40}$ monitored by mass detection. **B.** LC trace of $MA\beta_{1-42}$ monitored by mass detection. **C.** MS of $MA\beta_{1-40}$ displaying $[M+5H]^{5+}$, $[M+4H]^{4+}$, and $[M+3H]^{3+}$ peaks (expected values: 892.65, 1115.56, 1487.07). **D.** MS of $MA\beta_{1-42}$ displaying $[M+5H]^{5+}$, $[M+4H]^{4+}$, and $[M+3H]^{3+}$ peaks (expected values: 929.47, 1162.17, 1548.44).

doi:10.1371/journal.pone.0161209.g004

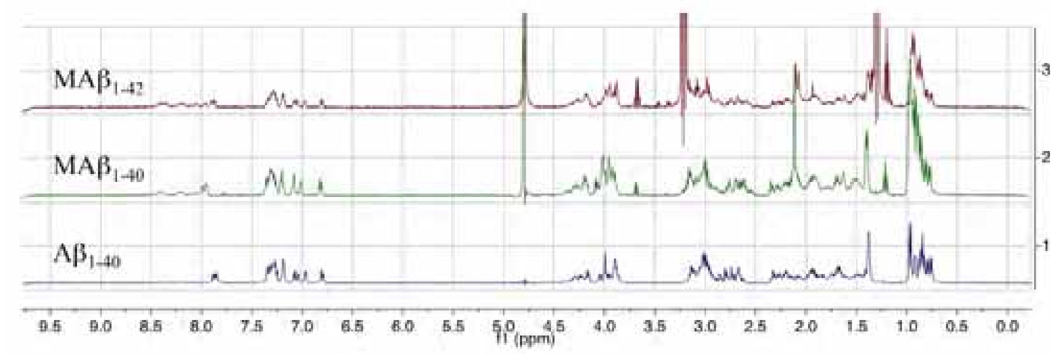

Fig 5. ^{1}H NMR of MAβ$_{1–40}$ and MAβ$_{1–42}$ compared with Aβ$_{1–40}$. Samples of MAβ in water are diluted to 100 μM in 100 mM phosphate buffer pH 7 in D_2O. Synthetic Aβ$_{1–40}$ is dissolved in NaOD and diluted to 100 μM under the same conditions. Signals at 4.75 ppm correspond to H_2O, and signals at 3.25 ppm and 1.25 ppm correspond to traces of ethanol.

doi:10.1371/journal.pone.0161209.g005

(*ca*. 7.8 ppm and *ca*. 7.1 ppm), which can be attributed to pH variations. The absence of signal *ca*. 7.5 ppm confirms the absence of Trp residue in the peptides. Expectedly, signals corresponding to Hα (4.5–3.8 ppm) and Hβ (3.2–2.6 ppm and 2.3–1.5 ppm) are more difficult to attribute in details. In the aliphatic region, signals corresponding to Lys 16 and 28 (1.4 ppm) and to Val and Leu (1.0–0.7 ppm) are observed. Finally, the signal at 3.9 ppm reveals the presence of a methionine residue for the recombinant peptides as expected.

Because most *in vitro* studies on Aβ peptides consist in studying their aggregative properties under various conditions, it was essential to ensure that the auto-assembling properties of the peptides are conserved after this purification process. Prior to this, it was important to remove traces of oligomeric species, to ensure a homogeneous aggregation process. The two peptides were thus submitted to SEC. To assess the apparent molecular weight of targeted peptides, a calibration curve was established using other unstructured peptides. It confirmed that the apparent molecular weight of the two peptides was about 4 kDa (S1 Fig). Fractions corresponding to monomeric peptides were then submitted to Th-T fibrillization assay. In 26 h, both peptides afford a characteristic sigmoidal aggregation curve, with aggregation half-times around 15 h (Fig 6). The MAβ peptides obtained through our purification procedure thus conserved their auto-assembling properties. The same results were obtained with peptide batches from different cultures, showing the high robustness of the purification procedure in terms of reproducibility. This purification protocol could thus be applied for routine lab-scale MAβ production. This also confirms that the presence of a *N*-ter Met residue does not affect the aggregation properties of MAβ peptides as previously reported [16]. Removing Met residue could be beneficial for specific studies such as metal coordination, but does not seem mandatory for classical aggregation assays.

Conclusion

We have here reported a rapid, straightforward and highly reproducible recombinant production and purification of MAβ$_{1–40}$ and MAβ$_{1–42}$. First, we showed that Th-S staining was reliable to monitor IB production during cell growth. Purification monitoring provided evidence that only the combination of UV-Vis spectrophotometry and gel electrophoresis analyses could properly allow the assessment of the peptide purity along the purification process.

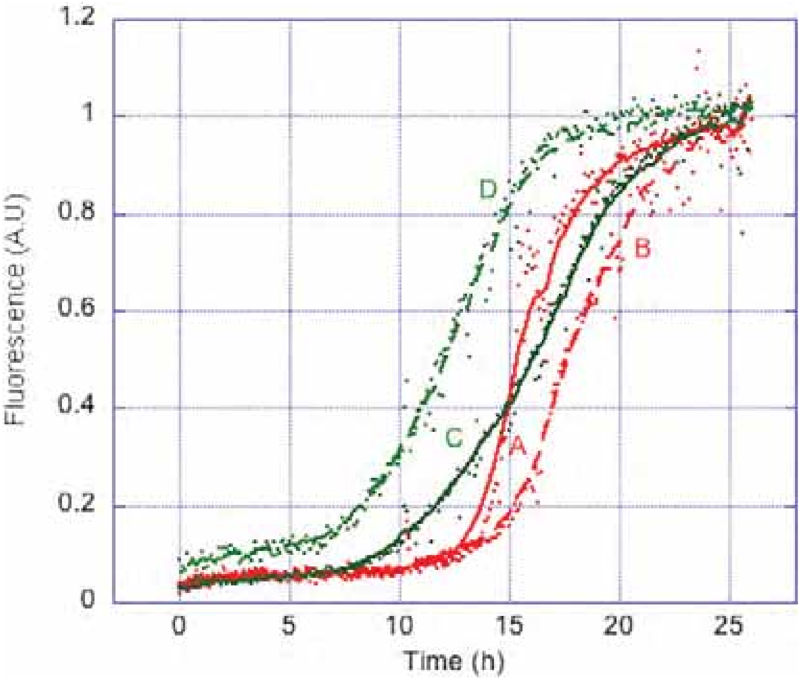

Fig 6. Normalized aggregation curves of MAβ_{1-40} and MAβ_{1-42}. Two different batches of MAβ_{1-40} (A and B) and MAβ_{1-42} (C and D) (20 μM) aggregate in the presence of Th-T (10 μM) in phosphate buffer (50 mM, pH 7). Assay was run at 37°C with gentle shaking. Each experiment was run in triplicates.

doi:10.1371/journal.pone.0161209.g006

In addition, we established that pH treatment of IBs is an efficient way to get rid of most nucleic acid and protein contaminants, contrasting with commonly used chaotropic agents. Additional purification steps consisting in simple ultrafiltrations, providing clean peptide preparations, as revealed by UV-Vis spectrophotometry, SDS-PAGE, LC-MS and ^{1}H NMR. With this protocol, up to 4 mg of peptides are produced within 2 days. In addition, the preparations are suitable for aggregation assays, which were highly reproducible from batch to batch, accounting for a robust purification procedure. Supplementary investigation might now be engaged to remove the *N*-ter methionine residue, in order to obtain the native Aβ, as already proposed by Walsh and co-workers and further improve the peptide yield [21].

Supporting Information

S1 Fig. SEC calibration curve with unstructured peptides. The different peptides were dissolved in NaOH 50 mM to 10 mg/mL and injected on a Superdex 75 10/300 GL. Samples were eluted with NaOH 15 mM at 1 mL/min monitoring at 220 nm and 293 nm. The arrows indicate the elution volume found for synthetic Aβ_{1-40} and the two recombinant MAβ_{1-40} and MAβ_{1-42} peptides.
(TIFF)

Acknowledgments

Christian Bijani is acknowledged for NMR experiments. ICEO platform (GenoToul) is acknowledged for granting access to the Aktä Purifier system.

Author Contributions

Conceptualization: CH PF EG IA MRS.

Funding acquisition: EG CH IA MRS.

Investigation: MH.

Methodology: MH YM RI MRS.

Project administration: EG MRS.

Supervision: EG MRS.

Validation: YM RI MRS.

Visualization: MH.

Writing - original draft: MH.

Writing - review & editing: MH YM RI CH PF EG IA MRS.

References

1. Henderson VW. Alzheimer's disease: review of hormone therapy trials and implications for treatment and prevention after menopause. J Steroid Biochem Mol Biol. 2014; 142: 99–106. doi: 10.1016/j.jsbmb.2013.05.010 PMID: 23727128
2. Delrieu J, Ousset PJ, Voisin T, Vellas B. Amyloid beta peptide immunotherapy in Alzheimer disease. Rev Neurol (Paris). 2014; 170: 739–748. doi: 10.1016/j.neurol.2014.10.003
3. Tong LM, Fong H, Huang Y. Stem cell therapy for Alzheimer's disease and related disorders: current status and future perspectives. Exp Mol Med. 2015; 47: e151. doi: 10.1038/emm.2014.124 PMID: 25766620
4. Schneider LS, Mangialasche F, Andreasen N, Feldman H, Giacobini E, Jones R, et al. Clinical trials and late-stage drug development for Alzheimer's disease: an appraisal from 1984 to 2014. J Intern Med. 2014; 275: 251–283. doi: 10.1111/joim.12191 PMID: 24605808
5. Chang Y-J, Chen Y-R. The coexistence of an equal amount of Alzheimer's amyloid-β 40 and 42 forms structurally stable and toxic oligomers through a distinct pathway. FEBS J. 2014; 281: 2674–2687. doi: 10.1111/febs.12813 PMID: 24720730
6. Hamley IW. The Amyloid Beta Peptide: A Chemist's Perspective. Role in Alzheimer's and Fibrillization. Chem Rev. 2012; 112: 5147–5192. doi: 10.1021/cr3000994 PMID: 22813427
7. Fu Z, Aucoin D, Davis J, Van Nostrand WE, Smith SO. Mechanism of Nucleated Conformational Conversion of Aβ42. Biochemistry (Mosc). 2015; 54: 4197–4207. doi: 10.1021/acs.biochem.5b00467
8. Soto C, Castaño EM, Asok Kumar R, Beavis RC, Frangione B. Fibrillogenesis of synthetic amyloid-β peptides is dependent on their initial secondary structure. Neurosci Lett. 1995; 200: 105–108. doi: 10.1016/0304-3940(95)12089-M PMID: 8614555
9. Zagorski MG, Yang J, Shao H, Ma K, Zeng H, Hong A. [13] Methodological and chemical factors affecting amyloid β peptide amyloidogenicity. Methods in Enzymology. Elsevier; 1999. pp. 189–204. Available: http://linkinghub.elsevier.com/retrieve/pii/S0076687999090151
10. Finder VH, Vodopivec I, Nitsch RM, Glockshuber R. The Recombinant Amyloid-β Peptide Aβ1–42 Aggregates Faster and Is More Neurotoxic than Synthetic Aβ1–42. J Mol Biol. 2010; 396: 9–18. doi: 10.1016/j.jmb.2009.12.016 PMID: 20026079
11. Shen M, Wang Q, Mu X, Xu H, Yan W. Expression, purification and characterization of recombinant human β-amyloid 1–42 in Pichia pastoris. Protein Expr Purif. 2009; 63: 84–88. doi: 10.1016/j.pep.2008.09.015 PMID: 18950715

12. Bockhorn JJ, Lazar KL, Gasser AJ, Luther LM, Qahwash IM, Chopra N, et al. Novel semisynthetic method for generating full length β-amyloid peptides. Biopolymers. 2010; 94: 511–520. doi: 10.1002/bip.21391 PMID: 20593467

13. Lee EK, Hwang JH, Shin DY, Kim DI, Yoo YJ. Production of recombinant amyloid-β peptide 42 as an ubiquitin extension. Protein Expr Purif. 2005; 40: 183–189. doi: 10.1016/j.pep.2004.12.014 PMID: 15721787

14. Garai K, Crick SL, Mustafi SM, Frieden C. Expression and purification of amyloid-β peptides from Escherichia coli. Protein Expr Purif. 2009; 66: 107–112. doi: 10.1016/j.pep.2009.02.009 PMID: 19233290

15. Alies B, LaPenna G, Sayen S, Guillon E, Hureau C, Faller P. Insights into the Mechanisms of Amyloid Formation of Zn ^{II} -Ab11-28: pH-Dependent Zinc Coordination and Overall Charge as Key Parameters for Kinetics and the Structure of Zn ^{II} -Ab11-28 Aggregates. Inorg Chem. 2012; 51: 7897–7902. doi: 10.1021/ic300972j PMID: 22765389

16. Szczepankiewicz O, Linse B, Meisl G, Thulin E, Frohm B, Sala Frigerio C, et al. N-Terminal Extensions Retard Aβ42 Fibril Formation but Allow Cross-Seeding and Coaggregation with Aβ42. J Am Chem Soc. 2015; 137: 14673–14685. doi: 10.1021/jacs.5b07849 PMID: 26535489

17. Liao Y-H, Chen Y-R. A novel method for expression and purification of authentic amyloid-β with and without 15N labels. Protein Expr Purif. 2015; 113: 63–71. doi: 10.1016/j.pep.2015.05.002 PMID: 25969353

18. Wiesehan K, Funke SA, Fries M, Willbold D. Purification of recombinantly expressed and cytotoxic human amyloid-beta peptide 1–42. J Chromatogr B. 2007; 856: 229–233. doi: 10.1016/j.jchromb.2007.06.003

19. Sharma SC, Armand T, Ball KA, Chen A, Pelton JG, Wemmer DE, et al. A facile method for expression and purification of 15N isotope-labeled human Alzheimer's β-amyloid peptides from E. coli for NMR-based structural analysis. Protein Expr Purif. 2015; 116: 82–89. doi: 10.1016/j.pep.2015.07.012 PMID: 26231074

20. Chhetri G, Pandey T, Chinta R, Kumar A, Tripathi T. An improved method for high-level soluble expression and purification of recombinant amyloid-beta peptide for in vitro studies. Protein Expr Purif. 2015; 114: 71–76. doi: 10.1016/j.pep.2015.05.015 PMID: 26118700

21. Walsh DM, Thulin E, Minogue AM, Gustavsson N, Pang E, Teplow DB, et al. A facile method for expression and purification of the Alzheimer's disease-associated amyloid β-peptide: Expression and purification of the amyloid β-peptide. FEBS J. 2009; 276: 1266–1281. doi: 10.1111/j.1742-4658.2008.06862.x PMID: 19175671

22. Espargaró A, Sabate R, Ventura S. Thioflavin-S staining coupled to flow cytometry. A screening tool to detect in vivo protein aggregation. Mol Biosyst. 2012; 8: 2839. doi: 10.1039/c2mb25214g PMID: 22868714

23. Neerathilingam M, Mysore S, Gandham SHA. Soni-removal of nucleic acids from inclusion bodies. Biochem Biophys Res Commun. 2014; 448: 45–49. doi: 10.1016/j.bbrc.2014.04.049 PMID: 24747565

24. Villar-Piqué A, Espargaró A, Sabaté R, de Groot NS, Ventura S. Using bacterial inclusion bodies to screen for amyloid aggregation inhibitors. Microb Cell Factories. 2012; 11: 55. doi: 10.1186/1475-2859-11-55

25. Allen SP, Polazzi JO, Gierse JK, Easton AM. Two novel heat shock genes encoding proteins produced in response to heterologous protein expression in Escherichia coli. J Bacteriol. 1992; 174: 6938–6947. PMID: 1356969

26. Beaven GH, Holiday ER. Ultraviolet Absorption Spectra of Proteins and Amino Acids. In: Anson KB M. L. and JTE, editor. Advances in Protein Chemistry. Academic Press; 1952. pp. 319–386. Available: http://www.sciencedirect.com/science/article/pii/S0065323308600224 PMID: 14933256

27. Long F, Cho W, Ishii Y. Expression and purification of 15N- and 13C-isotope labeled 40-residue human Alzheimer's β-amyloid peptide for NMR-based structural analysis. Protein Expr Purif. 2011; 79: 16–24. doi: 10.1016/j.pep.2011.05.012 PMID: 21640828

28. Kim E-K, Moon JC, Lee JM, Jeong MS, Oh C, Ahn S-M, et al. Large-scale production of soluble recombinant amyloid-β peptide 1–42 using cold-inducible expression system. Protein Expr Purif. 2012; 86: 53–57. doi: 10.1016/j.pep.2012.08.021 PMID: 22982229

Résumé en français

Introduction

C’est annoncé, le vingt-et-unième siècle sera celui de l’écologie. Dans le domaine de la chimie, cela se traduit par la mise en place des principes de la Chimie Verte, ayant pour but de rendre les procédés chimiques moins destructeurs pour la Planète. Cela inclut notamment l’utilisation de catalyseurs, dont l’utilisation en faibles quantités permet de convertir efficacement de grandes quantités de substrat. Cependant, même utilisés à l’état de traces, les métaux lourds et les ligands issus de nombreuses étapes de synthèse employés dans les catalyseurs sont à eux seuls une source de pollution. Les efforts de recherche sont donc dirigés vers l’élaboration de catalyseurs plus éco-compatibles.

Pour cela, la Recherche s’est intéressée aux catalyseurs existant dans la nature : les enzymes. Cela a inspiré différentes approches, qui incluent le développement de complexes mimant les sites actifs d’enzymes, la modification d’enzymes existantes pour modifier leur réactivité, et la création d’enzymes artificielles. Ce dernier domaine consiste à combiner l’efficacité des enzymes à variété et la versatilité de catalyseurs chimiques. L’utilisation de catalyseurs chimiques donne accès à une large gamme de réactivités et de substrats, tandis que la présence de la biomolécule confère à ces systèmes une accélération de la réaction, ainsi qu’une sélectivité et une spécificité.

Dans ce contexte, nous nous sommes intéressés à l’élaboration de systèmes hybrides basés sur les fibres amyloïdes. Ces agrégats de protéines présentent des propriétés uniques de rigidité, de solidité, et de résistance à la chaleur et aux solvants, qui en font de bons candidats pour une utilisation en catalyse. De par leur caractère insoluble, les catalyseurs formés seraient également recyclables.

Ce manuscrit présente les résultats obtenus pour l’élaboration de nouveaux catalyseurs bio-inorganiques préparés par incorporation de complexes métalliques dans les fibres de peptides β-amyloïdes. Dans ce contexte, un nouveau protocole d’expression et de purification des peptides β-amyloïdes dans *Escherichia coli* a été mis en place, permettant l’accès rapide à des échantillons fiables de peptides (voir Chapter V.II).

Une seconde partie du travail a consisté à développer une série de ligands capables de s’insérer de façon non-covalente dans les fibres amyloïdes. Inspirés par les différentes molécules intercalantes décrites dans la littérature, nous avons synthétisé une série de cinq ligands portant différents substituants. Les complexes métalliques correspondants ont été préparés, et caractérisés par différentes techniques (RMN, RPE, voltamétrie cyclique, Rayons X) (voir Chapter V.III).

L’interaction de ces différents complexes avec les fibres amyloïdes a ensuite été testée. Une étude spectrophotométrique a permis de discriminer les complexes capables de s’insérer dans les fibres. Des études ont ensuite été réalisées concernant la nature du site d’interaction, ainsi que le motif d’interaction sur les complexes. Ces premiers résultats ont été supportés par des études de Docking (voir Chapter V.IV).

Enfin, des études préliminaires de catalyse ont permis d’ouvrir des pistes d’optimisation de nos systèmes hybrides, incluant des variations sur les complexes et sur le peptide (voir Chapter V.V).

I. Contexte du projet

I.1. Contexte du projet : les metalloenzymes artificielles

Une alternative aux catalyseurs chimiques consiste à élaborer des enzymes artificielles. Différentes stratégies d’élaboration ont été développées :

- **Remplacer l’ion métallique d’une enzyme** : le remplacement de l’ion métallique peut permettre de modifier sa réactivité. Cela a été réalisé avec succès avec la carboxypeptidase A [26] et l’anhydrase carbonique [27,28].
- **Réaliser des mutations sur le site actif d’une enzyme** : une modification des résidus du site actif d’une enzyme peut permettre de modifier la gamme de substrats, voire de modifier sa réactivité. De nombreuses études de ce type ont été réalisées avec le cytochrome P450 [31,32,34,35].
- **Elaborer une protéine De Novo** : les progrès de la biologie moléculaire permettent de construire de nouveaux systèmes protéiques capables de coordiner des ions métalliques de manière parfaitement contrôlée. La réactivité de ces systèmes est elle aussi modulable [42,44].
- **Insérer un complexe de coordination dans une biomolécule** : l’objectif est alors d’ajouter à un catalyseur préexistant un environnement protéique capable de lui conférer des effets de sphère externe (accélération, sélectivité, spécificité...). On espère alors combiner l’efficacité des enzymes avec la modularité des catalyseurs chimiques. Cette stratégie a été utilisée avec de l’ADN [47], des protéines [73], des peptides [93] et des anticorps [89]. Selon les cas, il est possible de greffer le complexe de façon covalente, ou de tirer parti des interactions non-covalentes entre la biomolécule et le complexe. L’utilisation de cofacteurs naturels a également été proposée.

Cette dernière approche a été sélectionnée pour l’élaboration de nos catalyseurs. Parmi les différentes biomolécules susceptibles d’accueillir des complexes métalliques, notre intérêt s’est porté sur les fibres amyloïdes.

I.2. Les fibres amyloïdes comme bio-nano-matériaux

La définition des protéines amyloïdes est avant tout structurale: il s’agit de polypeptides qui, en plus de leur repliement natif, peuvent adopter un second repliement, très stable et structuré en un assemblage de feuillets β.

Les protéines amyloïdes ont initialement été découvertes dans le cadre de maladies humaines : la maladie d’Alzheimer [138], le diabète de type II [102], ou les maladies à Prions [104] impliquent tous la formation d’agrégats amyloïdes. Mais des structures amyloïdes ont depuis été découvertes chez d’autres organismes, jouant un rôle non plus délétère, mais structural [242,243].

Ces protéines sont très différentes en termes de taille et de séquence, mais partagent certaines caractéristiques : toutes sont capables de s’auto-assembler sous la forme de fibres de 6-12 nm de diamètres et de quelques μm de long, avec une structure cross-β caractéristique. Ces fibres sont très rigides et robustes, résistant à la chaleur et aux agents dénaturants.

Du fait de ces propriétés uniques, les fibres amyloïdes ont été proposées pour différentes applications, les utilisant comme support de greffage [121], comme moule pour la formation de nanoparticules [117–119] ou pour la formation d’hydrogels [122].

I.3. Description moléculaire des fibres amyloïdes

I.3.a. Peptide β-amyloïde

Le peptide β-amyloïde existe dans le cerveau sous deux formes majoritaires, de 40 ($A\beta_{1-40}$) et 42 ($A\beta_{1-42}$) acides aminés, respectivement. Leur séquence est constituée d’une partie dynamique et peu structurée en N-terminal (résidus 1 à 16), capable de coordiner les métaux [123,129,130]. Au contraire, la partie C-terminale est majoritairement constituée de résidus hydrophobes, qui sont à l’origine de la formation de la structure « cross-β » caractéristique des amyloïdes. Les résidus 17 à 20 semblent particulièrement importants.

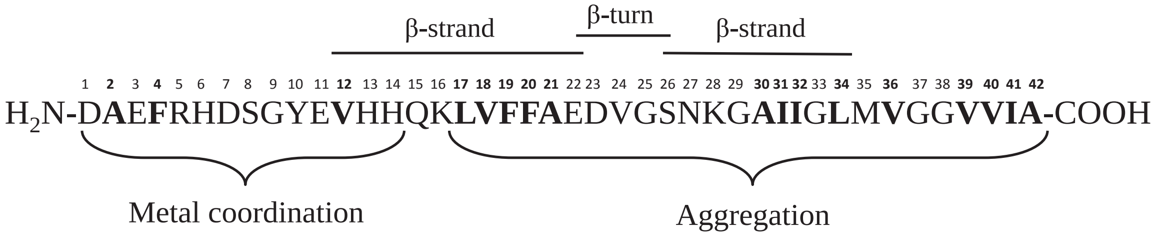

***Figure 58: Séquence de $A\beta_{1-42}$ et structure secondaire correspondante.** Les résidus hydrophobes apparaissent en gras.*

Avec leurs nombreux résidus hydrophobes, les peptides β-amyloïdes sont faiblement solubles dans l’eau et s’auto-assemblent rapidement. Il est donc courant de les solubiliser à des pH extrêmes.

Les peptides Aβ contiennent un résidu Tyr, qui est utilisé pour leur quantification par spectrophotométrie UV-Visible ($\varepsilon = 2400$ L.mol^{-1}.cm^{-1} à 293 nm à pH >12) [128]. Il confère également au peptide de faibles propriétés de fluorescence ($\phi = 0{,}14$ dans l'eau à 23 °C).

I.3.b. Fibre β-amyloïde

A température et pH physiologiques, les peptides amyloïdes s'auto-assemblent rapidement pour former les fibres amyloïdes. Bien qu'encore mal compris, le processus d'agrégation consiste généralement en trois phases : une phase de latence, suivi d'une phase d'élongation et d'un plateau (Schéma 39). Parmi les différentes méthodes existant pour suivre cette agrégation *in vitro*, la plus commune est de suivre la fluorescence de la Thioflavine-T (Th-T). Cette molécule, peu fluorescente en solution, subit une augmentation brutale de sa fluorescence lorsqu'elle s'insère dans les structures amyloïdes. Effectuer un suivi de la fluorescence de la Th-T permet donc de mettre en évidence la formation de fibres.

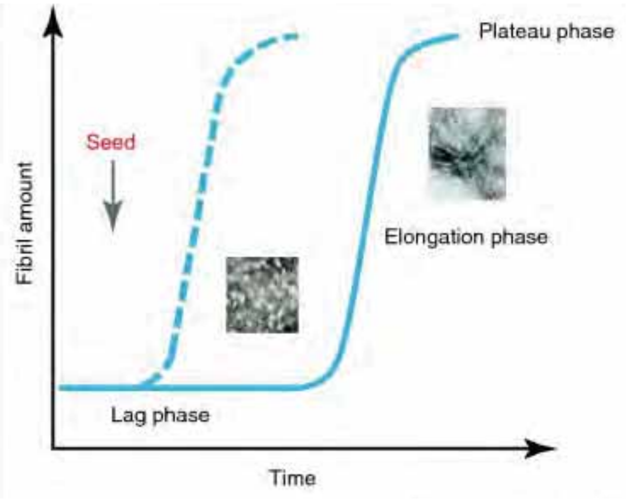

Schéma 39: Courbe d'agrégation typique des amyloïdes.

Les fibres amyloïdes étant insolubles et non cristallines, peu de techniques physico-chimiques permettent de les caractériser. La RMN du solide a permis d'obtenir quelques structures [141,143–145], mais nécessite trop d'échantillon pour être utilisée de façon routinière. Les microscopies AFM et TEM sont régulièrement utilisées, mais ne permettent d'avoir qu'une idée globale de la morphologie des fibres.

II. Production recombinante des peptides β-amyloïdes

II.1. Différentes méthodes de production des peptides β-amyloïdes

Le nombre d'études portant sur la maladie d'Alzheimer ayant considérablement augmenté ces dernières années, la question de la production de peptide β-amyloïde destiné aux études *in vitro* est devenu un problème clé.

La synthèse de peptides sur phase solide est souvent utilisée, mais reste compliquée dans le cas de peptide hydrophobes, et la purification et le stockage sont encore mal gérés [136]. Une différence de comportement a également été notée entre les peptides de synthèse et les peptides recombinants [150]. Pour cela, les peptides issus de la production recombinante sont parfois considérés comme de meilleurs modèles, les peptides ne subissant aucun traitement chimique. Cependant d'autres inconvénients apparaissent parfois, comme l'usage d'étiquettes facilitant la purification, mais qui ajoutent des acides aminés supplémentaires à la séquence native des peptides [154,155,158,159].

Dans le cadre de ce projet, nous avons réalisé trois constructions plasmidiques, les séquences correspondances apparaissant en Figure 59.

Construction 1: His-tagged A$\beta_{1\text{-}42}$

MGSS**HHHHHH**SSG**LVPR**^{T}**GS**HM**DAEFRHDSGYEVHHQKLVFFAEDVGSNKGAIIGLMVGGVVIA**

Construction 2: MA$\beta_{1\text{-}42}$

M**DAEFRHDSGYEVHHQKLVFFAEDVGSNKGAIIGLMVGGVVIA**

Construction 3: MA$\beta_{1\text{-}40}$

M**DAEFRHDSGYEVHHQKLVFFAEDVGSNKGAIIGLMVGGVV**

Figure 59: Séquences peptidiques ciblées. La séquence native de Aβ apparait en noir (*A$\beta_{1\text{-}42}$ pour les constructions 1 et 2, A$\beta_{1\text{-}40}$ pour la construction 3). Le tag 6xHis apparait en bleu, la séquence de reconnaissance de la Thrombine apparait en vert, les acides aminés supplémentaires apparaissent en gris. ^{T} indique le site de clivage à la Thrombine.*

II.2. Production du 6xHis-Thromb-A$\beta_{1\text{-}42}$

Dans un premier temps, nous nous sommes intéressés à la production de peptide A$\beta_{1\text{-}42}$ portant un tag 6xHis séparé du peptide par un site de clivage à la Thrombine. Cette construction présente l'avantage de permettre une purification du peptide par chromatographie d'affinité.

Des productions ont été réalisées dans *E.coli*, et le peptide a été purifié sur résine TALON. Cependant, les tentatives de clivage ont été incomplètes, nécéssitant d'autres étapes de purification.

Cette stratégie ne nous a donc pas semblé adaptée, et nous nous sommes concentrés sur la production de peptides dépourvus d'étiquettes.

II.3. Production des peptides Met-β-amyloïde 1-40 et 1-42

II.3.a. Observations préliminaires

Lors des premières expériences d'expression des peptides MAβ, nous nous sommes aperçu que la totalité des peptides exprimés était contenue dans la fraction insoluble. Après observation au microscope, il est apparu que ces peptides formaient des corps d'inclusions (ou inclusion bodies, IB) dans les bactéries. Nous avons souhaité tirer parti de cette caractéristique, tentant d'isoler ces IB pour les purifier par la suite.

II.3.b. Optimisation des paramètres d'expression

Une première étape a consisté à optimiser les paramètres d'expression des peptides dans *E. coli*. Pour cela, nous nous sommes servis de la capacité de fluorescence de la Thioflavine-S (Th-S) lorsqu'elle est insérée dans les IB bactériens (Figure 60) [163,165]. Différentes cultures de *E.coli* exprimant MAβ$_{1-42}$ ont donc été incubées à des températures différentes, pendant des durées différentes, et ont été induites avec différentes quantités d'inducteur.

Cela a permis d'établir les conditions optimales comme étant une expression à 37 °C pendant 4 h en induisant avec 0,5 mM d'inducteur.

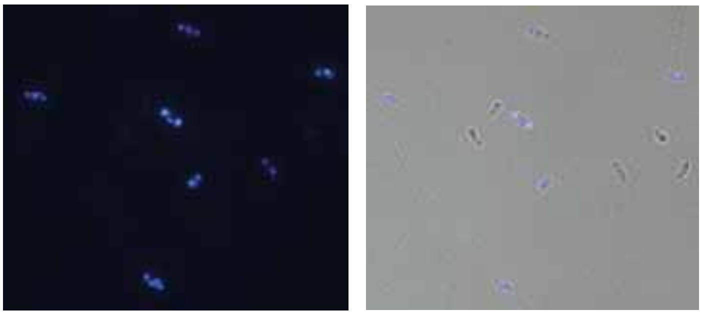

Figure 60: Visualisation des corps d'inclusion bactériens formés par MAβ$_{1-42}$. A. *Cellules E. coli exprimant MAβ$_{1-42}$ et incubés dans la Th-S observés par microscopie de fluorescence.* ***B.*** *Superposition des images de microscopie visible et de fluorescence.* ***Conditions expérimentales****: λ_{exc} = 340-380 nm, dichroic = 400, λ_{em} = 425 nm, grossissement 63x.*

II.3.c. Purification

Une fois les conditions optimales d'expression trouvées, nous nous sommes intéressés à la purification des peptides MAβ. Les corps d'inclusions ont été isolés des débris bactériens suivant une procédure préalablement décrite [162]. Cependant à la place de l'habituelle solubilisation des IB dans des solutions concentrées d'agents dénaturants (urée, chlorure de guanidinium…), nous avons proposé de les solubiliser en milieu basique. Une étape de neutralisation permet ensuite de faire précipiter les protéines contaminantes, alors que le peptide reste en solution. Afin d'optimiser les rendements, cette étape de solubilisation/neutralisation est réalisée deux fois. Une étape de filtration sur membrane 30 kDa, suivie d'une étape de concentration sur membrane 3 kDa permettent d'obtenir un échantillon pur de peptide. Une représentation schématique de ce protocole apparaît en Figure 61.A.

Afin d'évaluer le degré de pureté de nos échantillons, nous proposons l'utilisation combinée de la spectrophotométrie UV-Vis et des gels SDS-PAGE. En effet, les peptides cibles ne contenant pas de Trp, la présence d'une bande à 280 nm sur le spectre UV-Vis est un bon témoin de la présence d'un contaminant protéique. De même, une bande à 260 nm serait significative de la présence d'acides nucléiques. Dans notre cas, le maximum d'absorbance se situe à 293 nm à pH 12, ce qui correspond au tyrosinate du peptide (Figure 61.C) [128]. Le gel SDS-PAGE confirme également l'absence de protéine contaminante à la fin du processus de purification (Figure 61.B).

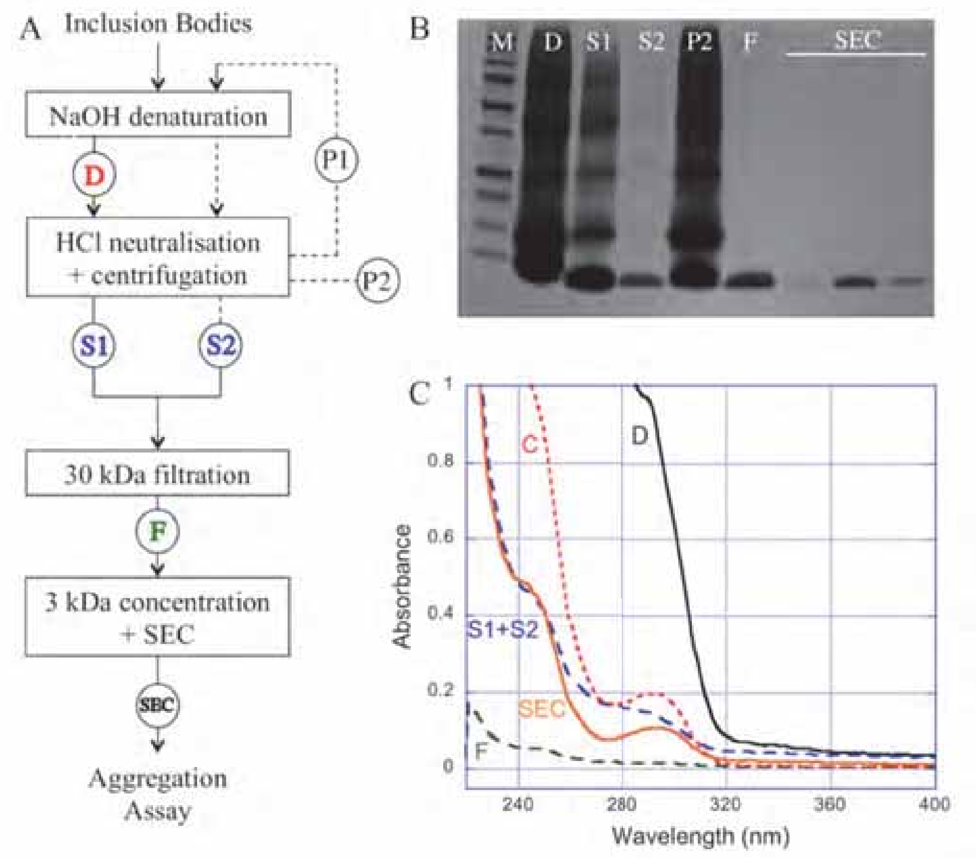

Figure 61: Suivi de purification de MAβ. A. *Schéma simplifié du protocole de purification. Les lettres cerclées correspondent aux échantillons prélevés pour les analyses UV-Vis ou sur gel. Les surnageants S1 et S2, et les culots P1 et P2 correspondent aux surnageants et aux culots obtenus pour les deux cycles de dénaturation/neutralisation.* ***B.*** *SDS-PAGE à différentes étapes de purification, comparé au marqueur 10-250 kDa (noté M).* ***C****. Spectre UV-Vis à pH 12 après dénaturation des IB (D), après les cycles de dénaturation/neutralisation (S1+S2), après ultrafiltration à 30-kDa (F), après concentration (C), et après chromatographie d'exclusion stérique (SEC).*

II.3.d. Caractérisation

Les deux peptides MA$\beta_{1\text{-}40}$ et MA$\beta_{1\text{-}42}$ ont été caractérisés par différentes techniques:

- **LC-MS**: Les deux peptides ont été soumis à l'analyse LC-MS en milieu acide, montrant des temps de rétention similaires. Le spectre de masse correspondant montre les peptides protonnés trois, quatre et cinq fois, comme observé pour le peptide A$\beta_{1\text{-}40}$ synthétique.
- **RMN**: Les spectres RMN ^{1}H des deux peptides ont été enregistrés, montrant des signatures similaires à celle du peptide A$\beta_{1\text{-}40}$ synthétique.
- **Agrégation**: Les deux peptides ont été soumis à une expérience d'agrégation suivie à la Thioflavine-T. A 20 et 50 µM, les deux peptides agrègent en suivant une courbe sigmoïdale typique des peptides amyloïdes.

Tous ces résultats confirment la fiabilité et la robustesse de ce nouveau protocole de purification. Les rendements obtenus sont de 4 mg par litre de culture, ce qui correspond aux résultats décrits dans la littérature. Ce protocole présente l'avantage de ne comprendre aucune étape chromatographique, et peut être réalisé en deux jours.

III. Elaboration des complexes de coordination

III.1. Elaboration des ligands

Différents points ont été pris en compte lors de l'élaboration des ligands:

- Leur facilité de synthèse, afin de pouvoir obtenir une série d'analogues,
- Leur coordination à différents ions métalliques,
- Leur capacité à faire des liaisons non-covalentes, afin de pouvoir s'insérer dans les fibres amyloïdes,
- Leur utilisation possible en catalyse.

Lorsque l'on observe les structures des molécules reportées dans la littérature pour leur bonne intercalation dans les fibres, on remarque qu'elles comportent de nombreux (hétéro)cycles aromatiques, ainsi que des hétéroatomes capables de former des liaisons H.

Parmi les différents ligands accessibles possédant ces caractéristiques, notre intérêt s'est porté sur les analogues de terpyridine. Ces ligands ont la propriété de coordiner différents ions métalliques [184,187,206], et ont été de nombreuses fois utilisés en catalyse [190,207,233]. Leur synthèse se fait en une étape à partir d'un aldéhyde et de 2-acetyl pyridine en milieu basique (Schéma 40) [192].

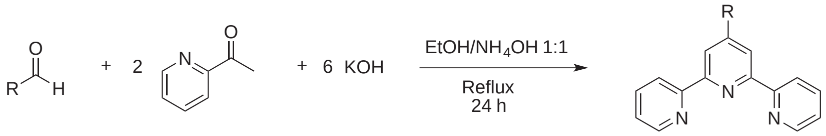

Schéma 40: Synthèse de la terpyridine suivant la méthode de Kröhnke.

Afin d’augmenter la surface aromatique, les ligands ont été fonctionnalisés avec un groupement phényl sur la pyridine centrale, portant différents substituants en position para. Les différents ligands synthétisés apparaissent en Schéma 41. Les ligands commerciaux terpyridine, bipyridine, phénanthroline et salophen ont été ajoutés à cette série.

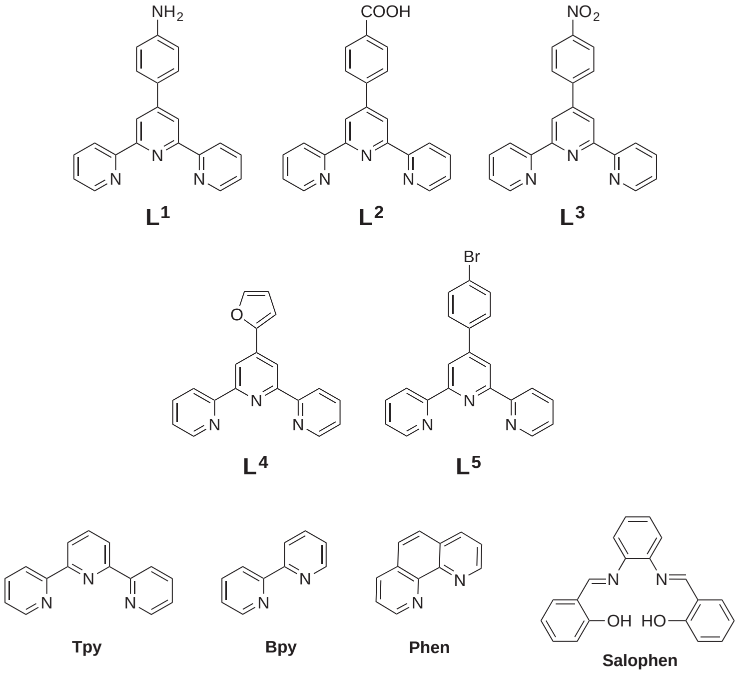

Schéma 41: Ligands utilisés dans cette étude. *Les ligands L^1 à L^5 ont été synthétisés, alors que Tpy, Bpy, Phen et Salophen sont commerciaux.*

III.2. Synthèse des complexes de coordination

Une fois les différents ligands synthétisés, les complexes de Cu(II), Fe(II) et Ru(II) correspondants ont été préparés (Schéma 42).

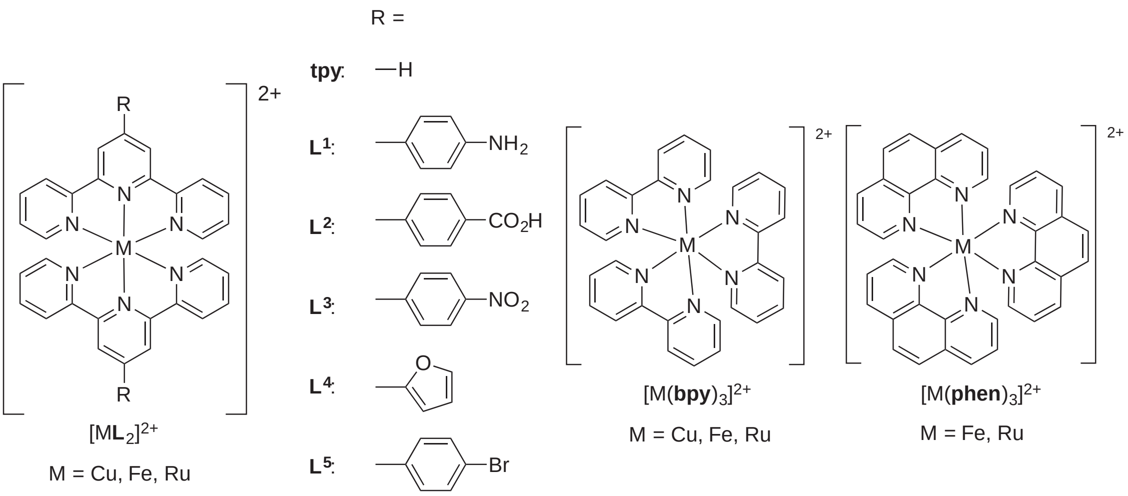

Schéma 42: Complexes métalliques synthétisés.

Les synthèses ont été réalisées au reflux du méthanol, à partir de sels de Cu(II), Fe(III) ou Ru(III), respectivement. Les complexes ont ensuite été isolés par précipitation suite à un échange d'anion avec l'hexafluorophosphate de sodium.

Les différents complexes ont ensuite été caractérisés à l'aide de différentes techniques :

- **La diffraction des rayons X** a permis de résoudre la structure de certains complexes. Cela a confirmé l'orthogonalité des terpyridine autour du cation métallique, ainsi que la légère rotation du groupement phényl.
- **La RMN** a permis de mettre en évidence la formation des complexes de Fe(II) et Ru(II), celle-ci se traduit par le déblindage global des signaux. La comparaison des différents complexes a montré que la nature du groupement fonctionnel sur le phényl n'avait que très peu d'influence sur les propriétés électroniques du complexe.
- **La RPE** des complexes de cuivre a confirmé une sphère de coordination de type 6N. Un effet Jahn-Teller dynamique a également été observé, caractéristique des complexes de terpyridine.
- **La voltamétrie cyclique** nous a permis d'obtenir les potentiels d'oxydation et de réduction des complexes de cuivre et de ruthénium, apportant confirmation que la fonctionnalisation du ligand n'interférait pas avec les propriétés électroniques du centre métallique.
- **Les spectres UV-Visible et de fluorescence** des différents complexes ont été enregistrés. Seuls les complexes de Ru(II) démontrent des propriétés de fluorescence.

Les différents complexes ont ensuite été étudiés pour leur interaction avec les fibres amyloïdes.

IV. Etude de l’interaction complexes de coordination-fibres amyloïdes

IV.1. Preuves expérimentales de l’interaction

IV.1.a. Validation de l’interaction

Afin de déterminer si certains des complexes démontraient une interaction avec les fibres amyloïdes, ceux-ci ont été mis en présence de peptide A$\beta_{1\text{-}40}$ monomérique que l’on a fait agréger. La présence de certains composés se traduit par une modification significative de la cinétique d’agrégation du peptide (Figure 62.A). En fin d’agrégation, les échantillons de fibres sont collectés et centrifugés. Certains culots de fibres apparaissent très colorés, témoignant d’une incorporation des complexes métalliques, alors que d’autres sont quasiment incolores (Figure 62.B).

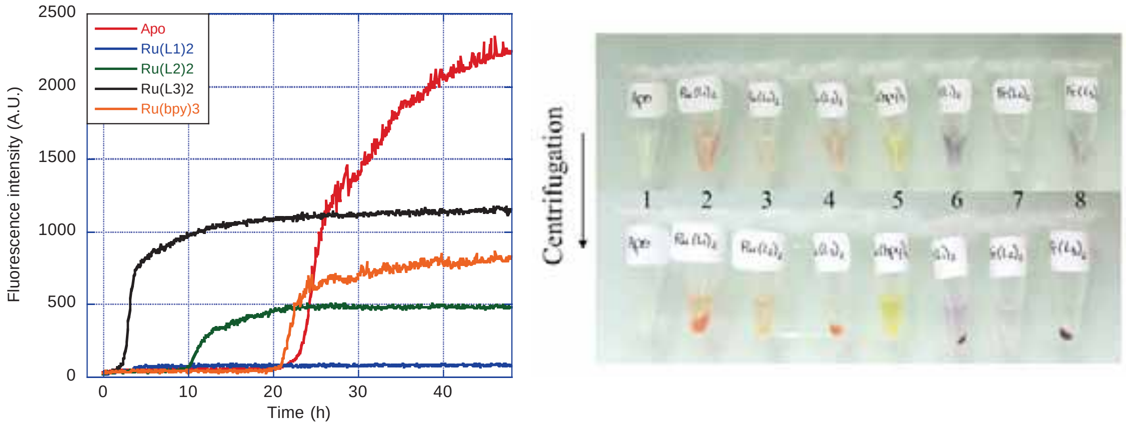

Figure 62: Validation de l’interaction entre les fibres de A$\beta_{1\text{-}40}$ et les complexes métalliques. A. *Effet des complexes métalliques sur la cinétique d’agrégation de A$\beta_{1\text{-}40}$. L’agrégation a été réalisée avec A$\beta_{1\text{-}40}$ seul (rouge) ou en présence de Ru(L^1)$_2$ (bleu), Ru(L^2)$_2$ (vert), Ru(L^3)$_2$ (noir), and Ru(bpy)$_3$ (orange)* ***Conditions:*** *[A$\beta_{1\text{-}40}$] = 50 µM, [Th-T] = 10 µM, [PB] = 50 mM, [complexe] = 50 µM, pH = 7, ACN 5%. Chaque courbe est la moyenne de triplicats.* ***B****. Photographie du contenu des puits en fin d’agrégation avant et après centrifugation.*

Un dosage soigneux des surnageants par spectrophotométrie UV-Visible a permis de quantifier la quantité de complexes insérée dans les fibres. Les résultats montrent une incorporation importante pour les ligands phényl-terpyridine, à l’exception du ligand **L^2**. Cela peut s’expliquer par une répulsion entre les peptides et les carboxylates présents sur les ligands. Les complexes de **bpy**, **tpy** et **phen** semblent également ne pas interagir, probablement du fait de leur surface aromatique trop limitée.

Table 27: Quantités de complexes insérées en fin d’agrégation du peptide A$\beta_{1\text{-}40}$.

Complexe	**% complexe inséré**
Ru(**bpy**)$_3$	1
Ru(**phen**)$_3$	2

Ru(**tpy**)$_2$	3
Ru(**L**^{1})$_2$	**55**
Ru(**L**^{2})$_2$	0
Ru(**L**^{3})$_2$	**100**
Fe(**bpy**)$_3$	10
Fe(**L**^{1})$_2$	**81**
Fe(**L**^{2})$_2$	0
Fe(**L**^{3})$_2$	**99**
Fe(**L**^{4})$_2$	**67**
Fe(**L**^{5})$_2$	**93**

Les caractéristiques spectrophotométriques des complexes sont également modifiées lorsqu'ils sont insérés dans les fibres. La bande d'absorbance de Ru(**L**^{1})$_2$ est légèrement décalée vers les hautes longueurs d'ondes (Figure 63.A), alors que sa fluorescence est amplifiée (Figure 63.B). Cela est cohérent avec un passage d'un milieu aqueux à un milieu hydrophobe [217].

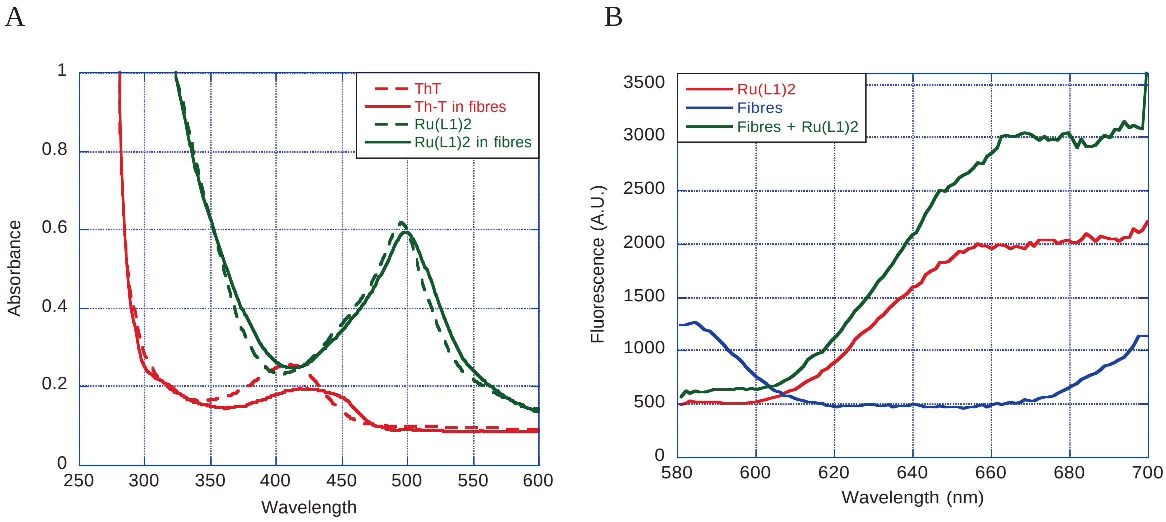

Figure 63: Effet de l'insertion dans les fibres sur les propriétés spectrophotométriques des complexes. A. *Spectres UV-Visible.* ***B.*** *Spectres d'émission de fluorescence.* ***Conditions:*** *[A$\beta_{1\text{-}40}$] = 50 µM, [Th-T] = 10 µM, [PB] = 50 mM, [complexe] = variable, pH = 7, agrégation pendant 4 jours à 37°C.*

IV.1.b.Etudes du site de liaison

- Site de la Thioflavine-T

Des investigations ont été menées afin de déterminer si les complexes métalliques pouvaient se lier sur le(s) même(s) site(s) que la Th-T. Pour cela, une expérience de compétition a été réalisée entre la Th-T et les complexes Ru(**L**^{1})$_2$ et Ru(**L**^{3})$_2$ présents en quantités croissantes. Les résultats montrent que même en présence d'un large excès de complexe, seule une petite quantité de Th-T est déplacée vers le surnageant. Il semble donc que la Th-T et les complexes métalliques s'insèrent dans les fibres sur différents sites.

- Etudes de peptides tronqués

Afin de déterminer les résidus impliqués dans l'interaction fibres-complexes, une étude similaire a été menée sur les peptides β-amyloïdes tronqués $A\beta_{1-28}$ et $A\beta_{1-28}$ (Schéma 43).

$A\beta_{11-28}$	EVHHQKLVFFAEDVGSNK
$A\beta_{1-28}$	DAEFRHDSGYEVHHQKLVFFAEDVGSNK
$A\beta_{1-40}$	DAEFRHDSGYEVHHQKLVFFAEDVGSNKGAIIGLMVGGVV

Schéma 43: Séquences des peptides $A\beta_{11-28}$, $A\beta_{1-28}$, and $A\beta_{1-40}$.

Les complexes Fe($\mathbf{L^1}$)$_2$, Fe($\mathbf{L^3}$)$_2$, Ru($\mathbf{L^1}$)$_2$ et Ru($\mathbf{L^3}$)$_2$ ont été ajouté au début de l'expérience d'agrégation. Une fois formées, les fibres sont collectées et centrifugées, et les surnageants sont dosés. Il s'avère qu'aucun des complexes ne semble s'insérer dans les fibres de peptides tronqués. Pour cela, deux explications sont envisagées : une interaction avec des acides aminés du segment 28-40, ou une différence de morphologie des fibres qui empêcherait l'interaction avec les fibres de peptides tronqués.

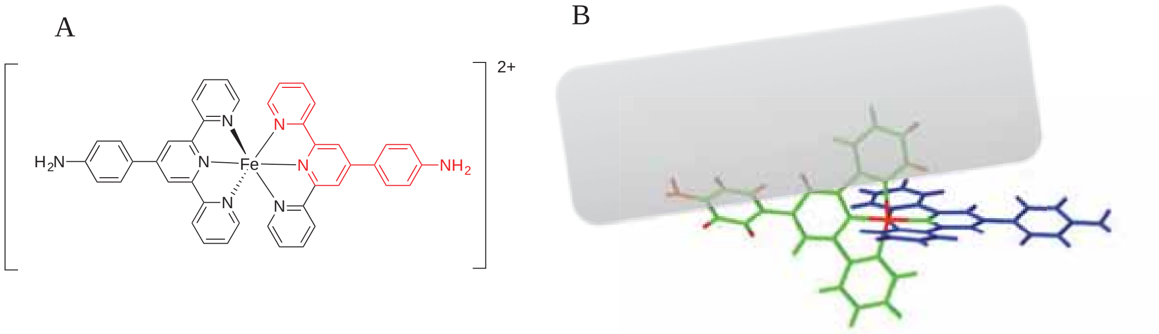

***Schéma 44: Motif d'interaction des complexes métalliques. A**: motif minimal d'interaction proposé; **B:** Modèle proposé pour l'interaction fibre-complexe. La fibre est représentée par un rectangle gris, les deux ligands terpyridines sont représentés en bleu et en vert, les atomes ayant démontrés expérimentalement une interaction avec les fibres apparaissent en rouge.*

IV.1.c. Etude du motif de reconnaissance

Une étude a également été menée afin de connaître le motif minimal nécessaire à l'interaction. La comparaison entre les complexes de Fe(II) et de Ru(II) n'a montré aucun effet de la nature de l'ion métallique. Au contraire, l'interaction observée pour Fe($\mathbf{L^1}$)$_2$ et Fe($\mathbf{L^3}$)$_2$ est complètement perdue avec Fe(**tpy**)$_2$; il semble donc que la présence du groupement phényl (et de ses substituants) soit primordiale à l'interaction.

Une expérience de RMN STD avec le peptide Aβ_{1-40} monomérique a permis de mettre en évidence l'interaction entre les protons des pyridines centrales et latérales avec le peptide [224]. Tout cela nous a permis de proposer un motif minimal d'interaction constitué d'une pyridine latérale, de la pyridine centrale, et du cycle phényl (Schéma 44.A). Un modèle d'interaction a également été envisagé, le complexe s'incorporant dans les sillons formés par les chaines latérales du peptide (Schéma 44.B).

IV.2. Modélisation des systèmes hybrides

IV.2.a.Fibres de Aβ_{1-40}

- Th-T

La Th-T a été dockée dans la structure de fibres de Aβ_{1-40} (code PDB 2LMN) [141]. Les résultats montrent trois sites principaux : à l'interface entre les deux filaments, dans la boucle β, et à l'extrémité de la boucle. Dans les trois cas, la Th-T est enfouie dans les fibres, positionnée parallèlement à l'axe de la fibre (Figure 64, gauche).

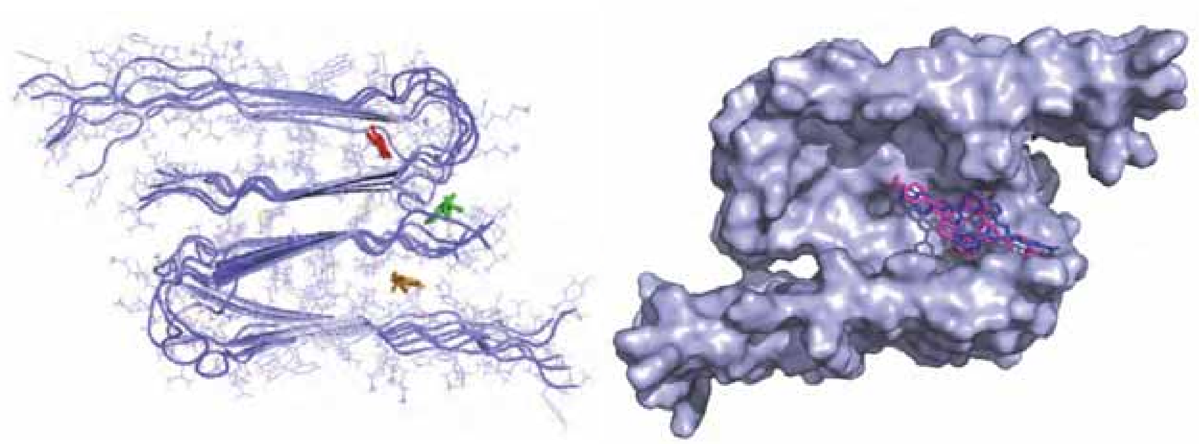

Figure 64: Résultats de docking de la Th-T (gauche) et de Fe(L^1)$_2$ et Fe(L^3)$_2$ (droite) sur la structure 2LMN.

- Fe($\mathbf{L^1}$)$_2$ et Fe($\mathbf{L^3}$)$_2$

Les complexes Fe($\mathbf{L^1}$)$_2$ et Fe($\mathbf{L^3}$)$_2$ ont également été dockés sur la structure 2LMN. Cependant, tous les résultats placent les complexes sur l'extrémité de la fibre (Figure 64, droite). Cela est peut-être dû à la longueur insuffisante de la fibre dans ce modèle. En effet, chaque filament n'est constitué que de six peptides, ce qui pourrait être insuffisant pour modéliser la fibre.

IV.2.b.Fibres de Aβ$_{1-42}$

- Th-T

La structure de la Th-T a été dockée sur la structure des fibres de Aβ$_{1-42}$ (Code PDB 2MXU) [145], montrant un site de liaison majoritaire le long du sillon entre Ile32 et Leu34 (Figure 65, haut). Là encore, la Th-T est positionnée parallèlement à l'axe de la fibre, à l'interface entre la partie rigide et la partie flexible.

- Fe($\mathbf{L}^1$)$_2$

Le docking de Fe($\mathbf{L}^1$)$_2$ a mis en évidence un site de liaison dans le sillon formé par les chaines latérales des Glu22 et Asp23 (Figure 65, gauche). Le groupement amine porté par le ligand forme deux liaisons H avec les carboxylates des chaines latérales. Ce résultat est cohérent avec l'observation expérimentale d'un site de liaison différent de la Th-T.

- Fe($\mathbf{L}^3$)$_2$

Fe($\mathbf{L}^3$)$_2$ a également été amarré sur la structure 2MXU. Contrairement à Fe($\mathbf{L}^3$)$_2$ aucun site n'a été mis en évidence à la surface de la fibre. Le résultat principal place le complexe en travers de l'ouverture de la fibre, empiétant en partie sur le site proposé pour la Th-T. Les résidus Glu11 et His14 étant très flexible, cette position pourrait ne pas être favorable (Figure 65, droite).

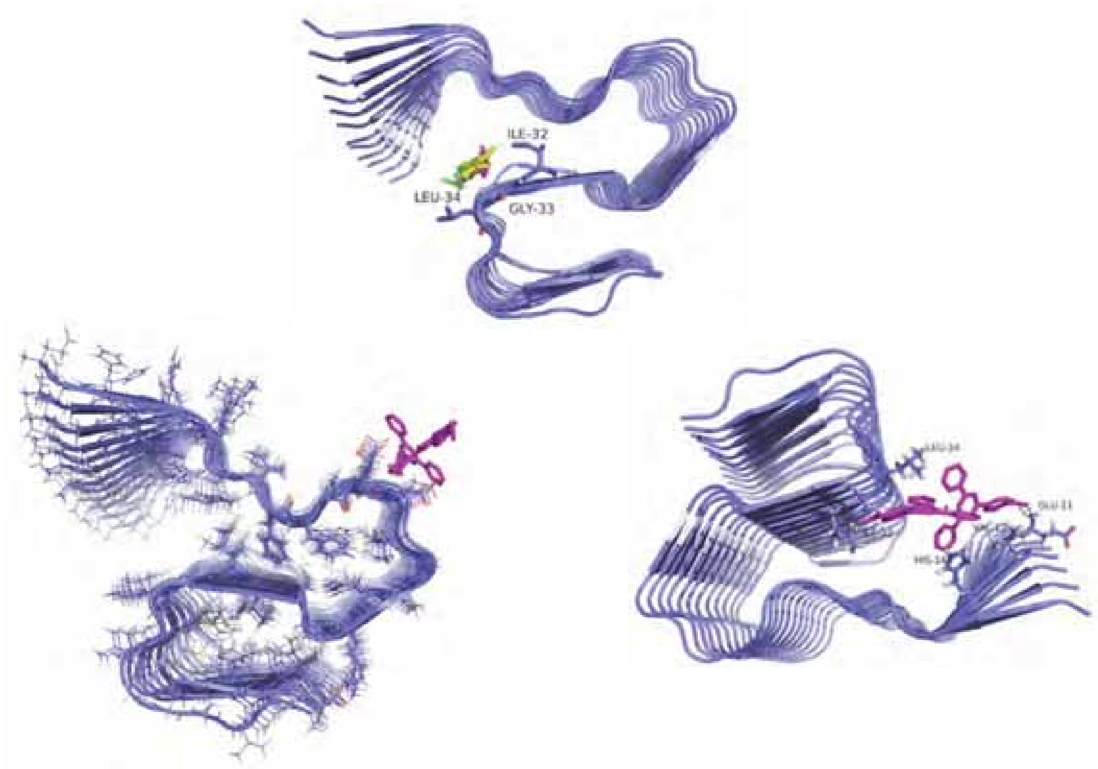

Figure 65: Résultats de docking de la Th-T (haut), de Fe(L^1)$_2$ (gauche) et de Fe(L^3)$_2$ (droite) obtenus sur la structure 2MXU.

Cette étude donne une idée préliminaire des différents sites d'interaction possibles sur ces deux structures de fibres. Cependant, des études dynamiques seront indispensables pour conclure sur la validité de ces sites.

V. Vers des catalyseurs bio-inorganiques hybrides

V.1. Etude des complexes Fe terpyridine en catalyse

Peu d'études de catalyse ont été reportées utilisant les complexes de type Fe(II) bis terpyridine, d'autant moins dans des conditions biocompatibles. En 2008, le groupe de Che a développé des complexes de Fe(II) bis- 4,4',4''-trichloroterpyridine capables de catalyser l'époxydation de différents types d'alcènes à partir d'Oxone et de bicarbonate d'ammonium dans un milieu ACN/eau et à température ambiante (Schéma 45) [234].

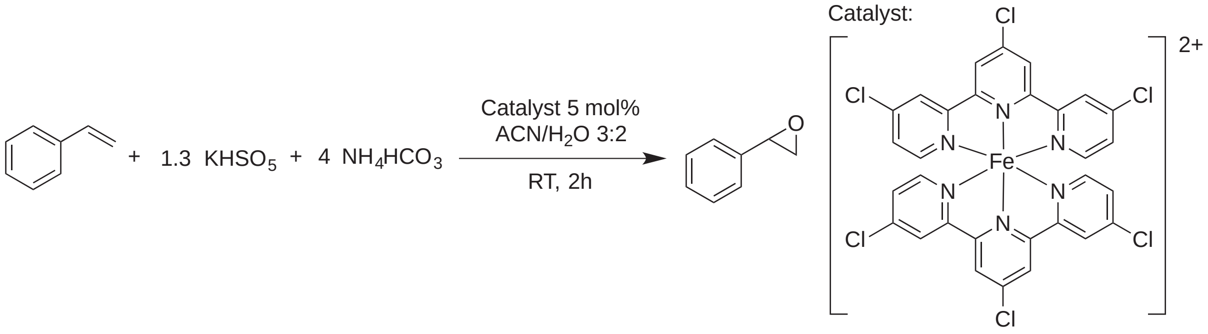

Schéma 45: Réaction d'époxydation décrite par le groupe de Che.

Nous avons choisi de tester cette réaction avec nos complexes de Fe(II). Cependant, alors que Che décrivait la formation quasi-exclusive d'époxyde, un total de cinq produits ont été détectés dans notre cas : le benzaldéhyde (majoritaire), l'époxyde, le diol, l'hydroxy phényl éthanone, et le phényalacétaldehyde (Schéma 46).

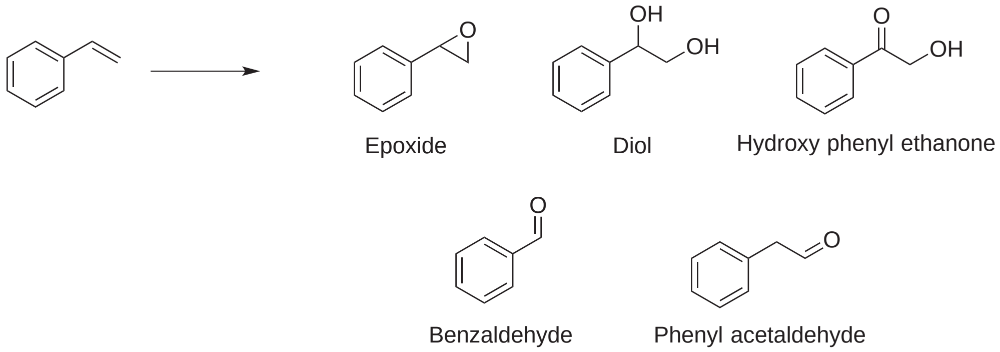

Schéma 46: Différents produits observés par GC pour l'oxydation du styrène.

Notre objectif étant d'observer un transfert de chiralité de l'environnement peptidique au substrat lors de la catalyse. Nous avons donc fait varier les différents paramètres de la réaction de catalyse afin d'observer majoritairement la formation d'un produit prochiral.

- Effet de l'oxydant

Tout d'abord, différentes quantités d'Oxone ont été testées, allant de 1,25 à 15 éq. Il semble que 5 éq soit la quantité nécessaire pour obtenir une conversion totale, formant majoritairement le benzaldéhyde. A partir de 10 éq, le produit majoritairement formé est le 2-hydroxy 1-phényl éthanone. Cependant, cela s'accompagne d'une dégradation du catalyseur.

D'autres catalyseurs, comme le peroxyde d'hydrogène ou le tert-butyl hydropéroxyde, avec différents additifs. Cependant, les conversions obtenues avec ces oxydants sont restées très basses.

- Rôle du bicarbonate d'ammonium

Nous avons cherché à connaître le rôle du bicarbonate d'ammonium dans la réaction. Un essai préliminaire nous a montré que sa présence était essentielle à la faisabilité de la réaction. Il semble que la quantité optimale à utiliser soit de 1 éq, une quantité excessive entrainant une baisse de conversion. Quelque soit la quantité utilisée, le produit majoritaire reste le benzaldéhyde.

- Charge catalytique

Différentes charges catalytiques ont été testées, allant de 0,5 à 5 mol%. Dans cette gamme, la quantité de catalyseur ne semble pas influencer la conversion ou la nature du produit majoritaire formé. Lors des expériences avec nos catalyseurs hybrides, il sera donc possible de descendre jusqu'à 0,5 mol% de catalyseur sans diminuer la conversion.

- Température

La température de réaction a également été modifiée. Les résultats montrent qu'elle n'a que peu d'effet sur la réaction : un passage de 4 à 60°C ne permet d'augmenter la conversion que de 80 à 100%, le produit majoritaire restant le benzaldéhyde. Une température de 25°C sera donc privilégiée, car moins susceptible d'entrainer une dégradation du catalyseur.

- Ordre d'addition

Au cours des expériences de catalyse, nous nous sommes aperçu que l'ordre d'addition des différents réactifs avait une importance pour la réaction. En effet, lorsque l'ajout de l'Oxone avait lieu avant l'ajout du substrat, cela donnait lieu à une dégradation du catalyseur, et à une chute des conversions. Lors des expériences suivantes, l'Oxone a donc été ajoutée en dernier.

Cette étude a permis de déterminer les conditions optimales à utiliser pour nos systèmes Fe(II) bis-terpyridine, mais n'a pas permis d'identifier des conditions menant à la formation majoritaire d'un produit prochiral. Ces conditions ont donc été appliquées à nos systèmes hybrides, afin de démontrer la faisabilité de cette réaction en présence de fibres.

V.2. Etude préliminaire: catalyse sur les systèmes hybrides

Une étude préliminaire a été menée afin de valider que l'activité catalytique des complexes métalliques était maintenue en présence des fibres. Pour cela, des échantillons de fibres contenant des complexes ont été collectés et les fibres ont été isolées par centrifugation. La quantité de complexe insérée dans les fibres a été évaluée par différence avec la quantité restant dans le surnageant après centrifugation. L'expérience de catalyse a ensuite pu être lancée, en prenant soin de réaliser le contrôle en absence de fibres. Les résultats apparaissent en Table 28.

Table 28: Résultats de catalyse en présence des catalyseurs hybrides.

Catalyseur	Oxone éq	Conversion (%)	Produit majoritaire
Fe($\mathbf{L}^1$)$_2$	4	93	Benzaldéhyde
Fe($\mathbf{L}^1$)$_2$	8	100	Benzaldéhyde
Fibres + Fe($\mathbf{L}^1$)$_2$	4	15	Traces
Fibres + Fe($\mathbf{L}^1$)$_2$	8	51	Benzaldéhyde
Fibres + Fe($\mathbf{L}^1$)$_2$ + Th-T	4	0	/
Fibres + Fe($\mathbf{L}^1$)$_2$ + Th-T	8	63	Benzaldéhyde

Il semble que pour une même charge catalytique, la quantité d'Oxone nécessaire pour réaliser la réaction soit supérieure en présence des fibres. Cela peut être dû à un enfouissement du catalyseur, ou à une oxydation du peptide. Il semble par contre que la présence de la Th-T n'interfère pas avec la réaction catalytique.

Ce résultat, bien que préliminaire, constitue une preuve de concept : une réaction peut être catalysée par un système formé d'un complexe de coordination inséré dans des fibres amyloïdes. Malheureusement, aucune induction chirale n'a pu être démontrée, le produit majoritairement formé étant le benzaldéhyde. D'autres substrats pourront donc être testés, afin de rendre possible une induction chirale de la fibre amyloïde vers le produit de catalyse.

V.3. Perspectives: évolution des systèmes hybrides

V.3.a. Autres activités catalytiques

Afin d'explorer toutes les possibilités offertes par nos systèmes catalytiques, d'autres réactivités devront être testées. Des études préliminaires des réactions d'aziridination [234] et de cyclopropanation [232] ont été réalisées, démontrant des conversions ne dépassant pas les 15%. Un test systématique des réactions de catalyse pourra être envisagé pour déterminer les réactivités les plus prometteuses.

V.3.b. Changement d'ion métallique

Les ligands choisis pour cette étude étant capables d'accommoder différents ions métalliques, un changement de métal pourrait également être envisagé. Par exemple, le complexe Mn(**salophen**) a démontré d'excellentes conversions pour la sulfoxydation du thioanisole [82]. Cependant les propriétés d'interaction des complexes de **salophen** avec les fibres s'étant montrées décevantes, une évolution de ce ligand devra être envisagée pour augmenter son intercalation.

V.3.c. Evolution des ligands

Restant sur la réaction d'oxydation des alcènes, différentes évolutions peuvent être imaginées pour nos ligands phényl-terpyridine. Que ce soit chez les enzymes ou parmi les catalyseurs chimiques, il semble que la majorité des sites actifs de fer contiennent quatre ligands et deux positions vacantes, qui permettent l'activation de l'oxydant. Des ligands tétradentes pourraient donc être envisagés, incluant des dérivés de quaterpyridine [244], de phénazine [208] ou de bases de Schiff (Schéma 47).

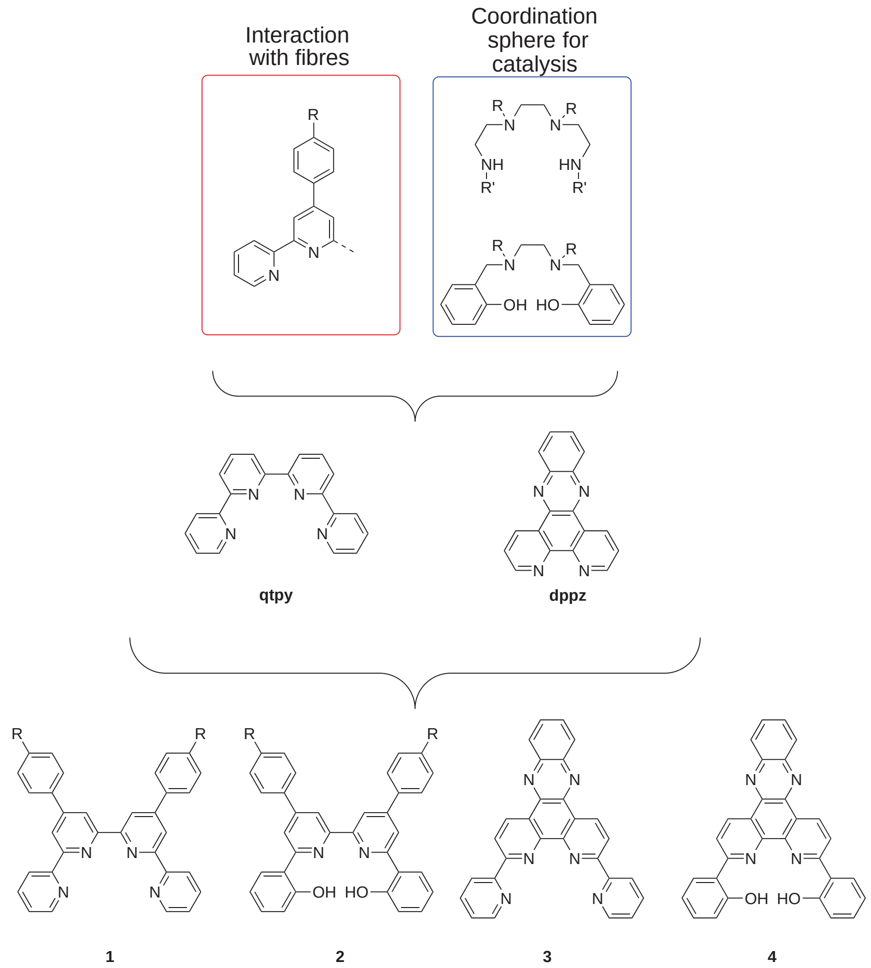

Schéma 47: Proposition d'une seconde génération de ligands.

V.3.d. Modifications sur le peptide

Afin d'augmenter l'interaction entre les complexes et les fibres, une autre possibilité consiste à réaliser une ou plusieurs mutations sur le peptide. Du fait du manque d'informations structurales, la mutagénèse aléatoire semble être la stratégie à privilégier. Bien que cela demanderait un lourd travail d'élaboration d'une méthode de criblage sur colonies, afin d'identifier les mutants d'intérêt, cela pourrait permettre d'augmenter significativement l'interaction.

Les protéines/peptides amyloïdes étant nombreux, il serait également envisageable de cribler les systèmes catalytiques formés à partir de ces différents amyloïdes.

Conclusion

Au cours de cette thèse, nous nous sommes intéressés à l'élaboration de catalyseurs bio-inorganiques hybrides préparés par incorporation de complexes de coordination dans les fibres amyloïdes. Cela s'est fait en trois temps : la production de peptide amyloïde par voie recombinante, la synthèse de complexes métalliques, et l'étude de leur interaction, l'objectif final étant l'étude des propriétés catalytiques du système final.

Pour cela, la production recombinante des peptides β-amyloïdes 1-40 et 1-42 a été réalisée dans *Escherichia coli*. Les conditions d'expression ont été optimisées, et un nouveau protocole de purification a été mis en place, exempté d'étapes chromatographiques. Les échantillons de peptides obtenus démontrent des caractéristiques physicochimiques similaires aux peptides β-amyloïdes commerciaux.

Une série de ligands para phényl terpyridine ont été synthétisés, portant différents substituants. Les complexes de Cu(II), Fe(II), et Ru(II) ont été synthétisés et caractérisés par différentes techniques physicochimiques.

Les complexes de Fe(II) et de Ru(II) ont été testés pour leur interaction avec les fibres de peptide $A\beta_{1-40}$. Parmi la série synthétisée, trois ligands semblent se détacher, démontrant d'intéressantes propriétés d'intercalation. Cela se traduit également par une accélération de la cinétique d'agrégation du peptide en présence des complexes correspondants.

Des études ont été réalisées afin de déterminer le motif de reconnaissance de ces ligands, montrant que l'enchainement pyridine-pyridine-phényl était essentiel à l'interaction. La nature de l'ion métallique semble quant à lui n'avoir aucune influence. Enfin, pour connaître la nature du site d'interaction, une étude a été réalisée avec des fibres de peptides tronqués, montrant une claire différence d'incorporation. Toutefois, le manque d'informations structurales ne permet pas de conclure quant à la nature précise du site de liaison.

Pour obtenir plus d'informations sur ce point, des études de docking ont été menées sur des structures des fibres $A\beta_{1-40}$ and $A\beta_{1-42}$ obtenues par RMN du solide. Les résultats confirment que la Th-T et les complexes métalliques ne se lient pas sur les mêmes sites de la fibre. L'amarrage de $Fe(\mathbf{L^1})_2$ sur le modèle de fibre de $A\beta_{1-42}$ propose la liaison du complexe dans les sillons formés par les chaines latérales à la surface des fibres, par le biais du groupement phényl et d'une pyridine latérale.

La dernière étape pour conclure cette étude consistait à tester l'activité catalytique des catalyseurs hybrides fibre-complexe. Pour cela, nous avons choisi d'étudier la réaction d'époxydation du styrène, décrite avec des complexes de Fe(II) bis terpyridine. Etonnamment, nos complexes n'ont permis de former que le benzaldéhyde. Des résultats préliminaires en présence des fibres ont validé que l’activité catalytique des complexes était maintenue après incorporation.

Ces travaux valident le concept de catalyseurs hybrides préparés à partir de fibres amyloïdes. Bien que ces systèmes présentent déjà des avantages, comme leur production rapide et leur biocompatibilité, ils devront être améliorés pour être à la hauteur des systèmes existants. Pour cela, une optimisation chimio-génétique, combinant des études structurales plus poussées, la mutagénèse du peptide avec l’évolution des complexes de coordination, pourra être envisagée.

Résumé

Le développement d'alternatives durables aux catalyseurs actuels est un sujet clé de la chimie verte. Parmi les différentes approches proposées, **l'élaboration de métalloenzymes artificielles** permet de combiner l'efficacité des enzymes avec la versatilité des catalyseurs chimiques. Dans ce contexte, nous nous sommes intéressés à l'élaboration de **nouveaux catalyseurs hybrides bio-inorganiques**, préparés par **incorporation de complexes métalliques dans les fibres amyloïdes**. Ces agrégats de protéines démontrent des propriétés mécaniques exceptionnelles en biologie, qui en font des candidats de choix pour une application en catalyse.

Une première partie de ce travail a consisté à **surexprimer les peptides β-amyloïdes** dans *Escherichia coli*. Une nouvelle méthode de purification des peptides a ensuite été établie permettant d'obtenir des échantillons de haute qualité en seulement quelques étapes. **Une série de ligands** organiques a également été synthétisée, ainsi que les **complexes de Cu(II), Fe(II) et Ru(II)** correspondants.

L'interaction entre ces complexes et les fibres amyloïdes a été évaluée à l'aide de différentes techniques (UV-Visible, fluorescence, RMN…) et étudiée par modélisation moléculaire pour donner accès à de nouvelles informations concernant les sites potentiels d'interaction.

Enfin, des **études de catalyse** ont été menées sur les complexes de Fe(II), démontrant des conversions élevées pour la réaction d'oxydation du styrène. Des résultats préliminaires sur les systèmes hybrides montrent que cette activité est maintenue en présence de fibres, validant le **concept de catalyseurs hybrides préparés à partir de fibres amyloïdes**.

Abstract

Developing sustainable alternatives to catalytic systems developed to date is a key point of the Green Chemistry Principles. Among the different existing approaches, the **artificial metalloenzyme strategy** aims at combining the efficiency of enzymes with the versatility of chemical catalysts. In this context, we turned our interest in developing a new type of **bioinorganic hybrid catalysts** through **incorporation of coordination complexes in amyloid fibres**. These protein aggregates display unique mechanical properties that make them good candidates for applications in catalysis.

In a first part, our work consisted in **overexpressing amyloid-β peptides** in *Escherichia coli*. A new purification procedure was set up that allowed to obtain peptides in a few steps. **A series of organic ligands** was synthesized, as well as the corresponding **Cu(II), Fe(II) and Ru(II) complexes**.

The interaction between amyloid fibres and metal complexes was assessed, using a set of techniques (UV-Visible, Fluorescence, NMR…). Docking studies were also conducted by molecular modelling to acquire further insights in the interaction.

Finally, **catalytic experiments** were performed with Fe(II) complexes, showing high conversion rates for styrene oxidation reaction. Preliminary results on the final hybrid systems show that the catalytic activity of metal complexes is maintained upon incorporation within fibres. This constitutes **a proof of concept for the elaboration of hybrid catalysts based on amyloid fibres.**